Imperial College London
Department of Materials

Oxygen Ion Transport and Dopant Segregation in Strained Oxide Thin Films

George F. Harrington
2015

Supervised by Prof. John A. Kilner, Prof. Stephen J. Skinner & Prof. David. W. McComb

Submitted in part fulfilment of the requirements for
the degree of Doctor of Philosophy of Imperial College London.

Declaration of Originality

I hereby declare that all work presented here which is not my own has been properly acknowledged.

George F. Harrington

The copyright of this thesis rests with the author and is made available under a Creative Commons Attribution Non-Commercial No Derivatives licence. Researchers are free to copy, distribute or transmit the thesis on the condition that they attribute it, that they do not use it for commercial purposes and that they do not alter, transform or build upon it. For any reuse or redistribution, researchers must make clear to others the licence terms of this work.

"Guess kids these days just can't tell their gravity from their rotating frame of reference"

- Iain M. Banks, "Consider Phlebas"

Acknowledgments

During my PhD I have been in the privileged position of having three supervisors: Prof. John Kilner, Prof. Stephen Skinner and Prof. David McComb. They have provided excellent guidance, council and encouragement throughout this process, without which this work could not have taken place. I am extremely grateful for the support they have given me.

I would like to express my utmost gratitude to Dr. Andrea Cavallaro, who has served as a mentor during this work. I am tremendously thankful for the time spent and the patience shown towards me. I am also particularly indebted to Dr. Ainara Aguadero for much support and advice throughout my PhD.

I express my thanks to Dr. Sarah Fearn and Dr. Richard Chater for their invaluable assistance and teaching regarding surface analysis with ion beams, tracer diffusion, and general scientific advice. I am grateful for the assistance and instruction from Mr. Richard Sweeney with x-ray diffraction, as well as Dr. Catriona McGilvery, Dr. Mahmoud Ardakani and Dr. Ecaterina Ware with transmission electron microscopy. I am also grateful for the coaching in electron microscopy sample preparation by Dr. Robert Williams of Ohio State University.

My thanks go to the past and present members of the Electroceramics group (formerly known as the Fuel Cells Group), as well as the greater network of the Department of Materials, for their help, support, friendship, and for making my time at Imperial College immensely enjoyable.

Abstract

Modified ionic transport at interfaces in oxide conductors has received significant interest recently, yet previous studies have provided inconsistent and often controversial results. Lattice strain occurring at heterogeneous interfaces or surrounding dislocations is often speculated as the cause for enhanced transport properties, yet direct evidence for this is lacking. The aim of this work was to investigate the possibility for modified oxygen conductivity at interfaces and develop a greater understanding of the underlying mechanisms.

In this work, it was shown that the crystallographic orientation of yttria-stabilised zirconia (YSZ) films fabricated by pulsed laser deposition (PLD), could be altered by the roughness and the temperature of the substrate during deposition. Furthermore, the films were seen to feature an expanded out-of-plane lattice parameter, which was found to be dependent upon the deposition temperature, substrate, the orientation of film, and the thermal history after growth.

The ionic transport of YSZ films fabricated on a range of substrates was assessed as a function of film thickness using electrochemical impedance spectroscopy (EIS) and a novel method of oxygen isotope exchange tracer diffusion (IETD). No enhancement over the conductivity of bulk YSZ was observed, despite expanded out-of-plane lattice parameters, substrates representing both positive and negative lattice mismatch, and a high density of interfacial dislocations. Instead, all interface regions were found to be more resistive due to a higher density of grain boundaries.

Finally, gadolinia-doped ceria (CGO) films were analysed by low energy ion scattering (LEIS), to investigate the effects of dopant segregation to

the surface and sub-surface regions. Gd segregation was found to occur for all films and observed to increase for higher annealing temperatures. Investigations into the affect of the lattice parameter on the rate of dopant segregation showed a possible link between segregation and lattice strain.

Contents

Acknowledgments **7**

Abstract **12**

Table of Contents **16**

List of Figures **31**

List of Tables **33**

1 Introduction **35**

1.1 Global Energy Demand 35
1.2 Solid State Oxygen-Ion Conductors 36
1.3 Potentials of Miniaturisation 39
1.4 Wider Context 40
1.5 Thesis Aims 41

2 Theoretical Considerations **43**

2.1 Defects in Crystalline Oxides 43
2.1.1 Fluorites 44
2.1.2 Intrinsic Defects 45
2.1.3 Extrinsic Defects 47
2.2 Ionic Conductivity 50
2.2.1 Arrhenius Relationship 52
2.2.2 Defect Association 54
2.3 Interfaces and Microstructure 60
2.3.1 Homogeneous Interfaces 61

2.3.2 Heterogeneous Interfaces 66
2.4 Surfaces 74
2.4.1 Surface Segregation 75
2.5 Summary 79

3 Literature Review **81**
3.1 Ionic Transport in Nanostructured Materials 81
3.1.1 Nano-granular Materials 82
3.1.2 Single Thin Films 88
3.1.3 Multilayer Structures 104
3.1.4 Macroscopically Strained YSZ 113
3.1.5 Computational Studies 113
3.1.6 Section Summary 117
3.2 Surface Segregation in Doped Fluorites 119
3.2.1 Cation Diffusivity 119
3.2.2 Surface Segregation: Experimental Studies 121
3.2.3 Surface Segregation: Computational Studies 123
3.2.4 Section Summary 124
3.3 Conclusion 127

4 Experimental Methods **129**
4.1 Pulsed Laser Deposition 129
4.1.1 General Deposition Procedure 130
4.1.2 PLD Target Fabrication 132
4.2 X-Ray Diffraction 132
4.2.1 $\theta/2\theta$ Scans 133
4.2.2 Pole Figures 134
4.2.3 Miscut Measurements 135
4.3 Transmission Electron Microscopy 136
4.3.1 Sample Preparation by Focus Ion Beam (FIB) Sectioning 139
4.4 Electrochemical Impedance Spectroscopy 140
4.4.1 EIS Measurement Method 143
4.5 Isotope Exchange Tracer Diffusion 144

4.5.1 Secondary Ion Mass Spectrometry 145
4.5.2 Time of Flight SIMS 146
4.5.3 Diffusion Theory 148
4.5.4 Experimental Setup 152
4.5.5 Method Optimisation 154
4.6 Low Energy Ion Scattering 165
4.7 Summary 168

5 Orientation and Lattice Strain of YSZ Films 169
5.1 Sample Production 169
5.2 Orientation Manipulation 170
5.2.1 Substrate Pre-treatment 171
5.2.2 Substrate Miscut 182
5.2.3 Substrate Temperature 183
5.2.4 Discussion 185
5.3 Lattice Parameter Manipulation 188
5.3.1 Discussion 192
5.4 Conclusion 198

6 Ionic Transport in Strained YSZ Films 201
6.1 Sample Production 202
6.2 Structural Characterisation 202
6.2.1 XRD: Orientation and Lattice Strain 202
6.2.2 XRD: Texture 207
6.2.3 TEM: Orientation and Microstructure 211
6.3 Transport Characterisation 217
6.3.1 EIS: Electrical Conductivity 217
6.3.2 IETD: Oxygen Diffusivity 220
6.4 Discussion 228
6.4.1 Orientation and Substrate Mismatch 228
6.4.2 Oxygen Ion Transport 231
6.5 Conclusion 241

7 Surface Segregation in Strained CGO Films **243**
7.1 Sample Production 244
7.2 Structural Characterisation 244
7.2.1 Orientation and Texture 244
7.2.2 Lattice Strain 249
7.3 Surface Segregation 253
7.3.1 Temperature Dependence 259
7.3.2 Lattice Strain and Orientation Dependence 260
7.4 Discussion 264
7.5 Conclusion 268

8 Conclusions and Outlook **269**
8.1 Conclusions 269
8.2 Outlook 274

A Appendices **277**
A.1 XRD $\theta/2\theta$ Patterns from the PLD Targets 277
A.2 XRD $\theta/2\theta$ Patterns from YSZ Films in Chapter 6 279
A.3 ^{18}O Lateral Diffusion Profiles for the YSZ Films in Chapter 6 283
A.4 Consideration of Errors from EIS Measurements in Chapter 6 287
A.5 LEIS Depth Profiles of CGO Films in Chapter 7 289

Bibliography **317**

List of Publications **319**
Journal Publications from this Thesis 319
Conference Contributions from this Thesis 319

List of Figures

1.1 A schematic diagram demonstrating the operating principles of a solid oxide fuel cell. 37

2.1 Cubic fluorite crystal structure represented as (a) a FCC metal cation unit cell and (b) simple cubic oxygen sublattice with alternating body filled centres. 44

2.2 Phase diagram of the ZrO_2 rich region of the ZrO_2 - Y_2O_3 binary system (adapted from Ref. [21]). 45

2.3 Change in density of ZrO_2 - CaO solid solutions quenched from (a) 1600°C and (b) 1800°C. The theoretical density of predicted from a vacancy and interstitial compensation mechanism is also plotted. Data taken from Diness and Roy [23]. 48

2.4 Measured lattice parameters of M_2O_3 - CeO_2 solid solutions with dopant concentrations, where M_2O_3 is a rare earth oxide. Data taken from Hong and Virkar [24]. 49

2.5 Local lattice relaxations around an oxygen vacancy (a) and a substituted cation with a radii larger than the host lattice (b). Adapted from Marrocchelli *et al.* [25]. 50

2.6 Potential energy of an ion in the lattice against distance with (a) no applied field and (b) an externally applied electric field. 52

2.7 Variations in the low temperature activation enthalpy and isothermal conductivity (at 182°C) as a function of composition, for the Y_2O_3 - CeO_2 solid solutions. Taken with permission from Wang *et al.* [34]. 55

2.8 Arrenhius plot showing the different stages of ionic conductivity. . 57

2.9 Activation energy of doped CeO_2 solid solutions as a function of dopant ionic radius and concentration. Taken from Kilner [43], data taken from Faber *et al.* [39]. 59

2.10 Calculated binding energies for a M^{3+} dopant to an oxygen vacancy. The radius of a Ce^{4+} cation is shown for comparison. Taken with permission from Minervini *et al.* [44]. 60

2.11 Schematic representation of a grain boundary, showing both the electrical and structural regions. 63

2.12 Schematic representation of grain boundary conduction pathways. Taken with permission from Guo and Waser [47]. 66

2.13 Schematic diagram of the brick layer model. Taken with permission from Guo and Waser [47]. 67

2.14 2D sketch representing the three classifications of interface: coherent (a), semi-coherent (b), and incoherent (c). Also included is the simplified dependence on the lattice mismatch, $f_{1,2}$. Taken with permission from Korte *et al.* [58]. 68

2.15 (a) Model of an edge dislocation in a cubic lattice, enclosed within a Burgers circuit. (b), the same circuit in a perfect crystal; the closure failure is equal to the Burgers vector. 72

2.16 (a) Schematic of an edge dislocation formed in a crystal. (b), A cylindrical ring representing the elastically strained region around the same dislocation depicted in (a). Adapted from Hull and Bacon [65]. 73

2.17 Distribution of charged and neutral planes at the surface of a crystal. (a) Type 1 surface: Neutral planes. (b) Type 2 surface: Charged planes but with no net dipole moment perpendicular to the surface. (c) Type 3 surface: Charged plane and non-zero dipole perpendicular to surface. Adapted from Tasker [66]. 75

2.18 Segregation and diffusivity in a binary system, plotted on (a) a linear axis and (b) as an Arrenhius diagram. The black line represents the surface concentration at $t = \infty$ given by Eq. 2.54. The dashed lines represent the surface concentration for given diffusion times, such that $t_1 < t_2 < t_3$. 77

3.1 Bulk conductivities and specific grain boundary conductivities for 3 mol.% YDZ at 550 °C as a function of average grain size. Taken with permission from Guo *et al.* [72]. Data included in the plot orginates from Mondal *et al.* [73]. 83
3.2 Literature activation energies of electrical conductivity of 20 mol.% CGO films as a function of grain size. Adapted from Ref [96]. Data taken for spin coating taken from Ref [94], flame spraying from Ref [95], spray pyrolysis from Ref [91], PLD1 from Ref [89], PLD2 from Ref [90], PLD3 from Ref [91], and RF sputtering [92]. . 87
3.3 (a) Lattice parameters of doped-CeO_2 films grown by Rupp *et al.* after heat treatments at 600°C and 1000°C. (b) Arrhenius plot of the CGO films for different lattice parameters after heat treatment. Data taken from Ref. [97]. 88
3.4 Measured conductivity of YSZ films of varying thickness using (a) a low-purity alumina support and (b) a high-purity alumina support. Taken with permission from Ref. [104]. 90
3.5 (a) The total resistance of the film/substrate system as a function of thickness for a range of temperatures. (b) An Arrhenius plot of the conductivity for varying thicknesses of YSZ thin films. Reproduced with permission from Ref. [107]. 92
3.6 (a) HR-TEM image of the the YSZ/MgO interface, taken with permission from [106]. (b) Fourier transformation indicating the (020) planes with the dislocations marked [110]. 93
3.7 (a) HR-TEM of the YSZ/MgO interface and (b) Arrhenius plot of the conductivity with respect to temperature for 12 and 25 nm thin films and bulk YSZ. Taken with permission from Ref. [113]. 94
3.8 (a) Arrhenius plot of the temperature dependent conductivity for a number of YSZ film grown on MgO and sapphire of varying thickness, with the single crystal conductivity for comparison. Reproduced with permission from Ref. [114]. (b) The effective resistivity normalised to thickness for the same films. Data taken from Ref. [114]. 96
3.9 (a) Dislocation network at the YSZ/MgO interface and (b) lateral ionic conductivity of the YSZ thin films of varying thicknesses on different substrates. Reproduced with permission from Ref. [115]. . 97

3.10 (a) Out-of-plane lattice parameters of the YSZ/ Al_2O_3 films measured both before and after EIS measurements and (b) Arrhenius plot showing the conductivity of the films. Reproduced with permission from Ref. [119]. 99
3.11 Maximum deviation in the in-plane conductivity of YSZ thin films compared to bulk. Data taken from Refs. [106, 107, 113–115, 117, 119–121]. 102
3.12 (a) Expected trend with ionic conductivity and thickness for multilayed samples and (b) the conductivity against reciprocal thickness for the CSZ/Al_2O_3 system. Taken with permission from Ref. [127]. 106
3.13 Relative ionic conductivity and diffusivity coefficients from the YSZ/RE_2O_3 multilayer systems against the reciprocal thickness, $1/d$. The fits are based on Eq. 2.49. Taken from Ref. [63]. 107
3.14 (a) Z-contrast HR-STEM image of the YSZ/STO interfaces of a 1 nm thick YSZ layer and (b) Arrhenius plot of YSZ/STO tri-layers with bulk YSZ for comparison. The insets show the conductance as a function of the number of layers and layer thickness. Reproduced with permission from Ref. [133]. 109
3.15 (a) HAADF-STEM images of the YSZ islands grown on STO. (b) Arrhenius plot showing the enhancement in the conductivity of the YSZ structures compared with those grown by García-Barriocanal *et al.* [133], bulk YSZ and bulk STO. Reproduced with permission from Ref. [102]. 110
3.16 (a) Bright-field HR-TEM image of a YSZ/CeO_2 multilayer and corrisponfing distributions of the strains (b) in-plane and (c) out-of-plane. Adapted with permission from Ref. [142]. Copyright 2012 American Chemical Society. 111
3.17 (a) TEM image of the dislocations induced in a 10 mol.% YSZ single crystal by 10% mechanical deformation and (b) the normalised conductivity as a function of plastic strain. Adapted with permission from Ref. [154]. 114
3.18 Computed relative changes in the oxygen diffusion coefficient in 9 mol.% YSZ under tensile strain. Taken with permission from Ref. [156]. 115

3.19 The simulated activation energies of oxygen ion migration on the dopant ionic radius and strain. Data taken from Ref. [161]. 116

3.20 (a) Depth profile for ^{88}Y in 11.1 mol.% YSZ after heating for 72 at 1598 °C and (b) the Arrhenius relationship of for the bulk and dislocation diffusion pathways for different dopant concentrations. Taken with permission from Ref. [165]. 120

3.21 Layered surface structures of YSZ reported by (a) Hughes [176] and (b) De Ridder *et al.* [177]. Adapted from Ref. [178]. 122

3.22 LEIS spectra (a) 3 keV $^{4}He^{+}$) of 10 mol.% YSZ after annealing at 600 and 1200°C. b) Arrhenius plot of the Y segregation to the surface of 3 and 10 mol.% YDZ. The line indicates the free energy for segregation. Reproduced with permission from Ref. [179]. . . . 123

3.23 MD simulations of 10 mol.% YSZ and CGO slabs. Dopant cation positions projected onto the x-y plane for (a) YSZ and (b) CGO. Dopant cation fractions along x-axis for (c) YSZ and (d) CGO. Host cation fraction for (e) YSZ and (f) CGO. Ratio of the dopant and host cations for (g) YSZ and (h) CGO. Oxygen vacancy fractions for (i) YSZ and (j) CGO. Reproduced with permission from Ref. [181]. 125

3.24 Segregation energies as a function of distance from surface calculated for the the three low index surfaces by atomistic simulations. Data taken from Ref. [183]. 126

4.1 Schematic diagram of the pulsed laser ablation process. (a) Initial absorption of the laser radiation (long arrows) and melting of the target material (short arrows). (b) Melting continues and vaporisation of the target occurs. (c) Laser-plume interactions due to absorption of the incident laser radiation by the plume causing plasma formation. (d) Melt front recedes and surface re-solidifies. Adapted from Ashford *et al.* [185]. 130

4.2 Schematic illustration of the PLD system setup. 131

4.3 Visualisation of the Bragg equation. 133

4.4 Schematic diagram of the axes and angles discussed with regards to XRD measurements. The dashed line represents the x-ray path. 134

4.5 Simplified schematic of the two basic operation modes of the TEM. (a) selected area electron diffraction mode (SAED) and (b) imaging mode. Adapted from Williams and Carter [189]. 137

4.6 Comparison of the position of the objective aperture for (a) bright field imaging and (b) dark field imaging. Adapted from Ref. [189]. 139

4.7 Nyquist plot for a typical polycrystalline ceramic electrolyte with the representative equivalent circuit. 142

4.8 (a) schematic of the electrode geometry used defining the notation used to describe the electrodes width B, length L and distance between them D. (b) the equivalent circuit for a thin polycrystalline film of an ionic conductor on an insulating substrate. (c) the modified equivalent circuit used to fit the Nyquist plots in this work. 143

4.9 Representation of the SIMS process. Dashed lines represent the collision paths. 145

4.10 Schematic diagram of the TOF.SIMS^5 instrument. It consists of Bi^+ LMIG for analysis (A), low energy Cs^+ sputter gun (S), electron flood gun (EF), extraction electrode (EE) and time-of-flight mass spectrometer (TOF), with reflectron (R) and detector (D). The components are housed in an ultra-high vacuum (UHV) chamber. Taken with permission from Ref. [195]. 147

4.11 Schematic diagram of the experimental apparatus used to anneal films in isotopically enriched gas. 153

4.12 Trench through a Au layer and YSZ film created using a diamond tipped scribe. 155

4.13 An optical image of the edge of a Au coated film snapped using a diamond saw (a). ^{18}O signal maps of the edge obtained by SIMS after exposure to isotopically enriched gas (b, c). Diffusion profile of the marked area in (b), fitted with Eq. 4.20 (c). 156

4.14 Schematic diagrams of the procedure used to create a ^{18}O diffusion profile in the films. 157

4.15 SEM micrographs of the Au edge created using a Omniprobe lift-out grid as a mask. 158

4.16 (a) normalised ^{18}O ratio after the incorporation step, compared to a step function. (b) the normalised ^{18}O ratio after the diffusion step, fitted using Eq. 4.21. The insets show the maps of the ^{18}O normalised concentration. Below are the differences between the real and idealised cases. 159

4.17 The raw ^{18}O and ^{16}O profiles for the data plotted in Fig. 4.16a. . . 160

4.18 Concentration gradient as a function of x. 161

4.19 The effect of the time constant, τ, on the D^* values and relative errors of a numerically fitted profile which was simulated according to Eq. 4.21 with a D^* of 1.00×10^{-9} cm^2 s^{-1}. 163

4.20 Normalised ^{18}O ratio after the diffusion step, fitted using Eq. 4.21. The insets show the maps of the ^{18}O normalised concentration. Below is the differences between the experimental data and the fit. The solid lines represent the region fitted using the χ^2 function, and the dashed shows the rest of the simulated profile for the final D^* value. Note that the x-axis is no longer centred at x =0, as it was in Figs. 4.16a and 4.16b, because this is no longer required for the numerical fitting procedure as it was for when fitting using the empirical solution Eq. 4.21. 164

4.21 Schematic of the components in a typical LEIS set-up. 167

5.1 (a) SEM micrograph and (b) AFM image of the unpolished MgO surface. (c) height profile along the grey line shown in the AFM image. 172

5.2 XRD $\theta/2\theta$ spectra of the YSZ films fabricated using substrates of different roughness. The peaks marked with $*$ are due to a reflection from the substrate peak coming from the Kβ radiation component. 173

5.3 XRD pole figures for the YSZ (220) and MgO (220) reflections for the films grown on polished and unpolished MgO substrates. . . . 174

5.4 Schematic representation of the orientation relationships for the YSZ films grown on (a) polished and (b) unpolished MgO substrates. 176

5.5 (a), (c), and (e) are of a YSZ film grown on a polished MgO substrate, and (b), (d), and (f) are of a YSZ film grown on an unpolished MgO substrate. SAED of the films are shown in (a) and (b), with the spots indexed. The grey/italic indices refer to the substrate reflections, the black/non-italic indices refer to the film reflections, and square brackets refer to the beam direction. (c), (d), (e) and (f) are TEM micrographs of the films. In (e) and (f), the lattice spacings correspond to the planes labelled on the images. The inset in (f) shows a FFT-filtered image of the marked region, displaying the presence of interfacial dislocations. 178

5.6 XRD $\theta/2\theta$ spectra of the YSZ films grown on as-received polished MgO, and onto homo-epitaxial buffer layers grown at 500°C and 850°C. The peaks marked with $*$ are due to a reflection from the substrate peak coming from the Kβ radiation component. 180

5.7 Calculated volume fraction for the (100) oriented grains form YSZ films grown on MgO substrates heat-treated at a range of temperatures for 2 hours. 182

5.8 Calculated volume fraction for the (100) oriented grains form YSZ films grown on MgO substrates heat-treated at a 1000°C for a range of times. 183

5.9 Fraction of (100) orientation for YSZ films against the miscut angle of the MgO substrates, δ. 184

5.10 Fraction of (100) orientation for YSZ films grown on MgO and Al_2O_3 for different substrate temperatures. 185

5.11 Gibbs free energy as a function of the radius for the formation of a new phase. The total Gibbs free energy is a sum of both the surface, $\Delta G_{Surface}$, and bulk, ΔG_{Bulk}, free energies resulting in an energy barrier with maximum at a radius $r = r^*$. 186

5.12 (111) YSZ peaks in the XRD spectra taken for films grown on MgO (a) and Al_2O_3 (b) substrates. Also plotted are the films grown at 600°C after a post-anneal at 1000°C for 6 hours. The fits for each film peak are pseudo-Voight functions. In addition is the (111) peak from a sintered pellet, fitted with a pseudo-Voight functions using both the $K_{\alpha 1}$ and $K_{\alpha 2}$ wavelengths. 190

5.13 Lattice parameters calculated from the (111) and (200) peaks in the XRD $\theta/2\theta$ for YSZ films grown on MgO and Al_2O_3 substrates as a function of growth temperature and post-growth thermal treatment. The grey shaded area denotes the lattice parameters measured after annealing the as grown films. The lines are only as a guide to the eye. The bulk YSZ lattice parameter is taken from the bulk sintered PLD target. 191

5.14 Lattice spacing calculated from XRD measurements for YSZ films from the literature. The author, substrate and film orientation are displayed in the legend. Details regarding the film properties are listed in Table 5.1. 193

6.1 XRD $\theta/2\theta$ spectra from >180 nm and ∼10 nm YSZ films grown by PLD on (a) MgO, (b) Al_2O_3, (c) LAO and (d) NGO. The peaks marked with a $*$ are due to the substrate peaks. 203

6.2 XRD $\theta/2\theta$ spectra from a 100 nm and 10 nm YSZ films grown by RF sputtering on Al_2O_3 substrates. 204

6.3 (111) YSZ peaks in the XRD $\theta/2\theta$ spectra from a 10 nm film and 110 nm film both as-grown and after annealing for 6 hours at 1000°C. The fits are pseudo-Voigt functions. 205

6.4 Out-of-plane lattice parameters as a function of film thickness calculated from the peak position of either the (111) or (200) reflection, corresponding to the dominate orientation of the film. The lattice parameter refined from the PLD target is also displayed. The fitted lines act only as a guide to the eye. 206

6.5 Out-of-plane lattice parameters as a function of film thickness calculated from the peak position of either the (111) reflection of the films grown on Al_2O_3 by PLD and RF sputtering. Also, the lattice parameters for the YSZ films reported in Ref. [119] are included. The growth temperature of each set of films is included in the legend. The fitted lines act only as a guide to the eye. 207

6.6 (a), (c), (e), and (g) show the pole figures corresponding to the (220) YSZ peaks for a films grown on MgO, Al_2O_3, LAO, and NGO respectively. Also displayed are the pole figures for the (b) MgO (220), (d) Al_2O_3 (012), (f) LAO (220), and (h) NGO (101) reflections. 208

6.7 SAED patterns taken from YSZ films grown on (a) MgO, (b) Al_2O_3, (c) LAO and (d) NGO. The black indices (non-italic) refer to the film and the grey (italic) to the substrate. The zone axis of the electron beam is shown in the bottom right of each pattern. 212

6.8 Bright field images of as-grown YSZ films on (a) MgO and (b) Al_2O_3 substrates and (c) Al_2O_3 after heat treatment of 1000°C for 6 hours. 213

6.9 Lattice images of low angle grain boundaries in films grown on (a) MgO and (b) Al_2O_3. The region between the dotted lines has been Fourier filtered, revealing the low density of misfit dislocations between the grains. 214

6.10 Lattice images of the film-substrate interface for YSZ grown on (a) MgO, (b) Al_2O_3, (c) LAO, and (d) NGO. Each image has been Fourier filtered using the YSZ (222) peak in (a) and the YSZ (220) peak in (b), (c), and (d). The dislocations are marked and the position on the interfaces indicated with dotted lines. 215

6.11 Conductance of a LAO and NGO substrate compared to a 185 nm thick YSZ film grown on Al_2O_3, using a similar electrode geometry. 217

6.12 Typical Nyquist plots taken for YSZ films of various thickness on (a) MgO and (b) Al_2O_3 substrates at approximately 510°C. 219

6.13 Arrhenius plot of multiple EIS measurements made on an 10 nm thick film on Al_2O_3. 220

6.14 Arrhenius plot of the conductivity of the films grown on MgO. All films were deposited at a nominal substrate temperature of 700°C and received no additional thermal treatment (other than the electrode application procedure) unless stated in the legend. The YSZ single crystal data is taken from Ref. [113]. 221

6.15 Arrhenius plot of the conductivity of the films grown on Al_2O_3. All films were deposited at a nominal substrate temperature of 600°C and received no additional thermal treatment (other than the electrode application procedure) unless stated in the legend. The YSZ single crystal data is taken from Ref. [113]. 222

6.16 Lateral profiles of the ^{18}O isotope fraction for YSZ films grown on (a, b) MgO, (c, d) Al_2O_3, (e, f) LAO, (g, h) and NGO. The insets show the ^{18}O isotope fraction integrated in the z-axis direction. In (a, c, e, and g) the ^{18}O distribution across the Au covered and uncovered region is shown after the incorporation step of 30 minutes at 300°C in ^{18}O enriched gas. In (b, d, f, and h) the subsequent ^{18}O distribution after annealing for 14 hours at 500°C is shown. The profiles in (b and d) are fitted using the numerical method in Section 4.5.5, and the profiles in (f and h) are fitted according to Eq. 4.21. 224

6.17 Lateral profiles of the ^{18}O isotope fraction for a 100 nm and 6 nm thick YSZ film grown by RF sputtering on Al_2O_3. The insets show the ^{18}O isotope fraction integrated in the z-axis direction. In (a and c) the ^{18}O distribution across the Au covered and uncovered region is shown after the incorporation step of 30 minutes at 300°C in ^{18}O enriched gas. In (b and d) the subsequent ^{18}O distribution after annealing for 2 hours at 480°C is shown. The profiles in (b and d) are fitted using the numerical method described in Section 4.5.5. 226

6.18 Schematic showing the preferential orientations of the YSZ films on (a) MgO, (b) Al_2O_3, (c) LAO, and (d) NGO substrates. 232

6.19 Normalised sample conductivity, $\sigma_{tot}/\sigma_{vol}$ and diffusivity D_{tot}/D_{vol} to the values obtained for the thickest films as a function of reciprocal lattice parameter. The lines are only present as a guide to the eye and do not represent any fitting. 235

6.20 Conductivity measured by EIS and IETD for the films as a function of lattice parameter. All the measurements were carried out at approximately 500°C as detailed in Table 6.1. (a) shows the as-grown films with no heat treatment other than the diffusion conductions or the electrode sintering. (b) shows the comparison between the as-grown films and the films after a high temperature (≥800°C) anneal. 238

7.1 XRD $\theta/2\theta$ spectra for 330 nm thick CGO films deposited on Al_2O_3, LAO and STO substrates. 245

7.2 (a, c, e) are XRD pole figures about the (111) CGO peak for films deposited on Al_2O_3, LAO and STO substrates respectively. Also shown are the pole figures from the (b) Al_2O_3 (104), (d) LAO (111), and (f) STO (111) reflections. 247

7.3 Schematic showing the orientations of the CGO films grown on (a) Al_2O_3, (b) LAO, and (c) STO. 248

7.4 (a) (111) and (b, c) (200) CGO peaks in the XRD $\theta/2\theta$ spectra for a range of film thicknesses grown on (a) Al_2O_3, (b) LAO and (c) STO substrates. 251

7.5 Out-of-plane lattice parameters as a function of thickness calculated from the peak position in the XRD $\theta/2\theta$ scans. The lines act only as a guide to the eye. 252

7.6 (200) CGO peaks in the XRD $\theta/2\theta$ spectra for films fabricated on LAO and STO substrates directly as-grown and after annealing at 800°C. 253

7.7 Surface 3 keV ^{4}He LEIS spectra for CGO films after heat treatment (a) without any solvent cleaning and (b) after solvent cleaning. . . 254

7.8 Typical 5 keV ^{20}Ne LEIS spectra for a CGO films (a) of the outermost surface, and after a sputter dose of (b) 0.47×10^{15} ions/cm^2, and (c) 13.9×10^{15} ions/cm^2. 256

7.9 Typical area of the Ce and Gd peaks as a function of sputter dose. The estimated depth was calibrated using a calculation in the SRIM software. The horizontal dashed lines are the peak areas taken as the bulk reference signal, $S'_{i,bulk}$. 257

7.10 Normalised cation coverage of Ce and Gd as a function of sputter dose. 259

7.11 Normalised Gd ratio as a function of sputter dose for CGO films grown on STO after a heat treatment at a range of temperatures. . 260

7.12 Arrhenius plot for the surface ratio of cation fractions of CGO films as a function of post growth heat treatment. The activation energy calculated from the fitted slope is 11.6 kJ/mol. 261

7.13 Normalised Gd ratios as function of out-of-plane lattice parameter for films of various thickness grown on Al_2O_3, LAO and STO substrates. The N'_{Gd} values are taken from (a) the surface spectra and (b) the sub-surface spectra after a sputter dose of 0.4-0.47$\times 10^{15}$ ions/cm^2. 263

A.1 XRD $\theta/2\theta$ pattern from the sintered YSZ PLD target prior to deposition. The pattern has been refined using the Le Bail method for a cubic fluorite structure yield a lattice parameter of a_{YSZ} = 0.5139 nm. 277

A.2 XRD $\theta/2\theta$ pattern from the sintered CGO PLD target prior to deposition. The pattern has been refined using the Le Bail method for a cubic fluorite structure yield a lattice parameter of a_{CGO} = 0.5418 nm. 278

A.3 XRD $\theta/2\theta$ patterns from the YSZ films grown on MgO substrates with a nominal substrate temperature of 700°C during deposition. The peak marked with a $*$ are due to the substrate peaks. The samples labels correspond to those in Table 6.1. 279

A.4 XRD $\theta/2\theta$ patterns from the YSZ films grown on MgO substrates with a nominal substrate temperature of 600°C during deposition. The peak marked with a $*$ are due to the substrate peaks. The samples labels correspond to those in Table 6.1. 280

A.5 XRD $\theta/2\theta$ patterns from the YSZ films grown on Al_2O_3 substrates with a nominal substrate temperature of 600°C during deposition. The peak marked with a $*$ are due to the substrate peaks. The samples labels correspond to those in Table 6.1. 281

A.6 XRD $\theta/2\theta$ patterns from the YSZ films grown on LAO substrates with a nominal substrate temperature of 600°C during deposition. The peak marked with a $*$ are due to the substrate peaks. 282

A.7 XRD $\theta/2\theta$ patterns from the YSZ films grown on NGO substrates with a nominal substrate temperature of 600°C during deposition. The peak marked with a $*$ are due to the substrate peaks. 282

A.8 Lateral profiles of the ^{18}O isotope fraction for YSZ films grown on MgO. The insets show the ^{18}O isotope fraction integrated in the z-axis direction. In (a, c, and e) the ^{18}O distribution across the Au covered and uncovered region is shown after the incorporation step of 30 minutes at 300°C in ^{18}O enriched gas. In (b, d, and f) the subsequent ^{18}O distribution after annealing for 14 hours at 500°C is shown. The profiles in (b, d, and f) are fitted using the numerical method in Section 4.5.5. 283

A.9 Lateral profiles of the ^{18}O isotope fraction for YSZ films grown on Al_2O_3. The insets show the ^{18}O isotope fraction integrated in the z-axis direction. In (a, c, and e) the ^{18}O distribution across the Au covered and uncovered region is shown after the incorporation step of 30 minutes at 300°C in ^{18}O enriched gas. In (b, d, and f) the subsequent ^{18}O distribution after annealing for 14 hours at 500°C is shown. The profiles in (b, d, and f) are fitted using the numerical method in Section 4.5.5. 284

A.10 Lateral profiles of the ^{18}O isotope fraction for YSZ films grown on LAO. The insets show the ^{18}O isotope fraction integrated in the z-axis direction. In (a, c, and e) the ^{18}O distribution across the Au covered and uncovered region is shown after the incorporation step of 30 minutes at 300°C in ^{18}O enriched gas. In (b, d, and f) the subsequent ^{18}O distribution after annealing for 14 hours at 500°C is shown. The profiles in (b, d, and f) are fitted according to Eq. 4.21. 285

A.11 Lateral profiles of the ^{18}O isotope fraction for YSZ films grown on NGO. The insets show the ^{18}O isotope fraction integrated in the z-axis direction. In (a, c, and e) the ^{18}O distribution across the Au covered and uncovered region is shown after the incorporation step of 30 minutes at 300°C in ^{18}O enriched gas. In (b, d, and f) the subsequent ^{18}O distribution after annealing for 14 hours at 500°C is shown. The profiles in (b, d, and f) are fitted according to Eq. 4.21. 286
A.12 Typical accuracy using a Solartron Analytical 1260 FRA and 1296 dielectric interface [242]. 287
A.13 Optical image of a typical set of Pt sputtered electrodes after electrical measurements. 288
A.14 Normalised cation coverage of Ce and Gd as a function of sputter dose for CGO films grown on LAO for a range of thicknesses. . . . 289
A.15 Normalised cation coverage of Ce and Gd as a function of sputter dose for CGO films grown on STO for a range of thicknesses. . . . 290
A.16 Normalised cation coverage of Ce and Gd as a function of sputter dose for CGO films grown on Al_2O_3 for a range of thicknesses. . . 290

List of Tables

3.1 Details of the experimental studies of YSZ films in literature. (All conductivity values listed are in the in-plane geometry). ($\perp$ and $\parallel$ denote out-of-plane and in-plane strain respectively). 103

4.1 Atomic masses and natural abundances of the stable isotopes of oxygen. Data taken from [204]. 152

5.1 Details of the YSZ films from literature, which have been plotted in Fig. 5.14. 194

5.2 Thermal expansion coefficients, α, for 8 mol.% YSZ, MgO and Al_2O_3 taken from the literature. 196

5.3 Axial ratios (c/a) in Y-doped ZrO_2 for a range of dopant concentrations. Data from Lamas and Walsöe de Reca [231]. 197

6.1 Details of the YSZ films in this study. The thicknesses are extrapolated from the samples studied by TEM, which is noted. The samples labelled A, B, C, or D are used for referring to the XRD spectra shown in Appendix A.2. The lattice parameters are calculated from the XRD $\theta/2\theta$ (111) and (200) peaks. The temperature given is that for the transport measurement by either EIS or IETD. PF and TEM refers to the samples the pole figures and TEM images were taken from. 227

6.2 Structural data for the substrates used. a, b, and c are the lattice constants. 229

Chapter 1

Introduction

The aim of this chapter is to give a broad overview of the demands for better performing solid state oxygen-ion conductors. This will act to provide the context for the research documented in this thesis. The chapter will be predominantly focused on the use of oxygen conductors for electrochemical devices such as the solid oxide fuel cell (SOFC), due to the potential of ionic conductors for energy storage and conversion technologies and because the importance of current and future energy supply. Finally the overall objectives of thesis will be presented.

1.1 Global Energy Demand

Access to sufficient, reliable, secure and inexpensive energy supply underpins economic development and advances in standard of living. Recent estimates have predicted a rise of over 40% in energy demand over the next two decades, predominantly stemming from emerging economies in the developing world [1].

Currently over 80% of the global energy supply is provided through combusting fossil fuels [2], but this form of generation is under threat. Fossil fuel resources by their nature are finite, and as the more accessible reserves are consumed this will inevitably lead to an increase in cost. Furthermore the resources are unevenly distributed around the globe and those countries not well endowed, and instead reliant on imports, are vulnerable to supply

disruption. In addition, the widespread combustion of carbon-based fuels causes the release of excessive levels of carbon dioxide into the atmosphere which is thought to increase its thermally insulating properties and therefore predicted to result in a rise of the mean global temperature between 1 and 5°C [3]. Climate change is expected to have significant impact on environmental and socioeconomic systems.

National and international energy policy has often been framed as a 'trilemma' due to the three main competing drivers [4]. Firstly the cost of energy must be kept at a level that ensures economic competitiveness for both consumers and producers. Secondly the environmental impacts must be kept to an acceptably low level. The third driver is energy security, which may either be in the form of price and access to primary energy resources (e.g. fuel) or the cost and availability of the means of energy conversion.

Future energy supply must adequately address each dimension of the trilemma. While renewable energy sources have received significant attention, they are neither economically viable to cater for all our energy needs nor do they produce output that is invariable over time or perfectly predictable. In order to meet global energy demands innovation is required not only for large scale energy generation but also on large scale energy storage and methods of efficient dissemination of energy such as through distributed generation.

Additionally, future energy supply must meet the demands of end-use. These range from large-scale national grids to electric vehicles to portable electronics. Efficient energy storage and conversion devices are required in many forms to meet the varying demands of energy density, specific energy, energy capacity, portability, start-up time, durability and cost.

1.2 Solid State Oxygen-Ion Conductors

Ceramics are a family of materials often characterised as crystalline inorganic solids. In some of these materials electrical properties can be determined by imperfections deviating away from the ideal crystalline state. Some of these materials, such as non-stoichiometric oxides, can facilitate the transport of ionic oxygen through the material while maintaining its crystal

structure (the mechanisms of which are explored in detail in Chapter 3). This represents both mass and charge transport.

Solid electrochemical cells based on ceramic oxygen ion electrolytes find uses in a number of applications such as oxygen sensors, including those found in automobiles to control the oxygen content of the effluent mixture entering the exhaust catalyst (lambda sensors) [5] to dual-phase oxygen permeable membranes used to reform natural syngas [6]. In essence each device relies on a ceramic membrane forming a solid barrier between oxygen rich and oxygen-poor environments whilst allowing selective transport of the oxygen species between the two.

One type of electrochemical cell that continues to receive considerable attention is the solid oxide fuel cell (SOFC), which directly converts chemical energy from a fuel to electrical power. Shown schematically in Figure 1.1, an SOFC consists of an ionic conducting electrolyte sandwiched between an anode and a cathode.

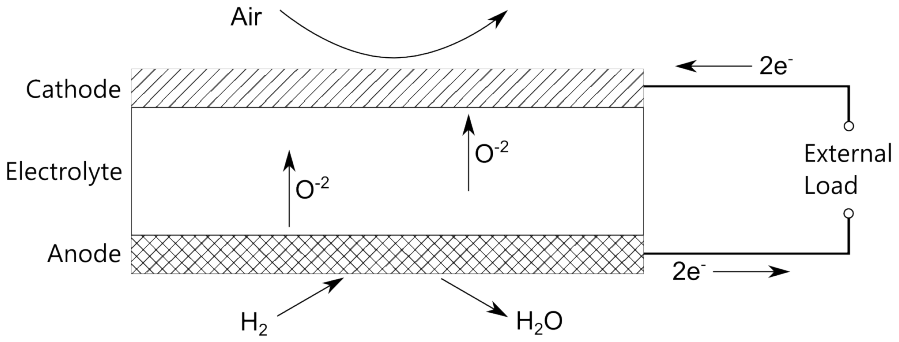


Figure 1.1: A schematic diagram demonstrating the operating principles of a solid oxide fuel cell.

At the cathode oxygen from the gas phase (typically air) is incorporated into the crystal structure via the oxygen reduction reaction (ORR), written in Kröger-Vink notation[1] [7]:

$$\frac{1}{2}O_2 + 2e' + V_O^{\bullet\bullet} \rightarrow O_O^x \tag{1.1}$$

The cathode is usually a mixed ionic-electronic conductor (MIEC), to

[1]See Chapter 2 for an explanation of Kröger-Vink notation.

provide a good connectivity of oxygen ions to the electrolyte and electrons to the cell interconnects, and highly porous to ensure high surface area for the ORR to take place and penetration of the oxygen rich gas.

Oxygen ions travel across the electrolyte (driven by the chemical potential gradient across the cell) to the anode where they react with the fuel (in this case hydrogen gas) via the reaction:

$$H_2 + O_O^x \rightarrow H_2O + V_O^{\bullet\bullet} + 2e' \tag{1.2}$$

Typically anodes have a similarly porous structure to the cathode and consist of a metal-ceramic composite referred to as a cermet. The flow of electrons liberated at the anode and incorporated at the cathode must pass around an external circuit, due to the electrolytes electronically insulating properties, thereby delivering electrical power in the external load.

As ionic conductivity and the reactions at the interfaces are thermally activated, SOFCs operate at high temperatures typically between 500°C to 1000°C depending on the choice of component materials. Because SOFCs directly convert chemical energy from the fuel to electrical power, they are inherently more efficient than conventional methods involving combustion and can theoretically exceed efficiencies of 50% [8]. Furthermore, when used in combined heat and power (CHP) applications, where the waste heat is utilised, efficiencies can be as high as 85% [9], unrivalled by any other energy conversion technology.

Another benefit of note is the ability of SOFCs to operate under a wide range of hydrocarbon and alcohol based fuels as well as pure hydrogen, allowing immediate and diverse use within our current energy infrastructure while providing the possibility for a smooth transmission to a future hydrogen-based economy. Moreover the principles of an SOFC can be employed in reverse (albeit with slightly different material requirements) as a solid oxide electrolysis cell (SOEC) where electrical input is externally applied to reform steam to H gas at the cathode [10].

SOFCs and SOECs are promising pieces of energy conversion and storage technology with huge potential for integration into energy supply systems. But despite being rather simple and elegant devices they represent a sub-

stantial engineering challenge. They are plagued with issues such as high cell costs, long start-up and shut-down times, and unacceptable degradation rates. As the effects of many of these issues can be subdued by lowering the operational temperature of the cells, considerable attention over the last decades has been focused to this end. A comprehensive review of SOFC/SOEC technology is beyond the scope of this thesis and the reader is directed towards the extensive literature detailing the fundamental concepts [11, 12] and up to date research efforts [13].

1.3 Potentials of Miniaturisation

While SOFCs have been commonly regarded as solutions to future energy demands within medium to large scale applications (0.1 kW to 1 MW), the possibility of miniaturisation has led to the feasibility of SOFCs to address our ever increasing demand for energy storage devices stemming from portable electronic devices (1 W), often referred to as μSOFCs (micro-SOFCs) [14].

Advantages of μSOFCs include a theoretical energy density and specific energy of up to 4 times that of Li-ion or Ni-metal batteries as well as longer operating times [15]. Advances in thin film fabrication techniques allow electrolytes to be manufactured at thicknesses as low as a few hundred nanometres, reducing the ohmic resistance of the component considerably. As a result, the operating temperature of μSOFCs can be reduced to below 600°C, and even down as low as 350°C. Thin film deposition methods such as pulsed layer deposition (PLD), magnetron sputtering, and spray pyrolysis typically fabricate ceramic at temperatures in the region of RT to 800°C, which opens up the possibility of integrating miniaturised SOFC systems onto Si wafers.

Traditionally ceramics are fabricated at temperatures approximately two thirds of the melting temperature (>1400°C), and the vast majority of research and understanding of ceramic processes is based on materials formed at this temperature, however, in μSOFCs the ceramic components are often formed at approximately one fifth of the melting temperature. To complicate matters further, for μSOFCs the processing and operation temperatures are very close or even overlapping. Combined with their extreme aspect ratios,

this acts to open up the possibilities for non-equilibration, meta-stability, strain effect, novel microstructures, and properties dominated by interfacial and surface effects. While this represents a significant gap in our understanding of ceramic processes, studying these materials also presents an exciting opportunity to harness potential desirable properties.

1.4 Wider Context

Ceramic ionic conductors have received widespread attention in the last century largely due to the promises of energy storage and conversion electrochemical devices such as the SOFC, owing to the considerable demands for alternative energy solutions. However, solid oxide ion conductors are also being examined for the role they may be able to play in prospective non-volatile memory technologies, such as the memristor.

Memristor devices are based on the concept of a resistive switch that can attain different resistance states, which are controlled by the polarity of magnitude of an applied bias. One way this can be achieved in a material is through oxygen anion migration, stimulated by high electric fields, combined with variations in the electronic resistance due to valence change [16]. Operating at room temperature, thin film geometries allow faster switching cycles and a bias as low as 1 V, promising the required properties of rapid switching, high density and low operation power [17].

As evidenced above, there is an ever-expanding interest in ionic conductors, for a variety of applications. Each has differing demands, ranging from geometries, thermal history, operation temperatures, stability and transport properties. Research has been directed along two district paths. One is focused on developing new material compositions and crystal structures, and the other restricted to studying and manipulating known materials through geometrical, microstructural, strain and processing effects.

Of the latter, strain effects have received most interest academically, that is perturbing the structure of existing materials through local applied stress, obtaining previously unseen and desirable properties. Typically induced by lattice mismatch as an interface of a thin film composite, by local applied stress or by chemical expansion, this route has been coined mechano-

chemical engineering.

1.5 Thesis Aims

The last decade has seen the proliferation of research into thin films of oxygen ion conductors, predominantly focusing on the transport properties. Studies directed towards doped-fluorites, yttria-stablised zirconia (YSZ) and gadolinia-doped ceria (CGO) have been most popular, as these materials are currently used commercially as electrolytes. As reviewed extensively in Chapter 3, reported modification of the ionic conductivity in thin films has been widespread, extreme and inconsistent. Variation in the O transport from that expected in bulk materials is routinely attributed to strain effects originated at the interfaces in the films due to lattice mismatch.

This thesis aims to address the possibility of altered ionic conductivity in YSZ through experimental studies. Due to the past findings being plagued with inconsistencies when taken as a whole, the prospects of chemo-mechanical engineering has proved a divisive issue [18]. An important theme of this work is that rather than stand alone, to be put into context of the previous body of research, where the validity of prior experimental results and theories may be assessed.

While transport properties in thin films have been a topic of great interest for a number of years, the stability and degradation effects have been largely overlooked, despite its importance for electrochemical devices. Nevertheless, understanding degradation phenomena must be extended from bulk ceramics to thin films. Hence the stability of thin film ionic conductors will also be examined, including the possible effects of lattice strain, through experimental studies on CGO.

Chapter 2

Theoretical Considerations

This chapter serves to form a basis of understanding of defect transport and dopant segregation in ionic crystalline solids, putting particular emphasis on phenomena dictating properties in acceptor doped fluorites. Much of the founding knowledge is based on work over the last 60 years predominantly studying bulk sintered ceramics, and hence is reliant on assumptions not necessarily valid for work on thin films. Next theories and predictions developed to explain properties observed in nanostructured materials will be presented. Despite on occasion originating from the same work, a detailed examination of the experimental and computational evidence for modified transport in nano-structured materials and surface segregation is left to Chapter 3.

2.1 Defects in Crystalline Oxides

Before exploring the effects of defects in crystals we must first briefly explain the idealised crystal structure of the materials in question in order to obtain a reference of what a defect is defective from. Solid state ionic conductors come in many forms both compositionally and structurally. Those structures which have received considerable interest include the fluorites, perovskites, apatites, brownmillerites and pyrochlores to name a few. For brevity, in this chapter the discussion will be limited to that relating to solid solutions of materials with the fluorite structure, in particular doped-zirconia and

doped-ceria, and reviews of the known solid oxide electrolytes can be found elsewhere [19, 20].

2.1.1 Fluorites

Many ceramic compounds are based on the close packing of one of the atomic constituents. For the binary oxides ZrO_2 and CeO_2, the cations (Zr and Ce) form a face-centered cubic (FCC) structure. The anions (O) are inserted in the tetrahedral interstitial sites to form the fluorite structure as shown in Fig. 2.1, named after the mineral fluorite, CaF_2. The valence states of the anions and cations are -2 and +4 respectively, and from the chemical formulas and Fig. 2.1 it is obvious that a 2:1 ratio is observed maintaining charge balance.

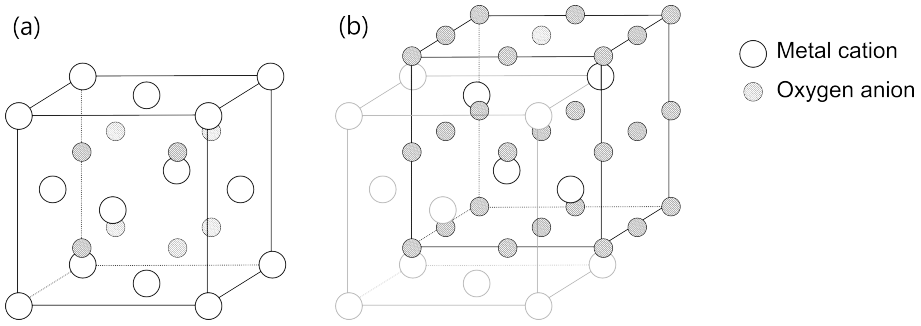


Figure 2.1: Cubic fluorite crystal structure represented as (a) a FCC metal cation unit cell and (b) simple cubic oxygen sublattice with alternating body filled centres.

Whilst pure CeO_2 possesses the cubic fluorite structure from room temperature to its melting point, for pure ZrO_2 there are in fact three distinct polymorphs of this compound. These are the monoclinic, tetragonal and cubic phases, which differ in their interatomic spacing and symmetry but not in the numerical coordination of the ions. Changes between phases can take place by *displacive* transformations and do not involve bond breaking or rearrangement. Because displacive transformations between polymorphs in ZrO_2 also lead to a change in the volume of the unit cell, they can accommodate local stress fields (such as those in proximity to cracks), which can lead to *transformational toughening*. Cubic ZrO_2 is the highest temperature phase and optimum for ionic conductivity due to its high symmetry and

open structure but is only stable between 2370°C and the melting point at 2680°C. However it may be *stabilised* below this temperature, with the addition of a few percent of dopants such as MgO, CaO and Y_2O_3. The phase diagram of ZrO_2-Y_2O_3 solid solutions is shown in Fig. 2.2. These dopants also act to introduce vacancies into the structure, which will be discussed in detail in Section 2.1.3.

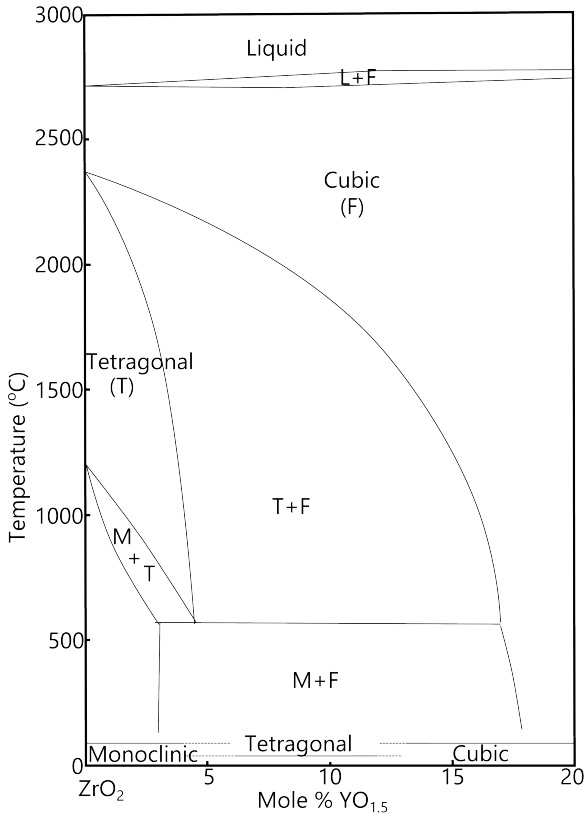


Figure 2.2: Phase diagram of the ZrO_2 rich region of the ZrO_2 - Y_2O_3 binary system (adapted from Ref. [21]).

2.1.2 Intrinsic Defects

In ceramics a great many phenomena are determined by imperfections from the idealised crystal structure such as electrical, diffusional, strength and

optical properties. Here the discussion will be limited to point defects[1], defined as missing, substituted or interstitial ions and will purposefully neglect discussion of electronic defects, which are deviations from the ground state electron orbital configuration.

Intrinsic defects are thermally generated in a perfect crystal typically in significant concentrations at temperatures only above half the melting point. The two most common causes of crystalline point defects are *Frenkel* disorder and *Schottky* disorder. Frenkel disorder is a displacement of an ion from its ideal site to an interstitial site forming a vacancy and interstitial pair. An example for ZrO_2 would be the displacement of a Zr ion to an interstitial site and can be represented in Kröger-Vink notation as:[2]

$$null \rightleftharpoons V_{Zr}^{''''} + Zr_i^{\bullet\bullet\bullet\bullet} \tag{2.1}$$

The term anti-Frenkel is commonly used to describe Frenkel defects forming from the anion sublattice.

Schottky disorder arises from the simultaneous creation of both anion and cation vacancies in the stoichiometric ratio, as to preserve electroneutrality. Using ZrO_2 as an example again, a Schottky disorder reaction may be written as:

$$null \rightleftharpoons V_{Zr}^{''''} + 2V_O^{\bullet\bullet} \tag{2.2}$$

It should be noted that Eq. 2.1 and 2.2 above are known as *quasichemical reactions* and must obey *charge*, *mass* and *site* balance (as opposed to ordinary chemical reactions where only charge and mass must be conserved).

As discussed in Section 2.2, the electrical conductivity of an ionic species is dictated by its charge, mobility and concentration. Neglecting the first two for the moment, an expression for the concentration of a Frenkel pair

[1] As opposed to *extended defects*, which may include *line defects* such as dislocations and aggregates of point defects such as *clusters*. Features such as surfaces, grain boundaries and stacking faults may also be described as *planer defects*.

[2] In Kröger-Vink notation the main body of the notation identifies the ionic species (e.g. O for an oxygen ion, V for vacancy), the subscript denotes the lattice site the ion occupies in the host lattice (i is used for interstitial), and the super script indicates the effective charge of the defect in relation to the perfect crystal lattice (where $^\bullet$ and $'$ represent an excess or a deficiency of a single electron charge respectively).

may be written as a chemical reaction for which there is an equilibrium constant which is governed by the law of mass action:

$$K_f = [V_{Zr}^{''''}][Zr_i^{\bullet\bullet\bullet\bullet}] \tag{2.3}$$

where K_f is the mass-action equilibrium constant, and the square brackets denote concentration, often given in mole fraction. Considering the energy expense of creating a Frenkel pair is given by the free energy, ΔG_f, it can be shown that the equilibrium number of defects is [22]:

$$K_f = \exp\left(-\frac{\Delta G_f}{kT}\right) = \exp\left(-\frac{\Delta S_f}{k}\right)\exp\left(-\frac{\Delta H_f}{kT}\right) \tag{2.4}$$

ΔS_f is defined as the change in non-configurational entropy[3] (associated with changes in lattice strains and vibrational frequencies accompanying the defect), ΔH_f is the formation enthalpy, k is Boltzmann's constant and T is temperature in Kelvin. From Eq. 2.4 it is clear that the number of defects is exponentially dependent on the formation free energy and temperature. Although for doped-fluorites in the temperature range relevant for many electrochemical devices the concentration of the predominant defect species ($V_O^{\bullet\bullet}$) is determined by the dopant concentration (extrinsic defects), the considerations above form the basis of our understanding of defect association, covered in Section 2.2.2.

2.1.3 Extrinsic Defects

Extrinsic defects may be introduced via solutes in a solid solution as substitutional or interstitial species. For ZrO_2 and CeO_2, substitutional solutes that are either divalent (Mg^{2+}, Ca^{2+}) or trivalent (Y^{3+}, Sc^{3+}, Gd^{3+}) will act to introduce oxygen vacancies. For divalent solutes, one oxygen vacancy will be created per substituted ion, and for trivalent species, one oxygen vacancy will be created for every two substituted ions, as shown in Eqs. 2.5 and 2.6 respectively.

$$CaO \xrightarrow{ZrO_2} Ca_{Zr}^{''} + O_O^x + V_O^{\bullet\bullet} \tag{2.5}$$

[3]This is opposed to configurational entropy, which is due to the possible arrangement of the defects and is intrinsically accounted for in the expression.

$$Y_2O_3 \xrightarrow{ZrO_2} 2Y'_{Zr} + 3O^x_O + V^{\bullet\bullet}_O \tag{2.6}$$

For ZrO_2 aliovalent doping not only introduces oxygen vacancies necessary for fast ionic conduction, in sufficient quantities it also acts to stabilise the optimum cubic polymorph at low temperatures. Despite the defect mechanisms in Eq. 2.5 and 2.6 being the commonly accepted cases in doped ZrO_2, some studies have suggested that other incorporation reactions may take place. By measuring the density of CaO-ZrO_2 solid solutions quenched from 1600°C and 1800°C, Diness and Roy [23] found that the defect compensation mechanism switched from vacancy dominated, as in Eq. 2.5 to one where Zr interstitials are formed as in Eq. 2.7. Data from this study is displayed in Fig. 2.3.

$$2CaO + Zr^x_{Zr} \xrightarrow{ZrO_2} 2Ca''_{Zr} + 2O^x_O + Zr^{\bullet\bullet\bullet\bullet}_i \tag{2.7}$$

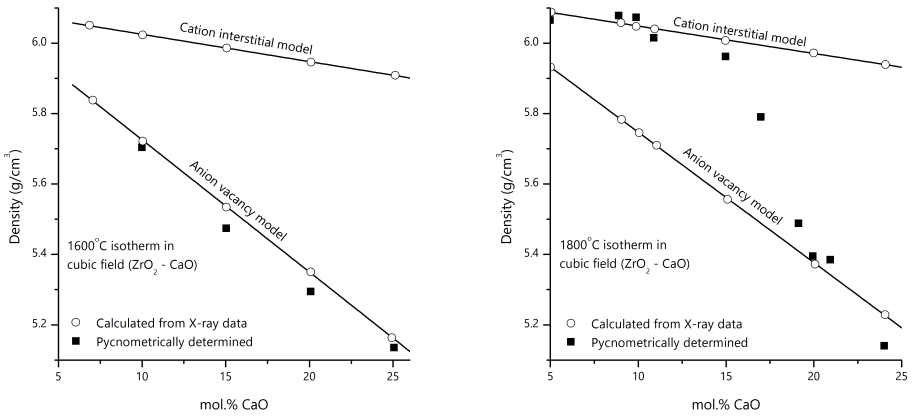


Figure 2.3: Change in density of ZrO_2 - CaO solid solutions quenched from (a) 1600°C and (b) 1800°C. The theoretical density of predicted from a vacancy and interstitial compensation mechanism is also plotted. Data taken from Diness and Roy [23].

Whilst net changes in the lattice parameter may be determined in a straight-forward manner by experimental techniques such as x-ray diffraction (XRD), estimating volume changes of solid solutions due to the intro-

duction of defects is non-trivial. Measurements on CeO_2 and ZrO_2 doped with a range of trivalent rare-earth cations have shown that the change in the lattice volume may be described empirically as an approximately linear relationship with the dopant concentration, in an analogous fashion to Vegards law often employed in metallurgy [24]. Fig. 2.4 shows the measured lattice parameter of CeO_2 doped with several rare earth oxides, note that both expansive and compressive changes in the lattice parameter are observed.

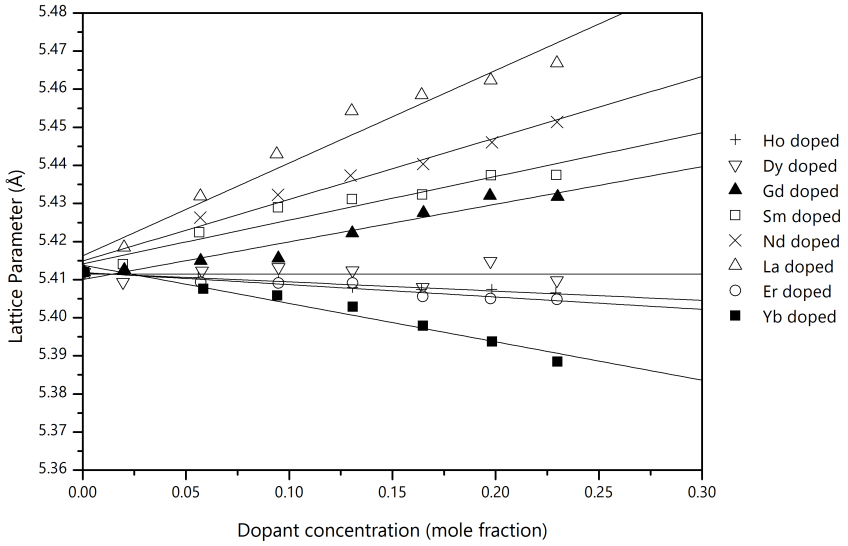


Figure 2.4: Measured lattice parameters of M_2O_3 - CeO_2 solid solutions with dopant concentrations, where M_2O_3 is a rare earth oxide. Data taken from Hong and Virkar [24].

Changes in the lattice volume due to anion and cation point defects is known as *chemical expansion*. Understanding the fundamental causes of chemical expansion is vital for designing stable electrochemical devices, but also for investigating transport mechanisms. Recent studies by Marrocchelli *et al.* [25, 26] have modelled chemical expansion around a substituted cation and oxygen vacancy in CeO_2 and ZrO_2 using molecular dynamics (MD) and density functional theory (DFT) simulations. The authors suggest that

chemical expansion is due to two competing factors. The removal of an oxygen ion causes the cations to relax away from the vacancy as their electrostatic repulsion is no longer screened, and the surrounding anions relax towards the effective positive charge (shown in Fig. 2.5a), described by the introduction of an effective oxygen vacancy radii. Secondly the introduction of substitutional cation species, which have an ionic radii different to that of the host cations causes a lattice distortion primarily due to steric effects (shown in Fig. 2.5b). Each factor is dependent on both the radii of the cations in the host lattice and of the dopant.

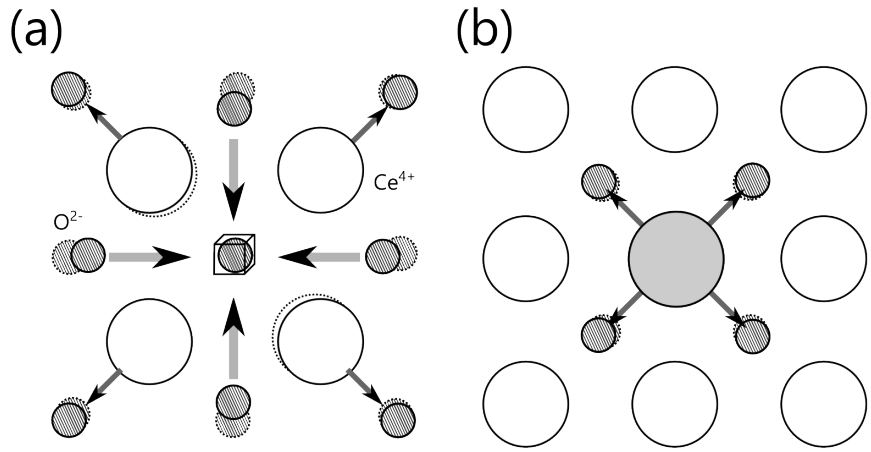


Figure 2.5: Local lattice relaxations around an oxygen vacancy (a) and a substituted cation with a radii larger than the host lattice (b). Adapted from Marrocchelli *et al.* [25].

2.2 Ionic Conductivity

Long range charge migration in ceramics may be either atomic or electronic in nature, consisting of anions, cations, electrons, or holes as the charge carrier. In most real ceramics the motion of multiple charge carriers will occur simultaneously, and the total conductivity may be described simply by the sum of the partial conductivities associated with each charge carrier,

i.

$$\sigma = \sum_i \sigma_i \tag{2.8}$$

Each partial conductivity, σ_i, is given by

$$\sigma_i = n_i q_i \mu_i, \tag{2.9}$$

where n_i is the carrier density per unit volume (m^3), q_i is the effective charge on the carrier, and μ_i is the carrier mobility, of which both the carrier density and mobility are dependent on changes in composition, temperature and atmosphere. Because μ_i and n may vary by tens of orders of magnitudes for different species in ceramic materials, it is often the case that one charge carrier will dominate and effects from minority carriers may be ignored. It should be noted that this is not always the case, and for a small sub-group of oxides, in the right conditions of temperature, composition and atmosphere both electronic and ionic charge carries simultaneously contribute in a major way to the total conductive properties. These are known as mixed ionic-electronic conductors (MIEC), which are a subject of great interest and have been reviewed elsewhere [27–29]. It is useful to describe the partial conductivity of a charge carrier as a fraction of the total conductivity,

$$t_i = \sigma_i / \sigma \tag{2.10}$$

where t_i is known as the transference number. For commercial electrolytes such as 8 mol.% Y_2O_3-doped ZrO_2 (8 mol.% YSZ) and 10 mol.% Gd_2O_3-doped CeO_2 (10 mol.% CGO), oxygen vacancies dominate the defect concentration. The abundance of vacancies in YSZ and CGO allows oxygen ion conduction to occur via a vacancy hopping mechanism. Combined with negligible electronic conduction in the electrolytes[4], the transference number for oxygen ion conductivity can be assumed to be unity.

[4]The reducibility of the cerium ion from Ce^{4+} to Ce^{3+}, causes CeO_2 based electrolytes to be electronic conductors at high temperature and low oxygen partial pressures (pO_2) [30, 31].

2.2.1 Arrhenius Relationship

The current flow in such materials occurs via ion hopping of the oxygen ions between crystal lattice sites with a superimposed drift due to an electric field. Ionic conductivity is highly temperature dependent, which is due to ion hopping being a thermally-activated process. In order to understand this in further detail, one must consider the energy barrier that must be overcome for such an event to occur. Figure 2.6a shows the variation of the energy of an O^{2-} ion with respect to distance in a crystal lattice. For an O^{2-} ion positioned at A, the energy barrier or activation energy, ΔG_m, must be overcome for a hop to B to take place (assuming B is a vacant site). Due to thermal energy, all ions in a solid vibrate at a frequency ν_0 around 10^{12} to 10^{13} Hz. The probability that the O^{2-} ion vibrational energy will be greater than the ΔG_m is proportional to $\exp(-\Delta G_m/kT)$, where k is Boltzmann's constant, and therefore the average number of jumps each ion makes per second will be proportional to $\nu_0 \exp(-\Delta G_m/kT)$.

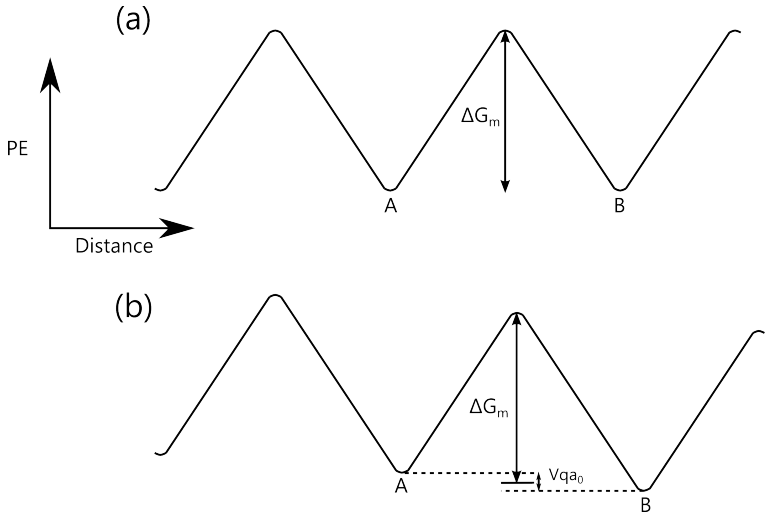


Figure 2.6: Potential energy of an ion in the lattice against distance with (a) no applied field and (b) an externally applied electric field.

At no net electric field the energies at A and B will be identical, and although some anions are able to hop, they will occur in all directions at random thus there is no net flow of charge. Yet when a field is applied

there will be a difference between the energy levels at A and B equal to Vqa_0 (Figure 2.6b) corresponding to the work done by the applied field V moving a charge q by a distance a_0 in the direction of the field. Therefore the energy barrier in the two directions of $A \rightarrow B$ and $B \rightarrow A$ will be given by $(\Delta G_m - \frac{1}{2}Vqa_0)$ and $(\Delta G_m + \frac{1}{2}Vqa_0)$ respectively, thus making hopping events in the direction of the electric field more probable.

Considering the possibility of both forward and backwards jumps with respect to the electric field, the probability of an ion at A jumping to B is given by [32]

$$P \propto \nu_0 \exp\left[\frac{-(\Delta G_m - \frac{1}{2}Vqa_0)}{kT}\right] - \nu_0 \exp\left[\frac{-(\Delta G_m + \frac{1}{2}Vqa_0)}{kT}\right], \quad (2.11)$$

which if rearranged to

$$P \propto \nu_0 \exp\left(\frac{-\Delta G_m}{kT}\right)\left[\exp\frac{Vqa_0}{2kT} - \exp\frac{-Vqa_0}{2kT}\right], \quad (2.12)$$

the terms in the square brackets can be expanded as a power series and reduced to Vqa_0/kT if it is assumed that $Vqa_0 < kT$, therefore

$$P \propto \frac{Vq}{kT} a_0 \nu_0 \exp\left(\frac{-\Delta G_m}{kT}\right). \quad (2.13)$$

As the mean velocity will be equal to $u = Pa_0$ and the mobility of the ions is $\mu = u/V$, therefore combining these with Eqs. 2.9 and 2.13 it can be seen that

$$\sigma T = \gamma n \frac{q^2}{k} a_0^2 \nu_0 \exp\left(\frac{-\Delta G_m}{kT}\right), \quad (2.14)$$

where γ is a geometric factor. If we recall that $\Delta G_m = \Delta H_m - T\Delta S_m$, where ΔH_m is the migration enthalpy and ΔS_m is the entropy of migration, then Eq. 2.14 may be expanded to

$$\sigma T = \gamma n \frac{q^2}{k} a_0^2 \nu_0 \exp\left(\frac{-\Delta S_m}{k}\right) \exp\left(\frac{-\Delta H_m}{kT}\right). \quad (2.15)$$

As in Eq. 2.4, ΔS_m is the non-configurational entropy and should be temperature independent. For oxygen ion conduction via a vacancy hopping

mechanism, the concentration of mobile charge carriers n, may be expressed as [33]

$$n = [V_O^{\bullet\bullet}]\{1 - [V_O^{\bullet\bullet}]\}N, \tag{2.16}$$

where $[V_O^{\bullet\bullet}]$ is the oxygen vacancy concentration given as a site fraction and N is the anion site concentration per unit volume. Combining Eqs. 2.15 and 2.16 gives an Arrhenius type expression for oxygen ion conductors.

$$\sigma T = N[V_O^{\bullet\bullet}]\{1 - [V_O^{\bullet\bullet}]\}\gamma\frac{q^2}{k}a_0^2\nu_0 \exp\left(\frac{-\Delta S_m}{k}\right)\exp\left(\frac{-\Delta H_m}{kT}\right) \tag{2.17}$$

From Eq. 2.17, one may expect that plotting $\ln(\sigma T)$ against $1/T$ (often referred to as an Arrhenius plot) gives a single straight line with the slope $-\Delta H_m/k$ for all temperature ranges, and that the maximum conductivity will be achieved when $[V_O^{\bullet\bullet}] = 0.5$[5]. In the next section we will explore why the two latter points are not the case for doped ZrO_2 and doped CeO_2.

2.2.2 Defect Association

Rather than increasing with dopant concentration according to Eqs. 2.6 and 2.16 (until the solubility limit of the host structure), the conductivity of doped fluorites observes a maximum at much lower dopant concentrations, in the region of 7-12 mol.%. An example of this is the Y_2O_3 doped CeO_2 system, the activation enthalpy, ΔH_σ, and isothermal conductivity of which is shown in Fig. 2.7. As can be seen the maximum in σ corresponds approximately to a minimum in ΔH_σ.

Returning to our assessment of the conductivity in the previous section, we made the assumption that the energy of each oxygen site is degenerate (disregarding the imposed electric field), but as mentioned in Section 2.1.3 in real ceramics this is not the case. Steric and electrostatic interactions between defects in the structure may act to destroy this degeneracy. This leads to preferential occupancy of some oxygen sites over others occurs due to the local environment surrounding the dopant ions within the host lattice. This is known as *defect association.*

[5]This is however unrealistic, as it would require a level of doping such that an Y ion would be present at every single Zr site!

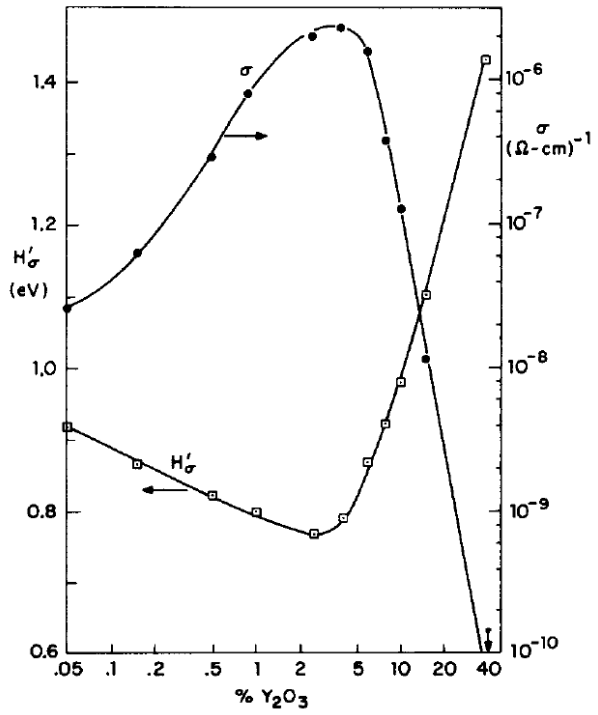


Figure 2.7: Variations in the low temperature activation enthalpy and isothermal conductivity (at 182°C) as a function of composition, for the Y_2O_3 - CeO_2 solid solutions. Taken with permission from Wang *et al.* [34].

In the case of a divalent substitute, an oxygen vacancy and a dopant ion can associate to form a neutral pair. But for YSZ, as the dopant is trivalent, two Y^{3+} ions are compensated with a single oxygen vacancy to form a neutral triplet as

$$2Y'_{Zr} + V_O^{\bullet\bullet} \rightleftharpoons (2Y'_{Zr} + V_O^{\bullet\bullet})^x. \tag{2.18}$$

To produce a neutral triplet, cation diffusion is required, yet this is thought to be negligible below ∼1000°C [35]. Assuming that instead all the Y^{3+} ions are distributed at random, association may take place to form partially compensated pairs as

$$Y'_{Zr} + V_O^{\bullet\bullet} \rightleftharpoons (Y'_{Zr} + V_O^{\bullet\bullet})^\bullet. \tag{2.19}$$

Therefore we can no longer consider all the oxygen vacancies to be free, as we did when formulating Eq. 2.17, instead it is necessary to define the number of vacancies that are free as a function of temperature. In an analogous way to our treatment of intrinsic defect concentration in Section 2.1.2, we can describe the concentration of free and associated vacancies according to the mass action equation

$$\frac{[Y'_{Zr}][V_O^{\bullet\bullet}]}{[(Y'_{Zr}+V_O^{\bullet\bullet})^{\bullet}]} = W^{-1}\exp\left(-\frac{\Delta G_A}{kT}\right), \tag{2.20}$$

where W represents half the number of pair orientations (W=4 for YSZ) [34], and ΔG_A is the free energy of association. The electroneutrality condition is given by

$$[V_O^{\bullet\bullet}]m + [(Y'_{Zr}+V_O^{\bullet\bullet})^{\bullet}] = [Y'_{Zr}], \tag{2.21}$$

where m is the oxygen to metal ratio to maintain site balance. Consistency in the total dopant concentration, C_M, maintains that

$$[Y'_{Zr}] + [(Y'_{Zr}+V_O^{\bullet\bullet})^{\bullet}] = C_M. \tag{2.22}$$

At low temperatures, vacancy association may be assumed to be complete, such that

$$[V_O^{\bullet\bullet}] < [(Y'_{Zr}+V_O^{\bullet\bullet})^{\bullet}], \tag{2.23}$$

which would imply that

$$[V_O^{\bullet\bullet}] = W^{-1}\exp\left(-\frac{\Delta G_A}{kT}\right). \tag{2.24}$$

Here we are assuming low vacancy concentration and therefore can make the assumption that there are no defect-defect interactions and that Eq. 2.16 simplifies to $[V_O^{\bullet\bullet}]N$. Inserting Eq. 2.24 into Eq. 2.17, gives

$$\sigma T = \frac{N}{W}\gamma\frac{q^2}{k}a_0^2\nu_0\exp\left(\frac{-(\Delta S_A+\Delta S_m)}{k}\right)\exp\left(\frac{-(\Delta H_m+\Delta H_A)}{kT}\right), \tag{2.25}$$

where ΔS_A and ΔH_A are the enthalpy and entropy of association, respectively. Eq. 2.25, predicts that in the fully associated regime an Arrhenius

plot would display a straight line with a gradient of $\Delta H_m + \Delta H_A$.

From Eq. 2.25, Eq. 2.17 and our considerations in Section 2.1.2, we may define three temperature regimes where the conductivity is dominated by different defect interactions [36]. At high temperatures the conductivity is dominated by intrinsic defects, which have a concentration dependence described by Eq. 2.4[6]. This region is known as stage I. Stage II occurs at intermediate temperatures, where the total vacancy population can be assumed to be free and hence the conductivity is described by Eq. 2.17. Finally in stage III, which occurs at lower temperatures, we can assume vacancy association to be complete and hence Eq. 2.25 is valid. Fig. 2.8 shows an expected Arrhenius plot for the three stages.

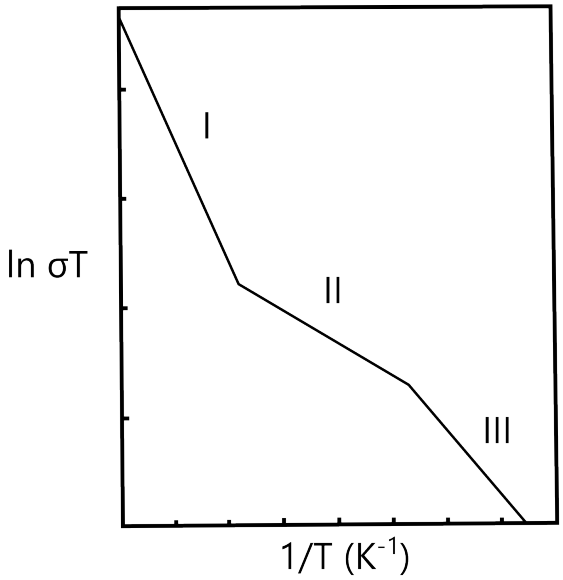


Figure 2.8: Arrenhius plot showing the different stages of ionic conductivity.

Often it is useful to describe the conductivity of both stages II and III using a single equation, so that data spanning across both regimes may be fitted. Eqs. 2.20, 2.21 and 2.22 may be combined to eliminate $[(Y'_{Zr} + V_O^{\bullet\bullet})^{\bullet}]$

[6]Or equivalent for Schottky defect formation.

and $[Y'_{Zr}]$ to give [37]

$$[V_O^{\bullet\bullet}]^2 + [V_O^{\bullet\bullet}]\left(\frac{C_M}{m} + \frac{E}{W}\right) - \left(\frac{C_M E}{mW}\right) = 0. \tag{2.26}$$

This quadratic equation may be solved for $[V_O^{\bullet\bullet}]$, to obtain

$$[V_O^{\bullet\bullet}] = -\frac{1}{2}\left(\frac{C_M}{m} + \frac{E}{W}\right) + \frac{1}{2}\sqrt{\left(\frac{C_M}{m} + \frac{E}{W}\right)^2 - \frac{4C_M E}{mW}}, \tag{2.27}$$

where E represents the exponential term in Eq. 2.20. Eq. 2.27 inserted into Eq. 2.17 has been used to describe the conductivity successfully for both the doped CeO_2 [34] and doped ZrO_2 [37] systems.

Despite defect association in doped ZrO_2, first being postulated as far back as 1969 [38], the current understanding of the mechanisms primarily responsible for defect interactions remain limited. For example, our treatment of defect formation energies in this section do not explain the minimum in ΔH_σ seen in Fig. 2.7. Whilst the high concentration increase in ΔH_σ may be attributed to complex defect clustering and ordering of dopant cations and oxygen vacancies, the increase in ΔH_σ at low concentration is less easy to explain.

Wang *et al.* [34] explain the minimum as a concentration dependent modification of the association enthalpy H_A, due to electrostatic interactions between the charges involved in the process of association, such that

$$\Delta H_A = \Delta H_A^0 - \Delta E_{int}, \tag{2.28}$$

where ΔH_A^0 is the association at infinite dilution, and ΔE_{int} is given by

$$\Delta E_{int} = \frac{2q^2(C_M)^{\frac{1}{3}}}{\pi\epsilon_0\epsilon_r\beta a_0}, \tag{2.29}$$

where ϵ_0 is the permittivity of free space, ϵ_r is the dielectric constant of the material and β is a dimensionless parameter such that $\beta a_0/(C_M)^{\frac{1}{3}}$ is the effective separation.

Faber *et al.* [39] instead reject the electrostatic arguments, and suggest that lattice relaxations of neighbouring ions screens the columbic field of

the defect charge. The authors instead introduce an interaction radius, r_c, dependent on the size of the dopant cation radius. As the concentration increases, Faber *et al.* suggest that the overlapping spheres of influence cause two competing mechanisms to develop. Percolation paths lead to interconnected pathways with a lowered energy barrier, but deep traps are also created due to multiple trapping, causing an optimum in the dopant concentration.

Kilner [40–42] suggested a correlation between the ionic radius of the dopant and the activation energy, supporting the concept of lattice distortions around defects. Fig. 2.9 shows the total activation energy, ΔH_σ, as a function of both concentration and ionic radius of the dopant cation. It is clear that a further minimum exists combining both the optimum dopant concentration and dopant size. Kilner suggested that the minimum occurs when the ionic radii of the host and dopant were close to each other such that the lattice elastic strain is minimised.

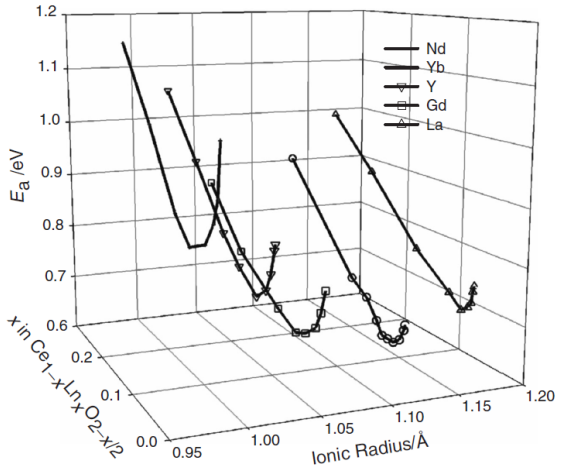


Figure 2.9: Activation energy of doped CeO_2 solid solutions as a function of dopant ionic radius and concentration. Taken from Kilner [43], data taken from Faber *et al.* [39].

Calculations by Minervini *et al.* [44] extend Kilner's hypothesis, by calculating the binding energy of dopant cation-vacancy pairs when the vacancy is situated in the first, second or third nearest neighbour site. Their results

suggest that the minimum in ΔH_σ occurs when the binding energy crosses from the first to the second nearest neighbour (shown in Fig. 2.10). They also found that this behaviour would extend to neutral defect trimers (as described in Eq. 2.18), which would be expected at higher dopant concentrations. A similar size dependence has been calculated in a similar way for doped ZrO_2 solid solutions [45].

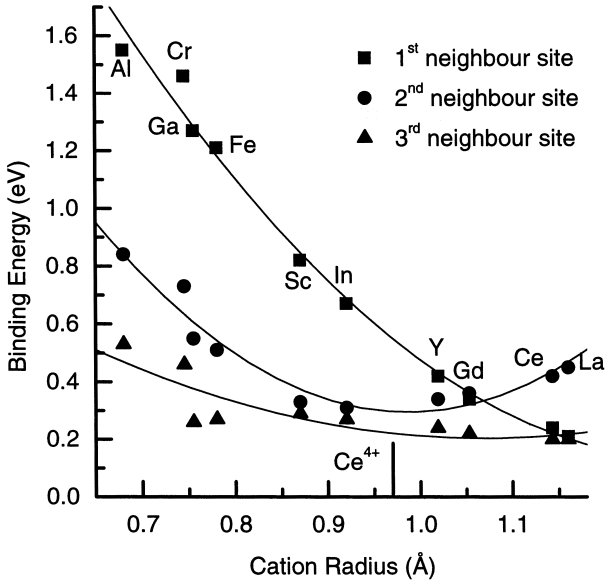


Figure 2.10: Calculated binding energies for a M^{3+} dopant to an oxygen vacancy. The radius of a Ce^{4+} cation is shown for comparison. Taken with permission from Minervini *et al.* [44].

Even recently, simulations by Marrocchelli *et al.* [25,26], have shed more light on the mechanisms of defect interactions which were discussed in Section 2.1.3. The authors suggest the relaxation mechanisms depend on both the size of the dopant cation and that of the host. In addition they calculate that the upper concentration limit for vacancy-vacancy interaction to have a probability of <95%, is as low as $[V_0^{\bullet\bullet}] = 0.025\%$.

2.3 Interfaces and Microstructure

The physical and chemical properties of interfaces can dramatically alter the ionic conductivity compared to that of the bulk. The exact mecha-

nism for modifications in the transport within close spatial proximity to the interface are not well understood, but changes in the charge carrier concentration, free energy of migration and free energy of association could all be expected. Solid-solid interfaces can be defined as either homo- or heterogeneous interfaces, depending on whether they separate two chemically identical or different materials respectively. Both types of interface will be covered in this section. The phenomena discussed (space charge regions, impurity phases, strain and dislocations) can occur at both types of interface, but as space charge and impurity layers are most well studied at grain boundaries, and strain and dislocations particularly relevant at heterogeneous boundaries, they will be grouped accordingly. Interfaces between different physical phases (i.e. solid-gas, solid-liquid and liquid-gas) are typically referred to as surfaces. These will be discussed in Section 2.4.

2.3.1 Homogeneous Interfaces

Homogeneous interfaces, commonly known as grain boundaries, are defined as the interface between two grains of the same phase where the atomic planes are disrupted to some extent. Some grain boundaries are well defined and can be described reasonably simply by the relative rotational misorientation of the two grains, the orientation of the grain boundary plane between them and any translations of the two crystals with respect to one another [22]. These are known as *special boundaries*. Much more common in ceramic materials are *general boundaries*, which do not possess a well-defined misorientation and instead adjoining atomic planes are incommensurate in their spacing.

Experimental techniques such as electrochemical impedance spectroscopy (EIS) are capable of separating contributions to the total electrical conductivity from features in the material such as bulk transport, grain boundary transport and electrode effects [33]. EIS is described in detail in Section 4.4. Since solid electrolytes were first studied using complex plane impedance analysis, when Bauerle [46] investigated YSZ in 1969, EIS has become the conventional tool for electrical measurements. Typically for doped ZrO_2 and doped CeO_2 solid solutions the specific grain boundary conductivity is

found to be at least two orders of magnitude lower than that of the bulk [47]. This is often attributed to the establishment of a space charge layer at the boundary, the formation of a secondary impurity phase between the grains, or a combination of the two.

Space Charge Model

At an interface the symmetry of the bulk is broken due to the introduction of structural discontinuity. In contrast to the bulk material, where electroneutrality must be strictly obeyed, at the interface violation of this rule may be allowed or even thermodynamically favourable. A large proportion of defects or a change from the bulk stoichiometry at a grain boundary or interface can cause a deviation from charge neutrality resulting in an electric field incident on the surrounding bulk material to a degree determined by the magnitude of the charge congregated at the interface and the spatial extent of the charge redistribution in the layer. This is known as the space charge layer, of which the effect in ionically conducting oxides has been developed by Maier [48–51]. Structurally the space charge layers are part of the bulk, but electrically they are part of the grain boundary. The thickness of a grain boundary is the thickness of the grain boundary core, b, in addition to the thickness of the two space charge regions, λ^*, and hence is given by $\delta_{gb} = 2\lambda^* + b$. A schematic of a grain boundary is shown is Fig. 2.11. Typically the width of the grain boundary core is around 1nm, as observed by transmission electron microscopy (TEM) [52].

As discussed in the previous section defect interactions are a combination of both electrostatic and elastic phenomena, making them difficult to predict in real systems. The situation can get even more complex at grain boundaries, where changes in bond length, broken bonds and defect formation can occur. MD simulations [53] have shown that structure relaxations produce intrinsic oxygen vacancies in the grain boundary core of 8 mol.% YSZ special boundaries, suggesting an excess of positive charge. This has been confirmed experimentally by an electron energy-loss spectroscopy investigation [54], where a deficiency of oxygen was observed in the core of special grain boundaries in both the 10 mol.% YSZ and 20 mol.% CGO solid

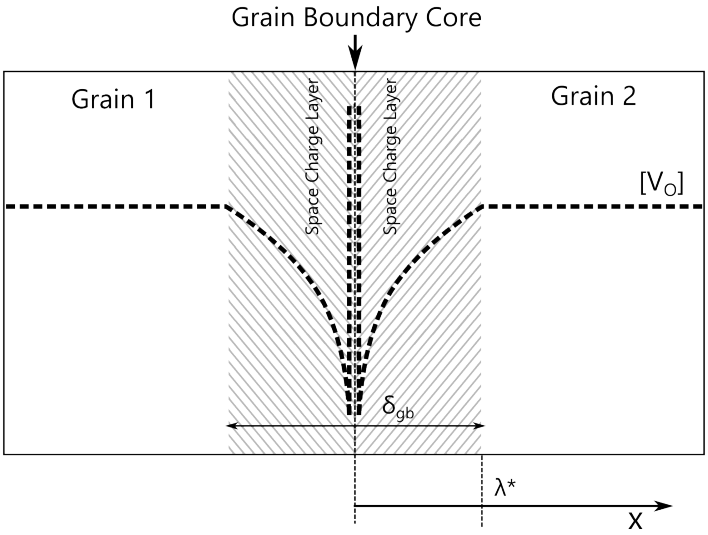


Figure 2.11: Schematic representation of a grain boundary, showing both the electrical and structural regions.

solutions. In this study aliovalent dopant enrichment was also observed in the adjacent region to the grain boundary core, but to an insufficient extent to fully compensate the oxygen vacancy population in the core.

An important factor when considering the width of a space charge layer is the ability for the ions to redistribute due to the charge anisotropy. If we consider the high temperature situation ($> 1000°C$), where all the ions are sufficiently mobile the space charge width λ^* can be thought as equal to the Debye length [47], given by

$$L_D = \sqrt{\frac{\epsilon_0 \epsilon_r kT}{2q_i^2 n_i(\infty)}}. \tag{2.30}$$

where $n_i(\infty)$ is the bulk carrier concentration. One might expect this to be the case for grain boundaries formed at high temperature during sintering, or materials aged at intermediate temperatures for long periods of time. Alternatively if we consider the low temperature situation ($< 1000°C$), where we can assume that the cations are immobile and hence the dopant concentration across the space charge region is equal to the bulk, such that

$[Y'_{Zr}](x) = [Y'_{Zr}](\infty)$, the space charge width becomes [47]

$$\lambda^* = L_D \sqrt{\frac{4q_i}{kT}\Delta\phi(0)}, \tag{2.31}$$

where $\Delta\phi(0)$ is the potential at the interface. This situation may be more appropriate for ceramics fabricated using low temperature processing routes, such as thin films. Eq. 2.31 describes a double Schottky barrier situation with a concentration of oxygen vacancies at a distance x away from the grain boundary core given by [47]

$$\frac{[V_O^{\bullet\bullet}](x)}{[V_O^{\bullet\bullet}](\infty)} = \exp\left[-\frac{1}{2}\left(\frac{x-\lambda^*}{L_D}\right)^2\right], \tag{2.32}$$

where $\frac{[V_O^{\bullet\bullet}](x)}{[V_O^{\bullet\bullet}](\infty)}$ is the fraction of oxygen vacancies at locus x to that in the bulk. However because of the high concentration of oxygen vacancies in YSZ, using Equation 2.31 and a value of 0.25 V as the space charge potential the width of the space charge region in 8 mol.% YSZ is approximately 4 $\mathring{A}$ at 500 °C.

In order to calculate the modification of the resistance across a grain boundary with space charge layers, where the oxygen vacancies concentration is described by Eq. 2.32, we must modify the conductivity as

$$\sigma(x) = \sigma_{bulk} \exp\left(-\frac{q\Delta\phi(x)}{kT}\right), \tag{2.33}$$

where $\Delta\phi(x)$ is the potential at the locus x. It can then be shown that the corresponding grain boundary resistance, $R_{gb}^{(1)}$ is given by [47]

$$\frac{R_{gb}^{(1)}}{R_{Bulk}} = \frac{\exp(q\Delta\phi(0)/kT}{2q\Delta\phi(0)/kT}\frac{8\lambda^*}{\pi w^2}d_g, \tag{2.34}$$

where R_{Bulk} is the grain resistance, d_g is the average size of a grain and w is the diameter of the grain-to-grain contact.

Impurity Phases

SiO_2 is a major impurity found in ZrO_2 and CeO_2 ceramics, which can accumulate at the grain boundaries during sintering to form an intergranular siliceous phase. This phase is dependent on effects such as composition, impurity concentration, wetting properties, location, and sintering temperatures, atmospheres and cooling rates. Studies investigating grain boundary transport in YSZ of varying dopant concentration [55], have shown the transport to be highly dependent on grain size, impurity levels and cooling procedures, with large changes in the specific grain boundary conductivity but minimal variation in the activation energy.

Intergranular siliceous phases are most commonly observed as a pocket at a triple grain junction [47]. Assuming a negligible oxygen ion conductivity through the SiO_2 phase, the modification of the grain boundary resistance, compared to that of the bulk can be deduced from geometric considerations as

$$\frac{R_{gb}^{(2)}}{R_{Bulk}} = f_{geo}\frac{d_g}{w}, \tag{2.35}$$

where f_{geo} is a geometric correction factor given by

$$f_{geo} = \frac{1 - w/d_g}{1 + w/(2d_g)}. \tag{2.36}$$

This situation is shown schematically in Fig. 2.12.

Brick Layer Model

The total grain boundary resistance, R_{gb}, in many real systems will be a combination of space charge and impurity phase effects such that

$$R_{gb} = R_{gb}^{(1)} + R_{gb}^{(2)}. \tag{2.37}$$

If we assume that the blocking effect from the impurity phase is negligible ($R_{gb} \approx R_{gb}^{(1)}$), and that the system made up of large uniform grains, then it may be approximated by the brick layer model (shown schematically in Fig. 2.13). The brick layer model treats the material as an array of cubic grains separated by grain boundaries of finite thickness. The model allows

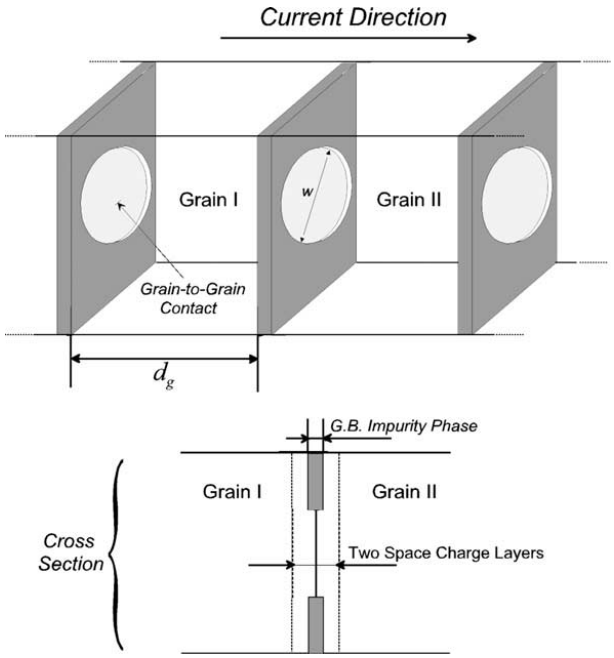


Figure 2.12: Schematic representation of grain boundary conduction pathways. Taken with permission from Guo and Waser [47].

for two parallel conduction paths through the material. The first is through the grains and perpendicularly across the grain boundaries, and the second path runs parallel through the grain boundaries. For doped ZrO_2 and doped CeO_2 systems the former path will dominate the conduction as $\sigma_{bulk} >> \sigma_{gb}$, and hence the total resistance will be a sum of R_{Bulk} and R_{gb}.

2.3.2 Heterogeneous Interfaces

Heterogeneous interfaces occur between two different chemical phases. Typically these are studied in fabricated nanoscale structures such as thin films, multilayers and nanocomposites. While both space charge regions and impurity phases are possible as they are at grain boundaries, often they are ruled out from dominating the total conductivity of the structures. This is because impurity phases can be avoided by using higher purity starting materials and the space charge regions are too small in the doped fluorites to dramatically alter the total transport properties parallel to the interfaces, even when the layer sizes are reduced to several nanometers [56, 57].

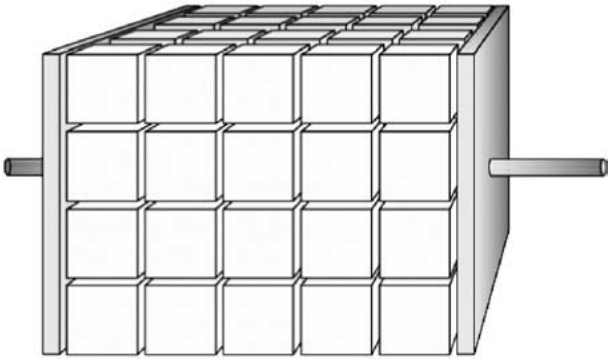


Figure 2.13: Schematic diagram of the brick layer model. Taken with permission from Guo and Waser [47].

If a phase grown on top of another is epitaxial, that is to some extent ordered based on the crystallographic orientations of the substrate crystal, one may define a lattice mismatch between the phases 1 and 2 as

$$f_{1,2} = \frac{d_{hkl,2} - d_{hkl,1}}{d_{hkl,1}} \tag{2.38}$$

where $d_{hkl,1}$ and $d_{hkl,2}$ are the lattice parameters of phases 1 and 2 respectively which are parallel to one another and perpendicular to the interface. If $f_{1,2}$ is small (<5%), then the mismatch may be completely compensated by elastic strain fields in the regions next to the interface. In this case there is no discontinuity of the atomic planes, and it is known as a coherent interface, as shown in Fig. 2.14a. As $f_{1,2}$ increases, a regular network of misfit dislocations can form at the interface to relieve the strain (see Fig. 2.14b), termed a semi-coherent interface. Each dislocation will be accompanied by a highly localised strain field, which will be discussed in Section 2.3.2. Finally, if the two phases have substantially different symmetries and incommensurate lattice parameters, an incoherent interface will form, resulting in a highly disordered or even partially amorphous interface, shown in Fig. 2.14c.

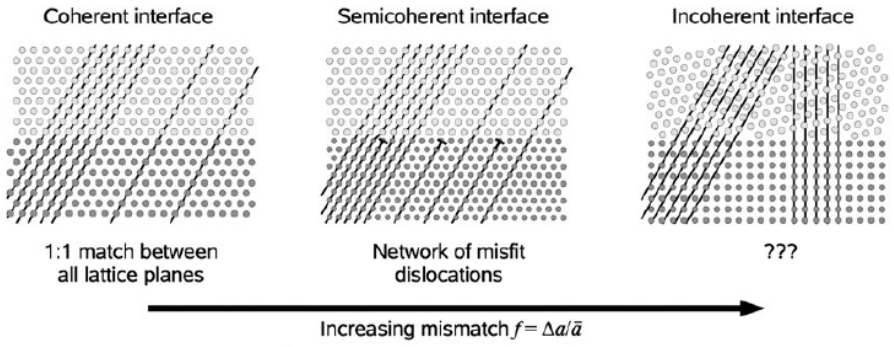


Figure 2.14: 2D sketch representing the three classifications of interface: coherent (a), semi-coherent (b), and incoherent (c). Also included is the simplified dependence on the lattice mismatch, $f_{1,2}$. Taken with permission from Korte *et al.* [58].

Strain Effects

In order to understand how strain may affect the oxygen ion transport in doped ZrO_2 and CeO_2, we must return to our previous assessment of the conductivity. For simplicity, we will assume that vacancy association is complete such that Eqs. 2.23 and 2.24 are valid and that the conductivity is described by Eq. 2.25. It is reasonable to assume that the entropic and the pre-exponential terms are pressure independent and may be combined into a single pre-exponential factor, σ^0, to give

$$\sigma = \sigma^0 \exp\left(\frac{-(\Delta H_m + \Delta H_A)}{kT}\right). \tag{2.39}$$

The free migration enthalpy and the free association enthalpy and therefore the conductivity are pressure dependent. We may differentiate Eq. 2.39 with respect to the pressure, p, to give[7]

$$\frac{\delta \ln \sigma}{\delta p} \approx \left(\frac{-(\Delta V_m + \Delta V_A)}{kT}\right), \tag{2.40}$$

where ΔV_m is the migration volume and represents the volume change when the oxygen ion reaches the transition point between two sites [59], and ΔV_A is the volume change between the associated pair and free defects whose

[7]For a system subject to isotropic strain, it is given that $\left(\frac{\delta \Delta H}{\delta p}\right)_T = \Delta V$ [59].

reaction is described by Eq. 2.19 [60]. The pressure dependence of the vibrational frequency of the lattice, ν_0, and the jump distance, a_0, are assumed to be negligible compared to the exponential term. From Eq. 2.40, it can simply be shown that

$$\frac{\sigma_{int}}{\sigma_{bulk}} = \exp\left(\frac{-(\Delta V_m + \Delta V_A)}{kT}\, p\right), \tag{2.41}$$

where σ_{int} and σ_{bulk} are the conductivity in an isotropically strained region and an unstrained region respectively. For an ion vacancy hopping type mechanism, the migration volume is expected to be positive [61]. Also, it is expected that the volume change from a defect associate to free separated defects is positive [62]. Therefore from Eq. 2.41, it can be seen that the conductivity is exponentially dependent upon pressure, such that a positive pressure would result in a decrease of the conductivity and negative pressure would enhance it. It is also reasonable to assume that these effects would be altered in different systems (e.g. dopant cations, host structure) due to changes in the migration and dissociation volumes.

To calculate the pressure, p, at an interface between an ionic conductor (phase 1) and an ionic insulator (phase 2), we must consider the trace of the stress tensor, $\boldsymbol{\sigma}$, given by

$$p = -\frac{1}{3} tr(\boldsymbol{\sigma}) = -\frac{1}{3}(\sigma_{xx} + \sigma_{yy} + \sigma_{zz}), \tag{2.42}$$

where the stress components σ_{xx} and σ_{yy} are parallel and σ_{zz} is perpendicular to the interface plane. Rather than being isotropic, at an interface the stress is biaxial such that

$$\sigma_{xx} = \sigma_{yy} = \frac{Y_1}{1 - \nu_1}\epsilon_{1,2}, \tag{2.43}$$

and

$$\sigma_{zz} = 0, \tag{2.44}$$

where $\epsilon_{1,2} = \epsilon_{xx} = \epsilon_{yy}$, Y_1 and ν_1 are the Young's modulus and Poisson ratio for phase 1 respectively. At a coherent interface between two phases with identical elastic properties, the lattice mismatch $f_{1,2}$ is compensated

entirely by elastic strain such that $f_{1,2} = 2\epsilon_{1,2}$. Therefore in close proximity to a coherent interface, the pressure is given by

$$p = -\frac{2}{3}\frac{Y_1}{1-\nu_1}\epsilon_{1,2} = -\frac{1}{3}\frac{Y_1}{1-\nu_1}f_{1,2}. \tag{2.45}$$

Korte *et al.* [63], have provided a more rigorous treatment of the strain states across a thin symmetric layer sandwiched between two insulating phases and bounded by coherent, strained interfaces. Considering an exponential decay in the elastic deformation, with increasing distance away from the interface, z, the pressure is given by

$$p(z) = -\frac{2}{3}\frac{Y_1}{1-\nu_1}\epsilon_{1,2}\frac{\cosh(z/\delta_0)}{d/2\delta_0}. \tag{2.46}$$

Here the phase boundaries are given by $z = -d/2$ and $z = d/2$, where d is the height of the layer and δ_0 is the height of the strained region. δ_0 is found by calculating the total elastic energy of the layer,

$$E_{elast} = \frac{1}{2}\int_V tr(\boldsymbol{\sigma}.\boldsymbol{\epsilon})dV, \tag{2.47}$$

and finding the minimum, by taking the derivative with respect to δ_0. For brevity we will skip straight to the only solution which is physically meaningful, and for a full derivation the reader is refereed to Ref. [63].

$$\delta_0 = \frac{1}{4}\sqrt{\frac{2}{3}\frac{1-\nu_1}{1+\nu_1}}\, l. \tag{2.48}$$

An important outcome of this treatment is that the size of a strained region close to an interface is dependent upon the width of the grains of the material l. Finally an expression may be constructed to give the total conductivity, σ_{tot}, of a strained layer of thickness d:

$$\sigma_{tot} = \sigma_{bulk}\frac{1}{d}\int_{-\frac{d}{2}}^{+\frac{d}{2}}\boldsymbol{\sigma}(z)dz = \frac{1}{d^*}\int_0^{d^*}\exp\left(\alpha\epsilon_0\frac{\cosh\ z^{'}}{\cosh\ d^*}\right)dz^{'} \tag{2.49}$$

where

$$z = z/\delta_0, \quad d^* = d/2\delta_0, \quad \text{and} \quad \alpha = \frac{2}{3}\frac{(\Delta V_m + \Delta V_A)}{kT}\frac{Y_1}{1-\nu_1}. \tag{2.50}$$

This model, introduced by Korte *et al.* [63], is an elegant and quantifiable description of strained ionically conducting layers. Despite making a number of idealistic assumptions, such as perfectly coherent interfaces, it is still predicted that the conductivity of such a layer would be dependent upon a large number of parameters such as lattice mismatch, layer height, grain size, and those affecting the association and migration volumes which are less well understood but may include variations in the host cation lattice, dopant type and dopant concentration. This makes comparisons between different experimental studies difficult.

Eq. 2.49, predicts a maximum of a *ten-fold* enhancement of the conductivity using literature values for V_m[8], a strain of 6-10 %, an average grain size of 20-100 nm, neglecting the association enthalpy, and considering that the highest strains can only be accommodated if the grains are small. This implies that any enhancement in the transport properties due to a strained layer, could be of the same magnitude as changes in the conductivity due to alterations in the microstructure as average grain size changes.

Our treatment of strain in this section is limited, as it is based on isotropic mechanical behaviour and we have always assumed isotropic pressure by not using the full anisotropic compliance tensor and thereby neglecting effects such as Poisson relaxation. In addition we have not considered the effects of complex defect formation beyond simple dimers, or defect ordering due to strain. For a comprehensive prediction of interfacial strain on the conductivity, we would also require the migration and association volume tensors as well as their partial derivative to the stress components. The outcome would then depend on the space group, the orientation of the grains and the oxygen migration direction at the interface.

[8]For 9.5 mol.% YSZ at 750° applying uniaxial pressure, the activation volume, ΔV_m, was measured as 2.08 cm^3 mol^{-1} [64]

Dislocations

As the lattice mismatch at an interface is increased beyond 1-2%, the chance of forming dislocations becomes more likely, and the strain will instead manifest itself much more locally surrounding a network of dislocations rather than uniformly along the interface. An edge dislocation appears as an extra half plane of atoms, as depicted in Fig. 2.15a.

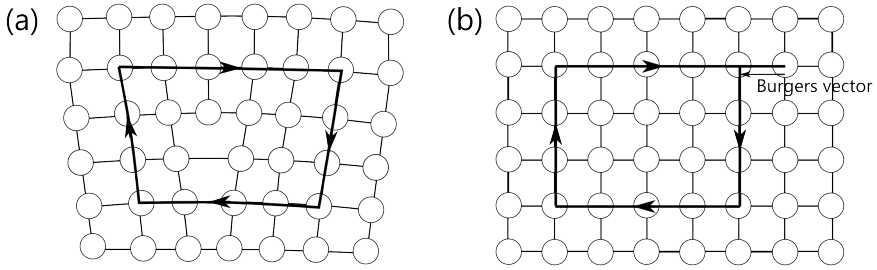


Figure 2.15: (a) Model of an edge dislocation in a cubic lattice, enclosed within a Burgers circuit. (b), the same circuit in a perfect crystal; the closure failure is equal to the Burgers vector.

Dislocations are described by a *Burgers circuit*, where an atom-to-atom path is taken in a closed loop surrounding a dislocation. If the same path is traced on a crystal void of dislocations, it should not close and an additional vector is required to form a closed loop. This is called the *Burgers vector*, and is shown in Fig. 2.15b. Another type of dislocation is the screw dislocation, described by a virtual shear stress, and in its most general sense a dislocation can be made up of both edge and screw types. Note that dislocations may not occur exclusively at heterogeneous interfaces and are also expected in bulk crystalline materials, indeed some special grain boundaries, such as low-angle tilt boundaries, are defined as an array of edge dislocations [22]. A generalised treatment of all dislocation types is out of the scope of this thesis and therefore we will limit our discussion to pure edge dislocations.

It is possible to calculate the strain field around a dislocation by assuming isotropic elasticity as we did in the previous section. Fig. 2.16 shows an edge dislocation with a Burgers vector, $\boldsymbol{b}$, parallel to the x-direction so that it runs along the z-direction. Considering the stress and strain components

around the dislocation it can be shown that the effective pressure is [65]

$$p = \frac{2}{6\pi}\frac{1+\nu_0}{1-\nu_0}\, G\, \boldsymbol{b}\, \frac{y}{x^2+y^2}, \tag{2.51}$$

where G is the shear modulus. This expression can then be inserted into Eq. 2.41, to give the modification in the conductivity surrounding the dislocation. The strain field is compressive above the slip plane and dilative below. Therefore depending on the direction of $\boldsymbol{b}$, at a heterogeneous interface between two phases, the dilative pressure could occur in either phase. It can be seen that our treatment breaks down as when $x, y \to 0$, $p \to \infty$, and is therefore only valid outside a critical core radius r_0. A reasonable value for this is when the stress reaches the theoretical maximum shear stress for an atomic lattice and is in the range of $\boldsymbol{b}$-4$\boldsymbol{b}$, or usually $\leq$1nm [65].

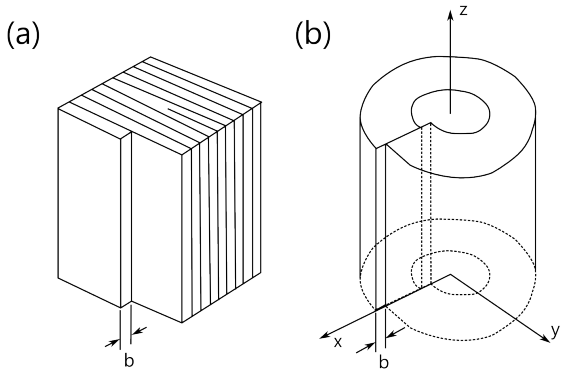


Figure 2.16: (a) Schematic of an edge dislocation formed in a crystal. (b), A cylindrical ring representing the elastically strained region around the same dislocation depicted in (a). Adapted from Hull and Bacon [65].

Fast pipe-like transport is therefore possible in the dilative strain field surrounding a dislocation core, with the magnitude of the modification dependent on the Burgers vector. In a material the total change in the conductivity will be critical to both $\boldsymbol{b}$ and the dislocation density, ρ_D. If the entire lattice mismatch $f_{1,2}$ is relieved by the formation of a dislocation network, then

$$\rho_D |\boldsymbol{b}| = |f_{1,2}|. \tag{2.52}$$

Therefore the greater the mismatch the greater the modification of conductivity; but due to the dipole nature of strain field, this could either enhance or reduce the transport in the conducting phase.

2.4 Surfaces

Surfaces are a type of heterogeneous phase boundary, often differentiated from heterogeneous interfaces, as discussed in Section 2.3.2, as they are boundaries between two different physical phases (such as solid-gas phase) as opposed to different chemical phases of different composition. The energy of a surface is defined as the change in the Gibbs free energy as the area of the surface, A, changes:

$$\lambda = \left(\frac{\delta G}{\delta A}\right)_{p,T,n}. \tag{2.53}$$

In a seminal work by Tasker [66], he describes surfaces of ionic materials as a stack of charged planes. Depending on the net charge on each plane and their stacking sequence three types of surface were defined. If the surface has a stoichiometric ratio in each layer it is neutral, as shown in Fig. 2.17a, it is known as Type 1. Type 2 surfaces have charged planes, however the repeat plane consists of three planes arranged in a symmetric manner, such that there is no dipole moment perpendicular to the surface (Fig. 2.17b). Both Type 1 and 2 are therefore stable, as additional planes make no contribution to the energy of the ions in the bulk crystal. If the stacking sequence consists of alternating planes of opposite charges, a dipole moment perpendicular to the surface is set up. This implies that as neutral repeat units are added to the surface, the energy of the crystal will diverge. This is a Type 3 surface (Fig. 2.17c) and is therefore charged and unstable, and will require substantial reconstruction or adsorption of additional charges. For the fluorite structure, the (110) surface termination is a Type 1 surface, the termination (100) is a Type 2 surface, and the (111) termination is the unstable Type 3 surface.

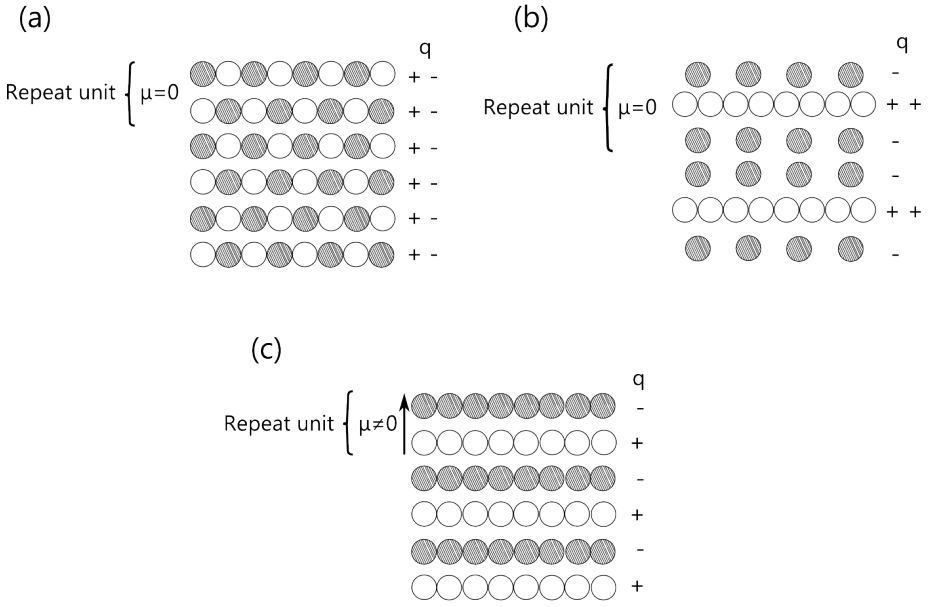


Figure 2.17: Distribution of charged and neutral planes at the surface of a crystal. (a) Type 1 surface: Neutral planes. (b) Type 2 surface: Charged planes but with no net dipole moment perpendicular to the surface. (c) Type 3 surface: Charged plane and non-zero dipole perpendicular to surface. Adapted from Tasker [66].

2.4.1 Surface Segregation

The segregation of dopants to the surface, occurs in many complex oxides, including the doped fluorites, as reviewed in Section 3.2. To understand the causes of surface segregation, we can consider a two component system consisting of a host cation lattice (species 1) with cation substitutionals (species 2), and for the moment ignore the anion sublattice. At equilibrium it can be shown that the ratio of the atomic fraction of the solute, X_2^{int}, to the atomic fraction of the solvent, X_1^{int}, at the interface is [67]

$$\frac{X_2^{int}}{X_1^{int}} = \frac{X_2^{bulk}}{X_1^{bulk}} \exp\left(\frac{\Delta S_S}{k}\right) \exp\left(\frac{-\Delta H_S}{kT}\right), \tag{2.54}$$

where X_i^{bulk} is atomic fractions of the ith component in the bulk region, and ΔS_S and ΔH_S are the entropy and the enthalpy of segregation respectively. From Eq. 2.54 it is clear that at high temperature ($T \approx \Delta H_S/k$) the

surface concentration is the same as the bulk and segregation is negligible. However at low temperature the driving force for segregation is much higher. Physically ΔH_S, can be thought of as the enthalpy change which results when ion 2 from the bulk is exchanged with ion 1 at the surface. In alloys it has been shown that a good approximation of the enthalpy of segregation is given by [68]

$$\Delta H_S = \Delta H_{int} + \Delta H_{bin} + \Delta H_{\epsilon}, \tag{2.55}$$

where ΔH_{int} is the interfacial energy contribution, given by

$$\Delta H_{int} = (\lambda_2 - \lambda_1)A, \tag{2.56}$$

where λ_i is the specific surface energy of the ith phases and A is the area per atom on the surface. ΔH_{bin} is the binary interaction contribution, which in the limits of infinite dilution and high temperature may be expressed as [69]

$$\Delta H_{bin} = \frac{-\Delta H_{mix}}{(\alpha X_1^{bulk} X_2^{bulk})}, \tag{2.57}$$

where ΔH_{mix} is the heat of mixing for binary solution, and α is a geometric constant dependent on the crystallographic orientation of the surface. If ΔH_{mix} is positive the system will tend towards clustering or phase separation and segregation will be enhanced. Alternatively if ΔH_{mix} is negative, atomic ordering is favourable and segregation will be suppressed. ΔH_{ϵ} is the solute strain energy contribution and takes the form [70]

$$\Delta H_{\epsilon} = \frac{-24\pi Y G r_1 r_2 (r_2 - r_1)^2}{4G r_1 + 3Y r_2}, \tag{2.58}$$

where G is the shear modulus, Y is the bulk modulus, r_i is the ionic radii of the ith ion. Here in Eq. 2.55, we have ignored any segregation due to a space charge stemming from a Type 3 surface or charged adsorbates. One might expect an additional term

$$\Delta H_{SC} = q_i \ \phi(0), \tag{2.59}$$

where $\phi(0)$ is the charge at the surface.

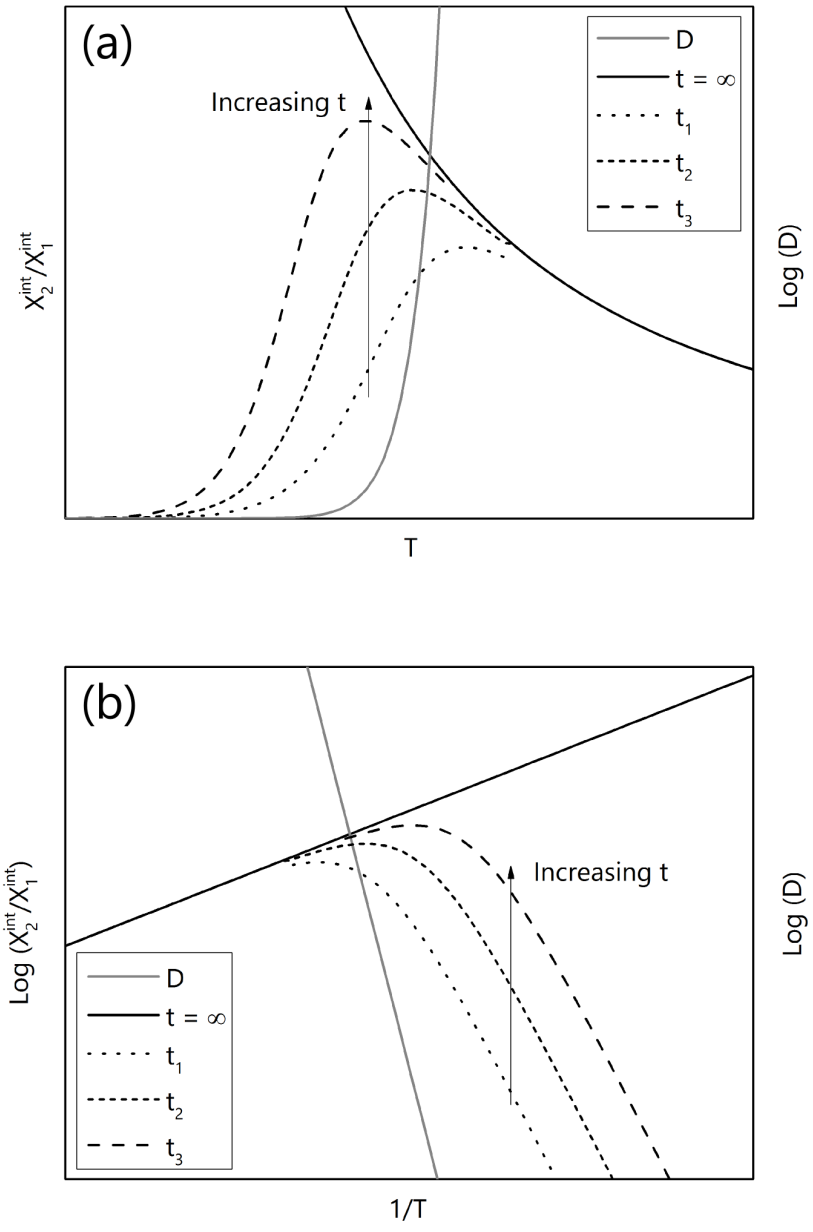


Figure 2.18: Segregation and diffusivity in a binary system, plotted on (a) a linear axis and (b) as an Arrenhius diagram. The black line represents the surface concentration at $t = \infty$ given by Eq. 2.54. The dashed lines represent the surface concentration for given diffusion times, such that $t_1 < t_2 < t_3$.

It must be noted that this model was originally proposed for covalently bonded metallic systems and is based on binary interactions due to nearest neighbour bond formalism [68]. For the case of ionic materials, columbic bonds act over much longer distances, and hence the question remains to the extent to which this model can be used to describe ceramics. Regardless, Eq. 2.54 should remain valid even if the mechanisms affecting the enthalpy of segregation are not quantitatively understood, and has previously it has been used successfully to describe CaO segregation in MgO single crystals [69].

In ceramics, often cation diffusion is very slow even for the timescales and temperatures of many experimental studies, and it cannot always be assumed that equilibrium has been reached. It is therefore often necessary to correct the surface species fraction taking into account the diffusivity of the species. The ratio of surface composition of species 2 at time t, $X_2^{int}(t)$, to that at equilibrium, $X_2^{int}(\infty)$, is expressed as [71]

$$\frac{X_2^{int}(t)}{X_2^{int}(\infty)} = 1 - \exp\left(\frac{Dt}{\beta^2 d^2}\right) \mathrm{erfc}\left(\frac{Dt}{\beta^2 d^2}\right)^{1/2}, \tag{2.60}$$

where D is the diffusivity, d is the width of the segregated layer, usually taken to be roughly the interplaner spacing, and β is

$$\beta = \frac{X_2^{int}(\infty)}{X_2^{bulk}}. \tag{2.61}$$

Diffusivity obeys the same Arrenhius type relationship as ionic conductivity (Eq. 2.14), and often can be treated analogously. The two properties are related by the Nernst-Einstein equation, given by

$$D_i = \frac{\sigma_i kT}{q_i n_i}. \tag{2.62}$$

Eq. 2.54 is substituted into Eq. 2.60 and plotted in Fig. 2.18, along with Eq. 2.54, and D, taken for reasonable values of d, ΔH_S, ΔH_m. Here it is assumed that the concentration of the solute is low, such that $X_2^{int}/X_1^{int} \approx X_2^{int}$. It can be seen that for isotemporal studies, the surface segregation observes a maximum at a certain temperature, which will be dependent upon the driving forces for segregation, such as ionic radii mismatch and

surface energy, as well as the diffusivity of the segregating species. As the diffusion time increases, the maximum shifts to lower temperature.

2.5 Summary

In this chapter the fundamentals of intrinsic and extrinsic defect formation in crystalline oxides has been introduced. Mass transport in ionically conducting materials has been discussed and models provided to describe the effects of temperature, concentration of charge carriers, migration enthalpy and association enthalpy. Changes in these effects in proximity to homogeneous and heterogeneous interfaces have been considered, paying particular attention to changes in the transport properties due to lattice strain, either caused by epitaxial strain or surrounding dislocations. Finally dopant segregation to the surface of materials was discussed.

Chapter 3

Literature Review

In this chapter previous reports into the modification of transport properties and surface segregation phenomena will be reviewed for doped ZrO_2[1] and CeO_2. Regarding O ion transport, the focus of this thesis is on heterophase boundaries in YSZ, but it is useful to first briefly review the literature on studies of nanogranular materials, where there is a high density of homophase boundaries. Next experimental and computational reports on the subject of ionic conductivity at heterointerfaces will be discussed. Finally studies on the segregation of dopants to the surface of fluorite materials will be reviewed.

3.1 Ionic Transport in Nanostructured Materials

In order to study properties at an interfacial between to different phases, often ionic conductors are fabricated in the form of thin films or multilayered heterostructures so that one dimension may be reduced while keeping the other suitable for most laboratory characterisation techniques. Sample fabrication methods can be vacuum-based techniques, such as pulsed laser deposition (PLD), RF-sputtering and molecular beam epitaxy (MBE), or precipitation based techniques such as chemical vapour deposition, atomic layer deposition, spray pyrolysis, sol-gel and flame spraying. These methods

[1] As a matter of practice, we will refer to Y doped ZrO_2 as YSZ if dopant concentration $\geq$ 8mol.%, and YDZ (yttria-doped zirconia) if not. Although this is an assumption that may not always be valid, it allows for instant recognition of whether it is expected to be in the cubic fluorite structure or not.

are often performed well below the usual sintering temperatures (>1400°C), and typically yield microstructures dramatically different from bulk ceramics, such as grain sizes approaching the nano-scale. Before we discuss reports of modified ionic conductivity in thin films (< 200 nm in thickness) and multilayers, it is beneficial to briefly review the literature on transport in nano-granular materials, such that these effects may be understood in isolation. In this section of the review the focus will primarily be on the ionic transport in YSZ. A full examination of the literature on doped-CeO_2 is out of the scope of this chapter and hence the discussion will be kept much more brief.

3.1.1 Nano-granular Materials

Nanocrystalline Bulk YDZ

By varying the sintering temperature and time, and by starting from nanoscopic powders it is possible to fabricate ceramic materials with an average grain size down to tens of nanometres. This was implemented by Guo *et al.* [72], who produced dense samples ($\geq$ 94% relative density) of 3 mol.% YDZ that were shown to have grain sizes varying from 1330-120 nm, separated by grain boundaries free from any siliceous second phase, as analysed by scanning electron microscopy (SEM) and high resolution transmission electron microscopy (HR-TEM). Employing EIS and the brick layer model, it was shown that the grain boundary conductivity increased and the bulk conductivity decreased for smaller grain sizes, as shown in Fig 3.1, but little change in the activation energy was observed for either. Guo *et al.* explained the results in terms of a space charge model, suggesting that the cause for the specific grain boundary conductivity rising was due to an increase in the number of oxygen vacancies in the space charge region, and that the decrease in the specific bulk conductivity was caused by a depletion of yttrium in the grains as it segregates to the grain boundaries. Previous works on nano-granular 2.9 mol.% YDZ [73], 8.2 mol.% YSZ [55] and 15 mol.% calcia- stabilized zirconia (CSZ) [74] were analysed in terms of this model and found to agree. The increase in oxygen vacancies was thought to be due to the decrease in the space charge potential [47], but this was only inferred

and no direct evidence was provided.

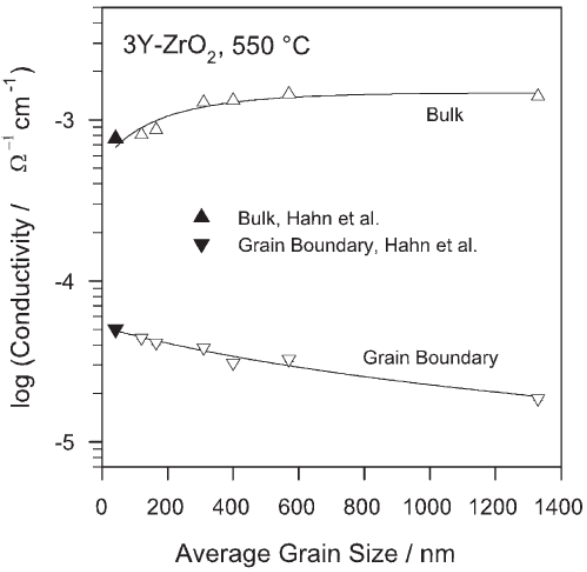


Figure 3.1: Bulk conductivities and specific grain boundary conductivities for 3 mol.% YDZ at 550 °C as a function of average grain size. Taken with permission from Guo *et al.* [72]. Data included in the plot orginates from Mondal *et al.* [73].

For 8 mol.% YSZ samples fabricated with a grain size of 800-17 nm [75] and 45 nm [76], qualitatively similar results have been observed with either an increase in the specific grain boundary conductivity or a decrease in the specific grain conductivity as the grain size is decreased from micro-granular YSZ.

Perry *et al.* studied partially sintered 8 mol.% YSZ [77] and 3 mol.% YDZ [78] in the range of 1000-10 nm grain sizes. The samples were analysed using EIS and a nano-grain composite model, which could describe the grain boundary conductivity more reliably than the brick layer model as the grain size approached that of the grain boundary width. Correcting for the porosity in the samples, the authors observed that the grain core conductivity was slightly decreased, whereas the specific grain boundary conductivity was enhanced up to an order of magnitude for decreasing grain sizes into the nano-regime, but not enough to improve the total conductivity, which was found to decrease due to the higher density of grain boundaries with respect to the micro-granular YSZ and YDZ.

The high concentration of oxygen vacancies observed in the core of grain boundaries in YSZ [54], has led some to postulate that rapid ionic conductivity may be possible in the grain boundaries. Knöner *et al.* [79] measured the oxygen transport in polycrystalline 6.9 mol.% YDZ with an average grain size of <100 nm using isotope exchange tracer diffusion (IETD)[2]. They found an enhancement in the diffusivity of up to three orders of magnitude over 9.5 mol.% single crystal YSZ, which they attributed to fast grain boundary diffusivity. Since, De Souza *et al.* [80] have repeated a similar experiment employing IETD on 8 mol.% YSZ with a grain size of 50 nm and showed that in fact the grain boundary diffusivity was much lower than the grain core. They suggested that the previous observed enhancement was due to porosity in the samples leading to permeation of the enriched gas phase extending the tracers profile in the material.

Nanocrystalline YDZ Films

Film deposition techniques can provide an alternative method for creating irregular microstructures, which are not possible using a conventional sintering of powders approach. Depending on the fabrication technique, the grains can vary in size from several microns to nanometres, from randomly oriented grains to those with a preferred crystallographic orientation, and even grains with unconventional aspect ratios such as columnar microstructures are possible. For films where the thickness is greater than 200 nm, it is expected that any effects on the transport due to the film/substrate interface will be minimal and the total film conductivity to be dependent only on the grains and grain boundaries. Hence in this section, the discussion is limited to films which are 200 nm or greater in thickness.

Kosacki *et al.* [81], fabricated 8 mol.% YSZ films on mono- and polycrystalline sapphire using a sol-gel process, varying the grain size between 1-220 nm for films between 400-700 nm in thickness. A two orders of magnitude increase in the total conductivity of the films was observed compared to polycrystalline bulk materials, as well as a decrease in the activation energy from 1.23 to 0.93 eV. The authors attributed this enhancement to the

[2]This technique is described in Section 4.5.

increase in the density of the grain boundaries.

In an attempt to repeat the work carried out by Kosacki *et al.*, Peters *et al.* [82] studied 400 nm thick 8.3 mol.% YSZ films grown on sapphire by the sol-gel technique. Varying the grain size from 782 nm to 5 nm, the authors observed no true size effects in the conductivity measured by EIS, and instead found a decrease in the total conductivity in accordance with the previous work carried out on nano-granular materials by Guo *et al.* [72], as discussed above. Similar results were found by Joo *et al.* [83], for films grown by PLD with a grain size of 100-60 nm, measured by EIS both in-plane and across-plane.

In an extensive study, Schlupp *et al.* [84], fabricated 8 mol.% YSZ films by aerosol assisted chemical vapour deposition, spray pyrolysis, and PLD, with thicknesses ranging between 220 nm and 600 nm. This allowed films with a range of microstructures to be studied such as amorphous, columnar grains, and randomly oriented grains with sizes between 3 and 9 nm. Measuring the conductivity across-plane, no enhancement in the conductivity was found, but depending on the microstructure the authors found that either bulk or grain boundary responses dominated the impedance spectra.

Other studies of Y doped-ZrO_2 films, have suggested unexpected effects on the transport properties due to the non-traditional fabrication routes. Chun *et al.* [85] found that the conductivity and activation energy of 4.9 mol.% YDZ films grown by metal-organic chemical vapour deposition, varied depending on the substrate when grown on sapphire, MgO and SiO_2 glass. As the films had a thickness of 0.5-2.5 μm, and no significant difference in the microstructures were observed, interfacial strain due to lattice or thermal mismatch between the film and substrate seems unlikely. Heiroth *et al.* [86], grew amorphous films by PLD at room temperature, and annealed them while measuring the conductivity. Interestingly they found a maximum in the conductivity during the heat treatment before a steady state was reached, although this only accounted for an enhancement of 5%. Finally, Jung *et al.* [87], studied the effects of dopant concentration for 1 μm thick YDZ films grown by reactive RF sputtering. The authors observed an enhancement of one order of magnitude over 9 mol.% YSZ bulk values, but also found that the optimum dopant concentration was at 6.5 mol.%,

rather than between 8-10 mol.%, as typically found in bulk materials. This was attributed to a metastable cubic phase forming at much lower dopant concentrations than that for bulk YDZ.

Nanocrystalline Doped-CeO_2 Films

Research into the properties of nanocrystalline CGO has also been extensive. Due to the ionic conductivity of CGO being substantially higher than YSZ at low temperatures (<800°C), it is better suited to applications such as μSOFCs where the device is fabricated on Si wafers and operates below 600°C. Low temperature film deposition techniques can be used to create thin electrolyte layers, as a reduced thickness is ideal for minimising the Ohmic resistance of the cell and because a high temperature sintering step would damage the Si support. As a consequence electrolyte layers with nano-sized grains often result, as discussed above. Doped-ceria films have been fabricated by vacuum-based physical vapour techniques, such as PLD [88–91] and RF sputtering [92, 93], as well as precipitation-based methods such as sol-gel [94], spray pyrolysis [91] and flame spraying [95].

For brevity we will not extensively review these results, and instead direct the reader towards a recent review by Rupp [96]. Comparing the transport properties of 20 mol.% CGO films of a thickness greater than 200 nm and fabricated by a variety of techniques, Rupp notes that the conductivity and activation energies in films are often found to be much higher (1.1 ± 0.3 eV) than in sintered bulk materials (0.78 ± 0.05 eV). As reproduced in Fig. 3.2, she showed that often the size of the grains is proportional to the activation energy of the films, but that this does not hold when comparing films with a similar grains size fabricated by different techniques, or that it is even repeatable using the same techniques fabricated by different research groups. Rupp attributes these differences to lattice strain, defined as the long range isotropic displacement fields of the atoms in a material, which is induced in the films during fabrication. Hence the lattice strain in the films is a function of the processing route, and sensitive to factors such as the temperature, oxygen partial pressure and chemistry conditions, as well as the thermal history of the films post-fabrication.

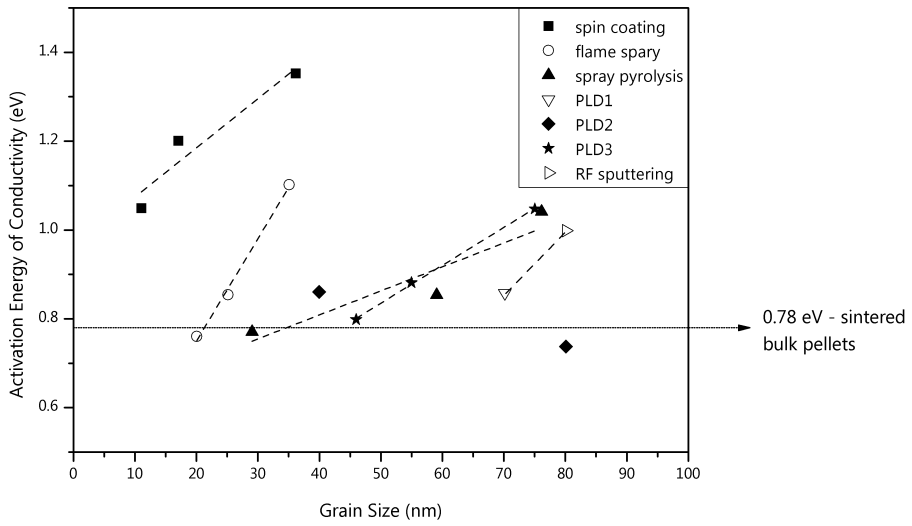


Figure 3.2: Literature activation energies of electrical conductivity of 20 mol.% CGO films as a function of grain size. Adapted from Ref [96]. Data taken for spin coating taken from Ref [94], flame spraying from Ref [95], spray pyrolysis from Ref [91], PLD1 from Ref [89], PLD2 from Ref [90], PLD3 from Ref [91], and RF sputtering [92].

Rupp *et al.* [97] developed this concept, studying films of ceria substituted with a Sc, Gd, La, and Lu grown by PLD at room temperature. They found that annealing the films at 600°C resulted in similar lattice parameters as their bulk counterparts, but for 1000°C heat treatments the lattice parameters of the films were substantially compacted by up to almost 2%. This is a similar magnitude to that which occurs when doping ceria with cations of different ionic radii, as seen in Fig. 2.4. Measuring the conductivity of the Gd-doped CeO_2 films as a function of the anneal temperature, the authors found that as the films became compressed the conductivity decreased and the activation energy increased from 0.7 to 1.1 eV, as shown in Fig. 3.3. Comparing the results to DFT calculations, they concluded that the most likely source of the change in activation energy was from a change in the oxygen ion migration energy, although modifications of the defect association energy could not be excluded.

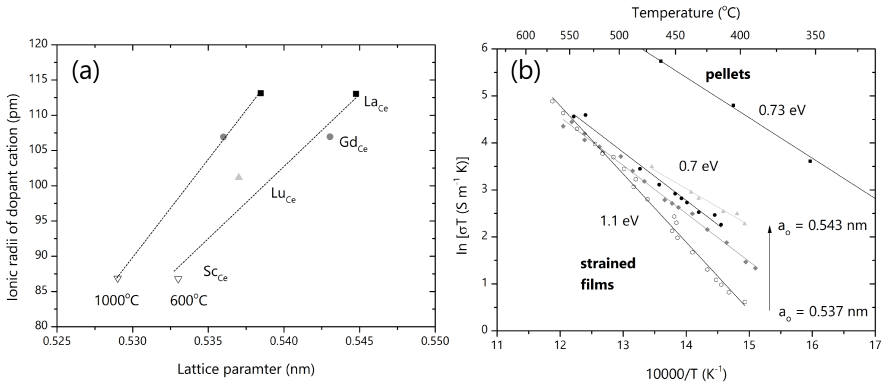


Figure 3.3: (a) Lattice parameters of doped-CeO_2 films grown by Rupp *et al.* after heat treatments at 600°C and 1000°C. (b) Arrhenius plot of the CGO films for different lattice parameters after heat treatment. Data taken from Ref. [97].

3.1.2 Single Thin Films

Heterointerfaces are typically studied using one of two sample configurations where a high density of interfaces may be studied: single thin films and multilayers. Thin films usually consist of ionic conductors grown on electrically insulated substrates, whereas multilayers are typically formed of multiple repeat units of either an ionic conductor and an insulator or two ionic conductors grown on insulating substrates. Each geometry has advantages and disadvantages. In this section the literature on single thin films will be reviewed, but firstly it is beneficial to highlight the potential experimental pitfalls of studying interfaces in thin films such that the published reports may be discussed more critically.

By their nature thin film systems are simpler to fabricate and characterise than multilayers due to their less elaborate structure. Through chemical and thermal pre-treatment it is possible to control the surface termination of the substrate [98], which can have a dramatic effect on the orientation and growth mechanisms of the subsequently grown film [99]. Indeed the remarkable 2D electron gas effects observed at the STO/LAO interface [100], have been found to be highly dependent upon the substrate treatment and termination [101]. Controlling interfacial terminations and orientation is much more challenging in multilayer structures and in extreme

cases can lead to structural discontinuity of the layers [102].

Probing interfacial effects using thin films is often approached by growing a set of samples in an identical manner, varying only the total thickness of the films. This acts to vary the volume fraction of the interfacial region compared to the total conducting body. Therefore if the transport properties are modified close to the interface, these changes will be more pronounced in thinner films. However, this method of investigating interfacial properties is not without its caveats. Firstly by simply reducing the thickness of films it is not only the film-substrate interface volume fraction which is being increased. The relative volume of the surface and sub-surface region are also varied with respect to the total film. Therefore any changes observed in the total films properties cannot be unambiguously attributed to the heterophase interface. Molecular dynamics (MD) simulations have suggested that in fact oxygen vacancies are immobile in the sub-surface region of Sc-doped ceria [103], but this has not been extended to YSZ nor does it consider mobile surface-adsorbed charge carriers.

Secondly, only substrates are used which are known to be nominally insulating, compared to the ionic conductors which are the subject of study. But caution must be taken here due to the extreme geometrical aspect ratio of the systems being measured. Typically commercial ceramic substrates are approximately 0.5 mm thick, but the films grown on them can be as thin as 5 nm or less. Therefore in the instance of a 5 nm film, in order to measure the conductivity to 2 significant figures accurately (i.e. the conductance of the substrate be at least 3 orders of magnitude lower than film), the conductivity of the substrate material must be at least 8 orders of magnitude lower! This is made increasingly hard to estimate, due to the intrinsic and extrinsic, ionic and electronic charge carriers possible in many common substrate materials which vary with impurity content and temperature.

Kim *et al.* [104] have shown that an 'illusional' interfacial effect can be observed when measuring the conductivity of YSZ films of decreasing thickness, due to current leakage through low impurity, but still nominally insulating, ceramic cements and alumina supports often employed in electrical testing rigs. Fig. 3.4 shows the conductivity of films of varying thickness measured using a low-purity (Fig. 3.4a), and high-purity (Fig. 3.4b) alu-

mina support. However it is possible to check against substrate leakage or systematic experimental error when measuring the conductivity electrically, by simply measuring the bare substrates in an identical fashion and the open circuit response of the electrical testing rig.

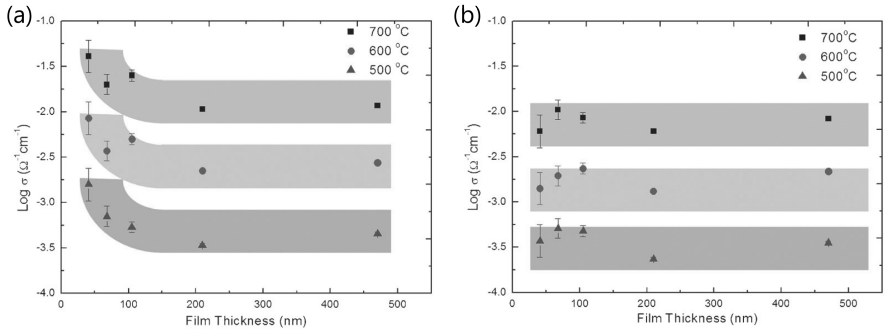


Figure 3.4: Measured conductivity of YSZ films of varying thickness using (a) a low-purity alumina support and (b) a high-purity alumina support. Taken with permission from Ref. [104].

More rigorously, one may employ techniques that verify the charge carriers to be ionic or even specifically oxygen ions. Measuring the conductivity at a number of oxygen partial pressures allows one to construct a Brouwer diagram. Electrical transport due to electrons or holes will be observed as characteristic slopes, with oxygen partial pressure, whereas ionic transport will remain constant. For more details the reader is referred to the substantial literature on the subject [27–29]. Alternatively one may directly track the diffusion path of particular ionic carriers using isotope exchange tracer diffusion (IETD).

Finally, depending on the crystal nucleation and growth mechanisms, it is possible that the microstructure, grain size, orientation, and dopant and defect concentrations may not be uniform over the entire thickness of the films, leading to an erroneous conclusion based on interfacial strain. Indeed, this was the conclusion of Gobel *et al.* [105], who despite observing an enhanced interfacial effect for pure ceria films, noted that the more likely cause was due to the decrease in grain size closer to the interface, observed by TEM.

Kosacki *et. al.*, 2004 [106, 107] - YSZ/MgO Films

Kosacki *et. al.* [106, 107] were one of the first to measure an enhancement in the conductivity of a YSZ thin film and attribute it to heterogeneous interfacial behaviour. Using PLD, the authors grew 9.5 mol.% YSZ thin films on MgO substrates varying the thickness from 2 μm to 15 nm. From XRD, TEM, and selected area electron diffraction (SAED) characterisation the films were found to be epitaxial with the substrate in the orientation:

$$\text{YSZ (001)||MgO (001)}$$
$$\text{YSZ [100]||MgO [100]}$$

The authors also claim little evidence for strain contours, dislocations or grain boundaries in the TEM images, which is particularly surprising considering the approximately -18% mismatch between the YSZ and MgO lattice parameters. The electrical conductivity was determined by two-probe EIS and four-probe DC measurements with Ag electrodes in the temperature range of 400 to 800°C. However Ag is known to be mobile of the surface of YSZ from temperatures as low as 250°C, and the self diffusion coefficient to be as high as 3 $\times 10^{-5} \text{cm}^2\text{s}^{-1}$ at 500°C [108].

As shown in Fig. 3.5a, for film thickness (d) from 2000 to 58 nm the resistance scales with $1/d$ indicating no change in conductivity and similar to that of single crystal YSZ. But when the thickness is reduced below 60 nm the resistance actually decreases indicting an enhancement in the conductivity of 2 orders of magnitude. Fig. 3.5b displays the Arrhenius behaviour of the films, where one can observe that the enhancement is coupled with a drop in the activation energy across the whole temperature range for 15 nm thick film but only above $\sim$ 650 °C for the 29 nm thick film.

As the conductivity was found to be independent of pO_2, Kosacki *et. al.* attribute the behaviour to an enhancement of the oxygen transport at the YSZ/MgO interface such that as the thickness is reduced below 60 nm there is a switch in the conduction mechanism from bulk diffusivity to interface controlled. Enhanced transport at the surface is rejected on the grounds of a previous study using low energy ion scattering (LEIS) to show

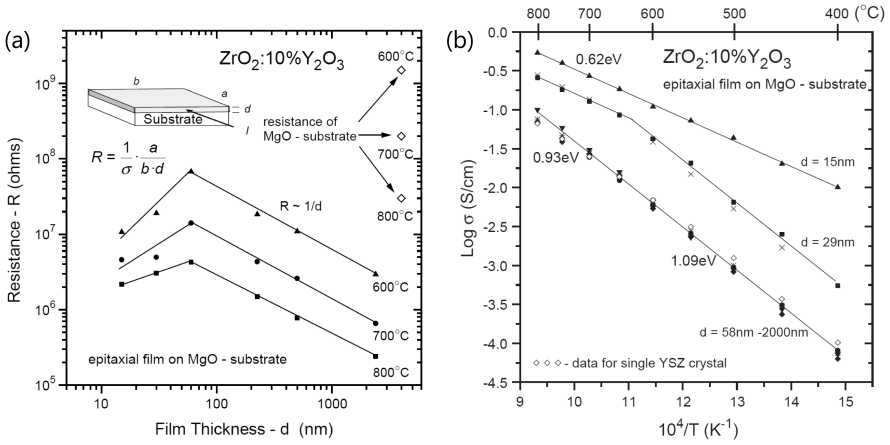


Figure 3.5: (a) The total resistance of the film/substrate system as a function of thickness for a range of temperatures. (b) An Arrhenius plot of the conductivity for varying thicknesses of YSZ thin films. Reproduced with permission from Ref. [107].

that insulating dopant and impurity segregation occurs at the surface of YSZ [109]. The authors fit the thickness dependent conductivity using a rule of mixtures model given by

$$\sigma_{tot}^{n} = \sigma_{int}^{n} f_{int} + \sigma_{vol}^{n}(1 - f_{int}) \tag{3.1}$$

where f_{int} is the volume fraction corresponding to the interface and is equal to δ/d where δ is the interfacial thickness and d the layer thickness. n is a parameter describing the connection between these two channels where $n = 1$ and $n = 0$ represent a parallel and series connection respectively. Matching Eq. 3.1 to the conductivity measurements, Kosacki *et. al.* find a value of $n = 0.31$ gives the best fit, which corresponds to δ value of 1.6 nm. As this is comparable to the width of the space charge layer for YSZ (see Section 2.3.1), the authors attribute the observed enhancement to a space charge effect. This corresponds to a specific interface conductivity 4 orders of magnitude higher than bulk and with an activation energy of 0.45 eV.

Unfortunately the authors do not provide any lattice parameters for the films as measured by XRD, so any information on strain resulting either from the growth or substrate mismatch is not available. Since Korte [110] has since carried out Fourier filtering on the HR-TEM images published by

Kosacki *et. al.* (Figure 3.6) and shown a high density of edge dislocations at the interface, prompting discussions about the dislocations as the cause of fast diffusion [61, 111, 112].

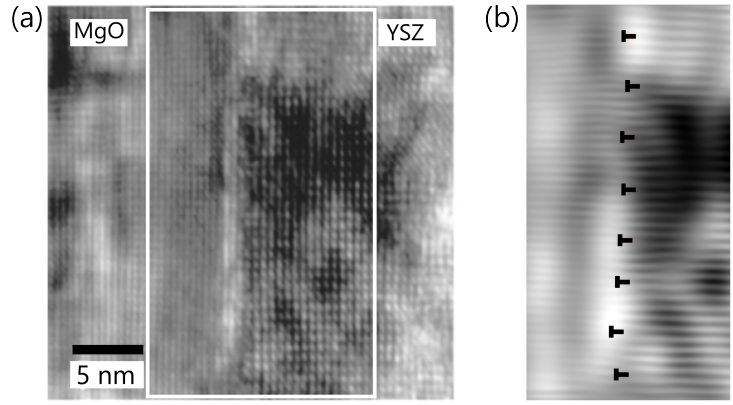


Figure 3.6: (a) HR-TEM image of the the YSZ/MgO interface, taken with permission from [106]. (b) Fourier transformation indicating the (020) planes with the dislocations marked [110].

In order to explain the reduction in the resistivity with decreasing thickness, one must assume that the cause of the enhancement (space charge, strain, dislocations) are not active for the thicker films. This is intuitively difficult to understand and cannot by simply explained by our current understanding of interface modified conductivity as discussed in Section 2.3.

Guo *et. al.*, 2005 [113] - YSZ/MgO Films

Using a comparable method to that of Kosacki *et. al.*, Guo *et. al.* [113] fabricated 8 mol.% YSZ films using PLD with thicknesses of 12 and 25 nm on MgO (100) substrates. Via TEM imaging and atomic force microscopy (AFM) it was shown that the films were polycrystalline with an average grain size of 76 and 88 nm for the 12 and 25 nm films respectively. Occasionally the same orientation relationship as observed by Kosacki *et. al.* was met and a high density of misfit dislocations was observed at the interface (Fig. 3.7a. However unlike that found by Kosacki *et. al.*, the conductivity was calculated to be independent of film thickness and furthermore, lower than the expected bulk conductivity by a factor of around 4, shown in Figure

3.7b.

Although dissimilarities in ionic transport between the two films may be expected due to only small differences in micro-structure and thickness, it is not clear why no enhancement is seen unlike the reports discussed above. The authors attribute the reduction in conductivity to the de-doping of the bulk material due to the nano-metric sized grain, as used to explain the drop in the ionic transport properties for polycrystalline bulk samples as discussed above in Section 3.1.1.

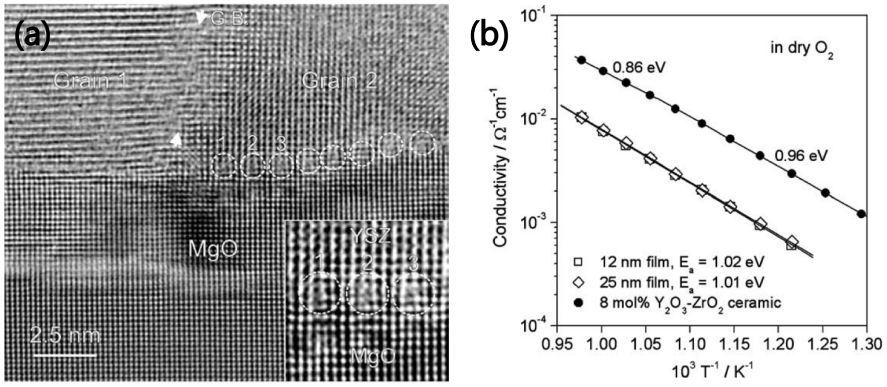


Figure 3.7: (a) HR-TEM of the YSZ/MgO interface and (b) Arrhenius plot of the conductivity with respect to temperature for 12 and 25 nm thin films and bulk YSZ. Taken with permission from Ref. [113].

Karthikeyan *et. al*, 2006 [114] - YSZ/(MgO, Al_2O_3) Films

Karthikeyan *et. al* [114] grew 9.5 mol.% YSZ thin films on MgO (100) substrates using electron beam deposition (EBD) at room temperature varying the thickness from 200 nm to 17 nm as well as growing 17 nm thick films on sapphire (0001) for comparison. From XRD it was shown that the films were polycrystalline with a number of orientations as well as being only partially stabilised in its cubic phase with a tetragonal contribution to the signal despite the high dopant concentration. The conductivity was measured via AC impedance spectroscopy between 700 and 940°C and reported to demonstrate an enhancement of up to an order of magnitude in the thinnest films, although the activation energy remained constant (Fig. 3.8a).

A lack of reported lattice parameters or TEM investigations to observe the microstructure, makes attributing the increase in the conductivity to strain or dislocations impossible. However, interestingly the same enhancement was seen in the 17 nm film grown on sapphire. Due to the large differences in symmetry and lattice parameter between the substrates it seems the enhancement observed is not a substrate specific effect. Based on this finding, the authors attribute the improved conductivity to a space charge zone, claiming that at higher temperatures defect association between the oxygen vacancies and the Y substitutions can extend the space charge zone to widths comparable to the thickness of the films.

This argument seems somewhat flawed when considering that defect association is reduced at higher temperatures, and measured to be negligible above roughly 650°C in 9.5 mol.% YSZ single crystals [37]. In an attempt to ensure current leakage effects are not providing a falsely positive result, Karthikeyan *et. al* measured the substrates under identical conditions and found them to be five to six orders of magnitude lower in conductivity. However the thinnest film is over 4 orders of magnitude thinner than the substrates[3], and therefore substrate leakage cannot be entirely ruled out. Extracting the conductivity data from the published results, one may normalise the conductivity to thickness in order to extract an effective resistance (Fig. 3.8b). Surprisingly there is no significant difference between the resistances of the films of varying thickness. While this may be coincidence, this would also be the behaviour one would expect if the EIS results were dominated by current leakage through the substrates or samples holder.

Sillassen *et. al.*, 2010 [115] - YSZ/(MgO, STO) Films

Sillassen *et. al.* [115] grew 8.7 mol.% YSZ thin films (420 -58 nm) on (111) and (110) oriented MgO and using reactive DC magnetron sputtering from metal targets. XRD $\theta/2\theta$ scans and pole figures were employed to demonstrate the highly textured epitaxial nature of the films. From shifts in the out-of-plane YSZ peak position in the $\theta/2\theta$ scans, the authors infer a 1% compressive strain in-plane at the interface, but also suggest that the strain

[3]It is assumed that the substrates are 500 μm thick which is typical, but this is not explicitly stated.

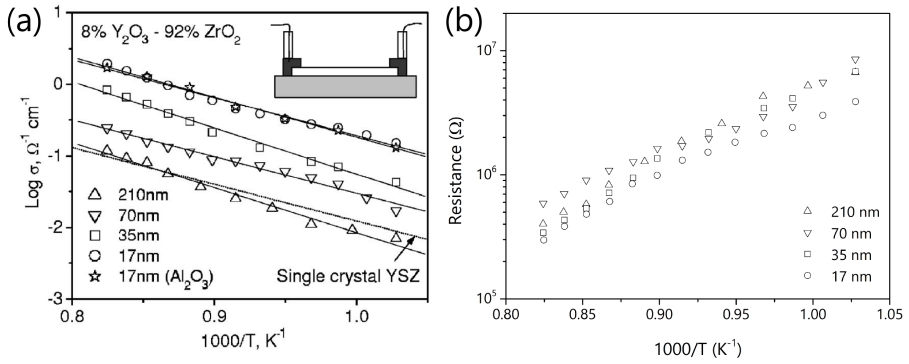


Figure 3.8: (a) Arrhenius plot of the temperature dependent conductivity for a number of YSZ film grown on MgO and sapphire of varying thickness, with the single crystal conductivity for comparison. Reproduced with permission from Ref. [114]. (b) The effective resistivity normalised to thickness for the same films. Data taken from Ref. [114].

in the films is independent of thickness. HR-TEM was used to show a negligible number of grain boundaries in the YSZ as well as a high density of dislocations at the YSZ/MgO interface, as reproduced in Fig. 3.9a. Measuring the conductivity using EIS at temperatures ranging from 150 to 500°C revealed an enhancement in the conductivity of around 3.5 orders of magnitude. Like Kosacki *et. al.* [106, 107], a change in the activation energy was also observed, however it was found to be comparable to the bulk at high temperatures (> 350°C) and reduced at low temperatures (< 350°C), displayed in Fig. 3.9b.

The authors identified this as a superposition of the bulk and interfacial conductivities, the former of which dominates the total conductivity at high temperatures and the latter at low temperatures. However if this was the cause one might expect that there would be a change in activation energy with thickness of the films as the volume fraction of the interface changes. Additionally the measured bulk contribution is still over two orders of magnitude higher than that expected for YSZ single crystals with a similar dopant concentration.

Sillassen *et. al.* also grew YSZ films on STO (100) substrates, and found similar enhancements in the conductivity (Fig. 3.9b). Coherent interfaces observed by HR-TEM demonstrate an interfacial strain based on the lattice

mismatch of 7.4%. Quoting the interfacial strain model discussed in Section 2.3.2, the authors attribute the enhancement in the conductivity of the YSZ/STO films to coherent interfacial strain and to the dislocation network in the YSZ/MgO films. Again the conductance of the substrates were measured under the same conditions as the films to rule out current leakage, and reported to be resistive enough not to effect the EIS measurements. It is important the note that the films were grown from a metal alloy target, at low temperature and oxygen partial pressures, and not exposed to higher than 500°C during the EIS measurements. Without a high temperature heat treatment, it is not possible to be certain that the films were fully oxygen stoichiometric and therefore pure ionic conductors.

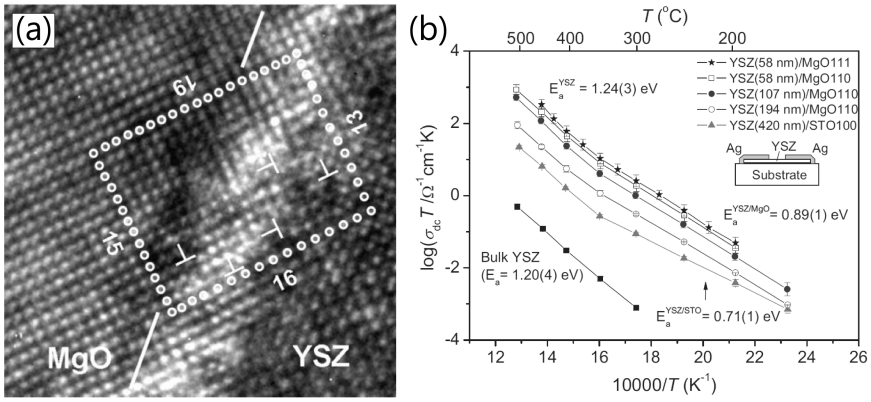


Figure 3.9: (a) Dislocation network at the YSZ/MgO interface and (b) lateral ionic conductivity of the YSZ thin films of varying thicknesses on different substrates. Reproduced with permission from Ref. [115].

Gerst *et al.* [116] - YSZ/(MgO, Al_2O_3, STO) Films

In an effort to more rigorously assess the transport properties of in YSZ films, Gerst *et al.* [117] employed a novel impedance method [118] and a novel two-step IETD procedure [116], the latter which will be discussed in Section 4.5.3. These were applied to 8 mol.% YSZ films grown on (100) MgO, (0001) Al_2O_3 and (111) STO by PLD, to investigate the interfacial effects. XRD $\theta/2\theta$ scans showed the films grown on MgO to be single orientation out-of-plane and the films grown on Al_2O_3 and STO to be mixed. Atomic

force microscopy was employed to access the grain sizes, and closely spaced interdigitated electrodes allowed the bulk and grain boundary contributions to be separated in the EIS spectra, such that the partial conductivities could be assessed.

Gerst *et al.* found the grain boundary conductivity to be between two and four orders of magnitude lower than the bulk for the YSZ/MgO and YSZ/Al_2O_3 systems. The total conductivity for the films grown on MgO and Al_2O_3, was then confirmed to be predominantly O ion transport by comparison to tracer diffusion measurements. However for the YSZ/STO films a much higher conductivity was measured electrically than that by IETD, implying electronic conductivity through the substrate. Unfortunately in this study the lattice parameters measured by XRD were not reported and the films were not studied by TEM, therefore the effects of lattice strain and dislocation networks could not be commented upon.

Jiang *et al.* [119] - YSZ/Al_2O_3 Films

9 mol.% YSZ films were grown on to (0001) Al_2O_3 substrates by Jiang *et al.* [119] by co-sputtering from Y and Zr targets in a reactive magnetron sputter chamber. The films were found to be highly textured, with only one orientation out-of-plane and two twinned orientations in plane as observed by XRD and SAED respectively. The authors found the out-of-plane lattice parameter to expand as the films were decreased in thickness from 100 to 6 nm (Fig. 3.10a). Measured by EIS between 300 to 650°C, the conductivity increased with decreasing thickness, which was combined with a decrease in the activation energy from 0.99 eV to 0.79 eV, such that the thinnest film was enhanced by 1.5 orders of magnitude at 300°C (Fig. 3.10b).

Jiang *et al.* attribute the improvement in the measured conductivity to out-of-plane expansion of the lattice and to dislocations observed by TEM. A dependency of the activation energy on the lattice parameter suggests a change in either the migration enthalpy or the association enthalpy. As a change of 0.2 eV is close to the association energy in 9.5 mol.% YSZ and the temperature range is still within the associated regime [37] (below 650°C), changes in migration or association energy barriers are possible. However

the cause of the out-of-plane expansion is not clear. The authors state that in-plane compression at the interface due to the lattice mismatch causes an expansion of the lattice parameter out-of-plane via Poisson relaxation, however this would lead to an overall decrease in the volume of the unit cell and therefore a decrease in the conductivity from the arguments of the interfacial strain model. Yet even for the thickest film (100 nm), the lattice parameter is still strained ∼1.5% tensile suggesting the modulations observed in the lattice parameter may not be entirely from the substrate film mismatch.

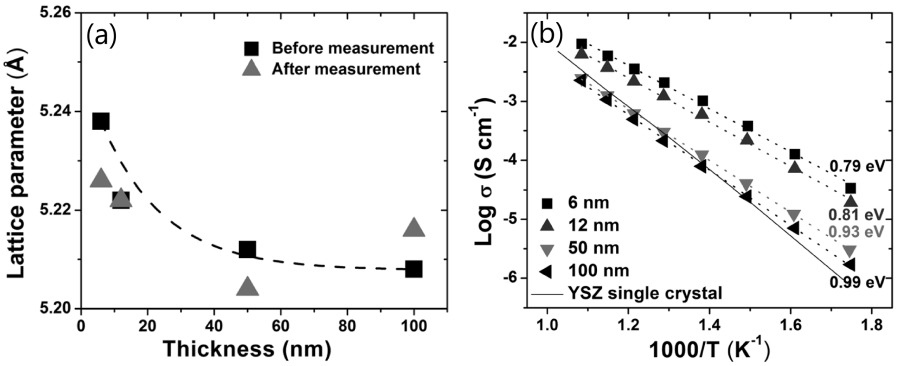


Figure 3.10: (a) Out-of-plane lattice parameters of the YSZ/ Al_2O_3 films measured both before and after EIS measurements and (b) Arrhenius plot showing the conductivity of the films. Reproduced with permission from Ref. [119].

Navickas *et al.* [120, 121] - YSZ/SiO_2 Films

All the studies discussed above in this section, have measured the conductivity in-plane, in order to observe interfacial effects as the thickness of the films are varied. Typically films grown by PLD and other physical vapour deposition (PVD) techniques result in columnar grains and a high density of grain boundaries perpendicular to the interface. Due to the insulating properties of the grain boundaries in YSZ as discussed in Section 2.3.1, these can dominate the in-plane conduction properties. Navickas *et al.* [120, 121], developed a method to simultaneously measure the in-plane and out-of-plane conductivity. PLD films (20-90 nm) were deposited by PLD onto Si substrates with a native oxide layer. Measuring EIS spectra across closely

spaced pad electrodes on top, the authors showed that the current path would switch from between in-plane and across-plane with frequency due to the insulating nature of the silica layer. The out-of-plane conductivity was found to be one order of magnitude higher and a lower activation energy (0.8 eV), than found in-plane (1eV). No change was found by varying the thickness of the films, however neither lattice parameters nor information on the microstructure was provided.

Doped-CeO_2 Thin Films

The effects of strain on the transport properties at the interfaces of doped ceria films has been studied far less than YSZ. A number of investigations have succeeded in growing doped ceria epitaxially on a range of substrates [88, 90, 122–124], but few have attempted to systematically vary the strain of the film in an attempt to observe the effect on the conductivity.

Kant *et al.* [125], however have investigated controlling the strain of 250 nm thick 10 mol.% CGO films grown on MgO using PLD by controlling the thickness of a STO buffer layer between the substrate and the film. The authors found that an in-plane tensile strain of up to 2% could be achieved using a 10 nm STO layer. The conductivity measured by EIS was found to be two to three orders of magnitude higher for the films with buffer layers compared to that of the CGO films deposited directly on MgO, and highest for the film with the largest measured strain. However the activation energy (0.93-0.94 eV), for the strained films was much higher than that measured in a polycrystalline film deposited directly onto MgO (0.81 eV). This result again does not fit the interfacial strain model discussed in Section 2.3 as an increase in conductivity should be coupled with either a decrease in the activation energy or an increase in the number of charge carriers. No remarks could be made on the presence of dislocations as a TEM investigation was not performed. Additionally no attempt was made to ensure the electrical measurements were indeed measuring ionic conduction. Jiang *et al.* [126] reactively sputtered 20 mol.% CGO films onto Al_2O_3 substrates, varying the thickness from 15 to 173 nm. Despite observing up to a 0.5% out-of-plane tensile strain for the thinnest films, no clear trend with the conductivity was

observed.

Single Thin Films Summary

In order to better compare the observed conductivity in YSZ thin films, the maximum deviation from bulk conductivity detailed in each report is plotted in Fig. 3.11, along with a literature value for single crystal 8 and 9.5 mol.% YSZ. At first inspection the graph can be clearly separated into two distinct groups. The films grown by Guo *et. al.* [113], Gerstl *et al.* [117] and Navickas *et al.* [120, 121], each have a lower conductivity than single crystal YSZ by up to approximately an order of magnitude, and similar activation energies (0.86-1.06 eV). This can be easily explained by the high density of grain boundaries expected due to the typical columnar growth for films grown by PLD, and agree reasonably well with each other. The second group contain those reported by Kosacki *et. al.* [106, 107], Karthikeyan *et. al* [114], Sillassen *et. al.* [115] and Jiang *et al.* [119] and each show considerable higher conductivity than that expected for single crystal YSZ. Yet, as is the case with the first group, in the films demonstrating enhanced transport properties, there is little agreement between them, either in terms of magnitude or activation energy. At first this is surprising, considering that the films are all nominally similar in terms of geometry and dopant concentration, however there are a number of subtle differences between each of the studies reviewed here. For easy comparison details of the discussed reports are listed in Table 3.1.

Firstly the fabrication methods used to produce the films are not the same for each study. PLD was used to grow all of the films in which no enhancement was seen, however Kosacki *et. al.* [106,107] observed a 2.5 order of magnitude enhancement using the same technique. In addition there is little consistency concerning the temperature at which the films were deposited. As discussed in Section 3.1.1, Rupp *et al.* [97] demonstrated the sensitivity of the strain and transport properties of doped ceria to the thermal history of the sample. Indeed the growth temperature and subsequent heat treatments may also effect the observed enhancement.

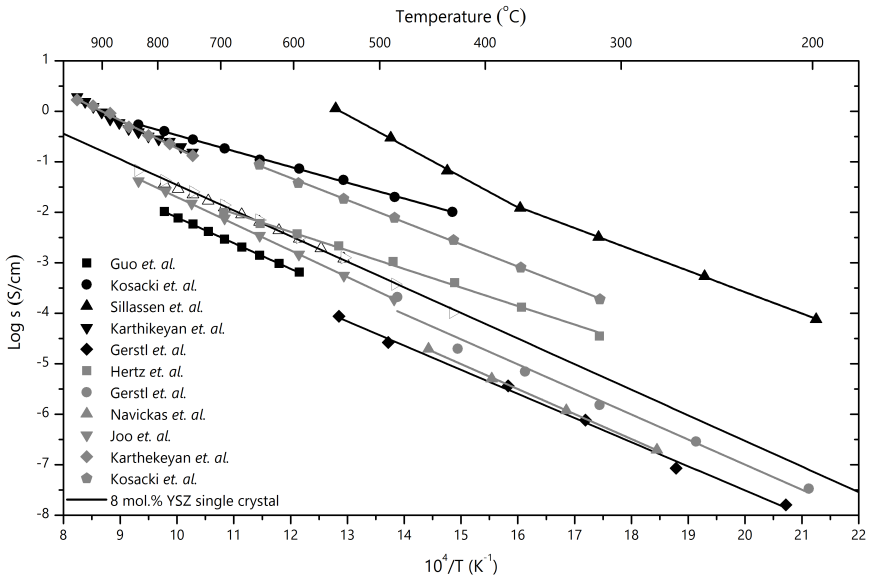


Figure 3.11: Maximum deviation in the in-plane conductivity of YSZ thin films compared to bulk. Data taken from Refs. [106, 107, 113–115, 117, 119–121].

Author	System	Growth Method	Growth Temp. (°C)	Thickness (nm)	EIS Temp. (°C)	Relative enhancment	Activation Energy (eV)	Grain size (nm)	Texture, orientation, coherency	Strain (ϵ)	TEM
Kosacki *et al.* [106, 107]	9.5 mol.% YSZ/MgO	PLD	500	2000-15	400-800	$\times 10^{2.5}$	0.62-1.09	-	YSZ (001)‖MgO (001), YSZ [100]‖MgO [100], semi-coherent, dislocation network	?	Y
Guo *et al.* [113]	8 mol.% YSZ/MgO	PLD	700	25-12	550-750	0.25	0.86-0.96	76 - 88	Polycrystalline, high density of dislocations at interface	?	Y
Karthikeyan *et. al* [114]	9.5 mol.% YSZ/MgO	EBE	RT	210-17	700-940	$\times 10$	$\sim$1.1	?	Polycrystalline	?	N
	9.5 mol.% YSZ/Al_2O_3			17							
Sillassen *et. al.* [115]	8.7 mol.% YSZ/MgO	DC sput.	400	420-58	197-508	$\times 10^{3.5}$	0.89-1.24	-	YSZ (110)‖MgO (110), YSZ [100]‖MgO [100], semi-coherent, dislocation network	$\sim$ -1% ‖	Y
	8.7 mol.% YSZ/STO		800	420		$\times 10^{3}$	0.71-1.24	-	YSZ (001)‖STO (001), YSZ [100]‖STO [110], coherent	?	Y
Gerst *et al.* [117]	8 mol.% YSZ/MgO	PLD	500-650	65	200-500	$\times 10^{-1}$(bulk), $\times 10^{-4}$(gb)	0.92(bulk), 1.3(gb)	90	YSZ (111)‖MgO (001)	?	N
	8 mol.% YSZ/Al_2O_3			250-28		$\times 10^{-1}$(bulk), $\times 10^{-4}$(gb)	0.94-1.02(bulk), 1.1-1.2(gb)	10-37	YSZ (111),YSZ (001)‖Al_2O_3 (0001)	?	N
Navickas *et al.* [120, 121]	8 mol.% YSZ/SiO_2/Si	PLD	600	90-20	200-500	0.25	0.96-1.06	?	Polycrystalline	?	N
Jiang *et al.* [119]	9 mol.% YSZ/Al_2O_3	RF sput.	650	100-6	300-650	$\times 10^{1.5}$at 300°C	0.79-0.99	10-20	YSZ (111)‖Al_2O_3 (0001), semi-coherent	$\sim$1.5% ⊥	Y
Kant *et al.* [125]	10 mol.% CGO/STO/MgO	PLD	750	250	400-900	$\times 10^{3}$	0.94	?	CGO (100)‖STO (100)‖MgO (100)	$\sim$2% ‖	N
Jiang *et al.* [126]	20 mol.% CGO/Al_2O_3	RF sput.	650	173-15	300-650	0.5	0.75-0.96	20-60	CGO (111)‖Al_2O_3 (0001)	$\sim$0.5% ⊥	Y

Table 3.1: Details of the experimental studies of YSZ films in literature. (All conductivity values listed are in the in-plane geometry). (⊥ and ‖ denote out-of-plane and in-plane strain respectively).

Secondly, it is difficult to make direct comparisons between the films due to the differences in the orientation, texture and thickness. Effects such as lattice strain and dislocation networks are often cited as being the cause for the observed enhancements in the conductivity, but in many of the reports these have been characterised to varying degrees or even not at all. Another variable to note is the composition of the YSZ. The phase transition between tetragonal and cubic YSZ is in the region of 8 mol.% (Section 2.1.1), which can lead to transformational toughening for compositions close to this. This may affect the way the transport of the material will be effected by extrinsic lattice strain originating from the substrate. Interestingly, all samples in which an improvement in the conductivity is observed are made with a dopant concentration higher than 8 mol.%, while all those showing a decrease were fabricated from 8 mol.% YSZ targets.

Finally, there is a large variation in the temperature range over which the electrical measurements were performed. Combined with the array of activation energies observed for the enhanced films, it is reasonable to suspect that more than one process is occurring leading to improved transport. With no direct evidence for enhanced oxygen diffusivity by IETD, other experimental errors must be considered, such as electrical leakage through the substrate, film surface or sample holders and impurities in the films altering the transference number.

3.1.3 Multilayer Structures

Multilayers (also known as heterostructures or super-lattices) overcome some of the problems encountered when studying thin films mentioned at the beginning of the previous section. In a typical study, the thickness and number of repeat units can be varied thereby keeping the total volume of material the same while controlling the number of heterointerfaces. As the total volume of the measured sample is not changing, current leakage effects are not so easily interpreted as enhanced conductivity as in thin films with reducing thickness. In addition, the ionically conducting layers are symmetric such that there is no free surface, allowing for surface effects to be ruled out. However, tailoring the interfaces becomes more difficult, as substrate

pre-treatments will have little effect after the first layer.

Janek *et al.* [58, 61, 63, 110, 111, 127–130] - (CSZ, YSZ)/(Al_2O_3, RE_2O_3) Multilayers

Much of the pioneering work into strain effects of doped-ZrO_2 conducting layers has been carried out by Janek and co-workers. Initially studying alternating layers of 8.7 mol.% Ca-doped ZrO_2 (CSZ) and Al_2O_3 [127], they found incoherent interfaces by HR-TEM, and an out-of-plane compressive strain of 0.7%. Varying the layer thickness, the authors found the conductivity was proportional to the number of interfaces (Fig. 3.12), displaying a two order of magnitude increase coupled with a drop in the activation energy from 1.47 eV to 0.96 eV for a layer thickness of 51 nm. Janek *et al.* attribute the enhanced ionic mobility to disordered core regions of the incoherent interfaces, and fit the thickness dependence to

$$\sigma_{tot} = \sigma_{vol} + 2\delta(\sigma_{int} - \sigma_{vol})\frac{1}{d} \tag{3.2}$$

where, σ_{tot} is the total conductivity of the system, σ_{vol} and σ_{int} are the partial conductivities of the volume and interfacial regions respectively, d is the layer thickness and δ in the interface width. Assuming a fixed interface width with enhanced transport properties, one would expect a linear increase plotting σ_{tot} against $1/d$, where the y-axis intercept would give σ_{vol} and when $d = 2\delta$, $\sigma_{tot} = \sigma_{int}$. The authors acknowledge the possibility of electronic conduction due to changes in the size or interface effects, but suggest that such phenomena would be unlikely after a long high temperature heat treatment.

This study was followed up with an extensive and highly systematic study into strain effects in YSZ multilayers with different rare earth metal sesquioxides RE_2O_3 with RE = Lu, Sc and Y, prepared by PLD on to Al_2O_3 (0001) substrates [58, 61, 110, 111, 128]. The rare earth metal sesquioxides have a bixbyite structure, which is closely related to the fluorite structure and therefore could be used to apply an interface mismatch of 3.09%, 1.02% and -4.37% for the YSZ/Y_2O_3, YSZ/Lu_2O_3, YSZ/Sc_2O_3 systems respectively.

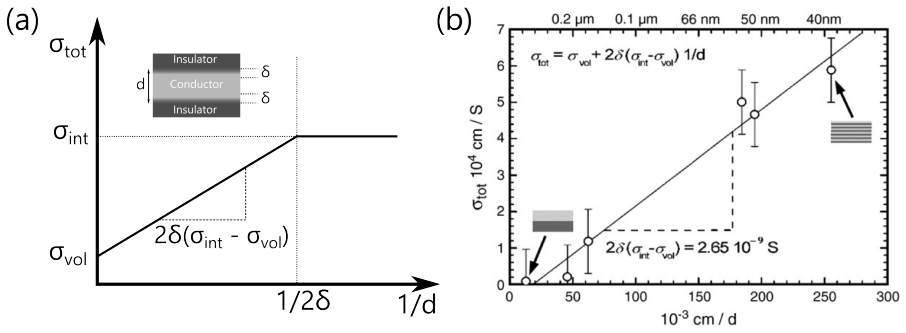


Figure 3.12: (a) Expected trend with ionic conductivity and thickness for multilayed samples and (b) the conductivity against reciprocal thickness for the CSZ/Al_2O_3 system. Taken with permission from Ref. [127].

The samples were grown for a range of layer thicknesses and characterised by SEM, HR-TEM, SAED and XRD including pole figure measurements. Each system was shown to be highly textured, consisting of columnar grains, and were found to have very few dislocations located in and close to the grain boundaries. The authors reported atomically flat phase boundaries which could be described as (quasi-)coherent interfaces with an ideal 1:1 match of the lattice plains. Measuring the conductivity using EIS in the range of 420-780°C, the conductivity was found to increase for the YSZ/Y_2O_3 system (expansive mismatch), decrease for the YSZ/Sc_2O_3 system (compressive mismatch) and show no clear trend for the YSZ/Lu_2O_3 system. As shown in Fig 3.13, the conductivity dependence on the thickness was fitted using Eq. 2.49, from which interface widths of 3.7 nm and 4.4 nm could be obtained for the YSZ/Y_2O_3 and YSZ/Sc_2O_3 systems respectively [63]. However the total change in the conductivity in each case was only approximately a factor of two, which is not significantly higher than the uncertainty in the EIS measurements.

In an attempt to provide direct evidence for modified oxygen transport, the multilayer structures were measured by IETD and time-of-flight secondary ion mass spectrometry (TOF-SIMS) [129, 130]. The results showed similar trends to those samples measured by EIS (shown in Fig. 3.13), leading the authors to claim that the electrically measured effects were oxygen ion conductivity. However, as discussed in Section 4.10, the analysis mode

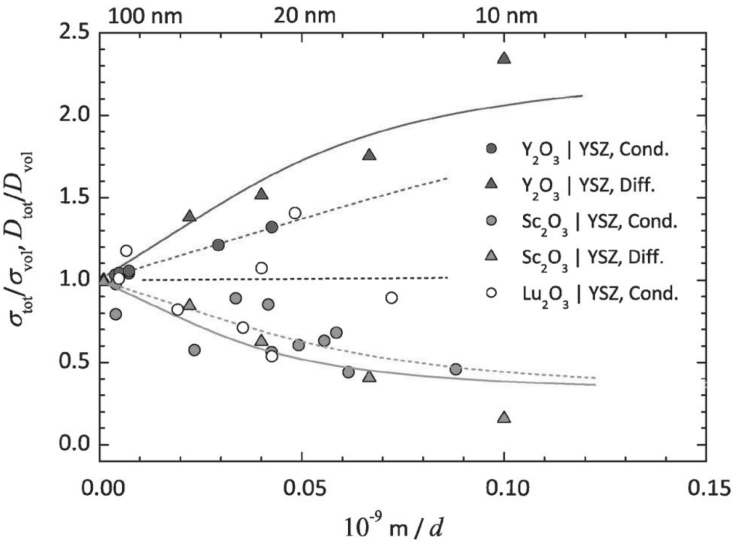


Figure 3.13: Relative ionic conductivity and diffusivity coefficients from the YSZ/RE_2O_3 multilayer systems against the reciprocal thickness, $1/d$. The fits are based on Eq. 2.49. Taken from Ref. [63].

used in the TOF-SIMS in these studies (high current bunched mode) has a lateral resolution of 2-10 μm [131], yet the diffusion profiles measured were in the range of 10 to 50 μm leading to considerable doubt in the accuracy of these analyses.

Karthikeyan *et al.* [132] - YSZ/(MgO, Al_2O_3) Multilayers

Following up work on their work on the YSZ/(MgO, Al_2O_3) single layer system, Karthikeyan *et al.* [132] investigated multilayers of 8 mol.% YSZ between amorphous Al_2O_3 and SiO_2 layers on MgO and Al_2O_3 substrates by RF sputtering. By XRD both cubic and tetragonal phases were observed, but again neither lattice parameters nor HR-TEM images were provided, and so the effects of lattice strain and dislocations on the transport cannot be commented upon. The authors found approximately a fivefold increase in the conductivity as the layer thickness was decreased from 33 to 3 nm, while keeping the total thickness of the structure constant, and a slightly higher activation energy of 1.3 eV was observed for all samples than that expected for bulk YSZ. As observed in their previous paper [114], Karthikeyan *et*

al. found no changes in the enhancement with different insulating layers, leading to the suggestion of a true size effect.

YSZ/STO Multilayers

By far the most substantial enhancement in conductivity of oxide heterostructures was reported by García-Barriocanal *et. al.* [133, 134] in 8 mol.% YSZ/$SrTiO_3$ (STO) tri-layers and multilayers produced by RF sputtering. Using high resolution scanning transmisson electron microscopy (HR-STEM) it was shown that the YSZ had grown coherently with the STO layers such that the unit cell was rotated 45° around the c-axis leading to a 7% lattice strain (Fig. 3.14a). From AC impedance measurements, the conductivity in the tri-layers was seen to increase between 2 and 5 orders of magnitude as the thickness of the sandwiched YSZ layer was reduced from 62 to 30 nm, whilst the total conductance of the structure remained independent of thickness. Moving on to heterostructures of 8 repeating units of varying thickness YSZ and 10 nm thick STO layers the authors showed the conductivity to be enhanced further to 8 orders of magnitude for 1 nm thick YSZ layers, with the total conductance scaling with number of interfaces (Fig. 3.14b).

This prompted García-Barriocanal *et al.* to attribute the effect to a high level of disorder at the interface due to the incommensurability of the oxygen sub-lattices of YSZ and STO brought about by the lattice strain. Due to the magnitude of the enhancement the authors labelled this *colossal* ionic conductivity. However it is worth noting that the only evidence for the conductivity measured being ionic in nature was the large drop observed in DC measurements.

Guo [135] pointed out that the nominally undoped insulating STO is often actually doped with acceptor type impurities leading to p-type conductivity. As the thickness of the STO layers in all the tri-layer structures is kept constant and the total conductance is found to be unchanging, Guo suggests that the conductive properties measured are electronic and originate from the STO. This is a possibility as the enhancement is only present when the YSZ is assumed to be the conductive channel and the thickness

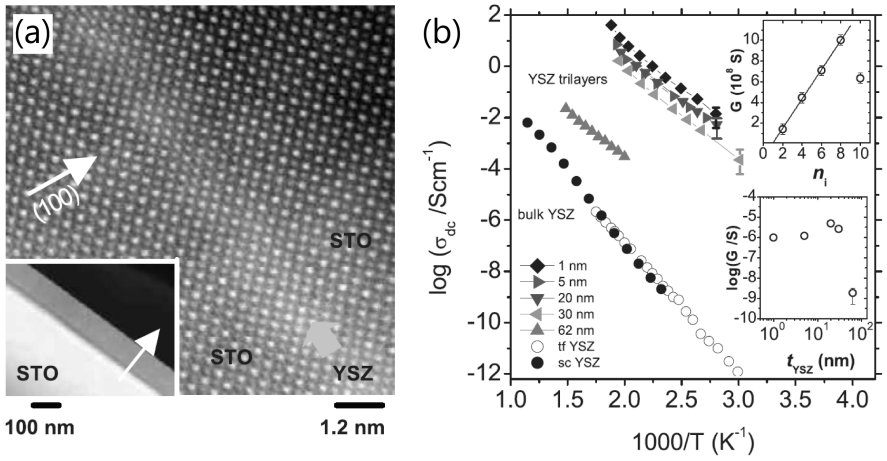


Figure 3.14: (a) Z-contrast HR-STEM image of the YSZ/STO interfaces of a 1 nm thick YSZ layer and (b) Arrhenius plot of YSZ/STO tri-layers with bulk YSZ for comparison. The insets show the conductance as a function of the number of layers and layer thickness. Reproduced with permission from Ref. [133].

taken into account. This theory is further supported in the results from the heterostructures, as the conductance scales with the number of interfaces, this also implies an increasing number of 10 nm thick STO layers. García-Barriocanal and co-workers have disregarded Guo's comments [136] and gone on to simulate the YSZ/STO tri-layers using DFT calculations [137, 138]. Here they argue that due to the lattice strain and incommensurable oxygen sub-lattices of the YSZ/STO interface, that at 350 °C the oxygen ions are highly disordered in the YSZ layer to an extent analogous to 7% strained bulk YSZ at 2000 °C. From this they estimate a comparable enhancement of $4x10^6$ compared to unstrained YSZ at 200 °C. HR-TEM and EELS analysis has been used to study this disorder in YSZ/STO multilayers and is suggestive of ill-defined oxygen columns in the YSZ [138, 139].

Cavallaro *et al.* [102] attempted to replicate the work of García-Barriocanal *et al.*, by growing identical structures using PLD. However using reflection high-energy electron diffraction (RHEED), high-angular annular dark-field (HAADF)-STEM and AFM imaging the YSZ layers were shown to have grown with a ∼15° tilt resulting in disconnected islands of YSZ in contrast to the continuous layers consisting of cube-on-cube epitaxy as previ-

ously reported [133]. This is shown in Fig. 3.15a. However, surprisingly a

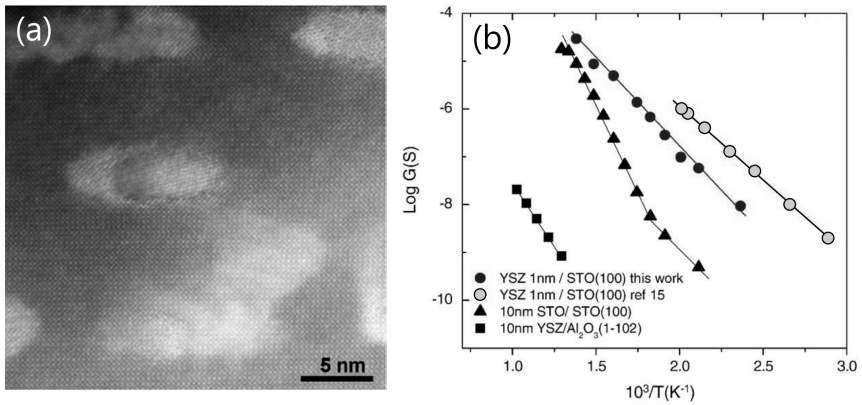


Figure 3.15: (a) HAADF-STEM images of the YSZ islands grown on STO. (b) Arrhenius plot showing the enhancement in the conductivity of the YSZ structures compared with those grown by García-Barriocanal *et al.* [133], bulk YSZ and bulk STO. Reproduced with permission from Ref. [102].

similar enhancement in the conductivity of the structures was observed by impedance (Fig. 3.15b). Cavallaro and co-workers assigned this to electronically dominated transport, showing a characteristic dependence measured as a function of pO_2. This was further supported by HAADF-STEM images suggesting the incorporation of Y and Zr ions into the STO matrix, which is thought to result in p-type conductivity. More recently Cavallaro *et al.* [99] identified the controlling mechanism determining the formation of cube-on-cube rather than $\sim$15° tilted island growth of YSZ on STO to be due to the presence of Sr termination of the STO crystal surfaces. This throws significant doubt on the DFT calculations performed by Pennycook *et al.* [137], which were based on the understanding that the STO at the YSZ/STO hetero-interfaces were Ti terminated. A Sr termination is supported by DFT calculations by Cheah and Finnis [140], who find that while fluorite ZrO_2 is highly unstable as a coherently strained layer, that a high energy metastable structure resembling the tetragonal fluorite is only stable on SrO-terminated and not TiO_2-terminated STO.

More recently in an analysis of the data provided by García-Barriocanal *et. al.* [133], Cavallaro *et al.* [102] and Guo [135], De Souza and Ramadan

[141] argued that the conductivity observed is predominantly ionic in the STO layers below 260°C based on the activation energy observed in each study. However, De Souza reject the possibility of vacancy transfer between the STO and YSZ phases leading to the observed enhancement casting doubt on the validity of the enhanced YSZ conductivity initially reported.

Pergolesi *et al.* [142] - YSZ/CeO_2 Multilayers

Pergolesi *et al.* [142] fabricated 8 mol.% YSZ/CeO_2 multilayer structures by PLD onto MgO substrates, keeping the total thickness constant (300 nm) while varying the thickness of the layers (60-5 nm) and number of interfaces (4-60). By using a STO buffer layer the layers were found to be highly textured from XRD analysis, and TOF-SIMS depth profiling showed minimal intermixing between the phases. A similar density of dislocations were observed as the quasi-coherent structures produced by Janek *et al.* [61], from TEM investigations. XRD and geometrical phase analysis (GPA) was used to show varying degrees of lattice distortions in the layers, which in places matched the theoretical lattice misfit of 5% (Fig. 3.16). The conductivity of the structures was measured by EIS and confirmed to by predominantly O ion transport by tracer diffusion. All multilayers were found to have similar conductivity and activation energy and were in agreement with the theoretical conductivity expected for a fully relaxed and highly textured bilayer of the two materials, implying no effect of interfaces or lattice strain on the transport properties.

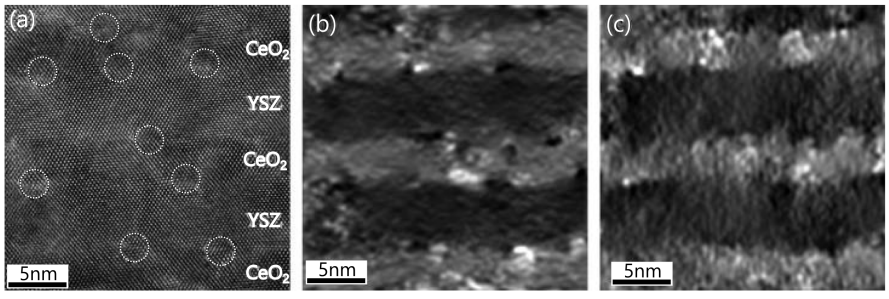


Figure 3.16: (a) Bright-field HR-TEM image of a YSZ/CeO_2 multilayer and corrisponfing distributions of the strains (b) in-plane and (c) out-of-plane. Adapted with permission from Ref. [142]. Copyright 2012 American Chemical Society.

Li *et al.* [143] - YSZ/$Gd_2Zr_2O_7$ Multilayers

PLD grown 8 mol.% YSZ layers have also been fabricated sandwiched between the fluorite-related pyrochlore electrolyte $Gd_2Zr_2O_7$ [143]. Due to the low mismatch of 3.0% between the two, Li *et al.* found the layers to be coherently strained by XRD and no apparent dislocations at the interfaces of the layers by TEM. EIS measurements suggested a fivefold increase in the total conductivity of the system as the number of layers is increased from 10 to 20 while keeping the total thickness constant. However, this is coupled with an increase in the activation energy suggesting either a higher migration or association enthalpy, inferring the enhancement in the conductivity must be due to increase in the charge carriers. The authors do not comment on this.

Doped-CeO_2 Multilayers

Thevuthasan *et al.* [144–147], in a series of publications studied multilayers of ceria and zirconia both doped with 12 mol.% Gd fabricated by oxygen plasma-assisted molecular beam epitaxy (MBE) on to Al_2O_3 substrates. They found the conductivity increased with number of layers while keeping the total thickness constant to a maximum of about 3 times higher than that of CGO for a layer thickness of 15 nm. A decrease in the activation energy was also observed. Yao *et al.* [148], reported similar results on samaria-doped ceria (SDC)/Al_2O_3 heterostructures grown by RF sputtering observing nearly a five times higher conductivity and slight decrease in the activation energy. Sanna *et al.* [149], also observed an enhancement in multilayers of SDC/YSZ grown by PLD of up to an order of magnitude. However in this case it was coupled with an increase in the activation energy.

There have also been reports of the ionic conductivity in doped CeO_2 multilayers being reduced due to biaxial compression. Shen *et al.* [150] fabricated layers of Y-doped CeO_2 (YDC) and Zr-doped CeO_2 (CZO) varying the thickness of layers and the dopant concentration of the CZO to invoke different amounts of strain in the YDC. The authors showed a one order of magnitude decrease in the conductivity for a 2.2% compressively strained layer and a decrease in the activation energy from 0.84 to 0.95 eV. Simi-

lar findings were reported by Schweiger *et al.* [151] in multilayer microdots of CGO/Er_2O_3. The authors found a two order of magnitude decrease in the conductivity for a 1.16% compressivly strained layer coupled with an increase in the activation energy from 0.75 to 1.06 eV. However, Perkins *et al.* [152], found no change in the transport properties of SDC/CeO_2 multilayers fabricated by PLD, despite the compressive lattice mismatch.

3.1.4 Macroscopically Strained YSZ

The vast majority of studies into the effects of strain and lattice distortions in YSZ have focused on interfacial applied strain occurring at heterophase boundaries in thin films and multilayers. There are however some studies where YSZ has been strained macroscopically in order to study the effects on the transport properties. Araki *et al.* [153] studied the effect of mechanical tensile stress on the ionic conductivity of 8 mol.% YSZ, measuring sintered bulk polycrystalline samples in a tensile loading setup while measuring EIS *in-situ*. They found that under applied stresses of 0.41 MPa the conductivity improved by 18%, but no change in the activation energy was observed.

Otsuka *et al.* [154] strained 10 mol.% YSZ single crystals to a plastic deformation of 1%, 3% and 10% at 1300°C inducing a high density of dislocations as observed by TEM (see Fig. 3.17a). The authors reported that the density of dislocations introduced in the YSZ was as high at 8×10^{12} m^{-2} for the 10% deformed sample. Measuring the conductivity by EIS, the conductivity was found to be approximately 9% higher for the 10% strained sample at 597°C (Fig. 3.17b). For this, Otsuka *et al.* calculate an effective conductivity for a dislocation to be two to four orders of magnitude higher than that of bulk YSZ.

3.1.5 Computational Studies

Initiated by the early tantalising experimental studies into confined electrolyte systems and encouraged by the promising results that have followed, there have been a number of computational simulations reported in an attempt to elucidate the origins of such enhanced transport.

Araki *et al.* [155] modelled 8 mol.% YSZ under various uniaxial and

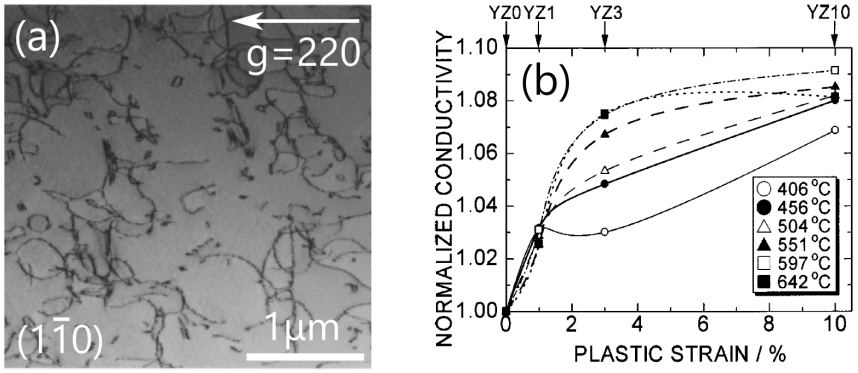


Figure 3.17: (a) TEM image of the dislocations induced in a 10 mol.% YSZ single crystal by 10% mechanical deformation and (b) the normalised conductivity as a function of plastic strain. Adapted with permission from Ref. [154].

hydrostatic stress conditions using molecular dynamics (MD) simulations in the temperature range of 1273 - 2000 K and at strains up to 0.6 %. It was found that tensile stress applied uniaxially enhances oxygen diffusion in the tensile direction, while compressive stress cause a reduction in the compressive direction. The authors attribute this enhancement to a change in the energy barrier for migration, but report no effect due to the association energy.

Kushima and Yildiz [156] showed through density functional theory (DFT) and nudged elastic band (NEB) computing that the migration barrier for ionic conductivity can be altered due to applied biaxial strain. They reported that in 9 mol.% YSZ there were two competing processes that act in parallel to alter the barrier for O migration; the steric constraint on the O ion and the cation-anion bond strength. Kushima and Yildiz calculated that up to a strain on 4% the migration barrier lowers due to an increase in the migration space and a weakening of the local cation-oxygen bonds leading to a reduction in the barrier of 0.4 eV and almost a 4 order of magnitude increase in the conductivity at 400 K (shown in Fig 3.18). Above 4% strain the migration barrier starts to increase due to a strengthening of the anion-cation bonds, indicating a transition from elastic stretching to local plastic relaxation. This study has recently been supported by Tarancón and Morata [157], who find a similar maximum around 3-4 % tensile strain by

molecular dynamics simulations. Here the authors attribute the increase in migration barrier above 4% strain to a strong distortion of the cationic sublattice and the formation of new equilibrium positions for the oxygen along the diffusion pathway.

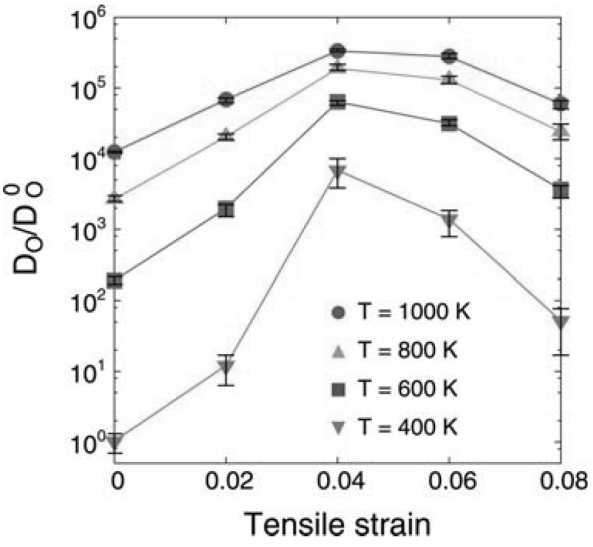


Figure 3.18: Computed relative changes in the oxygen diffusion coefficient in 9 mol.% YSZ under tensile strain. Taken with permission from Ref. [156].

A similar study using DFT and NEB modelling was carried out by Hirschfeld and Lustfeld [158] for cubic zirconia, with similar results due to expansive strain. As expected, they found that the migration barrier increases with compressive strain, but surprisingly a maximum barrier was observed at a compressive strain of $\epsilon = 0.914$, after which it decreases and eventually vanishes under increasing compression. This was attributed to the Zr ions pressing on the O ion at the initial position prior to a jump process along with a drop in the Zr-O repulsion at the saddle position due to changes in the inter-atomic distances.

De Souza *et al.* [159] performed static lattice simulation on oxygen vacancy migration in isotropically and biaxially strained CeO_2. They calculated a significant modification in the energy barriers, corresponding to an increase of about 10^4 with 4% strain at 500 K. These results agree well with the results for YSZ from Kushima and Yildiz [156], and Tarancón and

Morata [157], suggesting this may be universal for oxygen conductivity in the fluorite crystal structure. De Souza *et al.* also notes that the maximum enhancement achievable from the combination of a 7% tensile strain (such as claimed by García-Barriocanal *et. al.* [133]) and a space charge zone such that the oxygen vacancy site fraction is 0.5 would only give a $10^{6.4}$ maximum in conductivity, questioning the validity of the reported enhancement.

Much more modest enhancements were reported in the higher temperature range for doped CeO_2, by Burbano *et al.* [160] ($\times$3.5 for ϵ=2.1% at 1273 K), and Rushton and Chroneos [161] ($\times$101 for ϵ=5% at 1900 K). However both studies show that the impact of strain increases at lower temperatues suggesting an agreement with the previously discussed works. Interestingly Rushton and Chroneos, suggest the impact of strain varies depending upon the dopant used. Fig. 3.19, shows the calculated activation energy, E_a, for strained CeO_2 doped with a range of rare earth metals. It can be seen that under tensile strain the optimum dopant radii switched from that corresponding to Nd to that closest to Sm, suggesting the association enthalpy is indeed effected by strain.

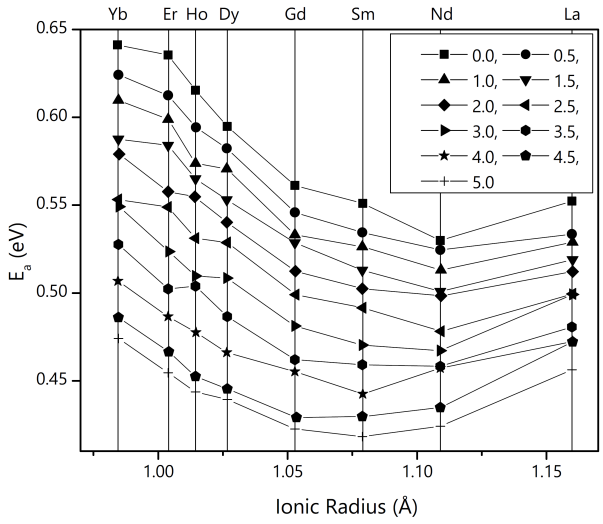


Figure 3.19: The simulated activation energies of oxygen ion migration on the dopant ionic radius and strain. Data taken from Ref. [161].

A number of computational studies have focused on simulating interfaces, such as those observed experimentally, attempting to identify the features which lead to enhanced conductivity. Sayle *et al.* [162] developed an amorphisation and recrystallization model which allows the natural evolution and features such as grain boundaries, crystal domains, point defects and dislocations. The authors applied this model to YSZ/CeO_2 interface and found that the structure of the interface agreed well with that observed experimentally by Thevuthasan *et al.* [144, 145]. However, a decrease in the diffusivity at the interface was observed in comparison to bulk simulated YSZ.

Employing the amorphisation and recrystallization model developed by Sayle *et al.*, Sankaranarayanan and Ramanathan [163] carried out an atomistic study, simulating YSZ thin films on a magnesium oxide substrate (MgO) with thicknesses of 3, 6 and 9 nm. Yttria segregation was observed at the YSZ free surface, while there was a thickness dependent reduction of the Y content at the YSZ/MgO interface of up to 80% compared to the bulk at 3 nm. Although no significant residual strain at the interface was observed, the diffusivity at the interface was found to increase as for decreasing film thickness in the temperature range of 1200 - 2000 °C. This was attributed to a lowering of the activation energy and calculated to result in an enhancement of the conductivity by 2 orders of magnitude at the interface between the 9 nm and 3 nm films.

3.1.6 Section Summary

Over the last decade there has been a substantial number of reports, both experimental and computational, investigating the modified ionic transport in the acceptor-doped fluorites as a function of strain. However, inconsistencies between the results detailed in the literature and a lack of irrefutable evidence, has led some to question the possibility of strain-engineered O-ion electrolytes entirely [18]. Indeed, direct and convincing evidence of an enhancement in the O diffusivity by tracer diffusion in the doped fluorites has not yet been reported.

At a heterogeneous interface between two materials with a similar lattice

parameter and symmetry, there are two ways an interface may form: either coherently, resulting in a uniform strain field along the interface, or semi-coherently, where a dislocation network will occur. As both effects have been attributed to fast ionic diffusivity, typically any alteration from bulk transport in thin films or multilayers will be attributed to at least one of the two. Yet direct evidence for either effect is lacking.

Based on our understanding from computational simulations and the interfacial strain model discussion in Section 2.3, there are two main criteria a system must fulfil for a claim of coherent interfacial strain-modified transport be plausible:

i A change in the lattice parameter corresponding to a variation in the volume fraction of the interfacial regions.

ii A modification in the activation energy, matching the change observed in the lattice parameter.

To the best of the author's knowledge, there are only two studies to date, which simultaneously fulfil both these requirements for an enhancement in the conductivity of YSZ. The study of thin films of YSZ/Al_2O_3 by Jiang *et al.* [119], and the multilayers of YSZ/RE_2O_3 (RE = Lu, Sc and Y) by Janek and co-workers [58, 61, 110, 111, 128]. Both report enhancements of less than one order of magnitude. This may suggest that the other reported improvements in the conductivity are caused by different mechanisms.

The colossal increase in the conductivity of YSZ/STO heterostructures [133], has been widely criticized. Computational studies have shown that enhancements of that magnitude cannot be achieved by strain or space charge effects [156, 157, 159]. In addition, strong experimental evidence suggests that the most likely cause for the observed effect is electronic conductivity through the STO layers [102,135]. The lessons that may be taken from this, are the difficulties and pitfalls one must be wary of when studying these nano-structured systems. Ensuring that electrical measurements are a true representation of the O ion transport is challenging in itself [104], let alone attributing the conductivity to interfacial features in the systems.

In addition, direct comparison between nominally similar systems yields vast inconsistencies. Films grown by PVD techniques often display drastic

differences in the microstructure, composition and stoichiometry by altering growth parameters such as temperature and oxygen partial pressure [164]. This is further complicated when, as in this case, we are endeavouring to understand phenomena by analysing systems from multiple deposition techniques. It has also been shown that thermal history may play a significant effect [96], yet often the details of which go unreported in the literature.

3.2 Surface Segregation in Doped Fluorites

In this section the literature on the subject of dopant segregation to the surfaces of doped ZrO_2 and CeO_2 will be reviewed. Surface segregation has been studied far less extensively than the transport properties of these materials, and in almost all cases has only been reported for bulk materials. As covered in Section 1.3, cation diffusion can be a rate determining factor for surface segregation, and so initially the investigations into dopant cation mobilities in the bulk will be briefly discussed. Next experimental and computational studies exploring the phenomena of dopant surface segregation will be reviewed.

3.2.1 Cation Diffusivity

The diffusivity of the dopants Ca and Y have been studied in 10-32 mol.% YSZ and 11-17 mol.% respectively between 960 and 1700°C by Kilo *et al.* [165]. The stable isotopes ^{44}Ca and ^{96}Zr were implanted at an energy of 150 keV, and the radioactive isotope ^{88}Y applied at the surface from aqueous solution. After annealing the samples were analysed by either SIMS depth profiling (for ^{44}Ca and ^{96}Zr), or by combining mechanical polishing and radioactivity measurements (as shown in Fig. 3.20a).

The authors observed in YSZ, that the Y diffusivity was dependent on stabiliser content, displaying a maximum at 10-11 mol.%. They claim that this indicates that Y cation transport occurs via single vacancies in the cation sublattice ($V_{Zr}^{''''}$). However, in CSZ no such trend with concentration exists, suggestive that the mechanism is mediated by bound vacancies ($V_{Zr}^{''''} - 2V_O^{\bullet\bullet}$). In addition Kilo *et al.*, found that the dislocation pipe diffusivity of Y, was approximately six orders of magnitude faster than bulk in the

temperature range 1400-1676°C, as well as lower in activation energy (3.5 eV compared to 4.2 eV) (Fig. 3.20b).

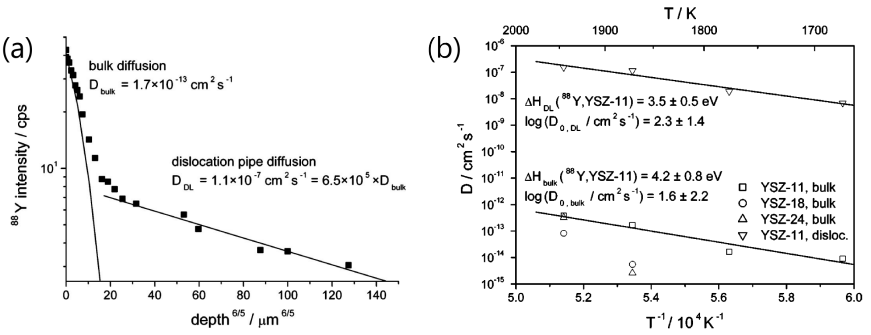


Figure 3.20: (a) Depth profile for ^{88}Y in 11.1 mol.% YSZ after heating for 72 at 1598 °C and (b) the Arrhenius relationship of for the bulk and dislocation diffusion pathways for different dopant concentrations. Taken with permission from Ref. [165].

Kilo *et al.* [166, 167] extended their work to the diffusivity of all the lanthanide impurities in YSZ and CSZ, deposited onto the surface using an acidic solution. They found that for lanthanides with a radius smaller than 1 $\AA$, that the diffusivity was constant and roughly equal to the zirconium self-diffusivity, while for the larger ionic radii the diffusivity approaches the stabiliser value. Other studies have investigated the self-diffusivities of various cations of different valence in YSZ [168–170], but a comprehensive review of these reports are beyond the scope of this thesis.

In a similar method to Kilo *et al.*, Drings *et al.* [171] measured diffusion profiles of the radioisotope ^{96}Zr into samples with an average grain size of 50 nm prepared by reactive sputtering. The bulk and grain boundary diffusivities were calculated in the temperature range 897-937°C. Unfortunately this range could not be extended to higher or lower temperatures due to grain coarsening and temporal limitations. The authors found a seven order of magnitude increase in the grain boundary diffusion compared to bulk.

The diffusivity of Gd into CeO_2 was studied by Rockenhäuser *et al.* [172] by depositing Gd_2O_3 films onto CeO_2 by PLD. Using TEM combined with quantitative EDXS analysis, the authors calculated the diffusivity of Gd into pure ceria for temperatures between 986 and 1175 °C. They calculated

a considerably lower activation energy than in YSZ of 2.3 eV, however no comment was made about the differences between grain and grain boundary contributions.

3.2.2 Surface Segregation: Experimental Studies

Segregation of impurities and dopants to the surface of commercial electrolytes such as YSZ and CGO has been studied using a range of techniques such as LEIS, x-ray photoelectron spectroscopy (XPS), Rutherford backscattering (RBS), and Auger electron spectroscopy (AES). In the vast majority of cases the dopant is found to segregate to the surface region as well as impurities such as Si, Na, and Ca despite only trace amounts being found in the bulk material [173, 174].

Theunissen *et al.* [175], using XPS and AES showed that in YDZ the surface concentration was in the range 19-23 mol.% after a 5 hour heat treatment at 1000°C and was independent of the bulk yttria content, which was varied from 3-21 mol.%. According to Eq. 2.54, this would suggest a change in the enthalpy of heat, ΔH_S, that is the driving force for segregation, with bulk dopant concentration. Hughes [176], also observed a deviation from the expected behaviour in 9.5 mol.% YSZ single crystals using XPS. In the temperature range of 900-1500°C, the free energy of segregation, ΔG_S, was found to be positive (6.4 to 12.1 kJ/mol), such that the segregation increased with temperature despite being in equilibrium. This compared to a value of -12.3 kJ/mol, for ΔH_S calculated according to Eq. 2.55. Hughes explained this as either a change in the entropy at the surface due to Y ordering, or interactions with Si impurities to form a stable layered surface (as shown in Fig. 3.21a).

De Ridder *et al.* [109, 179] studied isotopically enriched YDZ sintered pellets, such that the Y/Zr ratio could be analysed by LEIS. As discussed in Section 4.6, one of the advantages of LEIS is its surface specificity, allowing a more accurate observation of the outermost layer of the surface. The authors demonstrated complete coverage of Na, Si and Ca on the outermost layer of the surface after annealing samples to 1200°C. In a similar fashion to Theunissen *et al.* [175], the Y surface enrichment factor was also observed

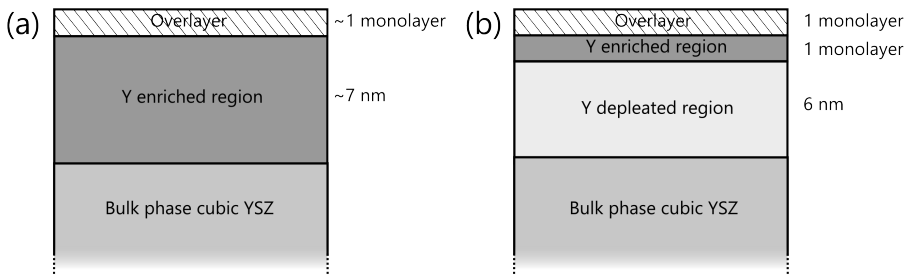


Figure 3.21: Layered surface structures of YSZ reported by (a) Hughes [176] and (b) De Ridder *et al.* [177]. Adapted from Ref. [178].

to vary with dopant concentration between 3 and 10 mol.% YDZ. For the 10 mol.% YSZ, the samples were found to be in equilibrium above 1000°C for heat treatments of 5 hours. De Ridder *et al.* observe a free energy of segregation of -21±3 kJ/mol, comparable to that calculated by Hughes [176] according to Eq. 2.55.

De Ridder *et al.* [177] went on to perform IETD on YSZ, tracking the oxygen tracer isotope using LEIS. The diffusion profiles suggested a two phase model, with a thin slow diffusing layer on top of the YSZ. From comparison to literature diffusion values, De Ridder *et al.* identified this top layer as a 6 nm thick Y depleted monoclinic phase, as shown in Fig. 3.21b. However the authors do not provide any direct evidence for the monoclinic phase, nor do they observe any depletion region in the Y signal from LEIS depth profiles [109]. It may be possible that a highly Y enriched region would also lead to a substantially lower diffusivity.

Nowotny *et al.* [178] proposed that the differences between De Ridder *et al.* and Hughes observations of the YSZ surface is due to two phenomena: *equilibrium segregation* and *non-equilibrium segregation*. They claim that damage induced by polishing and ion beam ablation are the cause of the depleted layer observed by De Ridder *et al.* [177], stating that the surface had not reached thermodynamic equilibrium.

Segregation to the surfaces of 20 mol.% Gd-doped CeO_2 has been investigated by Scanlon *et al.* by LEIS [180] and RBS. A single monolayer of either Ca or K was observed at the surface, although the exact species could

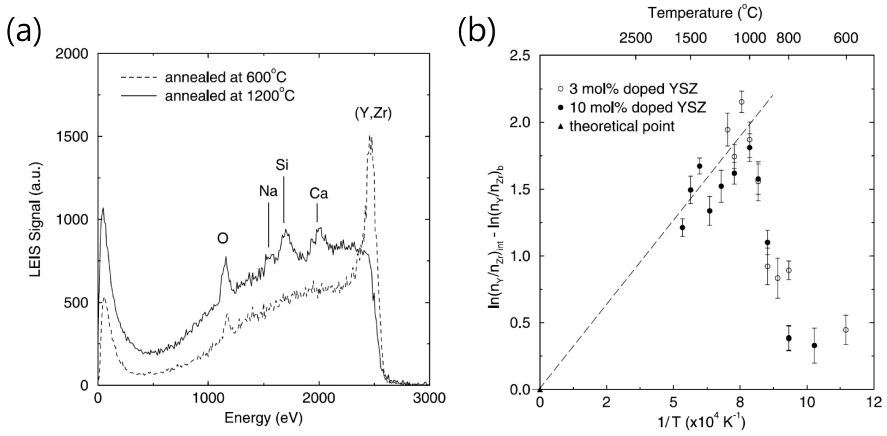


Figure 3.22: LEIS spectra (a) 3 keV $^4He^+$) of 10 mol.% YSZ after annealing at 600 and 1200°C. b) Arrhenius plot of the Y segregation to the surface of 3 and 10 mol.% YDZ. The line indicates the free energy for segregation. Reproduced with permission from Ref. [179].

not be determined due to limited mass resolution. The authors saw a 1:1 ratio of Ce/Gd at the surface, compared to 4.2:1 in the bulk. The enrichment region was found to extend to 5 monolayers in depth. No difference in the surface concentration was found at temperatures of 1300 and 1600°C, and no changes in the crystal structure were observed by XRD.

3.2.3 Surface Segregation: Computational Studies

The surface segregation of 10 mol.% YSZ and CGO has been simulated using MD by Lee *et al.* [181]. It was observed that in YSZ a 1.6 fold increase in the Y concentration was observed at the surface, but that the highest concentration was in the third cation layer (Fig. 3.23c). For CGO the surface concentration was 3.1 times higher than bulk and instead the highest Gd concentration was the outermost layer (Fig. 3.23d). Both enrichment factors agree well with LEIS studies by De Ridder *et al.* [109, 179] and Scanlon *et al.* by LEIS [180] in terms of magnitude and length scales. But as the cation mismatch between Y and Zr is higher than Gd and Ce, changes in strain energy does not explain the difference in segregation between the two.

Lee *et al.* propose that the distribution of oxygen vacancies drives cation segregation. For YSZ, the vacancy population is high on the outermost

layer, but depleted in the following two subsurface layers (Fig. 3.23i). The authors suggest that the high oxygen content blocks the segregation of Y to the surface. In the case of CGO, the vacancy depletion is much more uniform in the subsurface layers (Fig. 3.23j), and hence Gd segregates to the outmost layer.

Ismail *et al.* [182] simulated the (111) surface of Sm-doped CeO_2 using genetic algorithms and DFT. Interestingly, the Sm segregation was always observed to occur in the subsurface layers, and not to the outermost surface. They found that the segregation to the surface was limited due to the formation of energetically unfavourable vacancy pairs at high dopant concentration. The authors show that the surface enrichment factor decreased for higher dopant concentrations, agreeing with the work by Theunissen *et al.* [175] in YSZ.

Stanek *et al.* [183] employed atomistic simulation techniques to predict Y segregation to the (100), (101), (110) surface of tetragonal YDZ. The authors found a considerable difference between the segregation energetics in the simulations. Fig. 3.24 shows the segregation energy for the three surfaces. (Note that the segregation energy represents the difference between a defect cluster in the bulk and at the surface, and should not be confused with the enthalpy for segregation). For the (100) and (110) surface an energy minima is observed subsurface, suggesting that surface segregation will be most prominent in the subsurface region, agreeing with both Lee *et al.* [181] and Ismail *et al.* [182].

3.2.4 Section Summary

The segregation of dopants to the surfaces of the fluorite oxide has been studied to a far lesser extent than the transport properties. The reason for this may be due to an assumption that a nanoscale re-ordering of the dopants to the surface of an electrolyte layer would have a negligible effect on the performance of an SOFC.

It is generally thought that dopant diffusion occurs through a cation vacancy mechanism, however the interactions or oxygen vacancies remains unclear for individual fluorite systems. Cation diffusion is commonly found

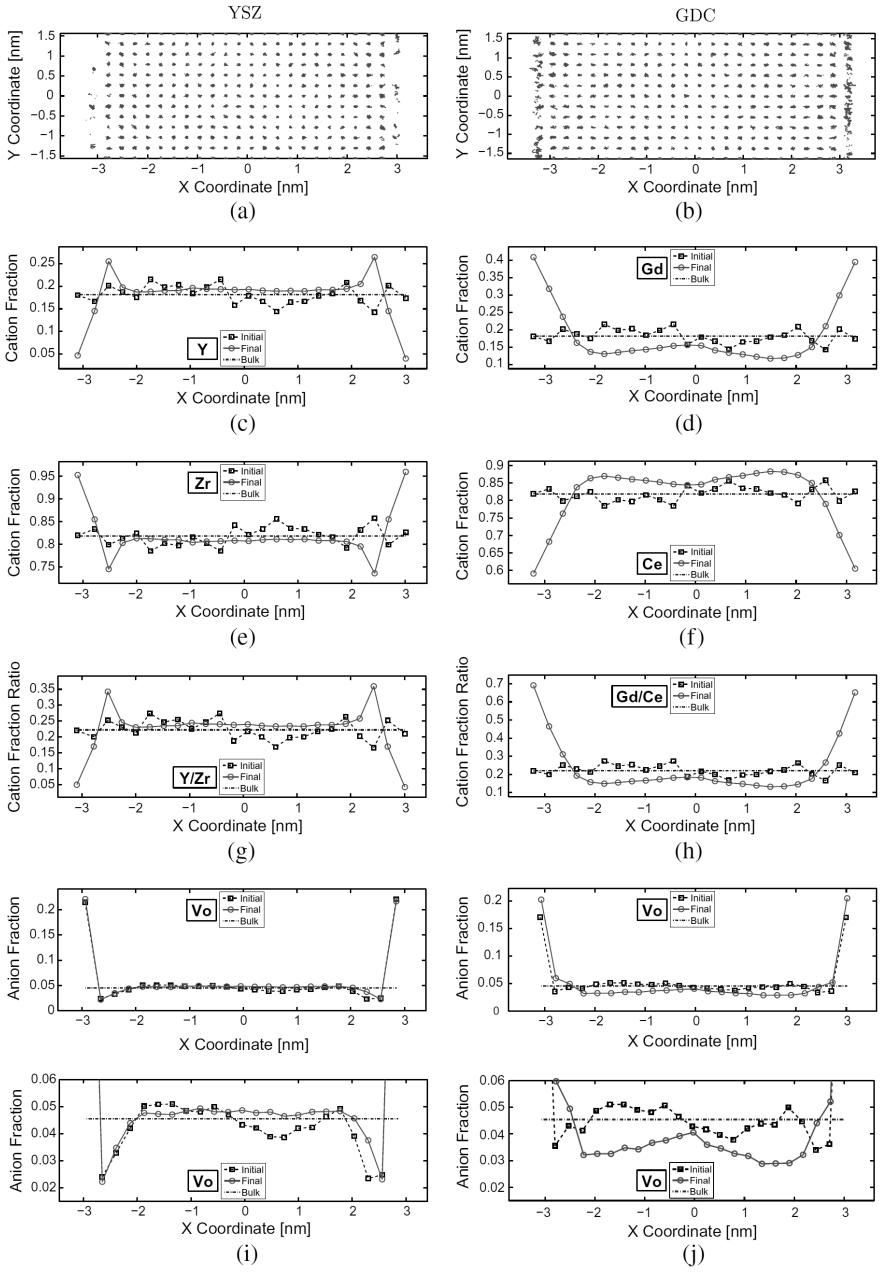


Figure 3.23: MD simulations of 10 mol.% YSZ and CGO slabs. Dopant cation positions projected onto the x-y plane for (a) YSZ and (b) CGO. Dopant cation fractions along x-axis for (c) YSZ and (d) CGO. Host cation fraction for (e) YSZ and (f) CGO. Ratio of the dopant and host cations for (g) YSZ and (h) CGO. Oxygen vacancy fractions for (i) YSZ and (j) CGO. Reproduced with permission from Ref. [181].

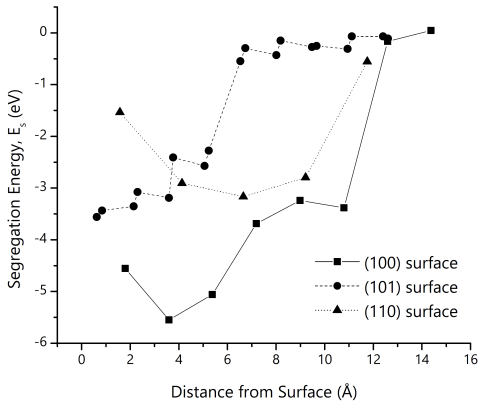


Figure 3.24: Segregation energies as a function of distance from surface calculated for the the three low index surfaces by atomistic simulations. Data taken from Ref. [183].

to be much higher through the grain boundary regions than bulk, and the relative size of the radius compared to that of the host cation is thought to affect the diffusivity.

In experimental studies of the surfaces of doped ZrO_2 and CeO_2, impurity layers of Si, Na and Ca have repeatedly been observed on the outermost surface layer, followed by a region enriched in the dopant cation. However, dopant depletion layers below the enriched region have been a topic of debate, with contradictory findings. Segregation of the dopant cation has also been predicted by computational simulations, however often the segregation has been calculated to occur in the subsurface region, as opposed to the outermost surface. This has not previously been reported experimentally. Surface orientation is also expected to be a controlling factor in surface segregation.

As discussed in the Chapter 1, there is much interest in thin film ionic conductors for electrochemical devices such as the μSOFC and memristor. Electrolytes are now being produced where the surface and sub-surface regions account for a considerable fraction of the total film volume. In addition, thin films are often fabricated far below the sintering temperature and are often thought to be meta-stable, yet segregation effects are not widely

studied for these systems. Finally with regards to the exciting prospects of strain engineering, no-one has yet studied the effects of strain on the extent and rate of degradation. However this will have considerable impact into the potential incorporation into electrochemical devices.

Thin films provide a model system to study segregation while controlling material properties such as surface orientation, microstructure and strain. In addition improving our understanding of the degradation behaviour is of critical importance for miniaturisation of electrochemical devices. Yet, to date, there have been no studies exploring these effects in the doped fluorites electrolytes.

3.3 Conclusion

Based on the review of transport in nanostructured materials, there are several open questions which will be addressed in this thesis:

i Does a modification of the lattice parameter affect the ionic conductivity in YSZ?

ii Do dislocations provide a path for enhanced transport in YSZ?

iii Can direct evidence be provided for improved diffusivity in YSZ by tracer diffusion?

From the examination of the literature on surface segregation, the flowing questions will be addressed in this work:

i What is the surface structure of CGO films grown by PLD?

ii How is the surface segregation in CGO films affected as a function of thermal history?

iii Can the rate or extent of segregation be engineered by modifying properties of the film such as strain and surface orientation?

Chapter 4

Experimental Methods

In this chapter the principal experimental techniques and methods will be outlined and details of the instrumentation given. Thin film production was carried out by pulsed laser deposition (PLD), and structural characterisation was performed by x-ray diffraction (XRD) and transmission electron microscopy (TEM) with selected area electron diffraction (SAED). The transport properties were assessed employing electrochemical impedance spectroscopy (EIS) and oxygen isotope exchange tracer diffusion (IETD) combined with secondary ion mass spectrometry (SIMS). In addition, segregation of dopant ions to the surface of the films was studied using low energy ion scattering (LEIS).

4.1 Pulsed Laser Deposition

The vast majority of the films investigated in this work were grown from a type of physical vapour deposition (PVD) technique known as PLD. Here, a bulk target of the desired film composition is ablated with a high energy laser, facilitating the stoichiometric transfer from the target to film. Fig. 4.1 is a schematic diagram illustrating the key elements of the pulsed laser ablation process. The photon energy of the laser pulse is transferred to the bulk material in the form of electronic excitation and in turn to the lattice, resulting in melting and vaporisation of the target [184]. The vaporised material forms a plume consisting of atoms, molecules, electrons and material

clusters. The plume expands away from interaction volume, and generally has a distribution symmetric about the target surface normal. The substrate is often heated to allow the deposited material sufficient energy for mobility on the surface enabling crystalline growth.

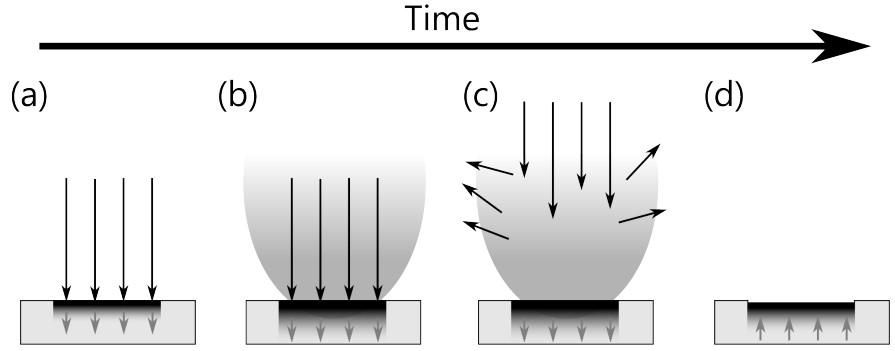


Figure 4.1: Schematic diagram of the pulsed laser ablation process. (a) Initial absorption of the laser radiation (long arrows) and melting of the target material (short arrows). (b) Melting continues and vaporisation of the target occurs. (c) Laser-plume interactions due to absorption of the incident laser radiation by the plume causing plasma formation. (d) Melt front recedes and surface re-solidifies. Adapted from Ashford *et al.* [185].

The growth mechanism and properties of the deposited films will depend upon the choice of substrate, the substrate temperature, and the relative kinetic energies and arrival rates of the ablated species in the plume. The latter will be dependent upon deposition conditions such as the laser energy and background gas atmosphere [185].

The configuration of the PLD set-up used in this work is shown schematically in Fig. 4.2. The laser was an UV KrF excimer laser (λ=248 nm, Lambda Physik COMPex 201), and the chamber base pressure was approximately 5 $\times 10^{-5}$ mbar. During deposition the target was positioned adjacent from the substrate and was rotated to avoid repeated ablation of a single spot.

4.1.1 General Deposition Procedure

Prior to deposition, the following ultrasonic cleaning procedure was applied to the as-received substrates: three minutes in acetone, three minutes in

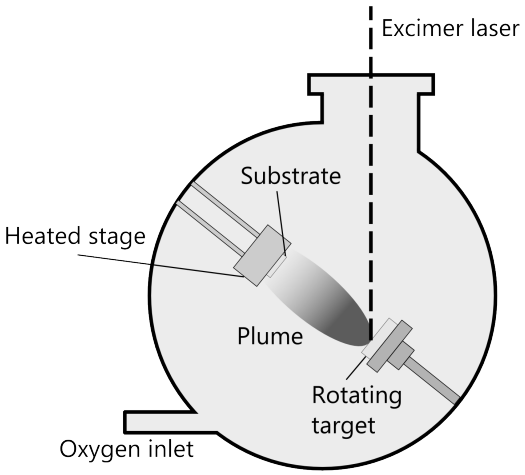


Figure 4.2: Schematic illustration of the PLD system setup.

isopropanol and finally three minutes in ultra-pure Milli-Q water. The substrates were then mounted to the heater plate using Ag paste to provide good thermal contact, and any surface dust removed using a N_2 gas gun. The surface of the target was frequently polished using SiC grit paper, in order to prevent extreme roughening from repeated ablation.

The chamber was then pumped to the base pressure and the heater plate ramped at 50°C/min to the desired temperature. When reaching the deposition temperature, the chamber was filled with O_2 at a pressure of 600 mbar to burn off any organic solvents and impurities from the Ag paste, before pumping back down to base pressure. The deposition pressure used for all PLD film growth in this work was 3.0 $\times 10^{-2}$ mbar. Before deposition, the target was ablated with 300 pulses to remove any surface contamination, while the substrates were protected by the use of a shutter. During deposition, the laser frequency was kept to 5 Hz for all films, however the number of pulses and the substrate temperature were varied, as detailed in Chapters 5, 6, and 7. After deposition the sample was cooled at a rate of 10°C/min in an O_2 atmosphere of of 600 mbar. All reported substrate temperatures during film growth described in this work refer to the nominal set temperature of the heater plate, as measured by a thermocouple in contact with the

reverse side of the heater.

4.1.2 PLD Target Fabrication

The targets for film growth were prepared from commercially available powders of 8 mol.% YSZ (Tosoh, Japan) and 10 mol.% CGO (NexTech Materials, USA). The powders were uniaxially pressed, and sintered at 1500°C for 10 hours with a heating/cooling rate of 5 °C/min. The density of the targets was calculated from geometrical measurements and found to be >95% of theoretical density. XRD patterns recorded from the targets were refined using Le Bail analysis in the FullProf software suite [186] and found to be cubic fluorite for both 8 mol.% YSZ and 10 mol.% CGO with lattice parameters of 0.5139 nm and 0.5418 nm respectively (see Figs. A.1 and A.2 in Appendix A.1).

4.2 X-Ray Diffraction

Diffraction is observed when electromagnetic (EM) radiation is incident on a material with a periodic structure so as the lattice spacing is of the same order of magnitude as the wavelength of the impinging radiation. For interatomic distances of 1-5 Å the appropriate EM radiation should consist of photons in the energy range of 2-12 keV, which corresponds to the energy band classified as x-rays [187]. XRD is a conventional method for determining the crystallographic structure and orientation of a material. In most cases it allows for rapid and non-destructive characterisation of materials, making XRD an extremely powerful and useful technique.

Using a monochromatic x-ray source, information about the lattice spacing of a crystalline specimen can be obtained due to constructive and destructive interference effects between photons scattered off different planes in the periodic lattice. Quantitatively this is explained via Bragg's law (Eq. 4.1) and a schematic of the phenomenon is shown in Fig. 4.3.

$$n\lambda = 2d\sin\theta \tag{4.1}$$

Where n is the order of the reflection and a positive integer, d is the lattice

spacing and θ is the angle of incidence with respect to the scattering planes. It can be easily visualised from Fig. 4.3 that the difference in path length between photons scattered off two different planes is $2d\sin\theta$, and therefore constructive interference will take place when this length is equal to an integer number of wavelengths.

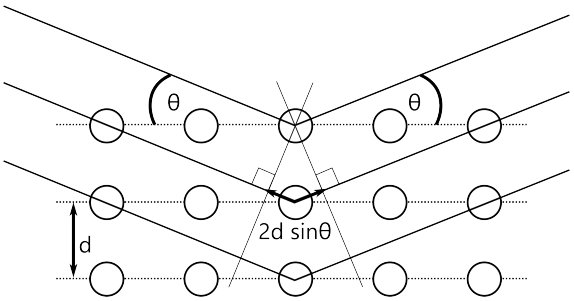


Figure 4.3: Visualisation of the Bragg equation.

In this work XRD $\theta/2\theta$ scans was used to investigate the out-of-plane orientation of the thin films prepared by PLD, as well as the strain state by quantifying the measured lattice parameters. In addition XRD pole figures were also obtained, yielding information about the in-plane orientation of the films. Finally in some cases, a series of rocking curves were taken in order to measure the miscut of the single crystal substrate. Fig. 4.4 provides a graphical representation of the relevant variable angles in a four-circle goniometer, which are referred to below.

4.2.1 $\theta/2\theta$ Scans

The equipment used to carry out the $\theta/2\theta$ scans was an x-ray diffractometer (PANalytical X'Pert Pro MRD), utilising parallel beam optics, Cu K_α radiation ($\lambda = 1.5418$ $\mathring{A}$), a Ni-β filter to remove the Cu-K_β signal, and a graphite monochromator. For all measurements a 1/16° divergent slit was used. Prior to the $\theta/2\theta$ scan acquisition the 2θ and ω angles were set to 0° in order to measure and correct the zero-position of the diffractometer. Next the films were precisely aligned such that the diffraction vector was perpendicular to the surface of the film, though a series of alignments in the

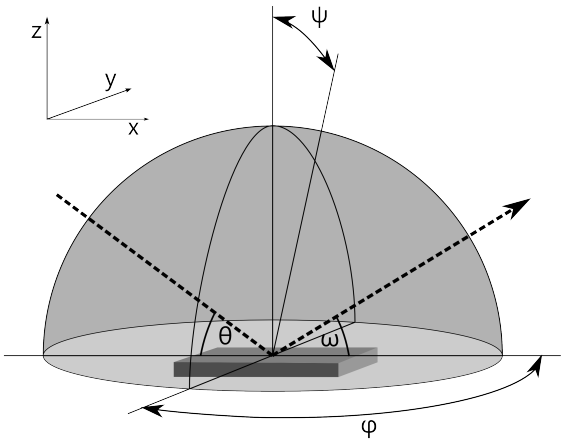


Figure 4.4: Schematic diagram of the axes and angles discussed with regards to XRD measurements. The dashed line represents the x-ray path.

z, y, ω, ψ and ϕ axes.

The lattice parameters of the films were calculated from the 2θ peak positions. First the substrate peak positions were refined using the Le Bail analysis in the FullProf software, in order to account for any errors in the 2θ=0 position. Next the film peaks were fitted using a pseudo-Voigt function and the lattice parameters calculated according to Eq. 4.2.

$$a = \frac{\lambda\sqrt{(h^2+k^2+l^2)}}{2sin\theta}. \tag{4.2}$$

4.2.2 Pole Figures

For powder and bulk material samples often it can be assumed that the orientation of the grains is random and isotropic and hence 2θ scans give a satisfactory amount of information. However in polycrystalline thin films this is rarely the case and a preferential orientation with respect to the sample reference frame is usually present. This anisotropy of the grain orientation is known as texture. A 2θ scan gives limited information on the texture of a thin film, and so pole figures of selected Bragg peaks are obtained to determine texture factors.

During the acquisition of a pole figure the 2θ angle is fixed to a value corresponding to the relevant Bragg peak of the sample. The sample is then

rotated through the azimuth angle ϕ ($0 \leq \phi \leq 360$) and tilted in through the tilt angle ψ ($0 \leq \psi \leq 80$) whereby a complete rotation of ϕ is obtained for each increment in ψ.

Diffraction via Bragg's law (Eq. 4.1) will only occur when lattice planes corresponding to the 2θ value (e.g. (200), (111)) are in the scattering plane, defined as the surface of the film at $\phi = \psi = 0$ but unchanging in the laboratory reference frame as ϕ and ψ vary. As ψ is increased planes with a d spacing corresponding to the 2θ value from grains in which this set of planes is not parallel with the surface of the film (and therefore would not contribute to the signal at this 2θ when $\psi = 0$) will be brought into the scattering plane and hence display a peak. The ψ values at which these peaks occur for different orientations are given by the interplanar angles and depend on the symmetry of the crystal unit cell. Furthermore, grain orientation in the plane parallel to the surface of the film can be inferred by the distribution of the signal as ϕ is varied. A uniform low intensity signal is characteristic of grains that are randomly oriented in the azimuth, whereas well defined peaks imply a strong degree of texture with the number of peaks relating to the number of preferred orientations and symmetry in ϕ.

All pole figures were obtained using a similar diffractometer to that used for the $\theta/2\theta$ scan (PANalytical X'Pert Pro MRD) but without the use of a monochromator.

4.2.3 Miscut Measurements

A method was developed by Doucette *et al.* [188] for measuring the miscut in single crystals, which avoids separate reference standards or precise alignment of the specimen to the holder. The technique involves taking a series of rocking curves, which is where the 2θ is kept constant (in this case the Bragg condition for the substrate peak) and then the sample is 'rocked' a few degrees along the ω angle.

The measurement requires a rocking curve to be taken at ϕ=0°, ϕ=90°, ϕ=180° and ϕ=270°, the sample to be removed from the stage and replaced after physically rotating the specimen by 180° in ϕ. The miscut, δ, can then

be calculated according to

$$(tan\,\delta)^2 = (tan\,\delta_{1,2})^2 + (tan\,\delta_{3,4})^2, \tag{4.3}$$

where

$$\delta_{1,2} = \frac{1}{4}[\omega'_1 - \omega'_2 + \omega'_{2t} - \omega'_{1t}], \tag{4.4}$$

$$\delta_{3,4} = \frac{1}{4}[\omega'_3 - \omega'_4 + \omega'_{3t} - \omega'_{4t}], \tag{4.5}$$

Here, ω'_1, ω'_2, ω'_3 and ω'_4 are the positions of the substrate peak in the rocking curves at ϕ=0°, ϕ=180°, ϕ=90° and ϕ=270° respectively. The t subscript denotes the same measurements after the sample has been removed and remounted. These analyses were carried out on the same diffractometer described in Section 4.2.1.

4.3 Transmission Electron Microscopy

Electrons are suited for characterisation of the microstructure of materials, as they can be accelerated to high energies (very small wavelengths) allowing a far greater spatial resolution than that obtainable through visible light waves, such as those used in optical microscopy which have a maximum resolution of a few hundred nanometres.

In a TEM, a highly accelerated electron beam (typically 200-300 keV) is incident on a sample that has been thinned to the extent (usually $<$ 100 nm thick) that a large proportion will pass through, so that the resultant micrograph will be formed from the interaction of the beam and the sample. Fig. 4.5, shows basic operation of the TEM system in the two principle modes: selected area electron diffraction and imaging mode. The TEM investigations detailed in this work consist of findings utilising these two modes of operation, and hence the discussion here will be limited. However, transmission electron microscopy is a vastly more diverse technique and the interested reader is directed to the excellent book by Williams and Carter [189].

As can be seen in Fig. 4.5, the transmitted electron beam is focused by

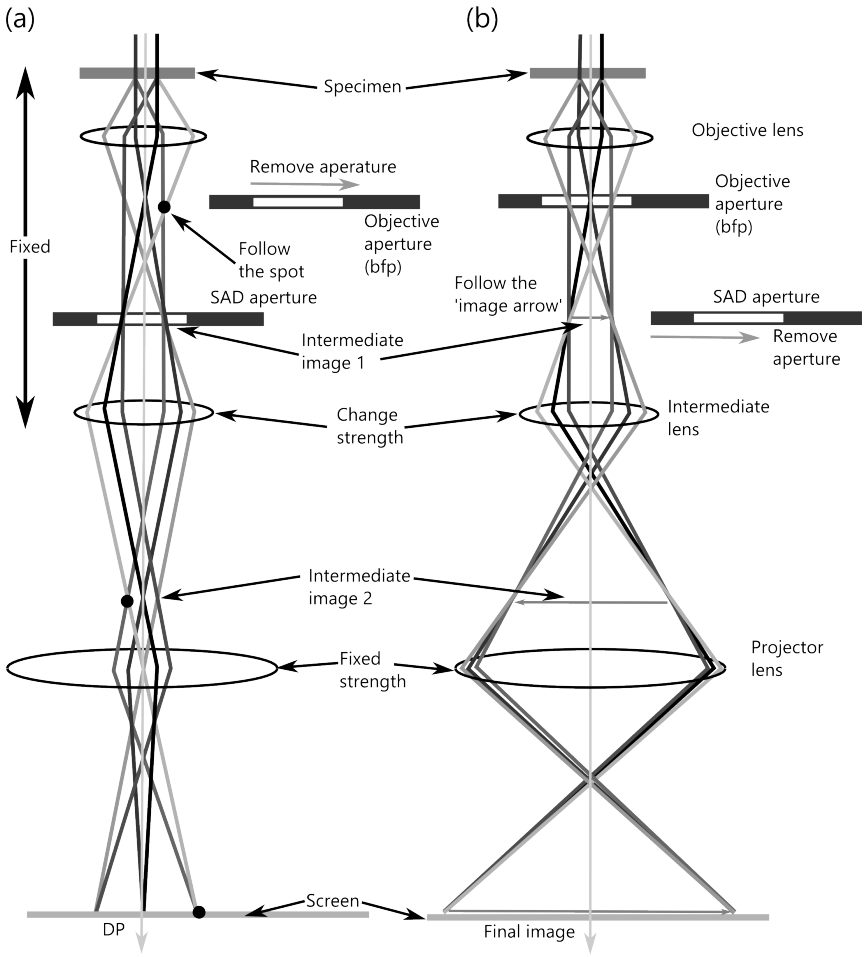


Figure 4.5: Simplified schematic of the two basic operation modes of the TEM. (a) selected area electron diffraction mode (SAED) and (b) imaging mode. Adapted from Williams and Carter [189].

the objective lens[1] to create a diffraction pattern at the back focal plane (BFP) and an image at the intermediate-image 1 position. Depending on the strength of the intermediate lens, either a diffraction pattern or image is formed through the projector lens onto the viewing screen or charge-coupled device (CCD) camera.

For electron diffraction, it is rarely useful to obtain diffraction patterns from the entire sample due to effects such as sample buckling and metal deposits from the lamella preparation. Therefore an aperture is placed in the intermediate-image 1 position (SAED aperture), which can be positioned with respect to the sample such that the diffraction pattern will come from a specific area. This is useful for identifying the diffraction spots coming from features in the sample such as the substrate and film.

When imaging in the TEM, contrast can be due to incoherent inelastic scattering which will vary due to effects such as the atomic mass, density and thickness of the lamella (mass-thickness contrast), as well contrast from coherent elastic scattering in the sample (diffraction contrast). Both of these fall under the category known as amplitude contrast.

It is possible to vary the effects of diffraction contrast on an image by inserting an aperture into the BFP, such that different parts in the diffraction pattern may be selected to form the image, thereby creating a greater contrast between the regions of the sample which scatter to different extents. In bright field (BF) imaging mode, the aperture allows the un-scattered beam to pass through and therefore in the image the regions of the sample which strongly scatter will appear very dark (Fig. 4.6a). In dark field (DF) imaging mode, only scattered parts of the beam are allowed to form the image and hence the strongly scattering regions will appear bright (Fig. 4.6b). DF imaging can be particularly useful for imaging the orientation of grains, by selecting the specific parts of the diffraction pattern using the objective aperture.

Contrast can also come from differences in the phase of the electron waves scattered by the crystal lattice of the specimen, this is known as phase contrast. If a sample is highly crystalline and a low-index zone axis aligned

[1] Rather than the glass lenses of an optical microscope, a TEM utilises magnetic electron lenses.

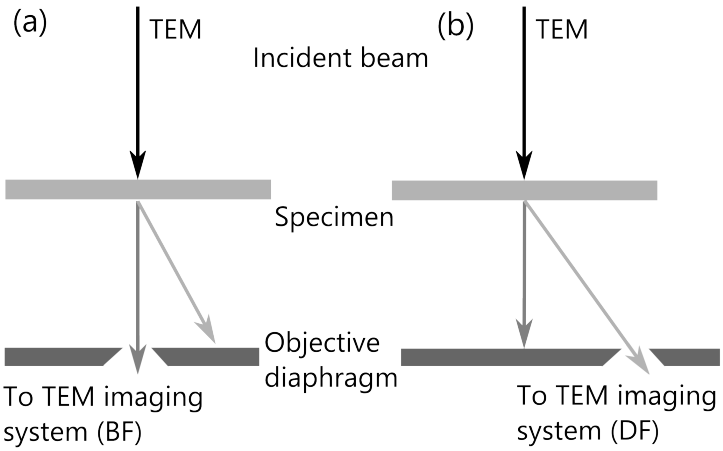


Figure 4.6: Comparison of the position of the objective aperture for (a) bright field imaging and (b) dark field imaging. Adapted from Ref. [189].

with the beam, then at high enough magnification a periodic contrast will be visible in the image. In general, this array of fringes may be directly related to the lattice spacing and orientation, however great care must be taken with regards to actual position of atoms in this HR-TEM imaging.

The TEM studies in this work were carried out on two microscopes. A JEM 2010 TEM (JEOL Ltd, Japan) operating at 200 keV and an aberration-corrected FEI Titan 80-300 (FEI Company, USA) with a Cs-corrector on the imaging lens, operating at 300 keV. The acquired images and diffraction patterns were analysed using the Digital Micrograph software.

4.3.1 Sample Preparation by Focus Ion Beam (FIB) Sectioning

Cross sections of the films grown by PLD were prepared for TEM analysis using the *in situ* 'lift-out' technique [190] on a dual-beam FEI Helios FIB/SEM NanoLab (FEI Company, USA). The surface of the films was first covered with a layer of Au or Cr with a thickness in the range of 5-100 nm, to protect the surface from beam damage and prevent the build-up of electrical charge. The samples were prepared and thinned at 30 kV and then subsequently at 5 kV and 2 kV to minimize the amorphous surface layer. Once mounted into the TEM holder, the lamellae were subject to cleaning

in a Solarus Advanced Plasma Cleaning System (Gatan Inc., USA) for 60 seconds in a H_2/O_2 gas.

4.4 Electrochemical Impedance Spectroscopy

Often when measuring the electrical conductivity of ceramics, there are a number of features in the samples, such as the grains, grain boundaries and electrodes which contribute in series to the total DC resistance. However, many of these types of features will have differing electrical relaxation or time constants when subject to an AC electric field. In EIS, measurements are made over a wide range of frequencies allowing for the identification and extraction of the resistances of the individual components.

A small sinusoidal electric field, ΔV, is applied to the sample given by

$$\Delta V(\omega, t) = V_0 \exp(i\omega t) \tag{4.6}$$

where V_0 is the magnitude of the field, $\omega = 2\pi f$ is the angular frequency, t is time and $i = \sqrt{-1}$. Care must be taken to ensure that ΔV is kept in the pseudo-linear region of the current-voltage response curve. If this is the case then a sinusoidal excitation voltage will result in a sinusoidal current response, ΔI, at the same frequency, f, but shifted in phase, ϕ.

$$\Delta I(\omega, t) = I_0 \exp(i[\omega t + \phi]) \tag{4.7}$$

The phase will be 0 for purely resistive responses and $\frac{\pi}{2}$ for purely capacitive responses.

Impedance extends the concept of resistance to AC circuits, and possesses both a magnitude and a phase component. In analogy to Ohms law, the impedance of the linear system can be calculated as

$$Z(\omega) = \frac{\Delta V(\omega, t)}{\Delta I(\omega, t)} = \frac{V_0 \exp(i\omega t)}{I_0 \exp(i[\omega t + \phi])} = |Z| \exp(i\phi). \tag{4.8}$$

Separated into the real, Z', and imaginary, Z'', parts, the impedance may

be written as

$$Z(\omega) = |Z|\cos\phi + i(|Z|\sin\phi) = Z' + iZ''. \tag{4.9}$$

The real and imaginary components can be plotted together on a 1:1 axis, known as a Nyquist plot. An example for a polycrystalline ceramic sample is shown in Fig. 4.7. Each process with a distinct relaxation time is recognisable as a characteristic arc and may be described as a resistor (R) and capacitor (C) in parallel. The time constant of the process, $\tau = RC$, is known as the dielectric relaxation time and is related to the arc peak angular frequency, ω_{max}, by

$$\omega_{max} = \tau^{-1}. \tag{4.10}$$

The total response of the sample may be fitted using an equivalent circuit of R-C elements, and the ω_{max} values for each element related to a process in the sample [191]. Often impedance arcs are distorted or depressed and can be better fitted replacing the capacitor with a constant-phase element (CPE). A CPE may be thought of as an imperfect capacitor with an impedance given by

$$Z_{CPE} = \frac{1}{Q(i\omega)^n}, \tag{4.11}$$

where n is a measure of the non-ideality of the device and is equal to unity for a perfect capacitor with capacitance of Q. The more extreme the depression of the arc, the further from one n will be. The effective capacitance of the CPE may be calculated according to

$$C = (R^{1-n}Q)^{1/n}. \tag{4.12}$$

In real ceramic samples, a depression in the arc relating to the grain boundary resistance is often observed. This is thought to relate to an inhomogeneity in the grain boundary properties in the material [192].

In the case of an in-plane measurement of a conducting film on an insulating substrate (as shown in Fig. 4.8a), one must also take into consideration the capacitance induced by the sample geometry, namely the substrate

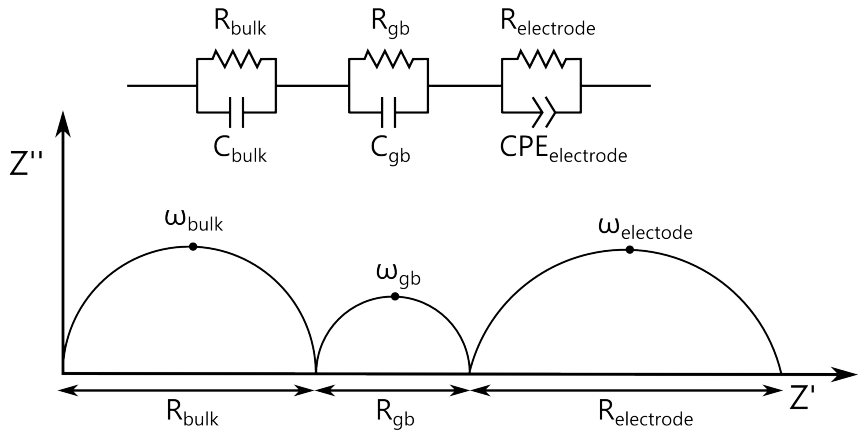


Figure 4.7: Nyquist plot for a typical polycrystalline ceramic electrolyte with the representative equivalent circuit.

($C_{substrate}$), and the capacitance coming from the contacting wires (C_{wiring}). The two contributions may be combined and the resultant capacitance labelled the total stray capacitance [118].

$$C_{stray} = C_{substrate} + C_{wiring}. \tag{4.13}$$

The capacitance of the contacting wires (C_{wiring}) is difficult to estimate, as it will depend on a number of factors such as the distance and size of the wires and how they are positioned with respect to one another. However the substrate capacitance may be simply described by

$$C_{substrate} = \varepsilon_{substrate} \frac{LB}{D} f_{geometry}, \tag{4.14}$$

where L, B and D are the electrode dimensions as defined in Fig. 4.8a, $\varepsilon_{substrate}$ is the substrate permittivity and $f_{geometry}$ is a geometry factor which depends on the ratio of B/D and takes into account the arrangement of the electrodes [118].

The equivalent circuit of a thin film must be modified from that for a bulk polycrystalline specimen shown in Fig.4.7, to include these effects (as shown in Fig. 4.8b). These additional capacitances can make the separation of the bulk and grain boundary responses impossible for certain electrode

geometries [118], and therefore the impedance response will often consist of a single arc, which may be interpreted using the equivalent circuit in Fig. 4.8c.

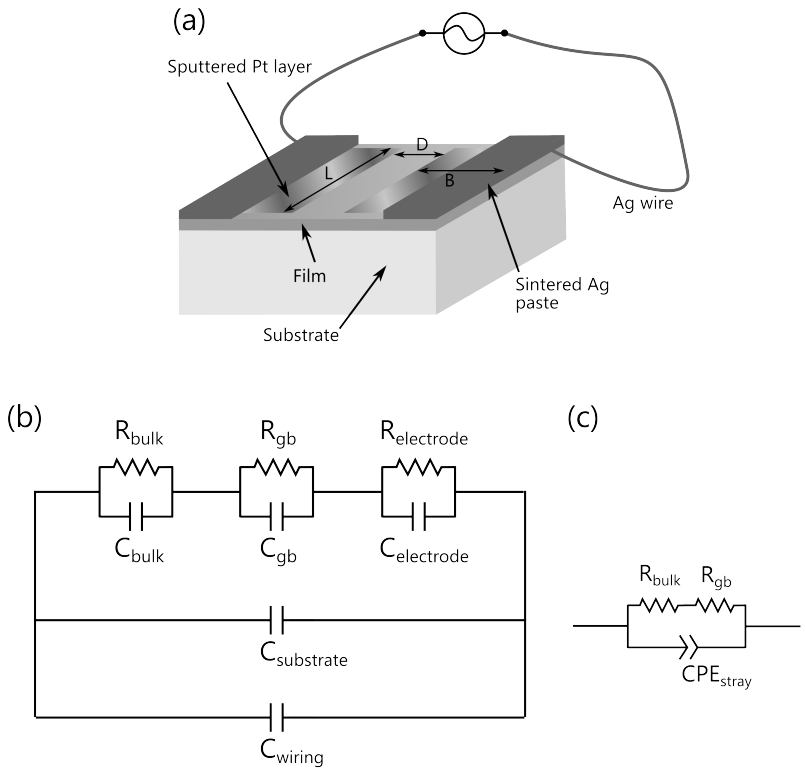


Figure 4.8: (a) schematic of the electrode geometry used defining the notation used to describe the electrodes width B, length L and distance between them D. (b) the equivalent circuit for a thin polycrystalline film of an ionic conductor on an insulating substrate. (c) the modified equivalent circuit used to fit the Nyquist plots in this work.

4.4.1 EIS Measurement Method

Two Pt pad electrodes were deposited onto the surface of the films at room temperature using a magnetron sputter coater (K575X, Emitech Ltd, UK or Q150T, Quorum Technologies Ltd, UK). The thickness of the electrodes was approximately 250 nm, as measured during deposition by a quartz crystal oscillator. The samples were then annealed at 600°C for 2 hours to ensure

good contact between the Pt and film surface. Next Ag wires were attached to the Pt pads using Ag paste, and the annealing procedure repeated in order to sinter the paste. The sample geometry is shown in Fig. 4.8a. An optical microscope was used to check the electrode morphology and to accurately measure the geometry both before and after the EIS measurements to ensure no changes in the electrodes took place.

The films were positioned in the furnace using a custom made sample holder, where the films were supported by the Ag contacting wires next to a thermocouple for an accurate determination of the temperature. Up until the point of contact the wires were shielded inside alumina tubes covered in Pt sheets. Measurements were taken in static air as a function of temperature for all films, both ramping up and down in temperature to ensure reproducibility, with the furnace being allowed to equilibrate for 1 hour between each measurement.

The EIS measurements were performed using a Solartron Analytical 1260 frequency response analyser (FRA) and Solartron Analytical 1296 dielectric interface (AMETEK Advanced Measurement Technology, UK). An amplitude of 1 V was used over a frequency range of 1 Hz-13 MHz with zero DC bias. The resultant spectra were analysed using the Z-View software [193].

4.5 Isotope Exchange Tracer Diffusion

As discussed in the literature review (Section 3), electrical measurements do not provide any direct evidence for the dominant charge carrier, leading to doubt over the extreme enhancements reported. Electronic n and p type conductivity can be identified by the characteristic slopes when measuring the conductivity in variable pO_2, however the lack of these slopes in a Brouwer diagram does not necessarily prove the existence of oxygen ion migration. IETD is one method that allows direct observation of the diffusion of the oxygen species. By annealing the material in a gas enriched with a stable isotope of oxygen, ^{18}O, the concentration profile of the tracer isotope into the material can be used to calculate the diffusivity and hence the conductivity. Typically, the tracer distribution in a sample is mapped using SIMS, and therefore before the isotope exchange and diffusion methods are

discussed it is useful to briefly discuss the operation principles of SIMS.

4.5.1 Secondary Ion Mass Spectrometry

SIMS is an extremely useful and versatile technique which allows elemental and isotopic information on surfaces and near-surfaces of vacuum compatible solids. Essentially a surface is bombarded with a beam of ions resulting in sputtered species, of which a fraction will be ionised. These *secondary* ions are extracted and mass analysed.

When a high energy (between 10 and 40 keV) ion impacts a surface, kinetic energy is transferred to the lattice by a billiard-ball type collision, resulting in a *cascade* of collisions between the atoms in the solid. Some of the particles in the cascade will move deeper into the material causing intermixing, while others will be ejected from the surface. Approximately 95% of the secondary particles will originate from the top two layers of the solid and can be ejected up to 10 nm away from the initial point of impact [194].

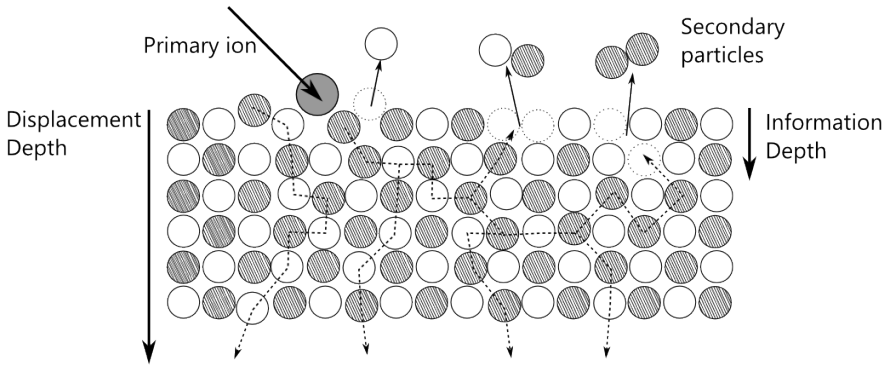


Figure 4.9: Representation of the SIMS process. Dashed lines represent the collision paths.

Ionization occurs at, or in close proximity to, the emission of the particles from the surface and is dependent on the electronic processes due to the surrounding matrix. Due to the complexity of the matrix effects at a surface the absolute quantification of species concentration at the surface is extremely challenging, if not impossible, using SIMS. However, isotopes of a single element are chemically undistinguishable and therefore should

act identically to each other, allowing a direct and quantifiable ratio between isotopes of the same elemental species. This is particularly relevant for tracer diffusion, where the relative ratio of oxygen ^{18}O and ^{16}O may be quantifiably mapped as a function of lateral distribution on the surface and as a function of depth.

Traditionally, SIMS operation is classified into two modes: *static* SIMS and *dynamic* SIMS. In dynamic SIMS, the dose density of the ion beam is high such that during the analysis, material from the surface is removed and that monitoring signals as a function of time will yield a distribution of the elemental species with depth. Static SIMS operates using a low dose density in a time scale that is very short with respect to the lifetime of the surface layer. Therefore, statistically no point on the surface would be impacted more than once and the surface can be thought of as static [194].

4.5.2 Time of Flight SIMS

The SIMS analysis carried out in this work was performed on a TOF.SIMS^5 time of flight SIMS instrument (ION-TOF Gmbh, Germany). This uses a Bi^+ liquid metal ion gun (LMIG) used to create secondary ions for analysis operating in static mode, combined with a second sputter gun emitting low energy, high current Cs^+ exclusively used for the removal of surface material, allowing depth profiles to be generated on acceptable time scales. The primary gun is pulsed, each pulse generating a packet of secondary ions, which are extracted perpendicularly to the sample surface with an electric potential of 2 kV entering a drift tube. In the drift tube the ions are separated according to their mass/charge ratio, and will arrive at different times to the detector accordingly. This can be performed for either the negatively or positively charged secondary ion species and is done while rastering the primary beam across the surface, as well as a function of depth using the sputter gun, thereby building up a three-dimensional image of the sample. The benefit of this method is that all masses are collected simultaneously, and therefore no *a priori* information about the species present is required. A low energy ($\sim$ 20 eV) electron gun is also often used to flood the surface avoiding the build-up of charge. A schematic of the instrument is shown in

Fig. 4.10

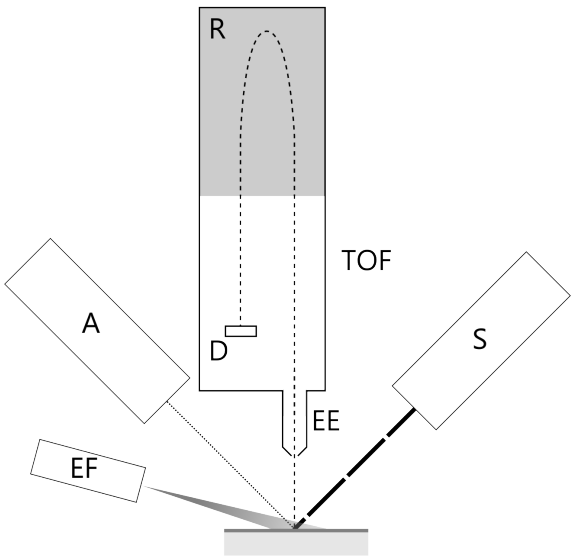


Figure 4.10: Schematic diagram of the TOF.SIMS^5 instrument. It consists of Bi^+ LMIG for analysis (A), low energy Cs^+ sputter gun (S), electron flood gun (EF), extraction electrode (EE) and time-of-flight mass spectrometer (TOF), with reflectron (R) and detector (D). The components are housed in an ultra-high vacuum (UHV) chamber. Taken with permission from Ref. [195].

The LMIG can operate in one of two modes, refered to in the ION-TOF nomenclature as *high current bunched mode* (HCBM) and *burst alignment* (BA). In HCBM, a ∼20 ns pulse of ions is sent through a condenser which bunches them to form a packet of ∼0.6 ns. This produces a high mass resolution ($m/\Delta m \sim 11,000$) and high signal yield, but at the expense of lateral resolution (2-10 μm) [131]. However, in this mode the primary isotope of oxygen, ^{16}O, will often saturate the detector when measuring oxides and lead to an incorrect calculation of the isotopic ratio [195].

Instead, the LMIG was operated in BA mode, where a long pulse (100 ns) is modulated with a MHz signal to cut several ∼1 ns bursts out of the larger packet. This allows the isotope ratio to be measured with high precision, in addition to improving the lateral resolution (∼250 nm) [131]. Both of these advantages are vital for mapping tracer diffusion in-plane profiles laterally in thin films. The drawback of BA mode is a reduction in mass resolution

in the low mass region ($m/\Delta m \sim 3500$), however for distinguishing between the ^{16}O and ^{18}O isotopes, this does not present a problem [195].

During the measurements in this work, the Bi^+ primary ion is rastered repeatedly over an area of the films surface (typically several hundred μm^2). Between each image acquisition the Cs^+ sputter gun is used to remove material from the sample, initially cleaning the surface followed by moving the analysis deeper into the film. The sputter area is kept substantially larger than the analysis region in order to avoid crater edge effects. The data analysis was carried out on the SurfaceLab software [196], and exported as two-dimensional data-sets for each species of interest in the x-y plane, x-z plane or y-z plane. Further analysis was then carried out in the MATLAB software [197].

The ^{18}O isotopic fraction was calculated according to

$$C = \frac{[^{18}O]}{[^{18}O] + [^{16}O]} = \frac{N^{18}}{N^{18} + N^{16}}, \tag{4.15}$$

where N^i, is the number of counts contained in the peak of the ^iO species.

4.5.3 Diffusion Theory

Diffusion was first put on a quantitative basis by Fick in 1855 [198], relating the rate of transfer per unit area of a section, F, to the concentration of the diffusing substance, C, the space coordinate measured normal to the section, x, and a diffusion constant, D.

$$F = -D\frac{\delta C}{\delta x} \tag{4.16}$$

Assuming one dimensional diffusion in an isotropic medium (i.e. if there is only a concentration gradient in the x axis), the change in the concentration with time may be derived.

$$\frac{\delta C}{\delta t} = D\frac{\delta^2 C}{\delta x^2} \tag{4.17}$$

Eqs. 4.16 and 4.17 are known as Fick's first and second laws of diffusion respectively. The diffusion constant of a species, i, with charge, q_i, and

concentration, n_i, is can be related to the conductivity, σ_i via the Nernst-Einstein equation:

$$D_i = \frac{\sigma_i kT}{q_i n_i}. \tag{4.18}$$

For the case of oxygen diffusion via a vacancy mechanism, it is possible to mistakenly attribute the concentration, n_i, to the available charge carriers, often quoted at the vacancy concentration ($[V_O^{\bullet\bullet}]$). But this is incorrect and the total concentration of the oxygen ions should be used. Here D refers to the self-diffusion coefficient, which is the diffusion of the oxygen ions in the lattice with no external driving force. Eq. 4.18 makes the assumption that the charge carriers move in such a way that the availability of mobile defects, as found at zero electric field, is unchanging by the presence of an external electrical bias and hence the diffusion coefficient is equal to the self-diffusion coefficient. If this is not the case a correlation factor must be introduced such that $D^\sigma = f_c D$.

In an IETD experiment, correlation effects arise for the tracer diffusion since the tracer ion can only hop into an adjacent vacant site. Therefore after a hopping event, there is an increased probability that the tracer ion will jump back into its original position. The difference between diffusion coefficients measured by tracer diffusion, D^*, and self-diffusion coefficients measured by electrical conductivity, D^σ, can also be related by a correlation factor, such that $D^* = f_D D$. The ratio of the two diffusion coefficients is known as the Haven ratio:

$$H_R \equiv \frac{D^*}{D^\sigma} = \frac{f_D}{f_c}. \tag{4.19}$$

Analytical solutions of the diffusion equations, Eqs. 4.16 and 4.17, can be obtained for a variety of initial boundary conditions providing the diffusion coefficient is constant. The challenge of accurately determining the diffusion coefficient by IETD, is to physically engineer a system where such conditions apply, while keeping the sample geometry suitable for SIMS analysis.

Tracer diffusion in bulk mono- and polycrystalline oxygen ion conductors is well established [199, 200]. Annealing a sample in isotopically enriched gas of a known concentration, a boundary condition is valid that specifies

the flux of the exchanging gas across the surface, $-D^*(\frac{\delta C}{\delta x})_{x=0}$, is directly proportional to the change in the ^{18}O concentration between the surface, C_s, and the gas, C_g, for a given time, t. The constant of proportionality is known as the exchange constant, k. This implies a set of boundary conditions, for which an analytical solution to Eq. 4.17 has been derived by Crank [201], given below as Eq. 4.20.

Due to the geometry and extreme aspect ratio of thin films, it is particularly challenging to design an experiment where the boundary conditions required for Eq. 4.20 to be valid will apply. Allowing the surface of the film to exchange and measuring a depth profile is possible, but because YSZ is surface limited, the concentration through the film thickness will be constant [117]. In addition this does not allow interfacial processes to be probed in-plane, and does not correspond to the direction of conduction in the EIS measurements (Fig. 4.8a).

Lateral diffusion has been measured in thin films by using a deposited Au layer to block the oxygen exchange with the surface, and cutting a trench into the film to create a well-defined region where ^{18}O may enter. This has been performed for $La_2NiO_{4+\delta}$ films [202], YSZ/STO multilayers [102], $Ba_{0.5}Sr_{0.5}Co_{0.8}Fe_{0.2}O_{3\delta}$ films [203], and YSZ/(Y_2O_3, YSZ/Sc_2O_3) multilayers [129, 130] with varying success.

Gerstl *et al.* [116, 117] developed a two-step tracer diffusion method and applied it to YSZ thin films. Here a blocking layer of Au was deposited onto the surface, but leaving a region uncovered such that there was a well-defined edge between the covered and uncovered regions. By annealing the sample at low temperature (300°C) in isotopically enriched gas, the authors showed it was possible to enrich the uncovered region of the sample, while minimising lateral diffusion. Therefore a step function in the ^{18}O profile between the two regions is created. Further annealing at a higher temperature (500°C) under vacuum, such that oxygen could not move in or out of the film[2], allowed the resultant profile to be fitted by another analytical solution to Eq. 4.17, also derived by Crank [201] labelled Eq. 4.21.

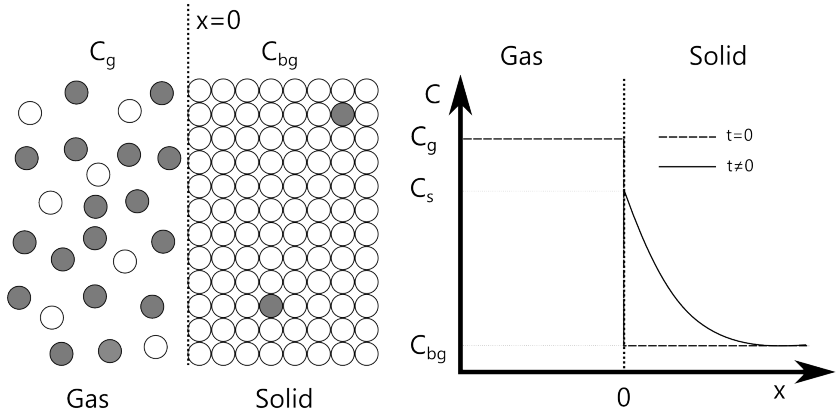
[2]It was assumed that YSZ would not reduce at such low temperatures.

Boundary Conditions 1:
At $t = 0$:
$C = C_g$, $x < 0$,
$C = C_s$, $x > 0$,
$C_g = constant.$

$$-D^*(\tfrac{\delta C}{\delta x})_{x=0} = k(C_g - C_s)$$

Solution 1:

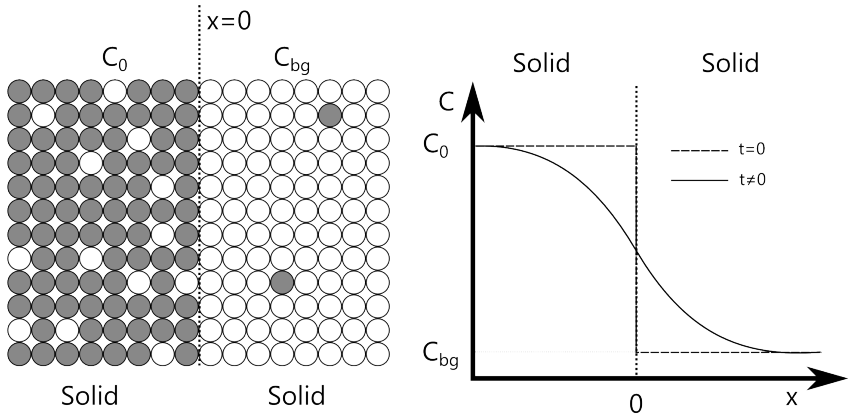
$$C'(x,t) = \frac{C(x,t) - C_{bg}}{C_g - C_{bg}}$$
$$= \operatorname{erfc}\left[\frac{x}{2\sqrt{D^*t}}\right] - \left[\exp\left(\frac{kx}{D^*} + \frac{k^2t}{D^*}\right)\right.$$
$$\left.\operatorname{erfc}\left(\frac{x}{\sqrt{D^*t}} + k\sqrt{\frac{t}{D^*}}\right)\right] \tag{4.20}$$



Boundary Conditions 2:
At $t = 0$:
$C = C_0$, $x < 0$,
$C = C_{bg}$, $x > 0$,

Solution 2:

$$C(x,t) =$$
$$= \frac{C_0 - C_{bg}}{2}\operatorname{erfc}\left(\frac{x}{2\sqrt{D^*t}}\right) + C_{bg} \tag{4.21}$$



4.5.4 Experimental Setup

The oxygen tracer diffusion method takes advantage of the natural abundances of the oxygen isotope species, as listed in Table 4.1. The ^{18}O isotope is ideal for this purpose, as it has a low natural abundance, and does not result in interference in the negative secondary ion spectrum from the $^{16}O^{1}H$ hydroxyl species which may exist in the residual gas in the SIMS instrument, which is the case for ^{17}O. Luckily the natural abundance of ^{17}O is low, and so interference from $^{17}O^{1}H$ species is negligible.

Isotope	Atomic Mass (amu)	Abundance (%)
^{16}O	15.995	99.762
^{17}O	16.999	0.038
^{18}O	17.999	0.200

Table 4.1: Atomic masses and natural abundances of the stable isotopes of oxygen. Data taken from [204].

A schematic of the experimental set-up used to introduce and diffuse the isotope tracer is shown in Fig. 4.11. The sample(s) was placed in a quartz holder, positioned next to a thermocouple inside a quartz tube. The tube was then evacuated to a pressure $< 5\times10^{-7}$ mbar, before gas enriched with the ^{18}O isotope was introduced. The pressure of the ^{18}O gas was kept to 200 mbar for all experiments, as this reproduces the pO_2 of an ambient air atmosphere. The position of both the sample holder and thermocouple could be moved inside the quartz tube, once it has been sealed.

A furnace suspended above the tube was pre-heated to the desired temperature and then lowered onto the tube, after which the sample holder was immediately moved within the tube to the hot-zone. Once the sample had been annealed for the desired time, it was removed from the hot-zone of the tube and the furnace raised off the tube. This facilitated rapid heating and cooling rates, allowing a well-defined anneal time. During this process the temperature was logged via a computer recording the thermocouple output. The effective anneal time and temperature were corrected according to the method introduced by Killoran [205], as discussed by De Souza *et al.* [206] for this application.

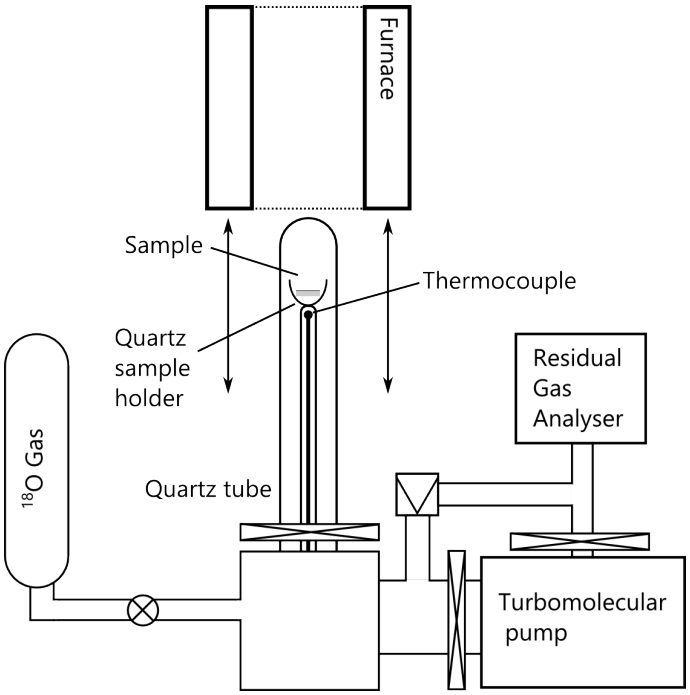


Figure 4.11: Schematic diagram of the experimental apparatus used to anneal films in isotopically enriched gas.

Once the ^{18}O enriched gas had cooled, a residual gas analyser (RGA) was used to check the concentration of the enriched gas which was >90% for all exchange anneals. Following this the gas was recovered into the storage reservoirs using molecular sieve sorption pumps for re-use.

4.5.5 Method Optimisation

Accurately obtaining diffusion profiles in thin films, such that a set of boundary conditions are valid allowing the profile to be fitted according to Eq. 4.20 or Eq. 4.21 is non-trivial. In this work a number of different exchange procedures and fitting methods were trialled and optimised to facilitate accurate, reliable and repeatable measurements of the diffusivity in-plane.

Boundary Conditions 1

In order to create an ^{18}O profile laterally in a film, such that it may be mathematically described by Eq. 4.20, requires the surface of the film to be blocking to the oxygen gas, but with an exposed edge allowing exchange. The surface blocking layer may be simply applied by depositing an Au film at room temperature via a sputter coater.

The most accurate and controllable way to expose an edge of the film would be to mill a trench through the Au layer using a FIB, however this would create substantial amorphous damage, which would prevent exchange with the ^{18}O gas. A commonly used method is to scratch the surface using a scalpel [202], diamond tipped scribe [102], or saw [203]. Fig. 4.12, shows images of a trench through a YSZ film with an Au blocking layer, created using a diamond tipped scribe. Substantial damage is done to the film creating an ill-defined rough edge. Surface roughness can dramatically alter the surface exchange coefficient, k, in YSZ [207], which can cause errors in the profile fitting. In addition the Au layer has peeled away from the film in a number of places due to poor adhesion with the film surface. This, combined with the shape of the trench creates an ambiguity as to where the exposed edge is ($x = 0$), which changes along the length of the trench. Ideally lateral maps of the ^{16}O and ^{18}O distributions are attained by SIMS and averaged over a large length in the y-axis to obtain a high signal-to-

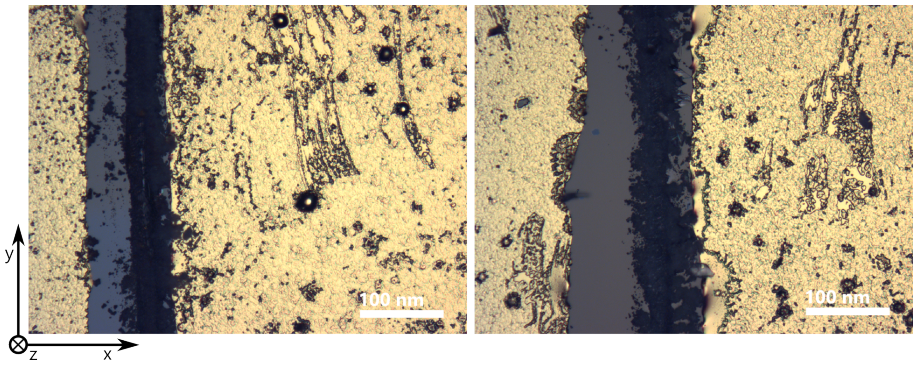


Figure 4.12: Trench through a Au layer and YSZ film created using a diamond tipped scribe.

noise ratio. However due to the shape of the exposed edge, this would lead to substantial errors for this method.

As an alternative to scratching the surface of the sample, a diamond saw was used to cut into the substrate from the opposite surface to that which the film was grown on. During the sawing, when the trench in the substrate became deep enough, the substrate/film would snap in two pieces, leaving a much sharper edge than that created by a scribe. The edge of a snapped film is shown in Fig. 4.13a. Optically the edge looks much more uniform than the scratch in Fig. 4.12, with no obvious roughening or delamination of the Au layer.

This sample was annealed in ^{18}O enriched gas for 2 hours at approximately 500°C. ^{18}O maps obtained from TOF-SIMS are shown in Figs. 4.13b and 4.13c. Despite a sharp edge observed by optical microscopy, the ^{18}O maps reveal that the exposed edge of the film is still markedly ill-defined, and a number of locally enriched regions around the edge of the film are seen most likely originating from pin holes in the Au blocking layer. The concentration gradient in the marked section in Fig. 4.13c, was used to assess the diffusivity and fitted according to Eq. 4.20, as shown in Fig 4.13d. Although the fit is reasonable by eye, it is difficult to ensure that over the area summed along the y-axis, the diffusion profile is uniform and that changes in the Au coverage are not leading to a lengthening of the profile, yielding an erroneously high D^* value.

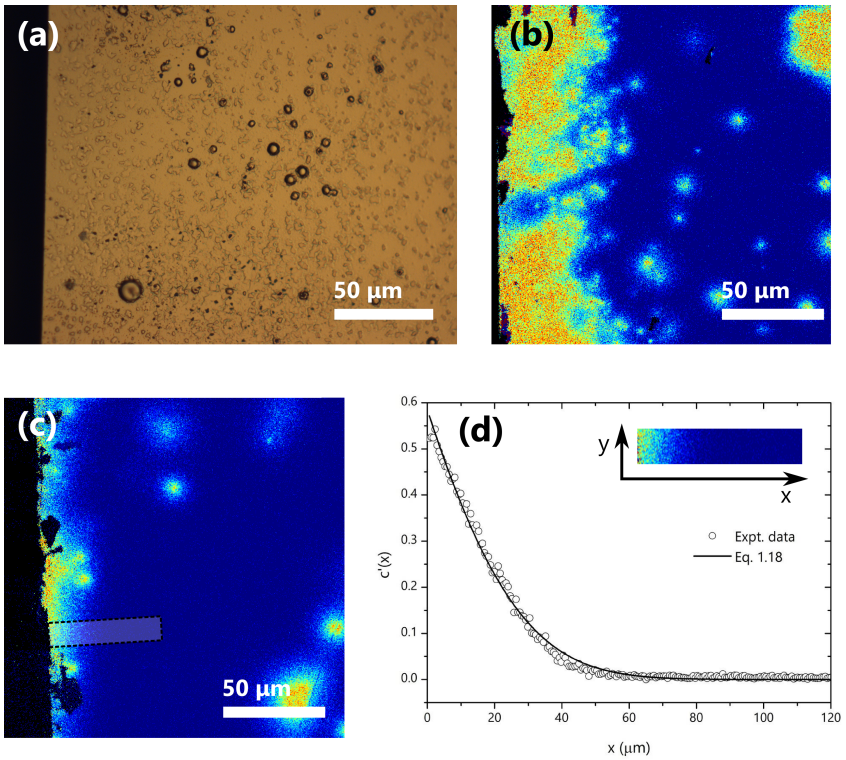


Figure 4.13: An optical image of the edge of a Au coated film snapped using a diamond saw (a). ^{18}O signal maps of the edge obtained by SIMS after exposure to isotopically enriched gas (b, c). Diffusion profile of the marked area in (b), fitted with Eq. 4.20 (c).

Additionally, both methods of creating an exposed edge of the film, rely on mechanically damaging the film, either by scratching the surface or via fracturing the film/substrate. The primary focus of this work is to study the effect of strain in thin films, yet both these methods may result in stresses applied directly to the region of interest. It would be much more preferable to create an oxygen profile in the film without any mechanical stresses applied.

Boundary Conditions 2

For a profile to be described mathematically by Eq. 4.21, at $t = 0$ the ^{18}O profile must be described by a step function where $C = C_0$ for $x < 0$ and $C = C_{bg}$ for $x > 0$. As proposed by Gerstl *et al.* [117], this could be

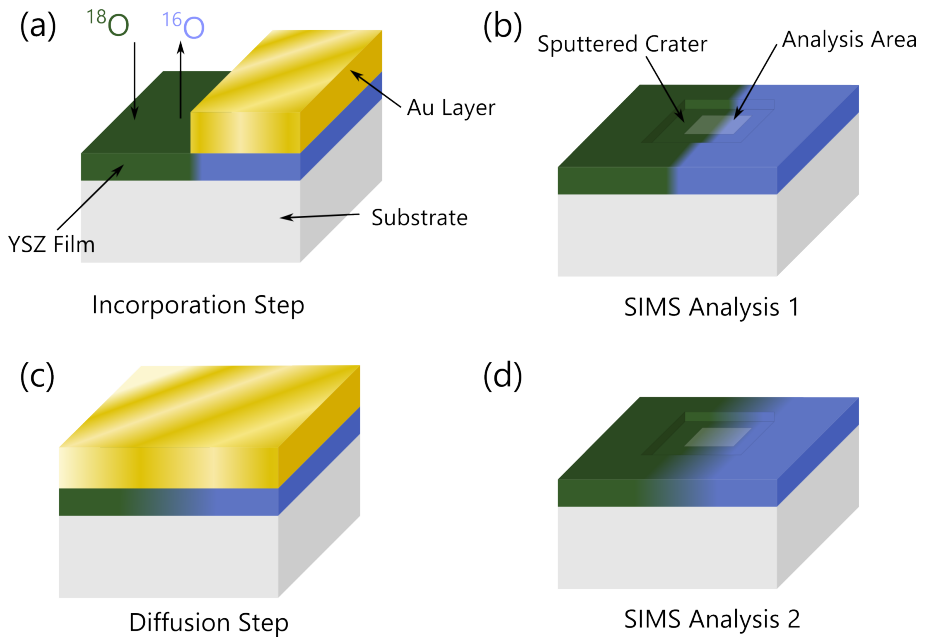


Figure 4.14: Schematic diagrams of the procedure used to create a ^{18}O diffusion profile in the films.

achieved by covering the film with a Au blocking layer, but leaving a part of the surface free such that there was a well-defined straight edge between the covered and free surface regions, as depicted in Fig. 4.14a. The film was then subject to a low temperature anneal at 300°C, referred to as the *incorporation step*. Next the Au layer was removed using adhesive tape and the ^{18}O profile mapped by SIMS analysis 4.14b, where the lateral diffusion could be shown to be minimal compared to the area of the SIMS maps.

Then another Au blocking layer was deposited onto the film, this time covering the entire surface such that oxygen could not move in or out of the YSZ (Fig. 4.14c). This was then annealed in the same furnace, but under vacuum and at 500°C, referred to as the *diffusion step*. Finally the Au layer was removed again and the ^{18}O concentration mapped by SIMS (Fig. 4.14d). The second SIMS analysis was always obtained in a different, but equivalent, area to first so that any beam damage induced by the first SIMS measurement did not affect the observed diffusion.

The Au layers were approximately 100 nm thick and were deposited at

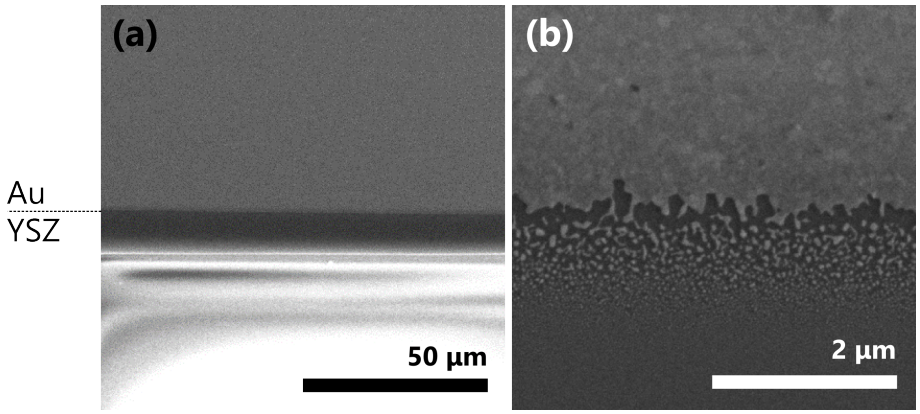


Figure 4.15: SEM micrographs of the Au edge created using a Omniprobe lift-out grid as a mask.

room temperature using a magnetron sputter coater (K575X, Emitech Ltd, UK or Q150T, Quorum Technologies Ltd, UK). A number of methods of masking the films were trialled, including razor blades, polyethylene terephthalate sheets, and Cu Omniprobe lift-out grids (Omniprobe Inc., UK) stuck down at the edges with Ag paste. It was found that the lift-out grids consistently yielded the best defined Au edge, as shown in the SEM images in Fig. 4.15 of such a Au layer after the incorporation step. There is no noticeable roughness of the interface over scales of several hundreds of μm (typical area size of SIMS map obtained), however the Au was found to ball up at the edge over an approximately 2 μm region, forming particles ranging from $\sim$100 nm to $<$50 nm. This region most likely occurs due to the Au layer thinning towards the edge of the film. This could be due to either shadowing effects from height of the mask, or the mask not lying flat on the film surface. The position of the Au edge was then marked using a FIB (FEI Helios NanoLab, FEI Company, USA), being careful not to damage any of the regions of interest with the ion gun.

Typical resultant ^{18}O profiles after the incorporation step, and the diffusion step are shown in Fig. 4.16a and Fig. 4.16b respectively. Commonly a sizable decrease in the ^{18}O concentration was observed after the diffusion step. The most likely cause for this would be diffusion into the substrate. Although nominally ionically insulating, only a short diffusion length into

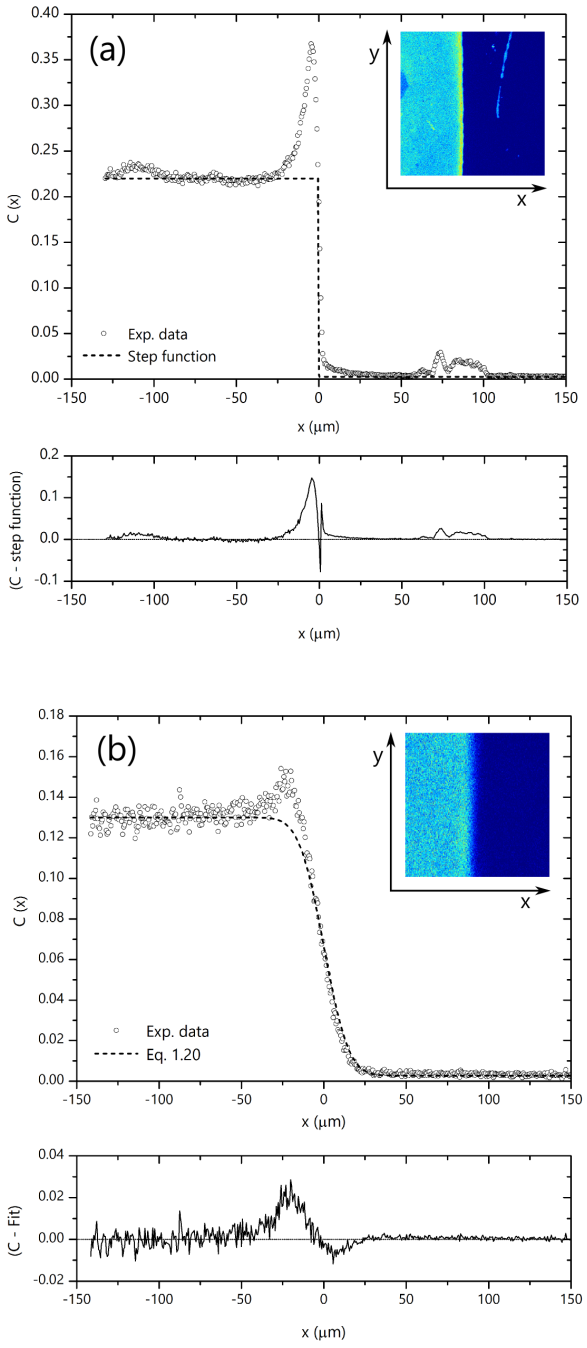


Figure 4.16: (a) normalised ^{18}O ratio after the incorporation step, compared to a step function. (b) the normalised ^{18}O ratio after the diffusion step, fitted using Eq. 4.21. The insets show the maps of the ^{18}O normalised concentration. Below are the differences between the real and idealised cases.

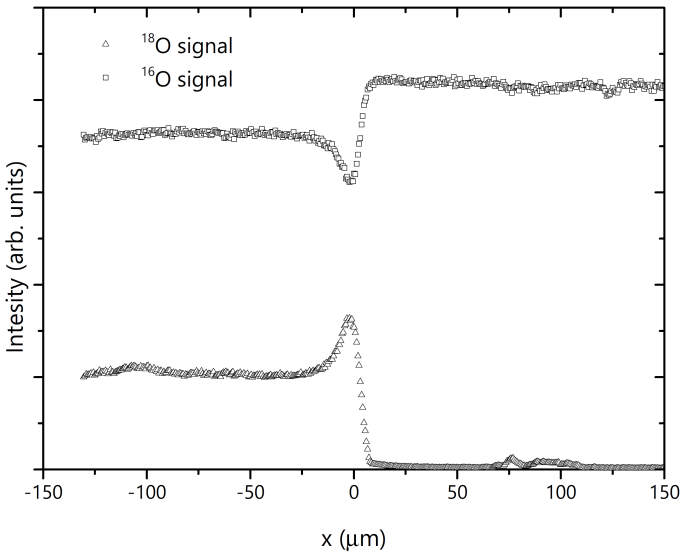


Figure 4.17: The raw ^{18}O and ^{16}O profiles for the data plotted in Fig. 4.16a.

the substrate would still significantly deplete the limited reservoir in the film. It is expected that the spike in the ^{18}O concentration at $x = 0$ is due to catalysis caused by the Au nanoparticles. Although Au is commonly thought of as chemically inert, when in the form of nanoparticles it has been shown to be a very active catalyst for the oxygen reduction reaction [208]. Alternatively, it is conceivable that the cause of the ^{18}O profile is due to residual Au nanoparticles left on the film surface during the SIMS analysis, leading to a change in the surface charging effects. A localised increase in the total ion intensity could lead to an incorrectly high ^{18}O concentration in that area. However, by plotting both the ^{18}O and the ^{16}O profiles as shown in Fig. 4.17, it can be seen that the ^{16}O, signal decreases at the Au interface signalling that the surface exchange is indeed enhanced by the Au nanoparticles.

The spike in the normalised ^{18}O concentration was observed for the majority of films measured using this method, however the size and shape of the enriched region was not consistent and varied for all specimen. Clearly the step function is not realised after the incorporation step, and therefore

the diffusion profile in Fig. 4.16b, cannot be accurately described by Eq. 4.21.

Numerical Fitting

By making the assumption that the areas measured after the incorporation step and diffusion step were equivalent after the incorporation step (i.e. that the Au interface is uniform along each edge), the initial profile may be used as the starting ^{18}O distribution and the final profile fitted numerically. Fig. 4.18 shows a concentration profile, divided into segments of width h, with C_1, C_2 and C_3 being the concentration at the neighbouring interfaces. The lines at R and S, denotes the midsections of the two adjacent layers.

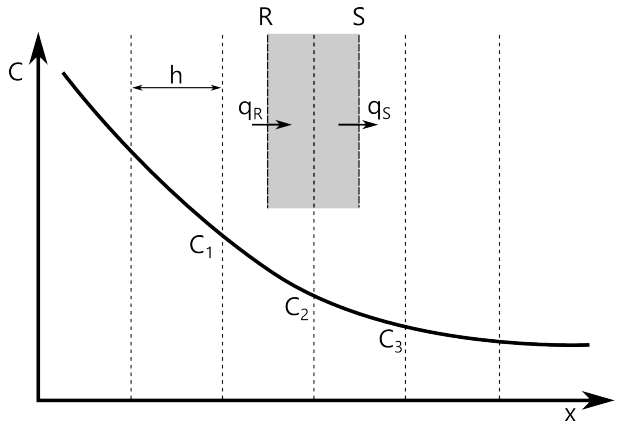


Figure 4.18: Concentration gradient as a function of x.

Recalling Ficks first law of diffusion (Eq. 4.16), it may be shown that in a short time, τ, the amount of diffusant entering the shaded region through the unit surface area R is given by

$$q_R = -\frac{D\tau}{h}(C_2 - C_1), \tag{4.22}$$

and similarly, the amount of diffusant leaving the shaded region through the unit surface S is given by

$$q_S = -\frac{D\tau}{h}(C_3 - C_2). \tag{4.23}$$

Hence the net amount of diffusant accumulating in the shaded region is

$$q_R - q_S = -\frac{D\tau}{h}(C_2 - C_1 - C_3 + C_2) = \frac{D\tau}{h}(C_1 - 2C_2 + C_3). \qquad (4.24)$$

Therefore, by taking C_2 to represent the average concentration of the narrow shaded region, the net change in the concentration of the segment can be approximated to

$$C_2' - C_2 = \frac{D\tau}{h^2}(C_1 - 2C_2 + C_3), \qquad (4.25)$$

where C_2' is the concentration at the end of the interval τ.

These calculations was performed in the MATLAB software using a home-written script. The profiles after the diffusion step were simulated for a range of D values, using the initial profiles as the starting concentration and the time of the diffusion step, t_{diff}. The goodness of fit was calculated using a χ^2 function, and the D values optimised to three significant figures. In addition to D as a fitting parameter, the simulated profiles were free to translate along the x direction to account for an offset in the centre position of the Au edge, and to multiply the entire set of y values by a coefficient to account for systematic errors in the calculated ^{18}O fraction and diffusion into the substrate between the initial and final profiles.

The width h, was taken as the width of a pixel. All maps taken in this work were (512 × 512) pixels. The time-constant, τ, needs to be sufficiently small to accurately simulate the resultant diffusion profile, however as τ is decreased the length of the calculation increases rapidly. Therefore, in order to optimise the τ values used, a simulated profile according to Eq. 4.21 (D^* =1.00×10^{-9} cm^2 s^{-1}, t_{diff} =5000 s, h =0.98 μm) was fitted numerically using a range of τ values. The numerically fitted D^* values are shown in Fig. 4.19, along with the relative error. From this it can be seen that there is minimal difference for $\tau \leq$0.05 s, and the error is close to ∼2%. Hence a value of τ =0.05 s is used in all the numerical fitting in this work, such that the calculations can be performed on acceptable time scales.

Fig. 4.20 shows the same profile plotted in Fig. 4.16b, here fitted numerically. The enriched area in the profile, occurring at the position of the

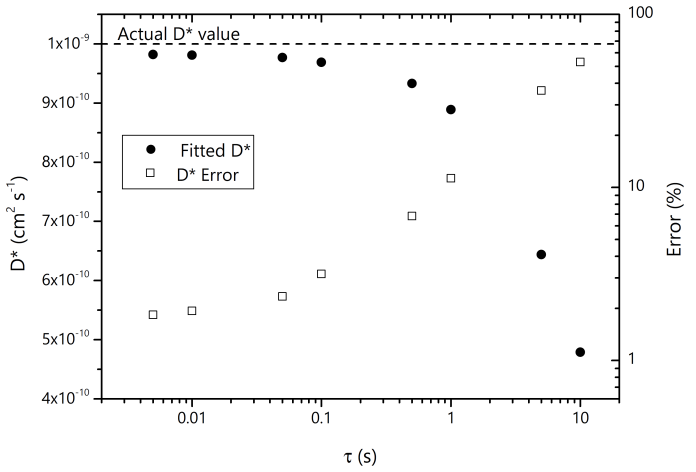


Figure 4.19: The effect of the time constant, τ, on the D^* values and relative errors of a numerically fitted profile which was simulated according to Eq. 4.21 with a D^* of 1.00×10^{-9} cm^2 s^{-1}.

Au interface is reproduced by the fitting procedure. The difference between the experimental data and the fit is plotted below, which is significantly improved compared to fitting by the empirical solution (Eq. 4.21) as in Fig. 4.16b. The poor agreement between the fitted and experimental profile around the $x \sim 25$ and $x \sim 225$ regions are due to artefacts in the initial profile as seen in Fig. 4.16a, are most likely originate from an imperfect Au blocking layer. However these regions are not included when fitting the data to obtain a D^* value.

The two step diffusion method, could be further optimised by extending the diffusion time, t_{diff}, from 2 hours (as it was in Figs. 4.16 and 4.20) to 14 hours, thereby lengthening the profile and reducing the error due to the focus of the SIMS analysis beam. As seen in Chapter 6, this also resulted in profiles similar in shape to Eq. 4.21 in some cases, reducing the sensitivity of the quality of fit on the initial profile after the incorporation step. This is beneficial, if there is a difference in the Au edge between the analysis areas used to obtain the profiles following the incorporation and diffusion steps.

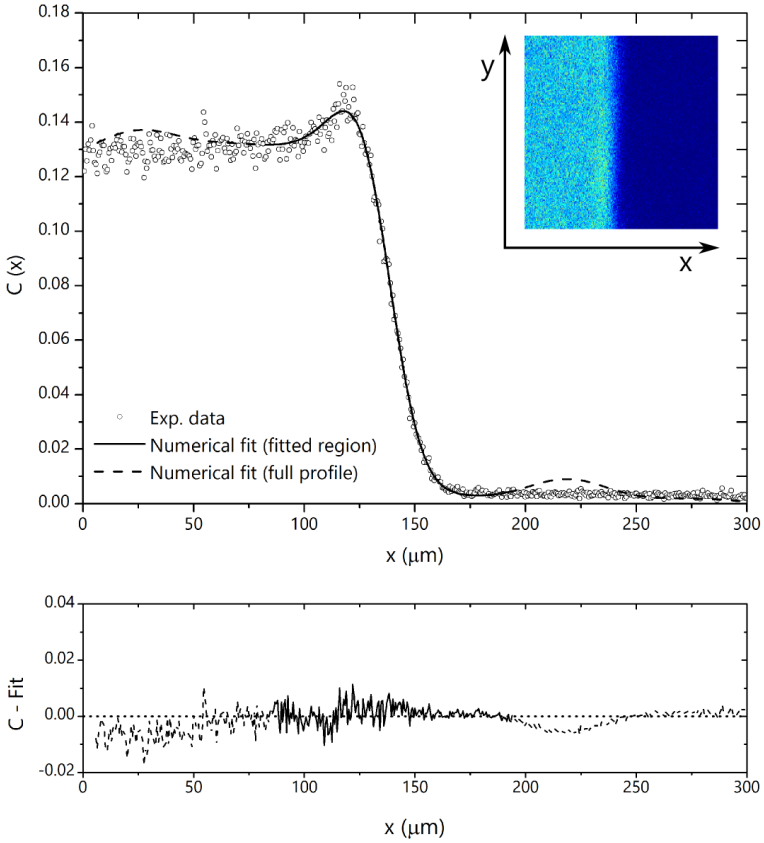


Figure 4.20: Normalised ^{18}O ratio after the diffusion step, fitted using Eq. 4.21. The insets show the maps of the ^{18}O normalised concentration. Below is the differences between the experimental data and the fit. The solid lines represent the region fitted using the χ^2 function, and the dashed shows the rest of the simulated profile for the final D^* value. Note that the x-axis is no longer centred at x =0, as it was in Figs. 4.16a and 4.16b, because this is no longer required for the numerical fitting procedure as it was for when fitting using the empirical solution Eq. 4.21.

4.6 Low Energy Ion Scattering

Low Energy Ion Scattering (LEIS) or Ion Scattering Spectroscopy (ISS) is an analytical tool which allows detailed information on the atomic composition of the surface of a material to be obtained. Noble gas ions (He^+, Ne^+, Ar^+) accelerated to a few eV, are elastically backscattered off a surface whereby the mass and the surface coverage of the scatterer can be inferred from the energy and intensity of the backscattered ions correspondingly.

In an elastic backscattering event the final energy (E_f) and the initial energy (E_I) of the projectile are related such that

$$E_f/E_i = K \tag{4.26}$$

where

$$K = \left(\frac{\cos\theta \pm \sqrt{\left(\frac{m_2}{m_1}\right)^2 - \sin^2\theta}}{1 + \frac{m_2}{m_1}} \right)^2 . \tag{4.27}$$

θ is the scattering angle, and m_1 and m_2 are the masses of the projectile and the surface atom respectively. The positive sign is taken when $m_2/m_1 \geq 1$ and both the positive and negative give solutions when $1 \geq m_2/m_1 \geq |\sin\theta|$. Furthermore, from Eq. 4.27, it can be shown numerically that backscattering ($\theta > 90°$) does not take place for scattering events where $1 \geq m_2/m_1$. Hence materials can only be probed with ions of a lower mass than that of the atoms present on the surface.

Artefacts in the spectra from diffraction effects due to crystal lattices in the target can be considered to be negligible as the de Broglie wavelength λ of the projectiles is far smaller than the periodic spacing in a lattice. Also, any contributions from phonons are essentially non-existent as the phonon energies are characteristically of the order of $\sim$0.03eV, which is typically around two orders of magnitude less than the energy resolution of the detectors used.

Unfortunately the surface coverage N_i of the atoms in the target of mass m_i is not the only factor to effect the yield of backscattered ions S_i, as shown

in Eq. 4.28 [209].

$$S_i = \frac{I_p}{e} t \xi R \eta_i N_i \tag{4.28}$$

I_p is the primary ion beam current, e is the elementary charge, t is the acquisition time, ξ is an instrumental factor, R is a factor that takes into account surface roughness and screening from neighbouring atoms and η_i is given by

$$\eta_i = P_i^+ \frac{d\sigma_i}{d\Omega} \tag{4.29}$$

where $\frac{d\sigma_i}{d\Omega}$ is the scattering cross section and P_i the probability of the projectile ions neutralising during the scattering event and hence becoming undetectable.

Although neutralisation may seem like an undesirable side effect during ion scattering acting only to reduce the intensity of the signal, it is actually this phenomenon that allows LEIS to be used as an almost exclusively surface sensitive technique. As the probability for neutralisation is high (∼5-10%) this dramatically reduces the likelihood of a projectile scattering off deeper layers by an order of magnitude in comparison to the surface. Neutralisation (and subsequent re-ionization) may occur through a number of routes such as resonant processes including the transitions between the target conduction band and the projectile (resonant neutralization), and transitions between the bound levels in the target atoms and the projectile (quasi-resonant neutralization), or via Auger neutralisation processes, whereby an electron fills the ground state of the projectile either directly or indirectly from the target conduction band. For most projectile-target combinations these lead to Eq. 4.29 acting as a well behaved function, however one must be careful that more complex energy dependent oscillations are not occurring. Fortunately many combinations of surfaces and projectiles have been studied and the presence or absence of complex neutralisation effects compiled and reported [209].

In theory, for absolute quantification of the surface composition each of the terms in Eq. 4.28 must be calculated or experimentally determined. Therefore it is common practice to instead normalise the intensity of the peaks corresponding to the species on the target to elemental standards or surfaces with known compositions under the same scattering conditions,

assuming a linear relationship between the yield and surface concentration.

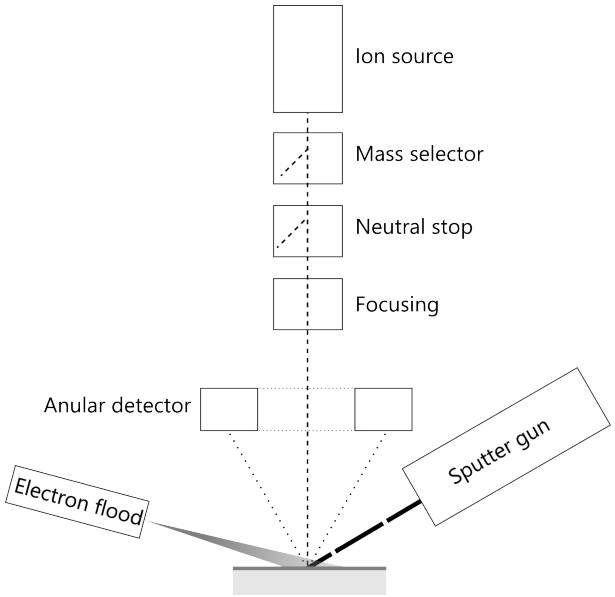


Figure 4.21: Schematic of the components in a typical LEIS set-up.

The basic components comprising a typical LEIS set-up are shown in Fig. 4.21 and operates at ultra-high vacuum (UHV). The ions are produced from either a pure gas or gas mixture and fed through a mass filter to isolate the one required and to insure the beam consists of a single isotope for the case of Ne. A neutral stop is implemented as neutrals in the beam would contribute to the LEIS signal but not the current measurement necessary for the I_p term in Eq. 4.28. Finally the beam is focused onto the surface on the sample and rastered over an area of the order of 1 mm^2 and the backscattered signal recorded by an electrostatic analyser (ESA) and detector. The ESA differentiates between the range backscattered energies via an anisotropic electric potential and tends to operate at a fixed scattering angle θ while accepting a high azimuth window.

Hydrogen based compounds adsorbed to surface can shield the signal coming from the surface atoms underneath as hydrogen is for all purposes invisible in LEIS due to its mass being less than the lightest of the noble gases. To combat this atomic oxygen cleaning can be performed which reacts strongly with hydrogen and acts to remove it from the surface. This

technique is also effective at removing carbon contamination at the surface, which occurs on samples even when kept for lengthy periods at UHV.

LEIS was carried out on a Qtac^{100} instrument (ION-TOF Gmbh, Germany), with a double toroidal analyser detecting scattered ions at 145°. Atomic oxygen cleaning was carried out in a preparation chamber adjacent to the instrument, such that the vacuum was not broken resulting in further surface contamination from the laboratory atmosphere. In addition a secondary argon ion sputtering gun, with an energy of 500 eV, oriented at 59° to the sample surface was employed, to remove surface material, thereby obtaining spectra as a function of depth. To prevent charging of insulating materials, low energy electrons (10 eV) were flooded over the sample surface during the measurements. In this work, ^{4}He and ^{20}Ne primary ions were used, with energies of 3 keV and 5 keV respectively, and the analyser pass energy maintained at 3 keV for all analyses.

As in SIMS, the primary ion will still cause sputtering processes at the surface of the sample, despite the lower energy. Therefore to maintain surface accuracy, the total dose of each analysis spectra was kept below the static limit of 5×10^{14} ions/cm^2 for ^{4}He and 5×10^{13} ions/cm^2 for ^{20}Ne projectiles [210].

4.7 Summary

The details of the experimental techniques employed in this work have been described in this chapter. Specific details about the experimental set-ups and equipment were given at the end of each respective section.

Substantial effort has been made in this work to develop a reliable and accurate method for carrying out IETD in thin film samples. Hence particular attention was paid to the IETD technique, and much of this effort has been detailed.

Chapter 5

Orientation and Lattice Strain of YSZ Films

As mentioned in Chapters 3 and 4, the structural and transport properties of films grown by PLD are highly dependent on growth conditions, thermal history and substrate pre-treatment. In this chapter, the effect on the film orientation due to the substrate properties and growth temperature will be discussed. The effects of substrate roughness, homo-epitaxial buffer layers, thermal pre-treatment, and surface miscut were investigated as well as effect of growth temperature. Additionally the influence of growth temperature and thermal history the films on the lattice parameter was also investigated. Although the focus of this work as a whole, was not to study the growth mechanisms of films synthesised by PLD, the ability to consistently fabricate well defined systems is essential to investigate the transport and segregation properties, which are the subjects of Chapters 6 and 7.

5.1 Sample Production

The films discussed in this chapter were fabricated by means of PLD using the set-up described in Section 4.1 by the author and Dr Andrea Cavallaro. All the films fabricated were grown from an 8 mol.% YSZ target, as detailed in Section 4.1.2. All films in this chapter were grown with 1500-6000 pulses, keeping all other conditions identical unless stated, and therefore no sub-

stantial difference in the thickness should be expected. However it should be noted that these films were grown over a long period of approximately two years, and therefore slight changes in the laser alignment cannot be excluded. The substrates used were (001) oriented MgO and (0001) oriented Al_2O_3 (MaTeck Material Technologie & Kristalle GmbH, Germany). The atomic force microscopy (AFM) and SEM in this chapter were also carried out by Dr Andrea Cavallaro.

5.2 Orientation Manipulation

In Section 3.1.2, the reported modification in the transport properties of YSZ when it is grown in the form of a thin film were discussed. Two of the most dramatic enhancements in the conductivity, were reported by Kosacki *et al.* [106, 107] and Sillassen *et. al.* [115], using MgO as a substrate. In both cases cube-on-cube epitaxial growth was observed with a high density of misfit dislocations at the interface such that the orientation was described by:

$$\text{YSZ } (001)||\text{MgO } (001)$$
$$\text{YSZ } [100]||\text{MgO } [100]$$

In addition, Jiang *et al.* [119] also observed enhanced conductivity for YSZ films grown on Al_2O_3 substrates where the following orientation was observed:

$$\text{YSZ } (111)||Al_2O_3 \ (0001)$$
$$\text{YSZ } [110]||Al_2O_3 \ [10\bar{1}0]$$

As interface effects are often thought to be cause for modified transport properties in YSZ films, it follows that the orientation relationship between the films and substrate may play a significant role. Therefore the ability to replicate films in these orientation is critical to understand the causes for such modified transport. In addition, films with a single orientation are much better defined than those with multiple orientation relationships.

Therefore interface and grain boundary properties as observed by TEM on a small section of the total sample can then be assumed to be representative of the whole sample.

5.2.1 Substrate Pre-treatment

Film structure is highly dependent on the growth mechanisms which can be significantly influenced through the surface morphology of the substrate. Therefore the substrate surface structural and chemical properties would expected to have an effect on the growth orientation. Here we study the effects of substrate surface roughness, homo-epitaxial buffer layers, pre-growth heat-treatment and substrate miscut on the orientation of the subsequently grown films. All YSZ films referred to in this section were grown at a nominal substrate temperature of 700°C.

Substrate Roughness

8 mol.% YSZ films were grown under identical conditions onto MgO substrates with varying roughness. Both the polished side of the substrates that had a root mean square (RMS) roughness of >3 nm according to the manufacturers note, and the unpolished side were used. Fig. 5.1a shows an SEM micrograph of the un-polished MgO surface. The extent of the roughness was characterised by AFM as shown in Fig. 5.1b and 5.1b, and observed to have a RMS of >800 nm.

Typical XRD $\theta/2\theta$ spectra of the YSZ films grown on the polished and unpolished substrates are shown in Fig. 5.2. The high signal-to-noise ratio for both films indicates that the layers were crystalline directly after deposition. Both films are highly textured displaying only one out-of-plane orientation each, however the preferential orientation switches from (111) for the polished substrates to (100) for the rough substrates.

To investigate the in-plane orientation of the films, XRD pole figures were obtained for the YSZ films. The signal intensities for the (220) YSZ and (220) MgO reflections are shown in Figs. 5.3a and 5.3b for the film grown on the polished substrate, and in Figs. 5.3c and 5.3d for the film grown on the unpolished substrate. In Fig. 5.3a twelve well-defined maxima are

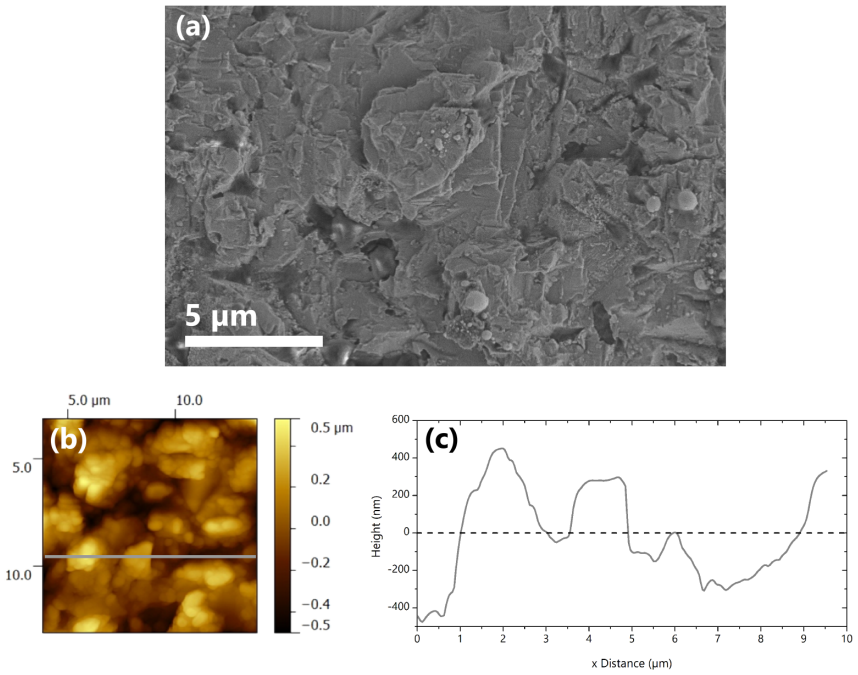


Figure 5.1: (a) SEM micrograph and (b) AFM image of the unpolished MgO surface. (c) height profile along the grey line shown in the AFM image.

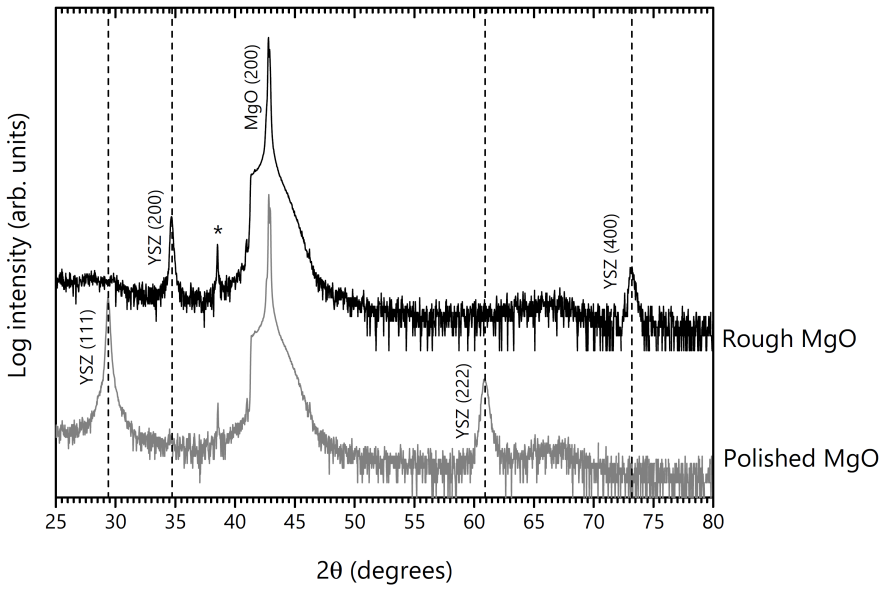


Figure 5.2: XRD $\theta/2\theta$ spectra of the YSZ films fabricated using substrates of different roughness. The peaks marked with $*$ are due to a reflection from the substrate peak coming from the Kβ radiation component.

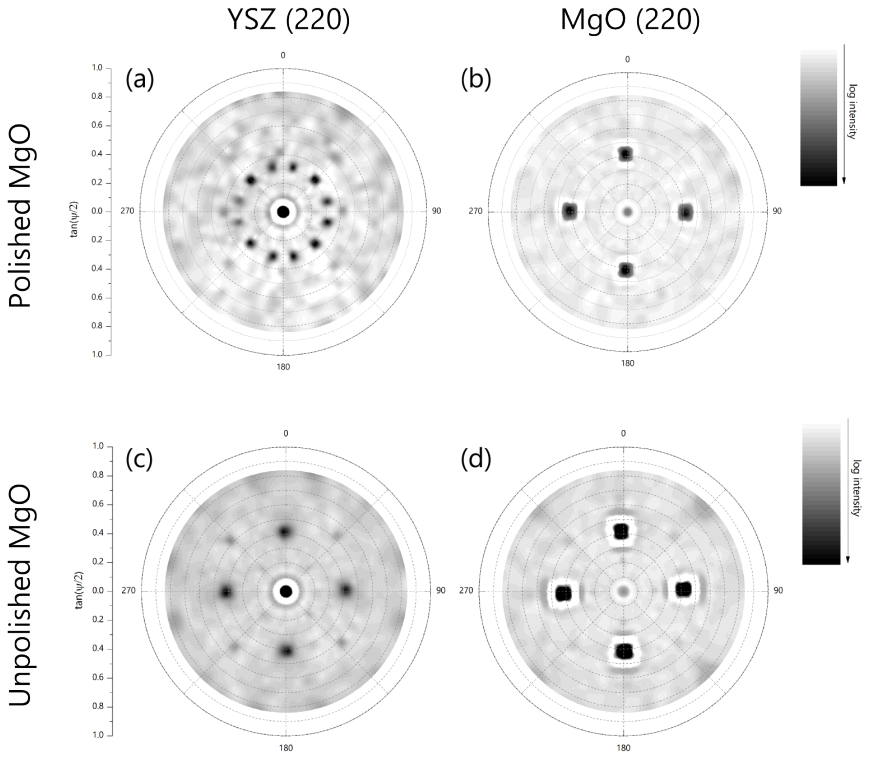


Figure 5.3: XRD pole figures for the YSZ (220) and MgO (220) reflections for the films grown on polished and unpolished MgO substrates.

visible at ψ ~35°, separated by 30° each in ϕ. This indicates a preferential in-plane orientation also exists for these films, as a uniform ring at the tilt angle would be present if this were not the case. The ψ of 35° corresponds to the interplaner angle of 35.3° expected from (111) planes aligned parallel to the surface of the film, in agreement with the $\theta/2\theta$ scans. A single in-plane orientation would yield three maxima at this ψ, and therefore four in-plane orientations must be present. From the $\theta/2\theta$ spectra (Fig. 5.2) and by comparing the orientations of the (220) YSZ and (220) MgO pole figures for the films grown on a polished substrate, the following orientation can be inferred:

(I) YSZ (111)||MgO (001)

(i) YSZ $[11\bar{2}]$||MgO $[1\bar{1}0]$
YSZ $[\bar{1}10]$||MgO [110]

(ii) YSZ $[11\bar{2}]$||MgO [110]
YSZ $[\bar{1}10]$||MgO $[\bar{1}10]$

(iii) YSZ $[11\bar{2}]$||MgO $[\bar{1}10]$
YSZ $[\bar{1}10]$||MgO $[\bar{1}\bar{1}0]$

(iv) YSZ $[11\bar{2}]$||MgO $[\bar{1}\bar{1}0]$
YSZ $[\bar{1}10]$||MgO $[1\bar{1}0]$

The case is different for the YSZ films grown on unpolished substrates, where in Fig. 5.3c only four maxima were observed at ψ ~45°. These correspond to an interplanar angle of 45°, expected due to the (100) plane parallel to the film surface, again in agreement with the $\theta/2\theta$ scans. Here only four maxima are observed again indicating highly textured in-plane growth. In addition, the four reflections positioned at the same ϕ as the substrate maxima in Fig.

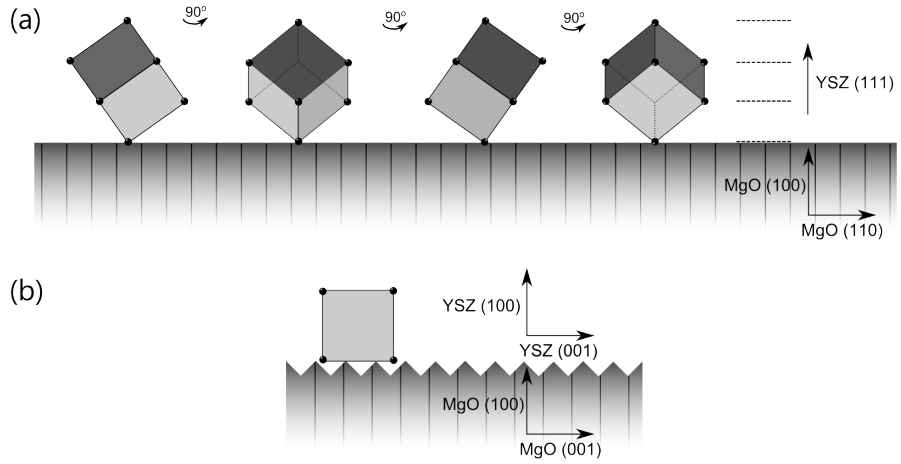


Figure 5.4: Schematic representation of the orientation relationships for the YSZ films grown on (a) polished and (b) unpolished MgO substrates.

5.3d, implying cube-on-cube growth. Therefore the orientation relationship for the YSZ grown on unpolished MgO is given by:

$$\begin{aligned} \text{(II) YSZ (001)}&\text{||MgO (001)} \\ \text{YSZ [100]}&\text{||MgO [100]} \end{aligned}$$

For clarity, a schematic of the two orientation relationship for the varying roughness is shown in Fig. 5.4.

Figs. 5.5a and 5.5b, show SAED obtained for the YSZ films grown on the polished and unpolished substrates respectively, taken over a large area containing the entire film. These confirm the orientation relationships obtained by the XRD results. In Fig. 5.5a, only the (111) spots are seen perpendicular to the interface plane due to the zone axis being aligned with the [100] MgO plain and therefore no in-plane Bragg reflections are observed. For the rough MgO substrate, the alignment of the two lattices is apparent in Fig. 5.5b, however the spots are not well defined and there is a slight tilting between two lattices. This could be due to misoriented grains in the films with respect to one another and the substrate lattice, a buckling of the

TEM lamella during FIB milling, or a combination of the two.

The TEM micrographs in Figs. 5.5c and 5.5d show columnar growth for both types of film, which is typical for layers grown by PLD. The sizes and distribution of the grains in the fabricated films will be discussed in detail in Chapter 6 with respect to the transport properties. The images in Fig. 5.5d show the extreme nature of the surface topography compared to the thickness of the thin film, when grown in an unpolished substrate. As indicated by the dotted line, variations in film thickness are observed over the length of the TEM sample, the lack of uniformity making it difficult to accurately describe the system geometrically.

HR-TEM images of the interfacial region are shown in Figs. 5.5e and 5.5f. The lattice imaging also confirms the orientations observed for the films from XRD and SAED. The interfaces are observed to be sharp for both films, with no sign of amorphisation or regions with a crystal structure differing from YSZ or MgO. In Fig. 5.5e, the arrows indicate the direction of the lattice fringes revealing a low angle grain boundary between the columnar grains. This is a typical example of those commonly found during the TEM investigation, in most cases oriented with respect to the growth direction. The acute misorientation is the reason the grain boundaries have little influence on the XRD and SAED results. The inset in Fig. 5.5f shows a fast Fourier transform (FFT) filtered image of the highlighted interfacial area using the YSZ (010) and MgO (010) reflections. A high-density dislocation network is observed at the interface. Due to the in-plane orientations of the film grown on polished MgO, no lattice fringes perpendicular to the interface are visible (Fig. 5.5e), and therefore the presence of a dislocation network could not be confirmed.

The orientation between the substrate and film observed for the YSZ grown on unpolished MgO is the same as that observed by Kosacki *et al.* [106, 107] and Sillassen *et. al.* [115] for the YSZ/MgO films reported to have dramatic enhancements in the conductivity. In addition, a high density of dislocations are observed at the interface as shown to be the case for the films grown by Kosacki *et al.* by Korte [110], and for the films fabricated by Sillassen *et. al.*. Therefore this orientation is ideal for reproducing these previous studies in order to confirm there transport measurement by

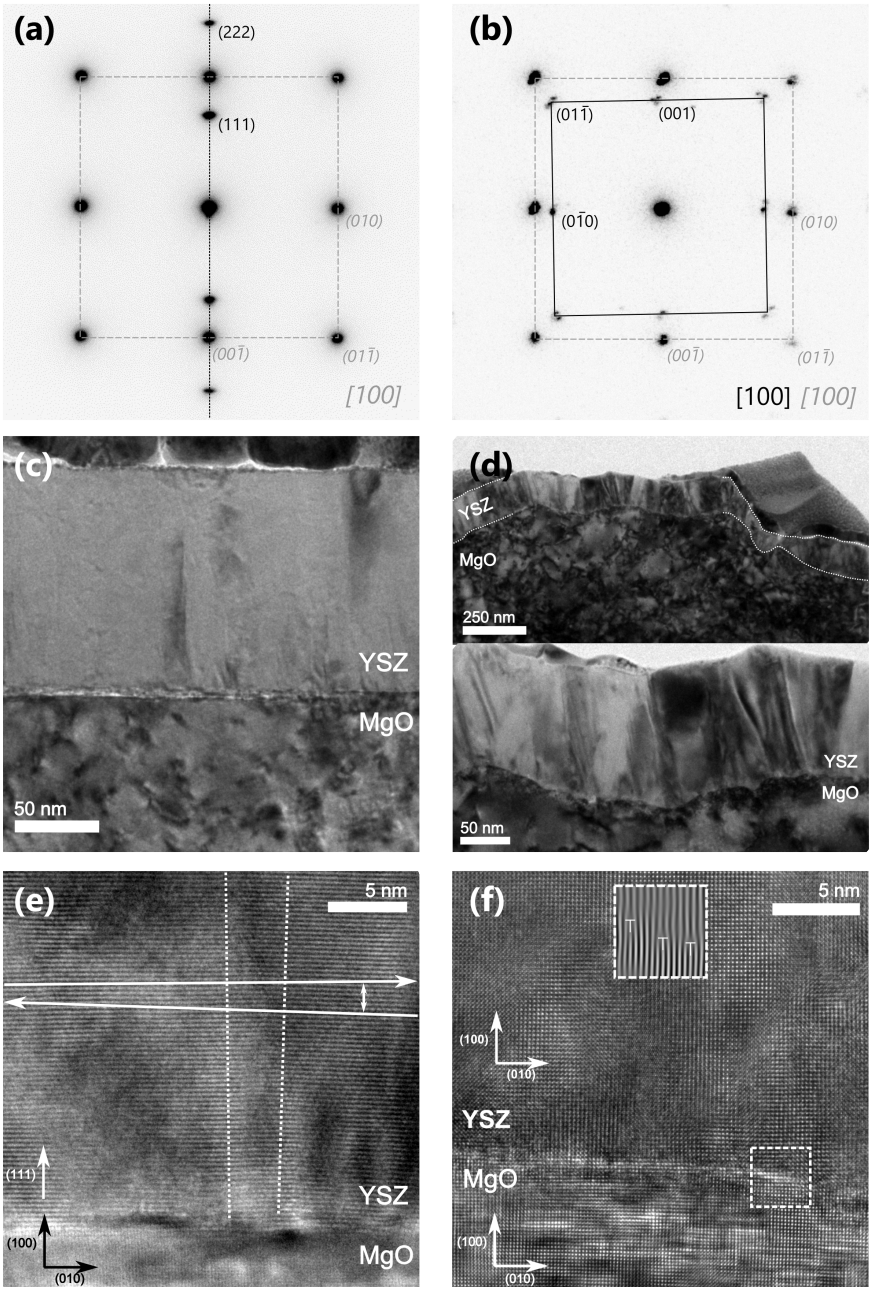


Figure 5.5: (a), (c), and (e) are of a YSZ film grown on a polished MgO substrate, and (b), (d), and (f) are of a YSZ film grown on an unpolished MgO substrate. SAED of the films are shown in (a) and (b), with the spots indexed. The grey/italic indices refer to the substrate reflections, the black/non-italic indices refer to the film reflections, and square brackets refer to the beam direction. (c), (d), (e) and (f) are TEM micrographs of the films. In (e) and (f), the lattice spacings correspond to the planes labelled on the images. The inset in (f) shows a FFT-filtered image of the marked region, displaying the presence of interfacial dislocations.

IETD and assess the effect of dislocation networks of the ionic conductivity. However, the extreme roughness as shown in Fig. 5.5d, means that it would be hugely challenging to correctly assess the transport electrically because of the uncertainties in the current path and by IETD due to the impracticalities of creating a well-defined Au blocking layer. Therefore, in the next section, the attempts to recreate this orientation on microscopically flat MgO substrates will be presented.

Homo-epitaxial Buffer Layers

Polishing is known to cause extensive damage to the surface region of MgO single crystals, which may be reduced by a high temperature thermal anneal [211, 212]. However, it has been shown that for MgO (100) single crystals, a 200 ppm bulk concentration of calcium can lead to an equilibrium segregation of 20% occupation of the surface cation sites [69]. With this in mind, it is likely that at the time of deposition the surface of the MgO substrates is either structurally or compositionally different from the bulk crystal or a combination of the two.

In order to increase the crystal quality of the substrate surface, and to minimise the effect of bulk impurities, homo-epitaxial MgO buffer layers were deposited by PLD onto the as-received substrates immediately prior to the YSZ films. While depositing at high temperature should lead to a higher quality crystalline buffer layer, this would also increase the extent of impurity segregation which should be depressed at lower temperatures due to reduced cation mobilities. Therefore MgO buffer layers were deposited at both 500°C and 850°C to observe any difference in the subsequent properties of the YSZ films.

Fig. 5.6, shows the XRD $\theta/2\theta$ spectra of the YSZ films grown on as-received polished MgO and homo-epitaxial buffer layers grown at 500°C and 850°C. There is very little noticeable difference between any of the spectra, each being dominated by the (111) and (222) reflections from the YSZ films.

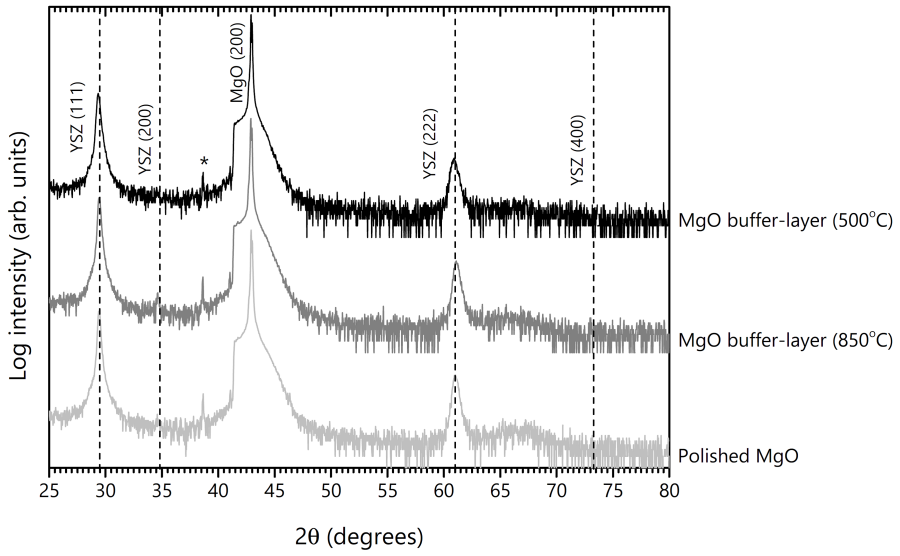


Figure 5.6: XRD $\theta/2\theta$ spectra of the YSZ films grown on as-received polished MgO, and onto homo-epitaxial buffer layers grown at 500°C and 850°C. The peaks marked with $*$ are due to a reflection from the substrate peak coming from the Kβ radiation component.

Substrate Heat-treatment

It has been shown that the surface morphology of as-received MgO substrates is affected by high temperature heat treatment in the range of 700°C to 1250°C [213]. Step-and-terrace structures were observed to vary in step height and density upon thermal annealing and various temperatures. From the effects of MgO surface roughness on the YSZ growth orientation, one would expect that either a high density of steps or a large step height would facilitate (100) oriented YSZ films. In order to assess this, MgO substrates were annealed in pure flowing O_2 gas at a range of temperatures and times, prior to deposition and the orientation of the YSZ films studies by XRD.

From the XRD $\theta/2\theta$ patterns, the YSZ (200) and YSZ (111) reflections were fitted using a pseudo-Voigt function in the FullProf software to obtain the peak areas I_{200} and I_{111} respectively, such that the volume fraction of the (100) oriented grains, f_{100}, could be calculated according to

$$f_{100} = \frac{R\, I_{200}}{R\, I_{200} + I_{111}} \tag{5.1}$$

where R is the reference intensity ratio, and is calculated by $\frac{I_{200}+I_{111}}{I_{200}}$ for the powder diffraction pattern and taken to be 4.717 (Fig. A.1 in Appendix A.1). One must be careful using this method to estimate the volume fraction of the various orientation as any slight misorientations of the grains with the substrate could yield erroneous results. However in this context it is only used as an estimate of the degree of preferential orientation.

Fig. 5.7 shows the (100) orientation fraction of the YSZ films grown on MgO substrates which had been annealed in the temperature range of 900°C to 1100°C for two hours. On occasion, close to 100% (100) orientation is achieved, however this was not found to be reproducible. Indeed for all heat treatments which were repeated, the orientation was not found to be reproducible.

For a heat-treatment of 1000°C, two of the four trials yielded >99% (100) oriented YSZ films. To test the effects of kinetics on MgO surface treatment at this temperature, the heat-treatment was performed for a number of anneal times as shown in Fig. 5.8. The (100) orientation fraction increased

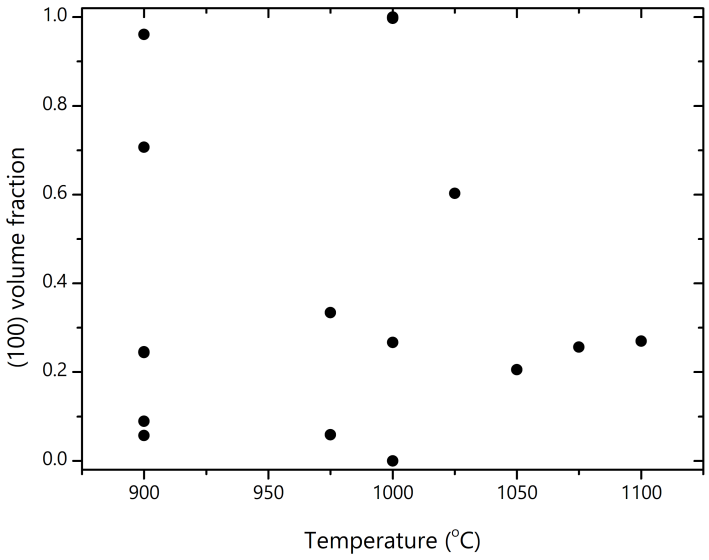


Figure 5.7: Calculated volume fraction for the (100) oriented grains form YSZ films grown on MgO substrates heat-treated at a range of temperatures for 2 hours.

for longer heat-treatments, but even for ten hours a fully (100) oriented film could not be achieved. In addition, the results were also not found to be consistently repeatable.

5.2.2 Substrate Miscut

The density and height of steps and terraces at the MgO surface is dependent upon the miscut of the substrate, δ, that is the angle between the surface and the (100) planes. This was not checked prior to the deposition of the films, and therefore may provide an explanation of the poor reproducibility observed in the orientation. To investigate this effect, the substrate miscut was measured for a selection of the YSZ films in which different (100) orientation fractions were observed for identical pre-treatments. The procedure used to calculate the miscut angle is described in Section 4.2.3.

Fig. 5.9 shows the fraction of the (100) grains for the calculated miscut angles. Films grown on polished and heat-treated substrates were measured. For the as-received polished MgO substrates, a higher miscut yielded a lower

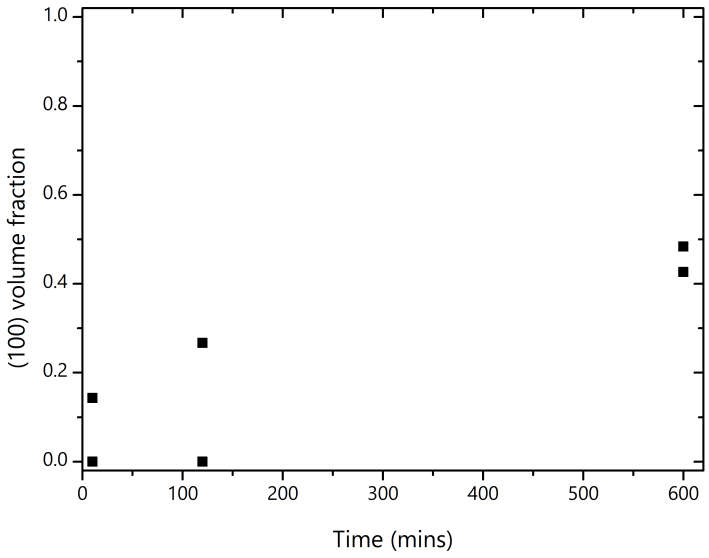


Figure 5.8: Calculated volume fraction for the (100) oriented grains form YSZ films grown on MgO substrates heat-treated at a 1000°C for a range of times.

fraction of the (100) orientation, but for the MgO which had been heat-treated, a higher miscut improved the (100) orientation fraction. It can be seen that in isolation, the substrate miscut does certainly not explain the varying orientations observed in the films. However it may be possible a high miscut angle combined with a thermal pre-treatment are required to yield a surface structure ideal for cube-on-cube growth for YSZ films.

5.2.3 Substrate Temperature

During the PLD process the substrate temperature will affect the mobility of the deposited species on the surface. It has been shown for YSZ and CGO films grown by PLD, that the microstructure can be significantly altered due to the temperature of the substrate [164]. Here, the substrate temperature during the deposition was varied, to observe the effect on the film orientation. Fig. 5.10, shows the calculated (100) oriented volume fraction of YSZ films grown on as-received MgO and Al_2O_3 substrates for a range of temperatures, keeping all other conditions identical.

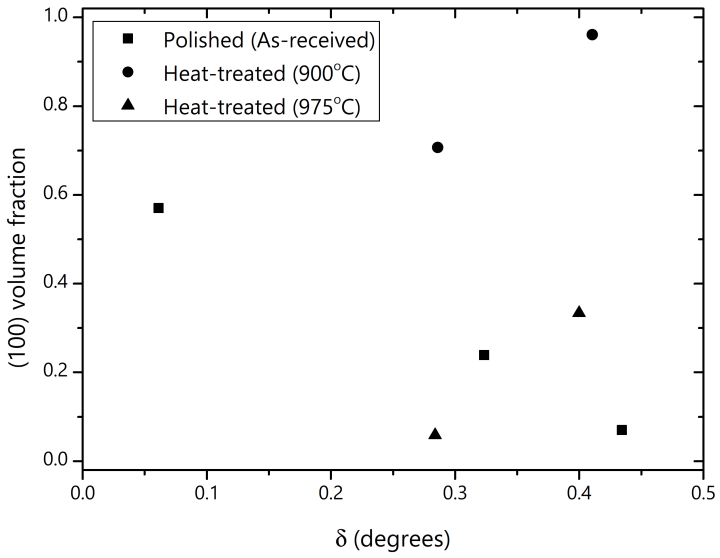


Figure 5.9: Fraction of (100) orientation for YSZ films against the miscut angle of the MgO substrates, δ.

For YSZ grown on MgO, the vast majority of the films have a predominant (111) orientation, regardless of temperature. A far larger number of films were grown at 700°C, for the purpose of assessing transport properties as detailed in Chapter 6, which gives the impression of a far greater spread in the data at this value. Despite being grown in nominally identical conditions, a small (100) oriented fraction often was observed for the films, but typically found to be less than 0.25.

A much clearer trend is observed for Al_2O_3 substrates. At 600°C, typically less than a fraction of 0.1 was observed for the (100) orientation, however this increased to approximately 0.9 when grown at 800°C, with 700°C being the intermediate case. For this substrate, many more films were grown at 600°C, leading to the apparent larger spread in the data at this temperature.

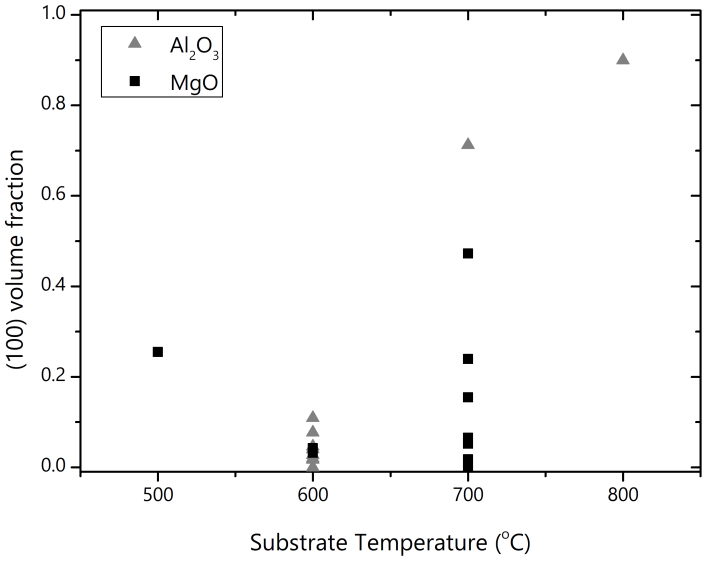


Figure 5.10: Fraction of (100) orientation for YSZ films grown on MgO and Al_2O_3 for different substrate temperatures.

5.2.4 Discussion

Film growth by physical vapour techniques can be described by thermodynamics and kinetics, covering a range of processes such as nucleation, adsorption and diffusion processes. The first step in the formation of a new thermodynamic phase is nucleation, which has an associated free energy barrier ΔG^*, due to changes in the bulk free energy, ΔG_{bulk}, and the surface free energy, $\Delta G_{surface}$. The new phase is only stable once its size is greater than a critical volume, as shown in Fig. 5.11, at which point the energy diverges and the growth of larger volumes of the new phase is favourable in a phenomenon known as Ostwald ripening.

For heterogeneous nucleation of YSZ from a vapour onto a substrate, the surface free energy, $\Delta G_{surface}$, will be a sum of the YSZ surface/vapour interface, Γ_{f-v}, the YSZ/substrate interface, Γ_{f-s}, and the substrate/vapour interface, Γ_{s-v}. The columnar microstructure observed in Fig. 5.5, suggests

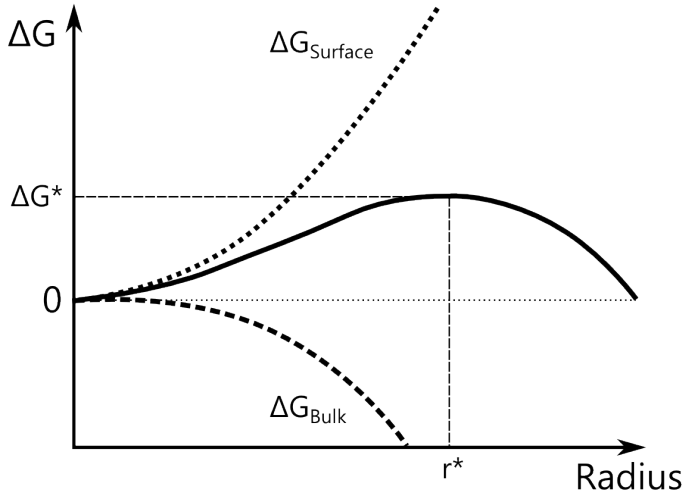


Figure 5.11: Gibbs free energy as a function of the radius for the formation of a new phase. The total Gibbs free energy is a sum of both the surface, $\Delta G_{Surface}$, and bulk, ΔG_{Bulk}, free energies resulting in an energy barrier with maximum at a radius $r = r^*$.

three dimensional island (Volmer-Weber) growth implying that

$$A_{f-v}\Gamma_{f-v} + A_{f-s}\Gamma_{f-s} > A_{s-v}\Gamma_{s-v} \tag{5.2}$$

where A is the area of each interface. *Ab initio* calculations carried out by Ballabio *et al.* [214], have calculated the surface energy of the (111) YSZ surface and (100) YSZ surface to be 65 and 109 meV $\mathring{A}^{-2}$ respectively. Therefore in absence of any changes between Γ_{f-s} for the different orientations, the (111) orientation would be expected.

Cell parameter mismatch will be a major role in the substrate/film interface energy. Considering the orientation relationships found, it is possible to calculate the nominal lattice misfit, f. For the YSZ $[11\overline{2}]||$MgO $[1\overline{1}0]$ direction, the atomic spacing of close packed Zr cations is equal to $\frac{3}{2}$ of the lattice spacing $d_{YSZ(11\overline{2})}$ and the atomic spacing of the close packed O anions is

equal to $d_{MgO(110)}$ giving

$$f_{MgO[1\bar{1}0],YSZ[11\bar{2}]} = \frac{d_{MgO(110)} - \frac{3}{2}d_{YSZ(11\bar{2})}}{\frac{3}{2}d_{YSZ(11\bar{2})}} = -5.34\% \qquad (5.3)$$

using the YSZ lattice parameter, $a_{YSZ} = 0.1539$ nm, as refined from the PLD target (See Appendix A.1) and MgO lattice parameter, $a_{MgO} = 0.4124$ nm [215]. Due to the differing symmetries of the YSZ (111) and MgO (100) surfaces the lattice mismatch is different in the YSZ [$\bar{1}$10]||MgO [110] direction. The atomic spacing of the anion and cation sublattices for both materials is half the $d_{(110)}$ spacing, such that

$$f_{MgO[110],YSZ[110]} = \frac{d_{MgO(110)} - d_{YSZ(110)}}{d_{YSZ(110)}} = -17.8\%. \qquad (5.4)$$

For the YSZ [100]||MgO [100] orientation observed on the rough substrate the mismatch is simply

$$f_{MgO[100],YSZ[100]} = \frac{d_{MgO(100)} - d_{YSZ(100)}}{d_{YSZ(100)}} = -17.8\%. \qquad (5.5)$$

Hence by growing such that YSZ (111)||MgO (100), the lattice mismatch is reduced from -17.8% to -5.34% in one direction, possibly lowering the interfacial energy, Γ_{f-s}.

Therefore if one were to assume that the substrate surface is atomically flat and free from defects, the YSZ (111) orientation is favourable due to a lower free surface energy, Γ_{f-v}, and also possibly due to a lower interfacial energy, from mismatch considerations. This conclusion is supported by the lack of change in the orientation due to the MgO buffer layers, which would be expected to improve the crystal quality and reduce surface contamination.

Rather than being perfectly flat, real substrate surfaces often have atomic size roughening in the form of steps and kinks, separated by flat terraces. Adsorbed molecules at these sites have a lower probability of desorption due to a higher number of bonds, making nucleation of a new phase more favourable than on terraces. The preferential cleavage plane of MgO is the (100) plane [216, 217], and therefore no change in the surface orientation

would be expected on the unpolished substrates, however there should be a substantially larger number of step and kink sites. Therefore it follows that cube-on-cube YSZ growth onto MgO is reliant upon the availability of these sites. The exact nucleation mechanism is unclear, however the interface free energy, Γ_{f-s}, at these preferential nucleation sites must be at least 44 meV $\mathring{A}^{-2}$ lower than on a flat surface to account for the higher (100) surface energy, Γ_{f-v}.

Thermal treatment of the substrates prior to growth did facilitate a partial change in the YSZ orientation, indicating an increase in the atomic roughness of the surface. However, single orientation (100) YSZ films could not be reproducibly attained, suggesting that the extent of the surface reconstruction during the pre-treatment did not yield a sufficiently high density of step and kink sites. The substrate miscut should also lead to a higher density of atomic roughness, yet no trend with the (100) orientation fraction was observed. It is possible that other unobserved variations in the substrate surface quality such as scratches could contribute to the lack of reproducibility of the YSZ films.

For YSZ films grown on MgO, no immediate correlation between the substrate temperature during growth and the orientation are observed, as shown in Fig. 5.10. However, for YSZ grown on Al_2O_3, the preferential orientation switched from (111) at 600°C to (100) at 800°C. The exact mechanisms causing this observation are unclear, but considering only the YSZ surface energy, one may expect the (100) orientation to have the highest nucleation energy barrier ΔG^*, as is so on the polished MgO substrates, and therefore this form of nucleation may only take place at higher temperatures.

5.3 Lattice Parameter Manipulation

The main focus of Chapter 6 is to relate changes in the lattice parameter to the transport properties of YSZ thin films. Thus it is of interest to study the changes in the lattice parameters of films grown at varying temperatures on Al_2O_3 and MgO substrates, in order to understand the origin of the strain observed. In this section all films were grown under nominally similar conditions, unless otherwise stated. For all films the thickness is expected

to be between 50 nm and 200 nm, depending on the number of pulses used.

The out-of-plane lattice parameters were calculated using XRD $\theta/2\theta$ patterns obtained for each film. The substrate peaks were refined using the Le Bail method to check for any 2θ offset during the XRD measurement. The (111) and (200) YSZ peaks were then fitted using a pseudo-Voigt function in the WinPLOTR software. Ideally both the (222) and (400) peaks should also be measured and the 2θ=180° values extrapolated according to the Nelson-Reilly function [218] to minimise systematic errors due to height misalignment and sample geometry. However, due to the low intensity of the high 2θ angle peaks, it was deemed that the error in the centre position of the pseudo-Voigt function would cause a larger error and only the (111) and (200) peaks were used.

In Fig. 5.12, the (111) reflections of YSZ films grown at a range of temperature and onto MgO (Fig 5.12a) and Al_2O_3 (Fig 5.12b) substrates are shown, each fitted using a pseudo-Voigt function. It can be seen for films grown on both substrates, there is a shift to lower 2θ angles as the temperature of the substrate during deposition decreased. The trend is much better defined in Fig. 5.12b for Al_2O_3 substrates. The films grown at 600°C for each substrate were annealed in air for 6 hours and re-measured, yielding a dramatic relaxation in the lattice parameter. To check for any systematic error due to the experimental equipment a sintered pellet of the target material (10 hours at 1500°C) was analysed using the same diffractometer, and refined using the Le Bail method to give a lattice parameter of 0.5140 nm as expected for bulk YSZ.

Fig. 5.13 shows the calculated lattice parameters according to Eq. 4.2, using the peak position of the fitted pseudo-Voigt functions once the 2θ offset had been calculated from the substrate alignment. The error from the peak fitting software is small and most likely an underestimate of the uncertainty in the peak position due to variations in sample height, 2θ-offset, and chromatic aberration of the x-rays. The error bars displayed were calculated assuming an uncertainty in the 2θ of twice the distance between measurement points in Fig. 5.12.

The films display out-of-plane lattice parameters expanded from that of bulk YSZ, with increasing lattice spacings for lower deposition temperature.

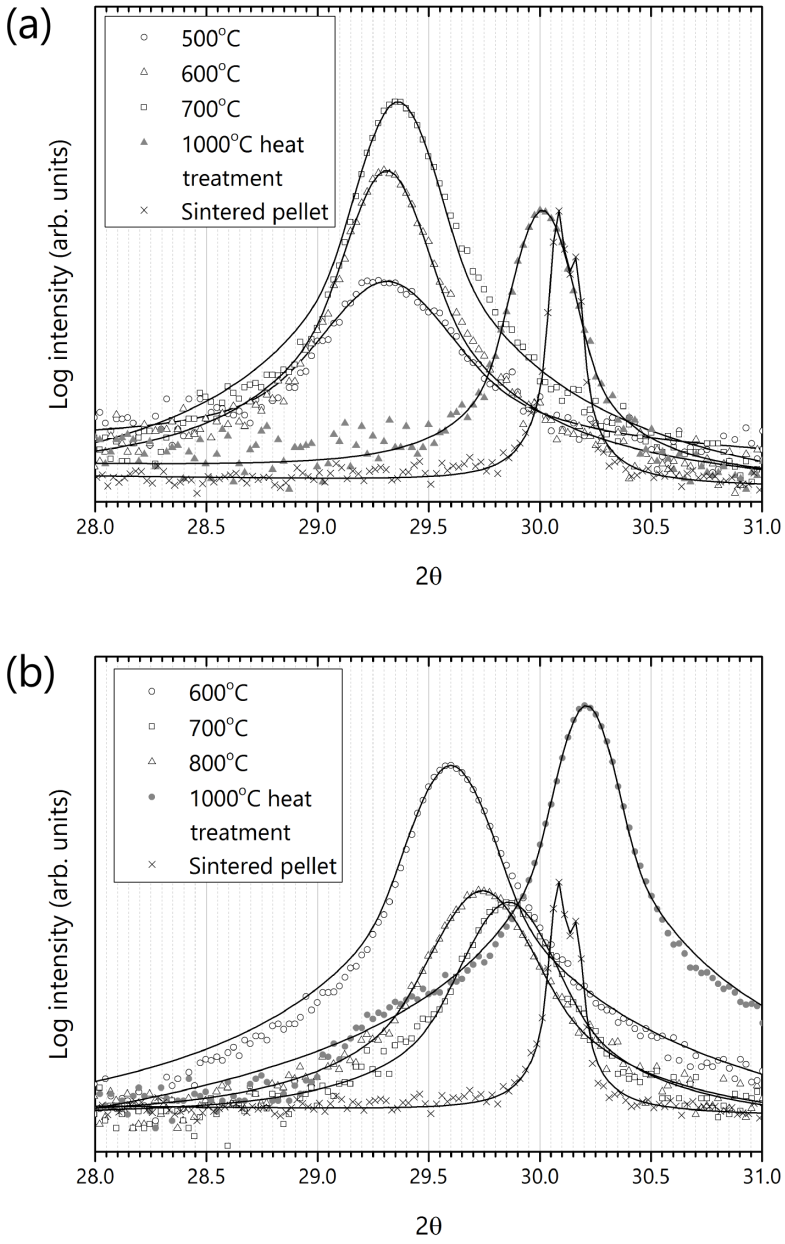


Figure 5.12: (111) YSZ peaks in the XRD spectra taken for films grown on MgO (a) and Al_2O_3 (b) substrates. Also plotted are the films grown at 600°C after a post-anneal at 1000°C for 6 hours. The fits for each film peak are pseudo-Voight functions. In addition is the (111) peak from a sintered pellet, fitted with a pseudo-Voight functions using both the $K_{\alpha 1}$ and $K_{\alpha 2}$ wavelengths.

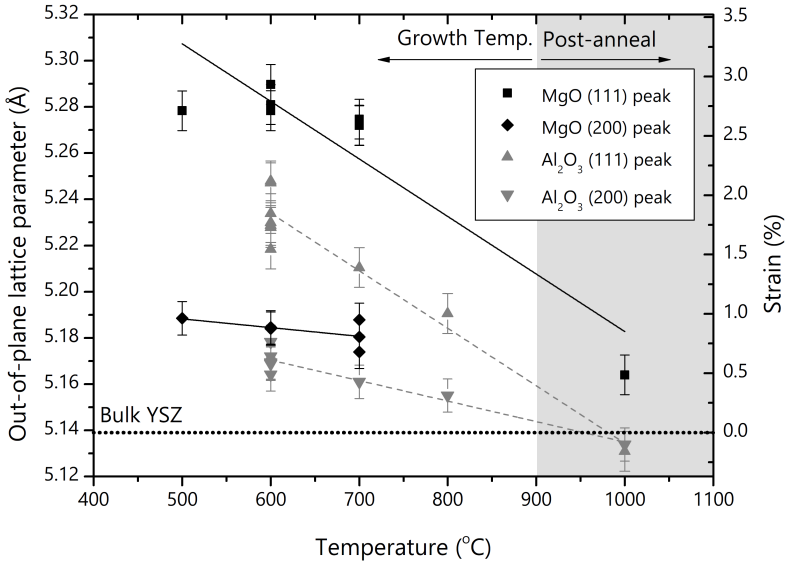


Figure 5.13: Lattice parameters calculated from the (111) and (200) peaks in the XRD $\theta/2\theta$ for YSZ films grown on MgO and Al_2O_3 substrates as a function of growth temperature and post-growth thermal treatment. The grey shaded area denotes the lattice parameters measured after annealing the as grown films. The lines are only as a guide to the eye. The bulk YSZ lattice parameter is taken from the bulk sintered PLD target.

Surprisingly, the lattice parameter taken from the (111) and (200) do not match for films grown on either substrate, where the (111) oriented grains display a significantly more expanded lattice parameter than the (200) oriented grains. For YSZ grown on MgO the lattice spacing calculated using the (111) peak was found to be strained expansively between 2.5-3%, whereas only between 0.5-1% for the (200) peaks. Using the (111) peak from the YSZ films on Al_2O_3, the lattice parameters are observed to be expanded by ∼1% at 800°C and increase to ∼2.5% at 600°C. From the (200) peak the strain was found to be ∼0.3% at 800°C and increase to ∼0.6% at 600°C. After annealing at 1000°C, the lattice of films grown on both MgO and Al_2O_3 relax substantially, to close to the expected bulk value. For the YSZ film on MgO a residual strain of ∼0.5% remained after the high temperature treatment.

5.3.1 Discussion

The degree and variation of the expansion in the out-of-plane lattice parameter is surprising for YSZ films, yet cannot be attributed to systematic error in the measurements due to the observed relaxation of the films after a high-temperature anneal and due to bulk sintered pellet measurements. In addition, a substantial difference in lattice spacing calculated from different oriented grains would be highly unexpected in bulk ceramics, however for thin films the same expectations may not apply. In films, crystallographic orientation has the potential to affect the free surface energy of the film, lattice mismatch between film and substrate, as well as other crystal growth kinetics such as growth rate. Therefore one cannot necessarily expect homogeneity between grains with varying orientation with respect to the substrate or growth direction.

Of the extensive literature on YSZ thin films, few publish the calculated lattice parameters from XRD data. Those works where the YSZ lattice parameters are available are plotted in Fig. 5.14, overlaying the data from Fig. 5.13. The details of the film properties from the literature are listed in Table 5.1. In addition to the data presented, Frison *et al.* [93] have also studied the properties of PLD grown YSZ films as a function post-

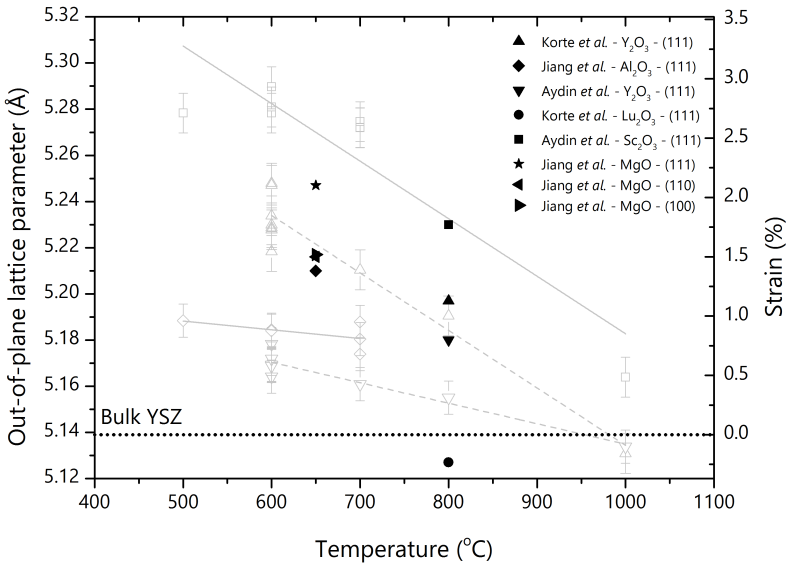


Figure 5.14: Lattice spacing calculated from XRD measurements for YSZ films from the literature. The author, substrate and film orientation are displayed in the legend. Details regarding the film properties are listed in Table 5.1.

growth heat treatment. The authors found for 8 mol.% YSZ grown on Al_2O_3 at 120°C the lattice parameter calculated from the (220) XRD peak relaxed from 0.5252 to 0.5125 nm as the film was annealed at 1100°C. These values are also in agreement with those from this work and the literature. Yet, to the best of the authors knowledge, to date no explanation for this phenomenon has been presented.

Author	Interface	Growth Method	Growth Temp. (°C)	Film Orientation	Theoretical Mismatch	Lattice Parameter ($\AA$)	Thickness (nm)
Jiang *et al.* [119]	9 mol.% YSZ/Al_2O_3 (0001)	RF sput.	650	(111)	-24.47%	5.21	100
Korte *et al.* [58]	9.5 mol.% YSZ/Y_2O_3 (111)	PLD	800	(111)	3.04%	5.197	526
Aydin *et al.* [129]	9.5 mol.% YSZ/Y_2O_3 (111)	PLD	800	(111)	3.04%	5.18	1000
Korte [110]	9.5 mol.% YSZ/Lu_2O_3 (111)	PLD	800	(111)	1.02%	5.127	250
Aydin *et al.* [130]	9.5 mol.% YSZ/Sc_2O_3 (111)	PLD	800	(111)	-4.37%	5.23	1000
Jiang *et al.* [219]	9 mol.% YSZ/MgO (100)	RF sput.	650	(111)	-17.8, -5.34%	5.247	50
Jiang *et al.* [219]	14 mol.% YSZ/MgO (100)	RF sput.	650	(100)	-17.8%	5.216	50
Jiang *et al.* [219]	9 mol.% YSZ/MgO (110)	RF sput.	650	(110)	-17.8%	5.216	50

Table 5.1: Details of the YSZ films from literature, which have been plotted in Fig. 5.14.

In Fig. 5.13 the difference in lattice spacing between the YSZ films grown on MgO and Al_2O_3 suggests the substrate-film interaction plays a role in the observed strain. In addition, the inconsistency between the lattice parameter between the (111) and (100) oriented grains may be caused by the interface between the film and substrate which will have a different mismatch for each orientation. However, the YSZ films are relatively thick and have grain widths on the order of 10-20 nm from the TEM images in Fig. 5.5, and therefore relaxation would be expected to occur away from the interface [220]. For such thin films the information obtained by XRD would be expected to come uniformly from the entire layer and hence it follows that if the average lattice parameter measured is up to 3% strained then at the interface the strain must be even higher, approaching the limit of the maximum strain expected at a coherent interface [63]. Furthermore, the out-of-plane lattice parameter is presented here, but the strain at a semi-coherent or coherent interface should be biaxial in the in-plane direction. This would result in a Poisson relaxation of the YSZ film, which typically has a coefficient of approximately 0.36 [221]. Therefore the interfacial strain would have to be as high as 10% in the case of (111) oriented YSZ on (100) oriented MgO. While the theoretical mismatches between YSZ with MgO and Al_2O_3 are as high as 18 and 25% respectively, the same cannot be said for the literature values plotted in Fig. 5.1 and detailed in Table 5.1.

Dissimilarities in thermal expansion properties between the substrates and films might explain the change of lattice parameter with different substrates and with temperature. However, as detailed in Table 5.2, the difference in the thermal expansion coefficient (TEC), α, between YSZ, MgO and Al_2O_3 is small. Taking the largest reported value of the TEC for MgO, $\alpha = 15.3 \times 10^{-6} K^{-1}$, the difference between 8 mol.% YSZ is approximately $\Delta\alpha = 0.5 \times 10^{-6} K^{-1}$, which would only account for a strain of 0.35% at 700°C. Also, as α for MgO is larger than that for YSZ and Al_2O_3 is smaller, the lattice strain should have opposite affect for the two substrates. In addition, TEC mismatch would not explain the difference in strain between the (111) and (100) oriented grains, as the TEC should be isotropic for cubic YSZ above with a concentration above 8 mol.% [222].

Rather than being a purely substrate induced effect, the expansive strain

Material	$\alpha(10^{-6}K^{-1})$	Temp. Range (°C)	Ref.
8 mol.% YSZ	10.1 - 10.5	20 - 1000	[223, 224]
MgO	10.5 - 15.3	27 - 927	[225]
Al_2O_3	7.28 - 8.11	27 - 827	[226]

Table 5.2: Thermal expansion coefficients, α, for 8 mol.% YSZ, MgO and Al_2O_3 taken from the literature.

observed may be partially due to growth mechanisms during the deposition process. From Table 5.1, it is clear that this phenomenon is not specific to PLD fabricated films, but is also observed in films grown by other physical vapour deposition techniques such as reactive sputtering. Changes in lattice parameter may occur due to chemical expansion [227] if the deposited films are not fully oxidised. In doped-CeO_2 films [152], reduced Ce^{3+} ions have been observed in as-grown films fabricated by PLD, however YSZ is much more difficult to reduce [228] and would be expected to fully oxidise immediately after growth as the films cooled down from deposition temperature in an oxygen atmosphere. Also, this would not explain the difference in lattice parameter between the (111) and (100) oriented grains. Furthermore, it has been reported that for polycrystalline 8 mol.% YSZ reduced at 1000°C in a 5% H_2 atmosphere for 6 hours, no change in the lattice parameter is observed [229].

The Y concentration in 8 mol.% YSZ, is such that the material is close to the structural phase boundary between the cubic and tetragonal phases [21]. It is well known that under certain PLD conditions changes in the stoichiometry of the films are observed, which are sensitive to parameters such as substrate-target distance, oxygen partial pressure, and laser energy [230]. Therefore it is conceivable that a change in the YSZ from the cubic to tetragonal structure, could account for the varying lattice spacings calculated from the different peaks in the XRD. However, in the tetragonal phase of YSZ, the axial ratio c/a listed for a range of dopant concentrations in Table 5.3, is not large enough to account for the maximum anisotropy observed in the YSZ films here.

Dopant Concentration (mol.%)	c/a
2.8	1.0156
4	1.0116
5	1.0085
6	1.0053
7	1.0026
8	1.0021
9	1.0011
10	1.0014
11	1.0012
12	1.0011

Table 5.3: Axial ratios (c/a) in Y-doped ZrO_2 for a range of dopant concentrations. Data from Lamas and Walsöe de Reca [231].

The defect compensation mechanism of Y doping in ZrO_2 is commonly accepted to be dominated by oxygen vacancies (Section 2.1.3), however by quenching bulk Ca-doped ZrO_2 from 1800°C a change in the defect structure from oxygen vacancies to Zr interstitials has been observed (Eq. 2.7 and Fig. 2.3) as discussed in Chapter 2. Quenching from high temperature is intuitively similar to physical vapour deposition techniques, where a high energy plasma condenses on a substrate where the temperature is low enough to prevent widespread cation diffusion. Estimating the effect of the Zr or Y interstitials on the lattice parameter is non-trivial due the difficulties in calculating the O vacancy and cation interstitial effective ionic radii. However, from the work of Diness and Roy [23] on 5 to 25 mol.% Ca-doped ZrO_2, the lattice volume due to Zr interstitials mechanism was observed to decrease compared to the oxygen vacancy mechanism, leading to a decrease in lattice spacing from 0.5130 to 0.5123 nm for the 10 mol.% Ca-doped ZrO_2. Due to the valence state of Ca (Ca^{2+}) a single Zr interstitial ($Zr_i^{\bullet\bullet\bullet\bullet}$) is produced for every two dopant Ca cations, yet for Y-doped ZrO_2 only one Zr interstitial would be created for every four Y cations, and therefore a smaller change in the lattice parameter (<-1.7%) would be expected.

Often microstrain is used to explain the expansion or contraction of the lattice parameter in films of doped-CeO_2 or Y-doped ZrO_2 [87, 96, 232]. Microstrain is defined to be the isotropic displacement field of atoms in a

material leading to larger variation of the lattice parameters in the film, whereas lattice strain is change in the average lattice parameter compared to the bulk material [97]. Microstrain has been observed for a number of YSZ and doped-CeO_2 films grown by physical vapour deposition techniques [93, 95, 97], which decreases as a function of post-fabrication thermal treatment. Rather than a substrate induced effect, it is thought that microstrain occurs due to the low temperature synthesis. A detailed description of the mechanisms governing microstrain during the deposition and crystallisation YSZ films has not yet been developed, and would still not explain the observed asymmetric shift to an expanded lattice.

5.4 Conclusion

8 mol.% YSZ films have been grown on MgO and Al_2O_3 substrates using PLD to investigate the effects of substrate roughness, homo-epitaxial buffer layers, substrate heat-treatment, substrate miscut, and growth temperature on the preferential orientation and lattice parameters on the films. These findings have important implications for fabricating strained, highly textured films for investigating modification in the ionic transport properties at heterogeneous interfaces.

The surface roughness of MgO substrates was found to lead to a change in the preferential orientation of YSZ films from (111) for polished MgO to (100) for rough MgO. This findings point towards a change in density of preferential nucleation sites for the (100) oriented nucleating grains as the MgO surface becomes rougher. However despite substantial investigation, structurally similar films could not be consistently reproduced via substrate heat treatment or miscut. For Al_2O_3 substrates the orientation was found to change from (100) dominated at a growth temperature of 800°C to (111) dominated at 600°C.

Out-of-plane expansion is observed for the lattice spacing of YSZ films as a function of growth temperature, substrate, and grain orientation. Lattice parameters are found to be consistent with those reported in the literature for a range of heterogeneous interfaces and PVD methods. Effects stemming from the substrate such as lattice mismatch and thermal expansion

coefficients, as well as intrinsic growth effects such as changes in chemical expansion, crystallographic structure, defect structure, and microstrain have all been considered as causes yet none provide a satisfying explanation of the observations. It is possible that a combination of several of these phenomena are responsible for the expansion of the YSZ film lattice.

Chapter 6

Ionic Transport in Strained YSZ Films

In this chapter, investigations into the effect of strain on the oxygen ion transport in YSZ films is presented. Thin films have been fabricated on a variety of substrates representing a range of interfacial lattice mismatches and are studied as a function of thickness, in order to explore modifications in the ionic transport at heterogeneous interfaces.

YSZ films have been grown onto MgO in an attempt to reproduce the dramatic enhancements in the conductivity observed by Kosacki *et. al.* [106, 107], Karthikeyan *et. al* [114] and Sillassen *et. al.* [115], so that an improvement in the conductivity may be unambiguously attributed to oxygen ion transport by tracer diffusion and the underlying mechanisms governing the phenomenon investigated. Also Al_2O_3 substrates were used due to the findings of Jiang *et al.* [119], also discussed in Chapter 3. Furthermore, YSZ has also been deposited on $LaAlO_3$ (LAO) and $NdGaO_3$ (NGO) substrates, as the theoretical lattice mismatch is such that an expansive strain should be induced in the YSZ and the conductivity enhanced according to the model discussed in Section 2.3.2.

In addition, YSZ films grown on Al_2O_3 using RF sputtering by Dr. Jun Jiang and Prof. Josh Hertz at the University of Delaware (Newark, USA), in an identical fashion to those reported upon in Ref. [119], were also analysed by IETD to assess the validity of the observed enhancement in the

conductivity found electrically.

6.1 Sample Production

All the films in this chapter fabricated using PLD were done so by the author at Imperial College London, as described in Section 4.1, grown from an 8 mol.% YSZ target prepared as detailed in Section 4.1.2. The PLD synthesised films were grown with a nominal substrate temperature of either 600°C or 700°C, varying the thickness between 200 nm and 10 nm by means of the total number of pulses. All other conditions were kept identical. The substrates used were (001) oriented MgO, (0001) oriented Al_2O_3 (MaTeck Material Technologie & Kristalle GmbH, Germany), (001) oriented LAO, (110) oriented NGO (Pi-Kem ltd., UK) and were grown with no treatment other than the cleaning procedure described in Section 4.1. The size of all the substrates used was (5 × 5) mm^2. After PLD growth, selected films were annealed in air for 6 hours at 1000°C, as noted below.

The 9 mol.% YSZ films were grown by Dr. Jun Jiang and Prof. Josh Hertz at the University of Delaware using RF sputtering in an identical method to that described in Ref. [119], on the experimental set-up detailed in Ref. [233].

6.2 Structural Characterisation

6.2.1 XRD: Orientation and Lattice Strain

Fig. 6.1 shows XRD $\theta/2\theta$ scans taken from >180 nm and ∼10 nm YSZ films grown on MgO, Al_2O_3, LAO and NGO substrates. In Appendix A.2, patterns from all the films referred to in this chapter are plotted. For all films, well defined peaks are observed indicating the layers were crystalline directly after deposition.

A preferential out-of-plane orientation is observed for all samples, each only displaying peaks related to the (111) or (100) orientations. For YSZ films grown on MgO and Al_2O_3 the (111) orientation dominates, whereas for LAO and NGO substrates only the (100) orientation is observed. The

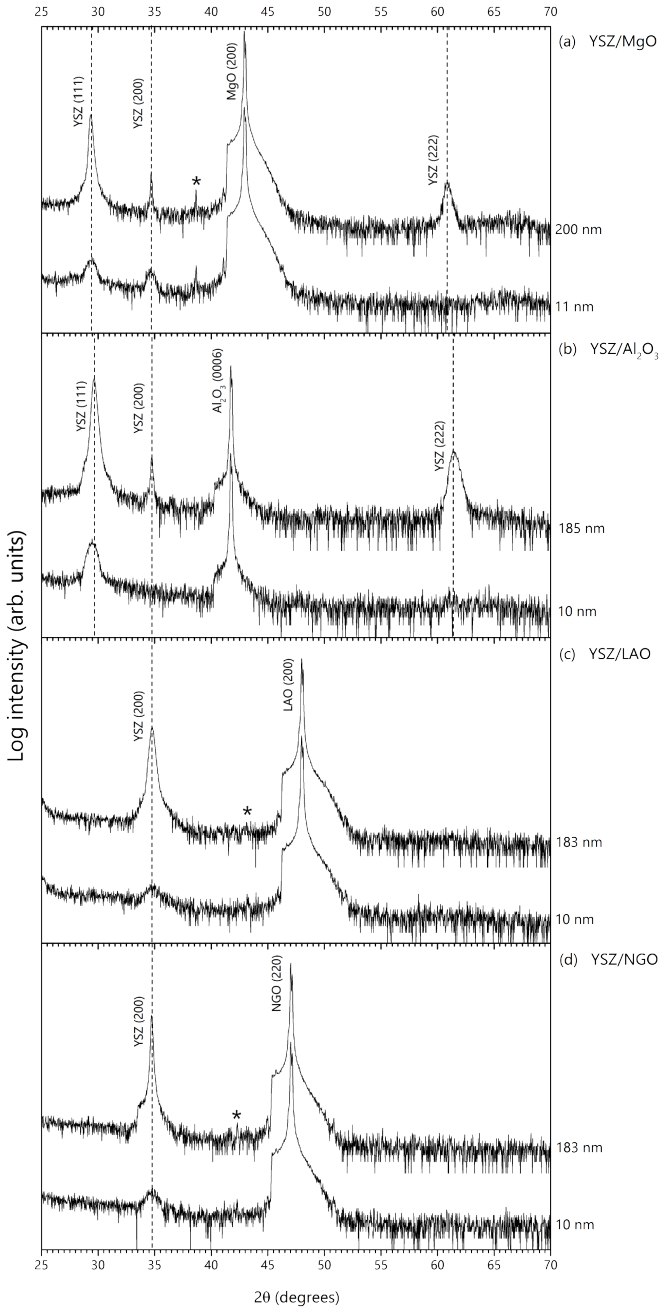


Figure 6.1: XRD $\theta/2\theta$ spectra from >180 nm and ∼10 nm YSZ films grown by PLD on (a) MgO, (b) Al_2O_3, (c) LAO and (d) NGO. The peaks marked with a $*$ are due to the substrate peaks.

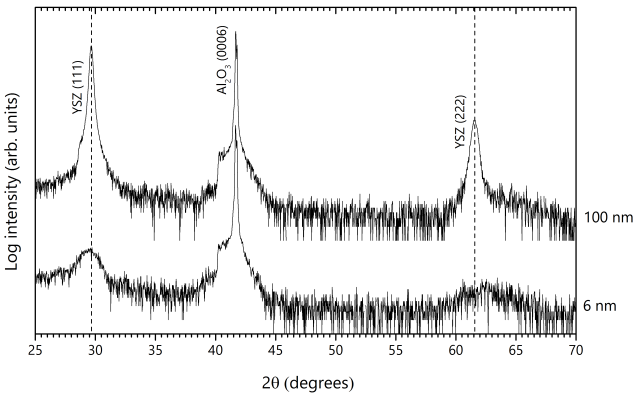


Figure 6.2: XRD $\theta/2\theta$ spectra from a 100 nm and 10 nm YSZ films grown by RF sputtering on Al_2O_3 substrates.

volume fraction of the (111) orientation for all the films are shown in Table 6.1, calculated according to Eq. 5.1. When no fittable peak is observed, a minimum/maximum fraction of the (111) orientation is estimated assuming a peak at the noise level in the $\theta/2\theta$ spectra. The layers fabricated by RF sputtering on Al_2O_3 also displayed a preferential (111) out-of-plane orientation (Fig. 6.2), comparable to those grown by PLD, and consistent with those previously published [119].

Fig. 6.3 shows the YSZ (111) peaks from a 10 nm film, and a 110 nm film both as-grown and after being annealed at 1000°C for 6 hours, both grown on Al_2O_3 substrates. The peaks are fitted with pseudo-Voigt functions. There is a small shift in the peak position between the 110 nm and 10 nm films, implying a slightly larger average lattice spacing for the thinner film. After the heat treatment, a substantial shift in the peak position of the 110 nm thick film is observed, indicating a dramatic decrease in the lattice parameter. The peak of the 110 nm thick film is also less broad after annealing, suggesting a decrease in the microstrain of the film.

The average out-of-plane lattice parameters were calculated from the peak positions in the $\theta/2\theta$ spectra, after correcting for the $2\theta = 0$ offset by refining the substrate peaks using the Le Bail method. In Fig. 6.4 the lattice spacing calculated from the peak corresponding to the dominate

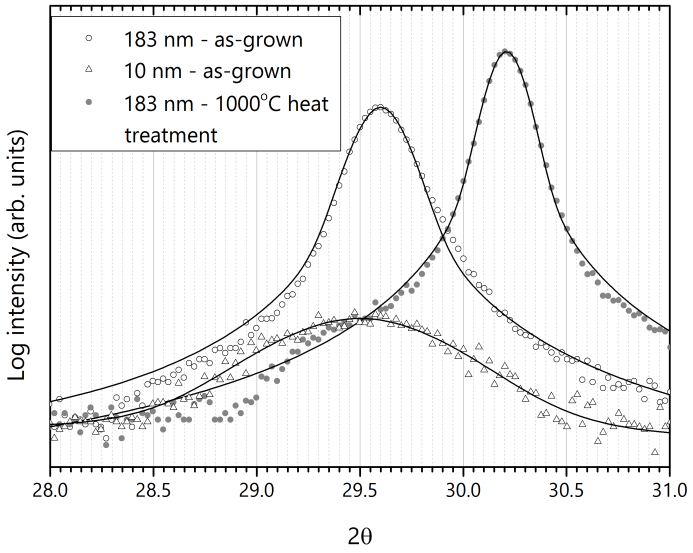


Figure 6.3: (111) YSZ peaks in the XRD $\theta/2\theta$ spectra from a 10 nm film and 110 nm film both as-grown and after annealing for 6 hours at 1000°C. The fits are pseudo-Voigt functions.

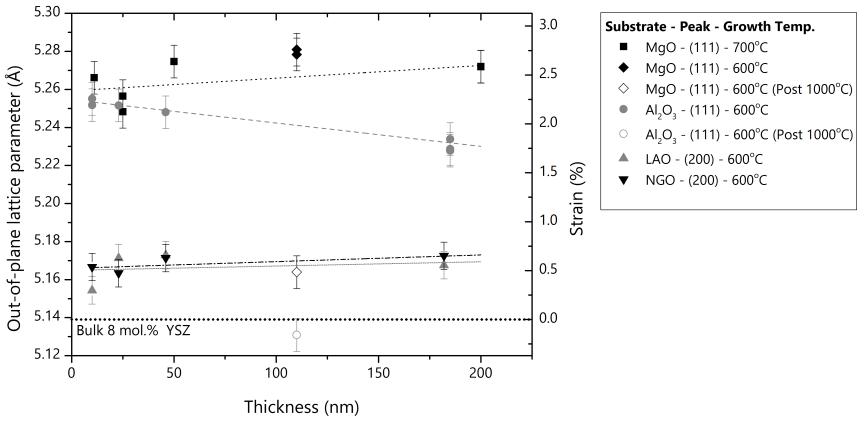


Figure 6.4: Out-of-plane lattice parameters as a function of film thickness calculated from the peak position of either the (111) or (200) reflection, corresponding to the dominate orientation of the film. The lattice parameter refined from the PLD target is also displayed. The fitted lines act only as a guide to the eye.

orientation for each film is displayed as a function of thickness. All lattice parameters are expanded out-of-plane compared to the bulk YSZ pellet. The (111) oriented films on MgO have the largest lattice parameter of all the films, expanded approximately 2.5% compared to the expected bulk values, and show no obvious trend with thickness. The films fabricated on Al_2O_3 substrates display an out-of-plane tensile strain of ∼1.7% for a thickness of 185 nm, which increases to ∼2.2% as the thickness is reduced to 10 nm. The 110 nm thick films grown on MgO and Al_2O_3 subject to a post-growth heat treatment, both display a substantial relaxation in the lattice to within ∼0.5% of bulk. The (100) oriented films grown on both LAO and NGO yield an out-of-plane expansion of approximately 0.5%. For both sets of films the lattice parameter is observed to decrease slightly with thickness, however the trend is within the experimental uncertainty. The lattice parameter calculated from both the (111) and (200) reflections when observed are listed in Table 6.1.

The lattice spacings calculated from the YSZ films grown on Al_2O_3 using PLD and RF sputtering are plotted in Fig. 6.5 for comparison. Also included are the lattice parameters reported by Jiang *et al.* [119]. The out-of-plane

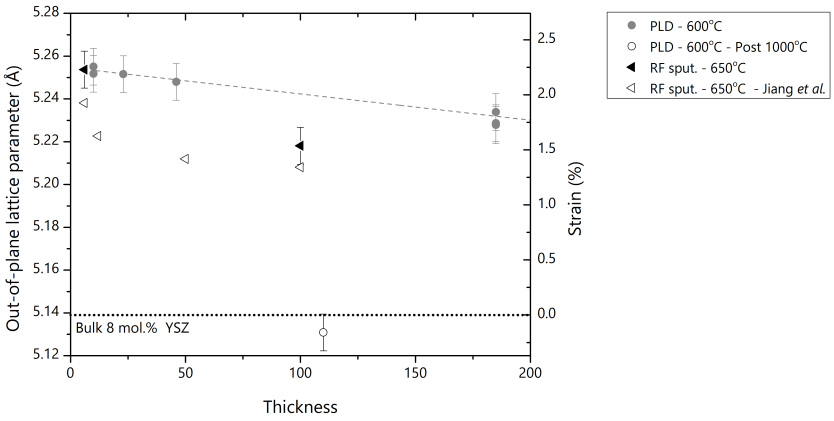


Figure 6.5: Out-of-plane lattice parameters as a function of film thickness calculated from the peak position of either the (111) reflection of the films grown on Al_2O_3 by PLD and RF sputtering. Also, the lattice parameters for the YSZ films reported in Ref. [119] are included. The growth temperature of each set of films is included in the legend. The fitted lines act only as a guide to the eye.

spacing in 100 nm and 6 nm thick films grown by RF sputtering agrees well with those previously reported. In addition the 6 nm thick film has a lattice spacing very close to those grown by PLD with a comparable thickness, however the 100 nm thick film has a slightly smaller lattice parameter than expected.

6.2.2 XRD: Texture

In Fig. 6.6, pole figures taken from films grown on each substrate are plotted. For each film a pole figure around the (220) YSZ reflection is displayed, as well as a characteristic reflection originating from the substrate, such that the orientation relationships for each system may be deduced. For each system both scans were obtained from the same film, without being removed from the diffractometer, such that the position of the signal in the ϕ axis may be compared.

Figs. 6.6a and 6.6b show the (220) YSZ and (220) MgO reflections for a 50 nm thick film. Twelve maxima are visible at $\psi \sim 35.3°$, corresponding to a (111) out-of-plane orientation. The peaks are equally spaced in the

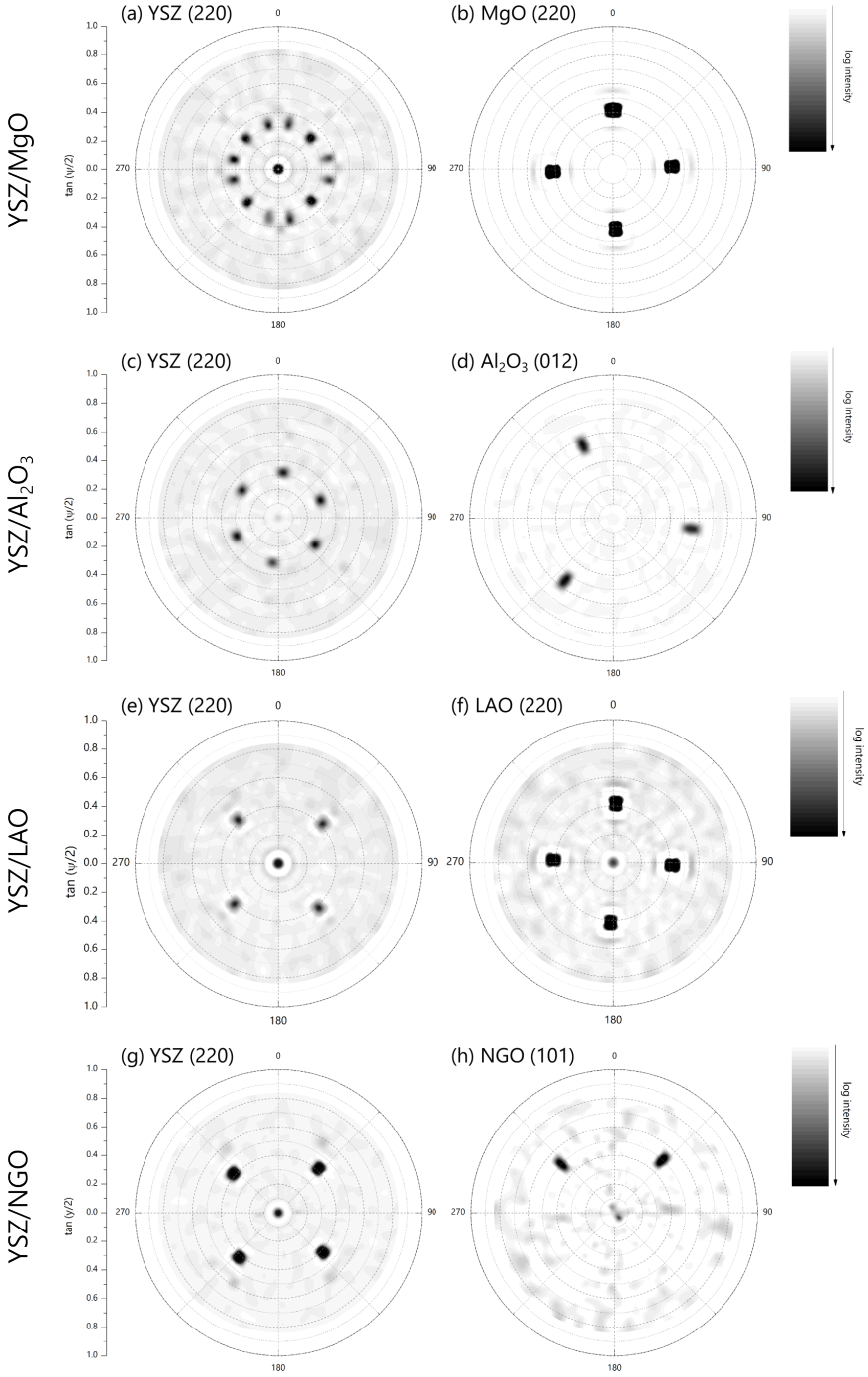


Figure 6.6: (a), (c), (e), and (g) show the pole figures corresponding to the (220) YSZ peaks for a films grown on MgO, Al_2O_3, LAO, and NGO respectively. Also displayed are the pole figures for the (b) MgO (220), (d) Al_2O_3 (012), (f) LAO (220), and (h) NGO (101) reflections.

azimuth direction, implying four distinct preferential in-plane orientation of the grains, each separated by 90°. Additionally there are four much weaker reflections at a $\psi = 45°$, corresponding to an out-of-plane orientation of (100). In this case, the four maxima indicate a single in-plane orientation for these grains. Both sets of peaks observed are in agreement with peaks observed in the $\theta/2\theta$ scans. By comparison with the positions of the maxima from the MgO pole figure in Fig. 6.6b, the following orientations are observed for the dominant out-of-plane orientation.

(I) YSZ (111)||MgO (001)

(i) YSZ $[11\bar{2}]$||MgO $[1\bar{1}0]$
YSZ $[\bar{1}10]$||MgO [110]

(ii) YSZ $[11\bar{2}]$||MgO [110]
YSZ $[\bar{1}10]$||MgO $[\bar{1}10]$

(iii) YSZ $[11\bar{2}]$||MgO $[\bar{1}10]$
YSZ $[\bar{1}10]$||MgO $[\bar{1}\bar{1}0]$

(iv) YSZ $[11\bar{2}]$||MgO $[\bar{1}\bar{1}0]$
YSZ $[\bar{1}10]$||MgO $[1\bar{1}0]$

The YSZ orientations are each related by a rotation of 90° or 180° in the azimuth. The minority out-of-plane orientation may be described by:

(II) YSZ (001)||MgO (001)
YSZ [100]||MgO [100]

These are the same as reported in Chapter 5, studying the effect of roughness.

Pole figures from the YSZ (220) and Al_2O_3 (012)[1] from a 46 nm thick YSZ film are displayed in Figs. 6.6c and 6.6d respectively. In Fig. 6.6c, six maxima are observed at $\psi = 35.3°$, consistent with grains with an out-of-plane (111) orientation. As with the YSZ/MgO system, the six equally spaced peaks point to a preferential in-plane texture, however in this case only two distinct orientations are observed, separated by a 60° rotation or mirror inversion. From the respective positions of the substrate peaks in Fig. 6.6d the following orientation relationships are inferred for the two in-plane rotations:

(I) YSZ (111)||Al_2O_3 (0001)

(i) YSZ $[\overline{1}\overline{1}2]$||$Al_2O_3$ $[11\overline{2}0]$
YSZ $[1\overline{1}0]$||Al_2O_3 $[\overline{1}100]$

(ii) YSZ $[1\overline{2}1]$||Al_2O_3 $[11\overline{2}0]$
YSZ $[10\overline{1}]$||Al_2O_3 $[\overline{1}100]$

In the sample analysed, the reflections from the minority orientation YSZ (100)||Al_2O_3 (0001), were not visible due to their low intensity.

In Figs. 6.6e and 6.6f, pole figures for the YSZ (220) and LAO (220) reflections taken from a 46 nm film grown on LAO are plotted. In both figures, four peaks are observed at a tilt angle of $\psi = 45°$, indicating single in-plane orientations. From the relative positions between the films and substrate maxima the orientation relationship is given by:

(I) YSZ (100)||LAO (100)
YSZ [001]||LAO [011]

This represents a highly ordered growth of the YSZ film on LAO, with a 45° in-plane rotation between the two unit cells.

Pole figures taken for the YSZ (220) and NGO (101) reflections of a 183

[1] $(01\overline{1}2)$ in 4-axis Miller-Bravais notation

nm thick film grown on NGO are displayed in Figs. 6.6g and 6.6h. Such as with the film grown on LAO, the single in-plane orientation of this film is confirmed by the four maxima observed at $\psi = 45°$. The orthorhombic nature of the NGO unit cell yields only two peaks at $\psi = 45°$ in Fig. 6.6h. The orientation relationship inferred from the pole figures is:

$$\begin{aligned} \text{(I) YSZ (100)}&\text{||NGO (110)} \\ \text{YSZ [011]}&\text{||NGO [00}\bar{1}\text{]} \\ \text{YSZ [01}\bar{1}\text{]}&\text{||NGO [1}\bar{1}\text{0]} \end{aligned}$$

6.2.3 TEM: Orientation and Microstructure

Selected area electron diffraction patterns for films grown on each of the substrates is displayed in Fig. 6.7, with the peaks indexed. The patterns were each taken from an area that contained the entire thickness of the film and a part of the substrate. In each, well defined reflections from the films are visible, as expected for highly crystalline films and confirm the orientation relationships inferred from the XRD $\theta/2\theta$ scans and pole figures. For Fig. 6.7a the beam was aligned with the MgO [001] zone axis, and therefore only the (111) reflections of the YSZ film are visible, and hence the in-plane rotations of the YSZ grains could not be established for comparison with the data from XRD. A slight broadening of the YSZ peaks for the SAED on MgO and Al_2O_3 substrates is visible, where the spots appear to be more elliptical. Kosacki *et al.* [107] observed a similar broadening in YSZ films grown on MgO and attributed it to strain in the YSZ, however as discussed below, low angle grain boundaries caused by slight titling of the grains with respect to one another seems a more likely origin.

A selection of samples were used to evaluate the film thickness and microstructure using TEM, as noted in Table 6.1. The thicknesses of the other samples were calculated from these measurements based on the number of pulses used during the deposition. In Table 6.1 the calculated thickness of each film is displayed. Bright field TEM micrographs of as-grown films fabricated on MgO and Al_2O_3 substrates as shown in Fig. 6.8, as well as a film

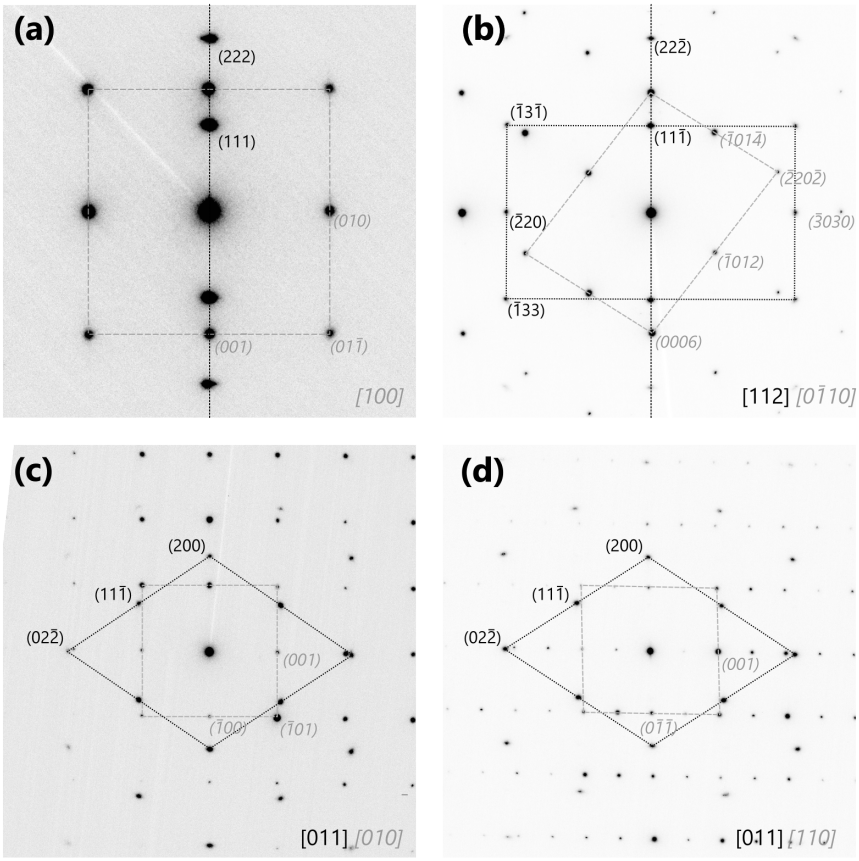


Figure 6.7: SAED patterns taken from YSZ films grown on (a) MgO, (b) Al_2O_3, (c) LAO and (d) NGO. The black indices (non-italic) refer to the film and the grey (italic) to the substrate. The zone axis of the electron beam is shown in the bottom right of each pattern.

after annealing at 1000°C.

From the TEM images the films were found to be fully dense, with no signs of nano-scale pinholes or secondary phases. For all films a columnar grain structure was observed, with the column widths found to be approximately 30-70 nm for the region greater than ∼70 nm from the interface, and approximately 5-30 nm for the region in closer proximity to the substrate. As all the samples were prepared under identical conditions, the microstructure found here should be representative for the entire thickness range, with the observations in proximity to the interface being indicative

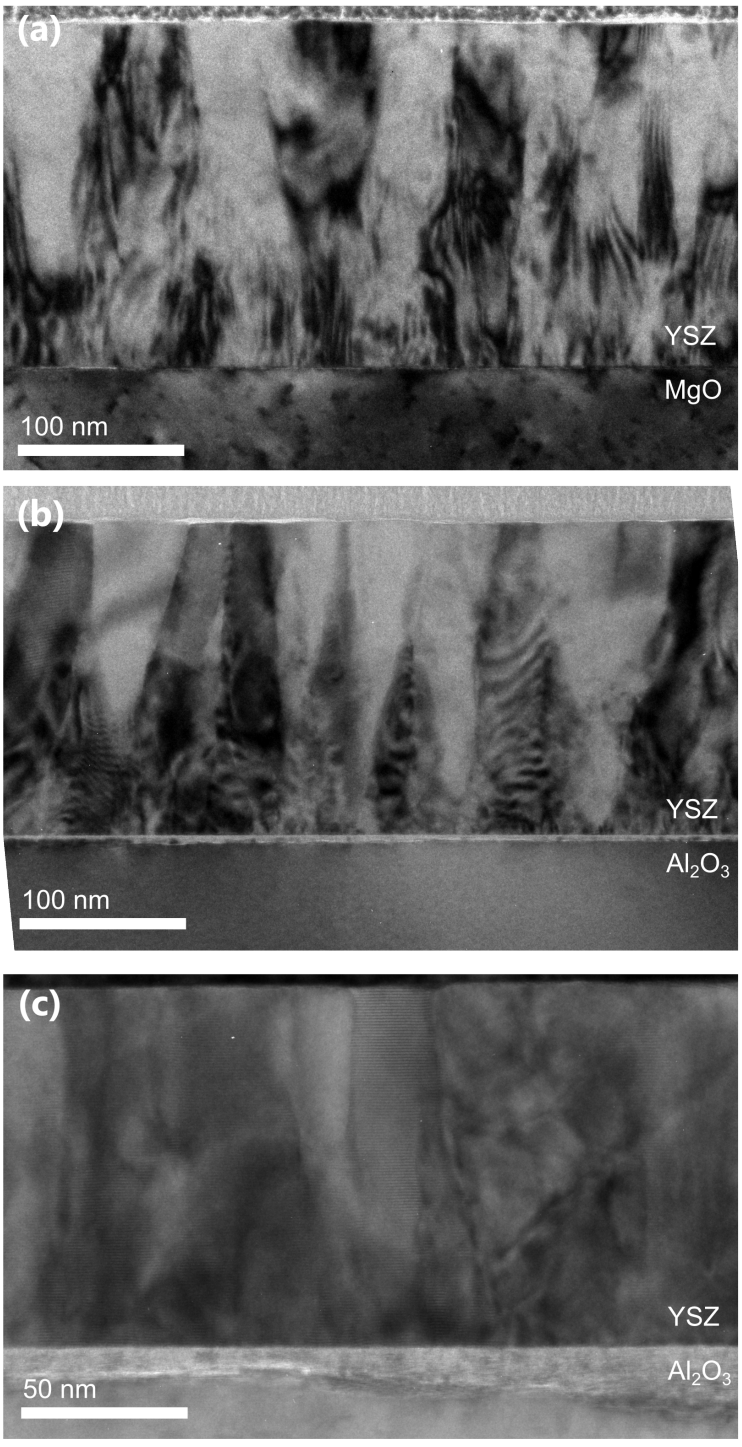


Figure 6.8: Bright field images of as-grown YSZ films on (a) MgO and (b) Al_2O_3 substrates and (c) Al_2O_3 after heat treatment of 1000°C for 6 hours.

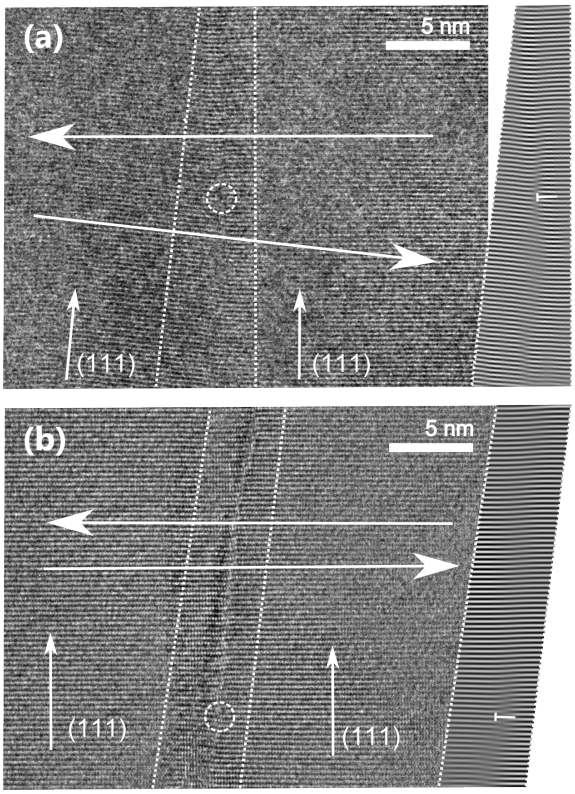


Figure 6.9: Lattice images of low angle grain boundaries in films grown on (a) MgO and (b) Al_2O_3. The region between the dotted lines has been Fourier filtered, revealing the low density of misfit dislocations between the grains.

of the microstructure for the thinner films. Fig. 6.8c shows a micrograph of a YSZ film on a Al_2O_3 substrate, after annealing at 1000°C for 6 hours. No obvious coarsening of the grains was observed.

In all films the columnar grains are separated by low angle grain boundaries, parallel to the growth direction. Two boundaries are shown in Fig. 6.9 for MgO and Al_2O_3 substrates. In Fig. 6.9a the misorientation is approximately 6°, but typically for all films it is found to be much lower such as in Fig. 6.9b. Due to the small degree of misorientation, the low angle grain boundaries were not observed in the XRD data, however they are the most likely cause of spot broadening in the SAED. Fourier filtering may be applied to images in order to highlight the periodicities of a certain spacing and direction. For each image the area between the dashed lines has

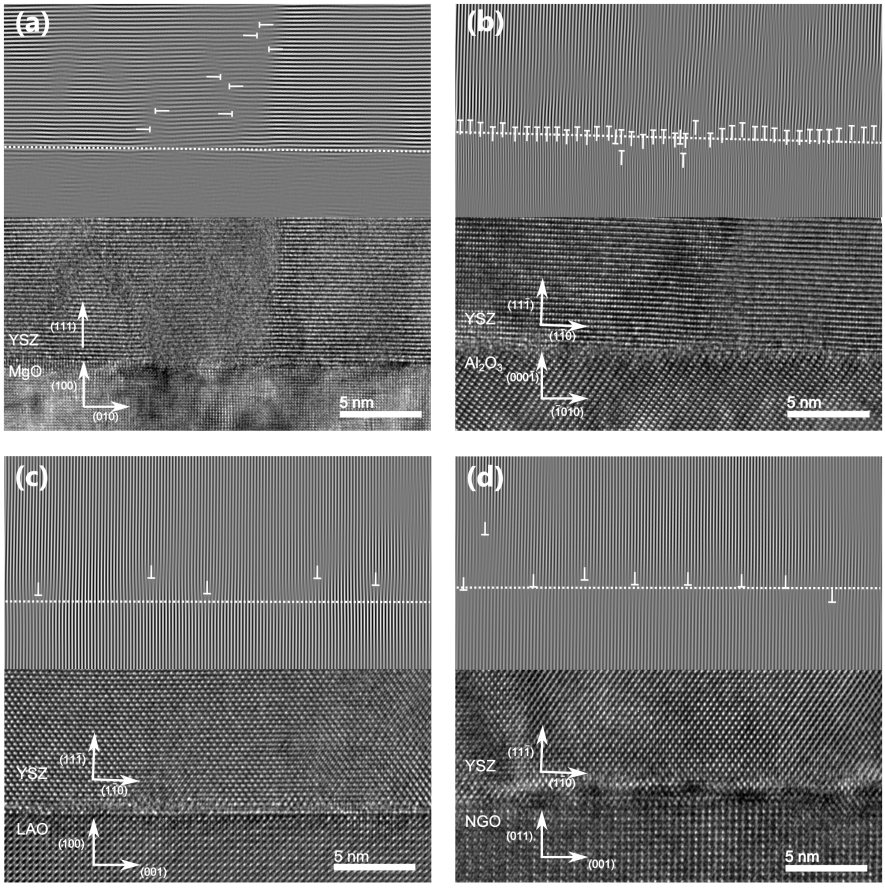


Figure 6.10: Lattice images of the film-substrate interface for YSZ grown on (a) MgO, (b) Al_2O_3, (c) LAO, and (d) NGO. Each image has been Fourier filtered using the YSZ (222) peak in (a) and the YSZ (220) peak in (b), (c), and (d). The dislocations are marked and the position on the interfaces indicated with dotted lines.

been Fourier filtered using the YSZ (222) spots in the fast Fourier transform (FFT). For both grain boundaries a single dislocation is observed in the area analysed, identified as a missed plane of atoms, and circled on the corresponding lattice image.

The film-substrate interface for films grown on each substrate is shown in Fig. 6.10. All are found to be sharp with no sign of secondary phases. Two types of dislocation were found in abundance close to the interfaces. The first type had Burgers vectors perpendicular to the interface, and the

second type had Burgers vectors parallel to the interface. In Fig. 6.10a, the image has been Fourier filtered using the YSZ (222) spots, to highlight the dislocations between the grains. Often several dislocation of this type appeared close to each other with anti-parallel Burgers vectors observed. All films displayed similar microstructures in this regard. The high density of grain boundaries and dislocations is expected closer to the interface to relieve the strain caused by the lattice mismatch between the film and substrate.

For the films grown on Al_2O_3, LAO, and NGO, dislocations with Burgers vectors parallel to the interface were observed, in the Fourier filtered image using the YSZ (220) peak and relevant substrate peak. Due to the orientation of the YSZ on MgO, lattice fringes perpendicular to the interface were not visible and therefore the dislocation density could not be assessed. Fourier filtered images using the YSZ (220) peak revealed an abundance of dislocations at the interface of the films grown on Al_2O_3, LAO, and NGO. In regions without any grain boundaries these frequently were observed as an ordered dislocation network with a semi-regular spacing, as shown in Figs. 6.10b, 6.10c, and 6.10d. In most cases the dislocations are observed to be centred directly at the interface, but occasionally they are seen several planes into the film and very rarely into the substrate. For YSZ films on Al_2O_3 (Fig. 6.10b), the missed plane usually originates from the direction of the substrate, and occur on average between four and five Al_2O_3 planes (1/2 of $d_{Al_2O_3(\bar{1}100)}$). In addition, there is a tilting of the YSZ planes with respect to those of the substrate by approximately 2.5°, which may further reduce the interfacial strain. For the LAO (Fig. 6.10c) and NGO substrates (Fig. 6.10d), the Burgers vectors are in the opposite direction, to that of Al_2O_3. For LAO the spacing between dislocations was found to alternate between 17-18 planes and 35-36 planes, yielding an average density of one dislocation every 27 YSZ planes (1/2 of $d_{YSZ(1\bar{1}0)}$). The spacing between dislocation for YSZ grown on NGO was found to vary between 14 and 17 YSZ planes, giving an average dislocation density of one every 16.6 YSZ planes (1/2 of $d_{YSZ(1\bar{1}0)}$).

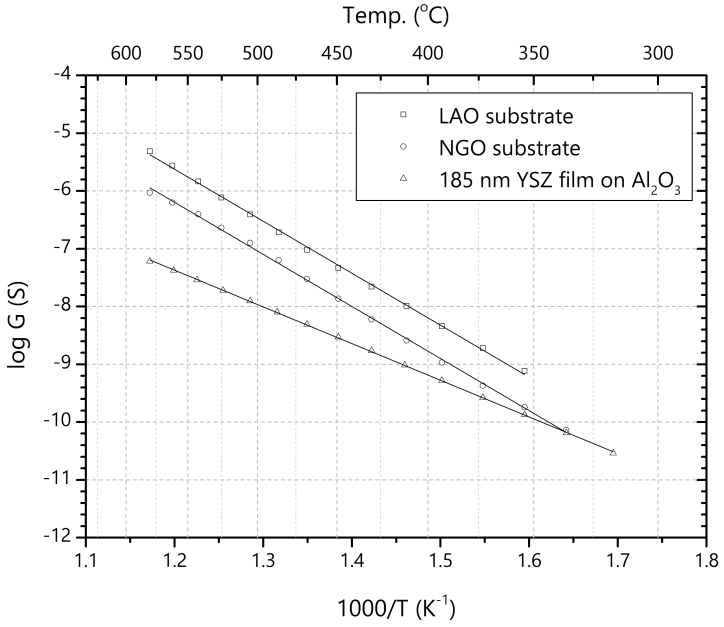


Figure 6.11: Conductance of a LAO and NGO substrate compared to a 185 nm thick YSZ film grown on Al_2O_3, using a similar electrode geometry.

6.3 Transport Characterisation

6.3.1 EIS: Electrical Conductivity

The electrical conductivity was measured using EIS as described in Section 4.4.1, between 300 and 580°C with spectra taken upon heating and cooling to ensure reversibility. As-received substrates were also measured using a comparable electrode geometry to assess their insulating nature and hence the ability of EIS to yield accurate values of the ionic conductivity through the YSZ films. The conductance of the MgO and Al_2O_3 substrates were found to be approximately two orders of magnitude lower than that of the thinnest YSZ films measured for the entire temperature range. However, both the LAO and NGO substrates conductance was much higher than even a 185 nm thick YSZ film grown on Al_2O_3, as shown in Fig. 6.11. Hence, the transport properties of the films grown on LAO and NGO were not assessed by EIS due to the high electrical leakage in the substrates.

Typical Nyquist plots from films grown on MgO and Al_2O_3 are shown

in Fig. 6.12. For all samples a single semicircle dominated the spectra, however small electrode contributions were observed at low frequency for higher temperatures, which were not included in the fits. The fits represent equivalent circuits as shown in Fig. 4.8c, with the x-axis intercept yielding the sample resistance. The capacitances calculated according to Eq. 4.12 for each spectra taken, were always found to be between 2-4 $\times 10^{-13}$ F. This is in good agreement with the parallel plate capacitance from the electrode geometry of 1.8 $\times 10^{-13}$ F, using a dielectric constant of 9.8 for MgO and Al_2O_3 [234]. Hence the capacitance of the response is assigned to the substrate, as in Fig. 4.8c. The resistance taken from the x-axis intercept is thus a sum of both the bulk and grain boundary contribution.

The temperature dependence of the conductivity was found to be reversible for all films, displaying very similar values for increasing and decreasing temperature, with the exception of the 10 nm thick film grown on Al_2O_3. Fig. 6.13 is an Arrhenius plot of multiple measurements made on the same 10 nm film for the entire temperature range. The initial conductivity decreases for each repetition of the temperature range, only stabilising after the second increase in temperature. This finding is surprising considering the film was grown and the electrodes were sintered on at a higher temperature of 600°C. In all following figures and in Table 6.1 the data from the third measurement is used.

Fig. 6.14 shows the temperature dependence of the conductivity for the films grown on MgO substrates. All obey an Arrhenius relationship, and are fitted with a single linear function. There is good agreement between the conductivity of all samples regardless of thickness. The films display a reduction in the conductivity by a factor between 10 and 35 compared to that of an 8 mol.% YSZ single crystal (also plotted using data taken from Ref. [113]). From the slopes taken from the linear fits the activation energy of the films was calculated and found to range between approximately 1.3 and 1.5 eV, which is higher than 1.09 eV expected for a 8 mol.% YSZ single crystal. No immediate trends in the activation energy with the thickness of the YSZ layers was found. Also, no substantial differences in either the conductivity or activation energy are observed between 110 nm thick films as-grown and after a 1000°C treatment.

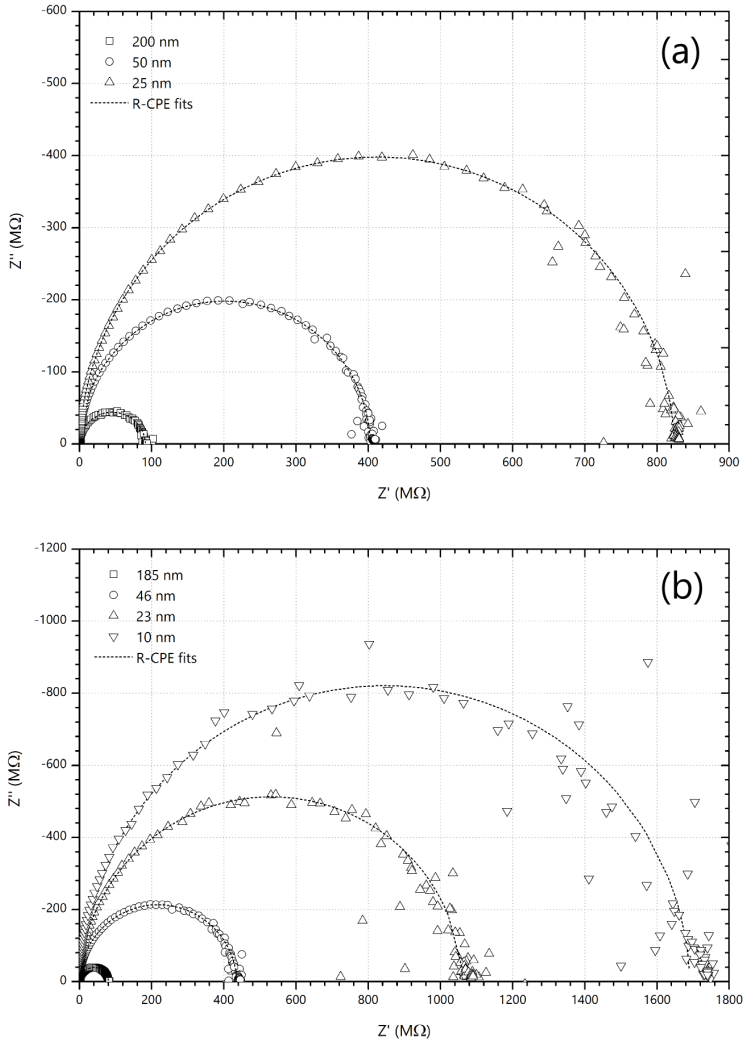


Figure 6.12: Typical Nyquist plots taken for YSZ films of various thickness on (a) MgO and (b) Al_2O_3 substrates at approximately 510°C.

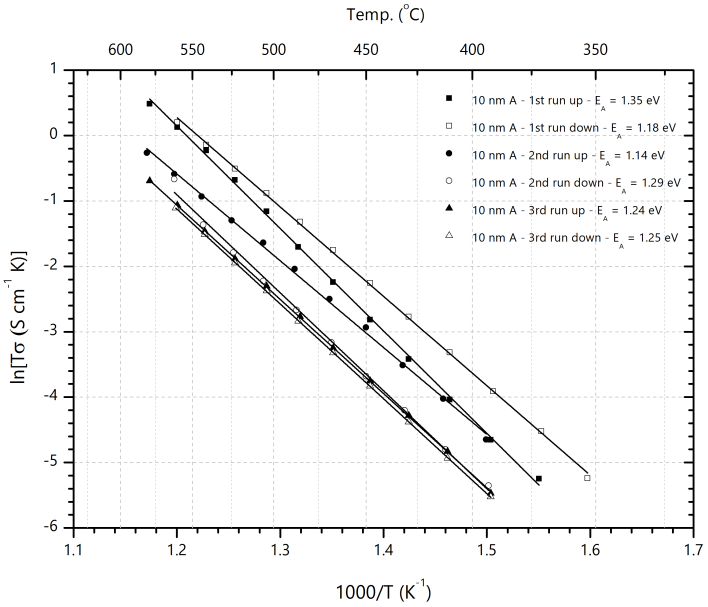


Figure 6.13: Arrhenius plot of multiple EIS measurements made on an 10 nm thick film on Al_2O_3.

The temperature dependence of the conductivity for the YSZ films grown on Al_2O_3 is displayed in Fig. 6.15. As with films grown on MgO, all displayed an Arrhenius relationship, and are fitted with a single linear function. There is factor of five variation in the conductivity between the films, which is much larger than those grown on MgO. Compared to single crystal values the conductivity is also reduced, in this case by a factor between 3 and 38. Similar activation energies to the film grown on MgO are observed in the range of 1.3 to 1.4 eV, but again no clear trends with thickness or lattice parameter are seen. There is a marked increase in the conductivity of the YSZ layers after undergoing a thermal anneal at 800°C and 1000°C, although no dramatic effect on the activation energy.

6.3.2 IETD: Oxygen Diffusivity

Oxygen tracer diffusion was performed on films of various thickness on each of the substrates, as described in Section 4.5.5. In Fig. 6.16, representative ^{18}O diffusion profiles measured by TOF-SIMS after the incorporation step

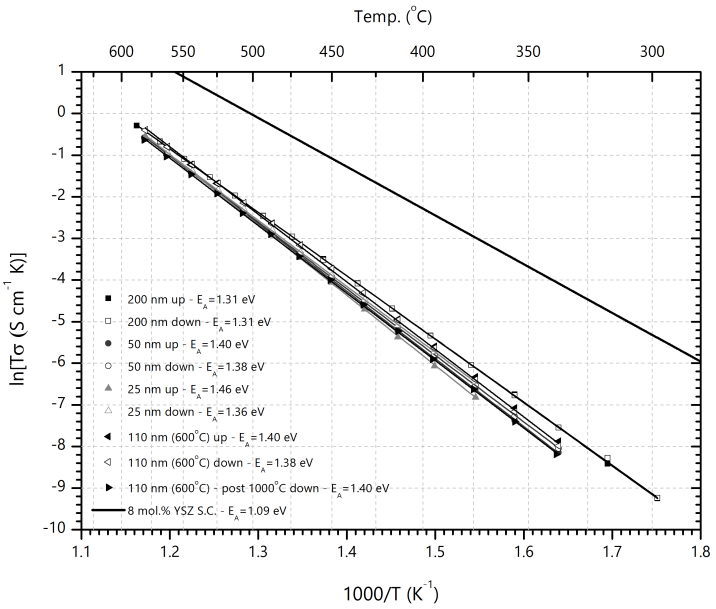


Figure 6.14: Arrhenius plot of the conductivity of the films grown on MgO. All films were deposited at a nominal substrate temperature of 700°C and received no additional thermal treatment (other than the electrode application procedure) unless stated in the legend. The YSZ single crystal data is taken from Ref. [113].

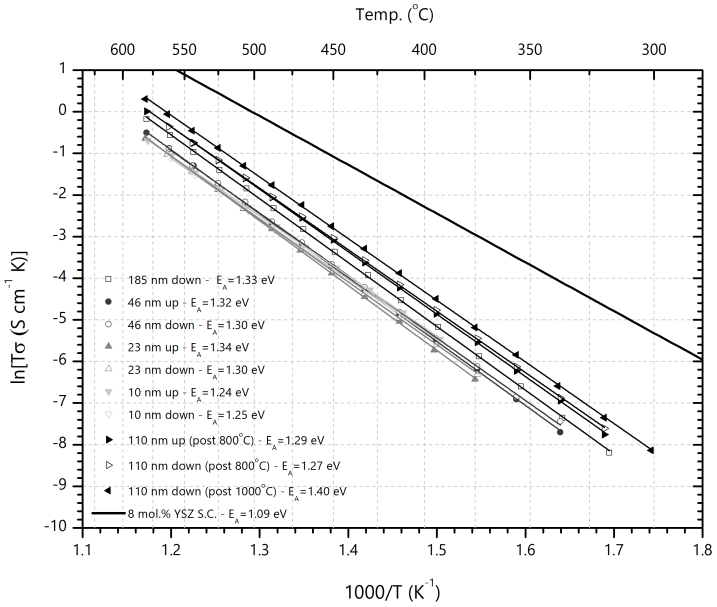


Figure 6.15: Arrhenius plot of the conductivity of the films grown on Al_2O_3. All films were deposited at a nominal substrate temperature of 600°C and received no additional thermal treatment (other than the electrode application procedure) unless stated in the legend. The YSZ single crystal data is taken from Ref. [113].

and after the diffusion step are displayed. Diffusion profiles from all the films analysed by IETD are displayed in Appendx A.3. The profiles were taken from the isotopic fraction integrated in the y-axis and z-axis and the lateral map for each measurement is shown in the insets. Due to the extreme aspect ratio of the films, the film thickness is less than a lateral width of a single pixel and therefore the ^{18}O concentration should be uniform throughout the thickness of the film within the accuracy of the measurement and the profiles should yield an accurate description of the isotopic distribution.

Figs. 6.16a, 6.16c, 6.16e and 6.16g show the ^{18}O isotopic fraction profiles after the incorporation step of 30 minutes at 300°C in ^{18}O enriched gas, of the boundary between the Au covered and uncovered surface. All display a significant enrichment of the ^{18}O isotope with a sharp edge between the two regions and with minimal lateral diffusion. As discussed in Section 4.5.5, in most cases the profiles could not be accurately described by a step function, and instead a highly enriched region next to the edge is observed, which is expected to arise from nanoscopic Au particles caused by the balling up of the Au oxygen blocking layer (Fig. 4.15). In Fig. 6.16e, a spike in the isotopic fraction is observed from the Au covered region, away from the interface. The most likely cause for this was a scratch or pinhole through the Au layer allowing the ^{18}O enriched gas to contact the YSZ surface.

Figs. 6.16b, 6.16d, 6.16f and 6.16h show the ^{18}O distribution after the diffusion step after annealing for 14 hours at approximately 500°C for all films. For the films grown on MgO and Al_2O_3 the profiles are fitted using the numerical fitting method described in Section 4.5.5. It can be seen that this provides an excellent fit to the experimental data. For the films grown on LAO and NGO, the diffusivity was found to be significantly higher and hence the diffusion profiles could be accurately fitted using the analytical solution given in Eq. 4.21, as shown in Figs. 6.16f and 6.16h.

In Table 6.1 the diffusion coefficients, D^*, for the films analysed are listed. If more than one analysis was made on a film, then the displayed D^* value is an average of each measurement. The diffusion coefficients for the films were found to be in the range of $4{\times}10^{-11}$ to $6{\times}10^{-10}$ cm^2s^{-1}, in good agreement with 8 mol.% YSZ films grown on MgO, Al_2O_3 and STO and measured using a similar method by Gerstl *et al.* [118]. For films grown

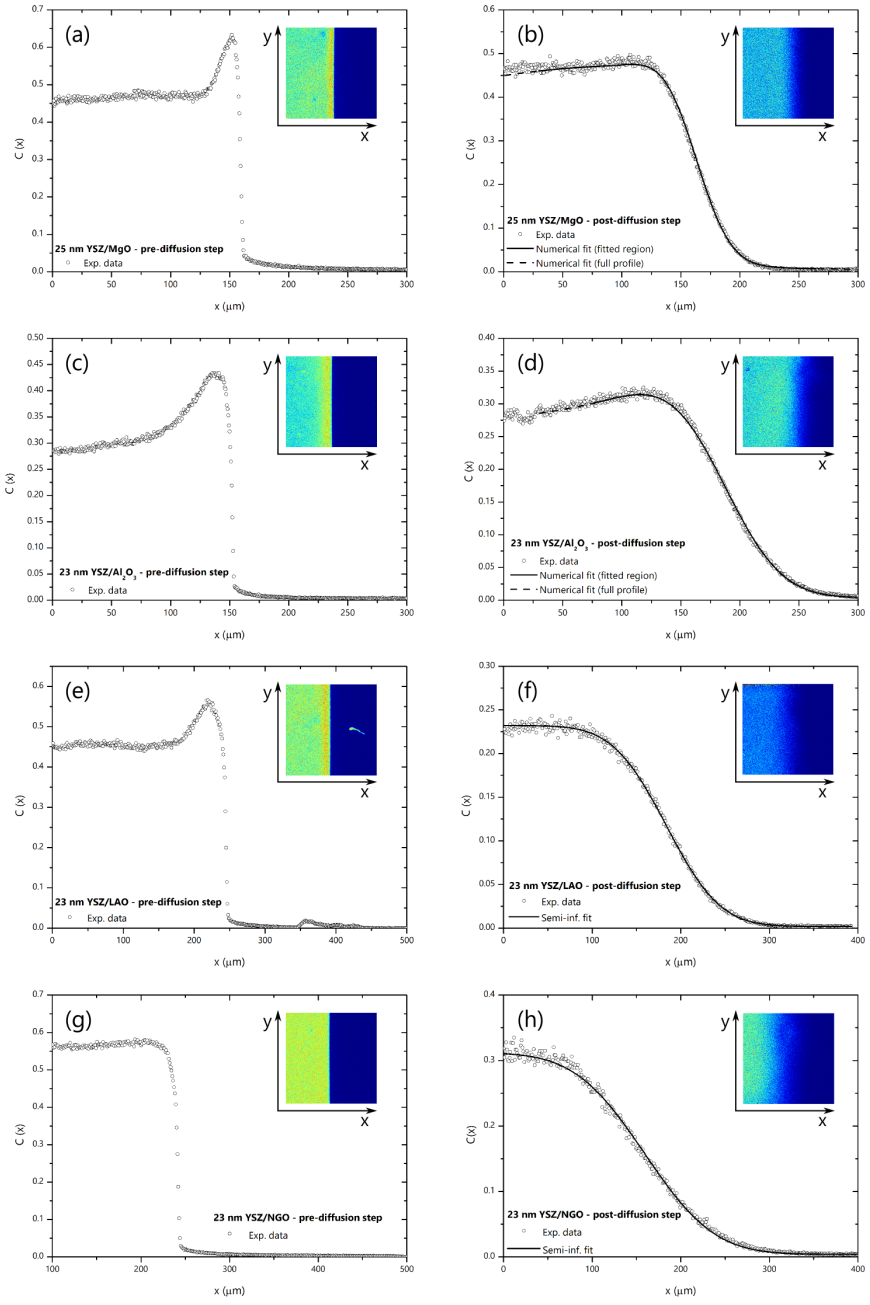


Figure 6.16: Lateral profiles of the ^{18}O isotope fraction for YSZ films grown on (a, b) MgO, (c, d) Al_2O_3, (e, f) LAO, (g, h) and NGO. The insets show the ^{18}O isotope fraction integrated in the z-axis direction. In (a, c, e, and g) the ^{18}O distribution across the Au covered and uncovered region is shown after the incorporation step of 30 minutes at 300°C in ^{18}O enriched gas. In (b, d, f, and h) the subsequent ^{18}O distribution after annealing for 14 hours at 500°C is shown. The profiles in (b and d) are fitted using the numerical method in Section 4.5.5, and the profiles in (f and h) are fitted according to Eq. 4.21.

on MgO and Al_2O_3, where nominally identical films have been measured by EIS, a Haven ratio, H_R, has been calculated and is displayed in Table 6.1. It is found to be between 0.25 and 0.69, which is comparable to the range of 0.33 to 0.48 measured in single crystal 9.5 mol.% YSZ [37]. This indicates that the electrical response in the EIS measurements was due to oxygen ion conductivity in the YSZ films, and that electrical leakage through the substrate did not significantly affect the EIS measurements for the films grown on MgO and Al_2O_3.

Isotope exchange tracer diffusion was also carried out on the YSZ films grown on Al_2O_3 by reactive sputtering. In Fig. 6.17, the ^{18}O isotopic fraction profiles are shown for the 100 nm and 6 nm thick film, after the incorporation step (Figs. 6.17a and 6.17c) and after the diffusion step (Figs. 6.17b and 6.17d). For these films the diffusion step used was $\sim$480°C, but for a much shorter period of 2 hours, as observed by the much narrower profiles. Both are fitted using the numerical procedure as above, which provides a good fit with the experimental data for the selected region, as seen in Figs. 6.17b and 6.17d. However in both cases, the simulated profile provides a poor description of the enriched region to the left of the position of the Au edge. This is attributed to changes in the initial ^{18}O distribution along the Au edge after the incorporation step due to variations in the morphology of the Au blocking layer at the edge.

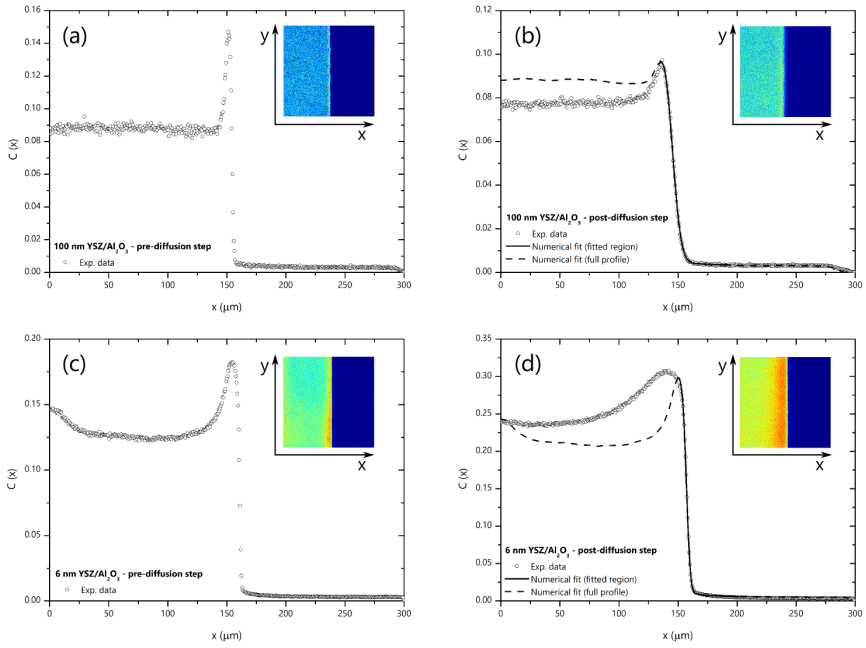


Figure 6.17: Lateral profiles of the ^{18}O isotope fraction for a 100 nm and 6 nm thick YSZ film grown by RF sputtering on Al_2O_3. The insets show the ^{18}O isotope fraction integrated in the z-axis direction. In (a and c) the ^{18}O distribution across the Au covered and uncovered region is shown after the incorporation step of 30 minutes at 300°C in ^{18}O enriched gas. In (b and d) the subsequent ^{18}O distribution after annealing for 2 hours at 480°C is shown. The profiles in (b and d) are fitted using the numerical method described in Section 4.5.5.

Growth Method	mol. %	Sub.	Growth Temp. (°C)	d (nm)	Sample	(111) vol. (%)	(111) peak a_{YSZ} (nm)	(111) peak Strain (%)	(100) peak a_{YSZ} (nm)	(100) peak Strain (%)	EIS or IETD	σ (S/cm) *(from IETD)*	D* (cm^2s^{-1})	Temp. (°C)	Ea (eV)	H_R	Remarks
PLD	8	MgO	700	200	A	93.5	5.272	2.59	5.174	0.68	EIS	1.76×10^{-4}	-	512	1.31	-	TEM
				200	B	94.8	5.272	2.59	5.180	0.81	IETD	*8.65×10^{-5}*	1.57×10^{-10}	497	-	0.49	
				50		76.1	5.275	2.64	5.188	0.95	EIS	1.23×10^{-4}	-	506	1.39	-	PF
				25	A	>95	5.256	2.29	-	-	EIS	1.22×10^{-4}	-	506	1.41	-	
				25	B	>95	5.248	2.13	-	-	IETD	*3.27×10^{-5}*	5.95×10^{-11}	500	-	0.27	
				11		33.7	5.266	2.47	5.178	0.77	IETD	*2.25×10^{-5}*	4.12×10^{-11}	502	-	-	
			600	110	A	96.8	5.278	2.71	5.185	0.89	EIS	1.50×10^{-4}	-	506	1.39	-	
				110	B	95.8	5.281	2.76	5.184	0.88	-	-	-	-	-	-	
				110	B	>95	5.164	0.49	-	-	EIS	1.17×10^{-4}	-	507	1.40	-	Post-1000°C
		Al_2O_3	600	185	A	89.1	5.229	1.74	5.169	0.58	EIS	2.03×10^{-4}	-	505	1.32	-	TEM
				185	B	96.0	5.228	1.73	5.172	0.64	IETD	*1.40×10^{-4}*	2.54×10^{-10}	497	-	0.69	
				110	A	98.0	5.230	1.77	5.169	0.59	-	-	-	-	-	-	
				110	A	95.4	5.218	1.54	5.164	0.49	EIS	2.61×10^{-4}	-	506	1.27	-	Post-800°C
				110	B	92.3	5.234	1.85	5.169	0.58	-	-	-	-	-	-	
				110	B	97.3	5.131	-0.16	5.134	-0.10	EIS	3.69×10^{-4}	-	507	1.28	-	Post-1000°C - TEM
				46	A	98.3	5.248	2.12	5.178	0.76	EIS	1.45×10^{-4}	-	506	1.31	-	PF
				23	A	>95	5.252	2.19	-	-	EIS	1.25×10^{-4}	-	507	1.32	-	
				23	B	>95	5.252	2.19	-	-	IETD	*8.13×10^{-5}*	1.49×10^{-10}	504	-	0.65	
				10	A	>90	5.255	2.26	-	-	EIS	1.24×10^{-4}	-	504	1.25	-	
				10	B	>90	5.252	2.19	-	-	IETD	*3.14×10^{-5}*	5.74×10^{-11}	502	-	0.25	
		LAO	600	182		<5	-	-	5.168	0.56	IETD	*3.15×10^{-4}*	5.72×10^{-10}	497	-	-	TEM
				46		<5	-	-	5.173	0.66	-	-	-	-	-	-	PF
				23		<5	-	-	5.171	0.63	IETD	*1.26×10^{-4}*	-	504	-	-	
				10		<10	-	-	5.154	0.30	IETD	*1.20×10^{-4}*	2.19×10^{-10}	502	-	-	TEM
		NGO	600	182		<5	-	-	5.172	0.65	IETD	*2.84×10^{-4}*	5.15×10^{-10}	497	-	-	PF
				46		<5	-	-	5.171	0.63	-	-	-	-	-	-	
				23		<5	-	-	5.163	0.47	IETD	*2.97×10^{-4}*	5.45×10^{-10}	504	-	-	
				10		<10	-	-	5.167	0.54	IETD	*1.29×10^{-4}*	2.35×10^{-10}	502	-	-	
RF sput.	9	Al_2O_3	650	100		>95	5.218	1.54	-	-	IETD	*4.07×10^{-5}*	4.60×10^{-11}	479	-	0.28	
				6		>95	5.254	2.23	-	-	IETD	*5.67×10^{-6}*	6.40×10^{-12}	479	-	0.0041	

Table 6.1: Details of the YSZ films in this study. The thicknesses are extrapolated from the samples studied by TEM, which is noted. The samples labelled A, B, C, or D are used for referring to the XRD spectra shown in Appendix A.2. The lattice parameters are calculated from the XRD $\theta/2\theta$ (111) and (200) peaks. The temperature given is that for the transport measurement by either EIS or IETD. PF and TEM refers to the samples the pole figures and TEM images were taken from.

The D^* values extracted from the fits in Figs. 6.17b and 6.17d, are listed in Table 6.1. The diffusivity of the 100 nm thick films is comparable to those measured for the films grown by PLD, however the 6 nm thick film yields by far the lowest diffusivity of all the films and is reduced by a factor of over seven compared to its thicker counterpart. From the conductivity data taken from Ref. [119], the Haven ratio was calculated for the two films. The 100 nm thick films yields a $H_R = 0.28$, within the range of those calculated for the PLD grown films. However for the 6 nm thick films it is dramatically lower, yielding a Haven ratio of 0.0041.

6.4 Discussion

6.4.1 Orientation and Substrate Mismatch

From the XRD $\theta/2\theta$ scans and pole figures the dominant orientation relationship for the YSZ films grown on MgO is given by:

YSZ (111)||MgO (001)

In plane, four discrete orientations were observed, each related by either a 90° or a 180° rotation in the azimuth, as shown schematically in Fig. 6.18a. From the relationships given above it can be seen that for each orientation the family of YSZ (112) planes is parallel to the family of MgO (110) planes. The atomic spacing of the close packed Zr cations is equal to 3/2 of the lattice spacing, $d_{YSZ(112)}$, of the YSZ (112) planes. For MgO the atomic spacing of the close packed O anions is equal to the (110) spacing, $d_{MgO(110)}$. Using the lattice parameters in Table 6.2, the lattice mismatch in this direction can be calculated as

$$f_{MgO(110),YSZ(112)} = \frac{d_{MgO(110)} - \frac{3}{2}d_{YSZ(112)}}{\frac{3}{2}d_{YSZ(112)}} = -5.34\% \qquad (6.1)$$

Due to the different symmetries of the YSZ (111) and MgO (100) planes, the lattice mismatch is different for the two in-plane perpendicular directions. For the YSZ (110) planes parallel to the MgO (110) planes, the Zr spacing

Substrate	Structure, Space Group	Lattice Paramters ($\AA$)	Reference
MgO	Rocksalt, $Fm\bar{3}m$	a= 4.124	Ref. [215]
Al_2O_3	α-corundum, $R\bar{3}$c	a = 4.754	Ref. [58]
		c=12.99	
LAO	Perovskite, $Pm\bar{3}m$	a=3.791	Ref. [235]
NGO	Perovskite, $Pbnm$	a=5.380	Ref. [236]
		b=5.413	
		c=7.621	

Table 6.2: Structural data for the substrates used. a, b, and c are the lattice constants.

is equal to the lattice spacing, $d_{YSZ(110)}$, of the YSZ (110) planes, and so

$$f_{MgO(110),YSZ(110)} = \frac{d_{MgO(110)} - d_{YSZ(110)}}{d_{YSZ(110)}} = -17.8\%. \qquad (6.2)$$

These are equivalent for each of the in-plane orientations of the YSZ grains. Such a large lattice mismatch would almost certainly result in dislocations forming along the interface, however these could not be observed by TEM. Hence the values here represent the upper limit of the strain occurring at the substrate-film interface.

For the YSZ films grown on Al_2O_3, the dominant out-of-plane orientation is given by:

YSZ (111)||Al_2O_3 (0001)

From the XRD pole figures and SAED patterns, it was shown that two in plane orientations existed for the grains, each related by a rotation of 60° or a mirror inversion, shown in Fig. 6.18b. From the relationships given in Section 6.2.2, one may see that for the two orientations the YSZ (110) planes are aligned along the Al_2O_3 ($\bar{1}$100) planes. As before, the spacing of the Zr cations are equal to the lattice spacing, $d_{YSZ(110)}$, and the close packed spacing of the O anions is equal to 1/3 of the lattice spacing, $d_{Al_2O_3(\bar{1}100)}$, in Al_2O_3. From the HR-TEM analysis, a dislocation occurs every 4 or 5 columns (1/2 of $d_{Al_2O_3(1100)}$), therefore between a 4:5 and 3:4

commensurability.

$$f_{Al_2O_3(\bar{1}100),YSZ(110)} = \frac{4(5)\frac{1}{3}d_{Al_2O_3(\bar{1}100)}3(4)d_{YSZ(110)}}{3(4)d_{YSZ(110)}} = 0.703(-5.59)\%. \tag{6.3}$$

Hence, depending on the exact density of the dislocation network, the lattice mismatch is between +0.703 and -5.59%. In the perpendicular direction, The atomic spacing of the close packed O anions is equal to the lattice spacing $d_{Al_2O_3(\bar{1}\bar{1}20)}$, in Al_2O_3, however no information on the dislocation density could be obtained from the TEM analysis.

$$f_{Al_2O_3(\bar{1}\bar{1}20),YSZ(112)} = \frac{\frac{3}{2}d_{Al_2O_3(\bar{1}\bar{1}20)}\frac{3}{2}d_{YSZ(112)}}{\frac{3}{2}d_{YSZ(112)}} = 24.47\%. \tag{6.4}$$

As with the YSZ/MgO interface, this represents the upper limit of the interfacial strain.

From the XRD analysis and SAED the out-of-plane orientation for the YSZ films grown on LAO substrates was confirmed to be:

YSZ (100)||LAO (100)

As shown schematically in Fig. 6.18c, a single in-plane orientation was observed. LAO adopts the perovskite crystal structure, with a slight distortion from the cubic symmetry $\alpha = 90.096$, however this is expected to have little impact here and the structure is treated as cubic. The surface termination of the perovskite oxides is commonly thought to be AO plane terminated [237]. For an AO surface the atomic spacing between the atomic O anions is equal to the LAO (001) lattice spacing, $d_{LAO(001)}$, along the (001) plane. The spacing of the Zr cations on the YSZ (110) plane is equal to the lattice spacing, $d_{YSZ(110)}$. From the HR-TEM imaging, a dislocation was found to occur on average every 27 YSZ (220) planes. Hence assuming a 27:26 commensurability the lattice mismatch is calculated as:

$$f_{LAO(001),YSZ(110)} = \frac{26\, d_{LAO(001)} - 27\, d_{YSZ(110)}}{27\, d_{YSZ(110)}} = 0.44\%. \tag{6.5}$$

For the YSZ films grown on NGO substrates the following orientation

were observed by XRD:

YSZ (100)||NGO (110)

NGO is a perovskite material which adopts an orthorhombic crystal structure. A single in-plane orientation was found according to the analysis from pole figures and SAED. The spacing between the O anions in the NGO $[00\bar{1}]$ direction is equal to the NGO (001) spacing, and the NGO (110) spacing in the $[0\bar{1}0]$ direction. The dislocation density from the TEM was found to occur on average every 16.6 YSZ (220) planes. Therefore assuming the density of dislocations are the same in both in-plane directions, and a commensurability of 83:78 the lattice mismatch is given by

$$f_{NGO(001),YSZ(011)} = \frac{78\, d_{NGO(001)} - 83\, d_{YSZ(011)}}{83\, d_{YSZ(011)}} = 0.13\%. \tag{6.6}$$

$$f_{NGO(110),YSZ(011)} = \frac{78\, d_{NGO(110)} - 83\, d_{YSZ(011)}}{83\, d_{YSZ(011)}} = 0.15\%. \tag{6.7}$$

Once again for all substrates it is clear the observed strain in the lattice cannot be satisfactorily explained by considering only the substrate lattice mismatch. The cause of the strain observed is not clear at this point, as extensively discussed in Chapter 5. Only the films grown on Al_2O_3 showed a clear trend as the thickness was decreased, which could conceivably be due to an additional interfacial strain, which is independent from the cause of the strain in the thicker films.

6.4.2 Oxygen Ion Transport

Activation Energy

The activation energies of all the films measured by EIS were found to be significantly higher (1.3-1.5 eV) than that expected for a single crystal (∼1.1 eV). One must consider that for the temperature regime investigated in this study (<600°C) the activation energy will be a sum of the free migration

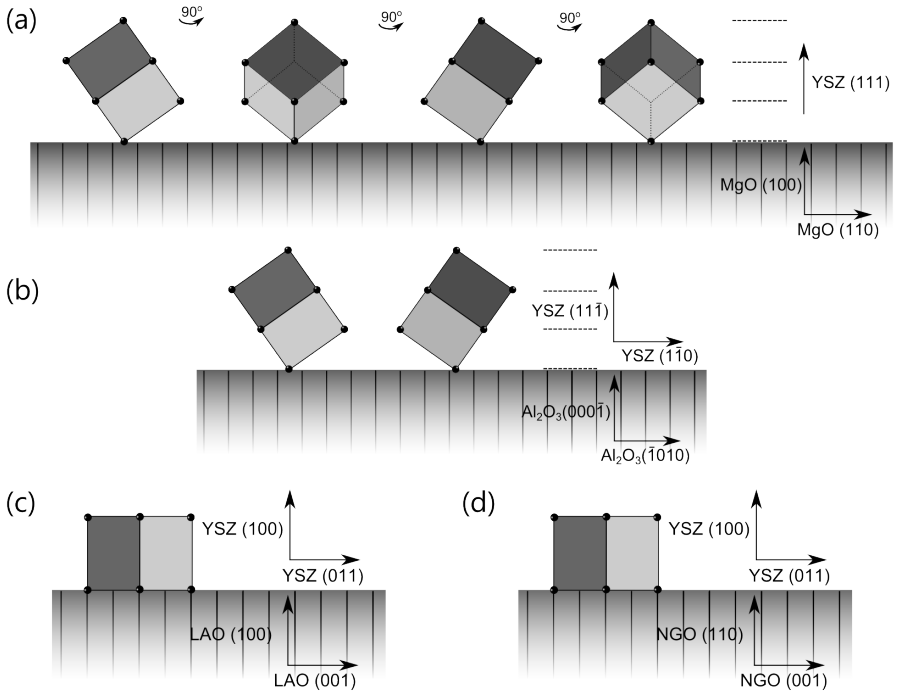


Figure 6.18: Schematic showing the preferential orientations of the YSZ films on (a) MgO, (b) Al_2O_3, (c) LAO, and (d) NGO substrates.

enthalpy and the free association enthalpy.

$$E_A = \Delta H_m + \Delta H_A \tag{6.8}$$

For 9.5 mol.% single crystal YSZ, ΔH_m and ΔH_A have been measured to be 0.89 eV and 0.21 eV respectively [37]. As discussed in Section 2.3.2, lattice strain is expected to affect both these terms due to a change in the migration and association volume. However for the films in this study no trend in the activation energy is seen with lattice parameter, even due to the dramatic change after the high temperature heat treatment.

As the grain and grain boundary responses could not be separated in the Nyquist plots (Fig. 6.12), the activation energy of the grain boundaries may influence or even dominate the total electrical response. The activation energy of the grain boundaries in polycrystalline 8 mol.% has been measured to be 1.16 eV, which is substantially higher that the bulk [238]. Although this does not account for the observed magnitude of the activation energy in the films, grain boundary properties may be highly dependent upon factors such as impurities and thermal history. Work on nano-granular YSZ has shown a variation in the activation energy of the grain boundaries with varying grain size [77], and 8 mol.% YSZ films grown by PLD have previously been reported to have a grain boundary activation energy up to 1.3 eV [117] and 1.38 eV [118].

Substrate Mismatch, Film Thickness, and Lattice Spacing

A simple comparison of the absolute magnitude of the conductivity and diffusivity with other experimental studies may be misleading due to variations between the systems such as the YSZ composition, impurity content, microstructure, and thermal history. If the total conductivity, σ_{tot}, of the layers is modified by a strained interfacial region of thickness, δ_0, then one would expect to observe a change in σ_{tot} as the total thickness of the film, d, is varied. Assuming parallel diffusion paths through the strained and unstrained regions, it may be shown that [58]:

$$\sigma_{tot} = \sigma_{vol} + \delta_0(\sigma_{int} - \sigma_{vol})\frac{1}{d}, \tag{6.9}$$

where σ_{vol} and σ_{int} are the conductivities in the strained and unstrained regions of the film. This is a somewhat simplified version of the model discussed in Section 2.3.2, assuming strained interface regions with an unrealistically uniform conductivity, however for the purposes here the model will be sufficient. Normalising the observed conductivity σ_{tot}, to that of the unstrained region, σ_{vol}, it follows that:

$$\frac{\sigma_{tot}}{\sigma_{vol}} = 1 + \frac{\delta_0}{d}\left(\frac{\sigma_{vol}}{\sigma_{int}} - 1\right) \tag{6.10}$$

Due to the small size of the grains at the interface, observed to be 5-30 nm from the TEM analysis, it would be expected that the lattice strain due to the lattice mismatch would decay over a short length such that for the films where $d > 180$ nm, the width of the strained region $\delta_0 << d$. Therefore for the film where $d > 180$ nm, the conductivity measured, σ_{tot}, should be well approximated by σ_{vol}. By plotting $\frac{\sigma_{tot}}{\sigma_{vol}}$ against reciprocal thickness, $\frac{1}{d}$, one would expect a linear relationship if $d > \delta_0$ with a slope of $\delta_0(\sigma_{int}/\sigma_{vol} - 1)$. Once the thickness of the film was less than the strained region $d < \delta_0$, then the measured conductivity would remain constant with thickness ($\sigma_{tot} = \sigma_{int}$).

Although this model has been applied to diffusivity coefficients, D^*, measured by IETD previously [63, 129, 130], the assumption of parallel diffusion paths does not apply to tracer experiments, where diffusion perpendicular to the interface plane will readily take place [152]. Due to the extreme thinness of the films in comparison to the lateral dimensions of the diffusion profiles, it may be assumed that the observed diffusivity is due to the fastest path in the film. Hence taking the analogue of Eqs. 6.9 and 6.10 for D^*, one would expect that $D^*_{tot} = D^*_{int}$ if $D^*_{int} > D^*_{vol}$ for all thicknesses. Alternatively, if $D^*_{int} < D^*_{vol}$, then $D^*_{tot} = D^*_{vol}$ for $d > \delta_0$ and $D^*_{tot} = D^*_{int}$ for $d \leq \delta_0$.

In Fig. 6.19, the measured σ and D^* measured at ~500°C for all films grown by PLD is normalised to that of the thickest films and is plotted against reciprocal film thickness. The lines are a guide to the eye and do not represent any fitting. It may be observed that all films show a reduction in the transport properties as the thickness of the layers are decreased. For the YSZ films grown on MgO and Al_2O_3 measured by EIS, the conductivity

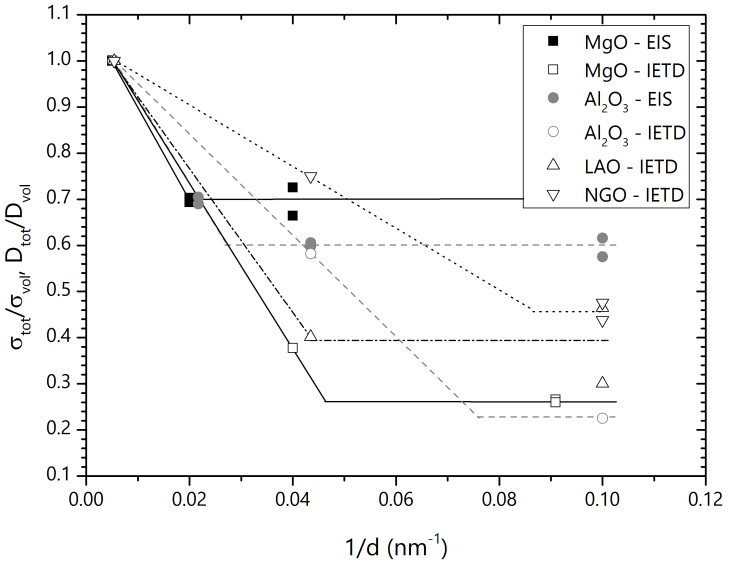


Figure 6.19: Normalised sample conductivity, $\sigma_{tot}/\sigma_{vol}$ and diffusivity D_{tot}/D_{vol} to the values obtained for the thickest films as a function of reciprocal lattice parameter. The lines are only present as a guide to the eye and do not represent any fitting.

drops initially to 0.6-0.7 of the original values as the thickness is reduced from >180 nm (>0.0056 nm^{-1}) to ≤50 nm (<0.04 nm^{-1}), but shows little change in thinner films. If the conductivity is modified by a strained layer at the interface, then the plateau in the relative conductivity would imply that $\delta_0 > 50$ nm. The normalised D^* values for the films also show a relative reduction in magnitude to 0.2-0.5 of the initial values as the film thickness is decreased, regardless of the substrate. From the considerations above this would imply a region with modified transport extending to $\delta_0 > 20$ nm. However it seems unlikely that the strain would be compressive for all films regardless of mismatch and that the strained region would extend so far away from the interface due to the small grains as observed by TEM.

As discussed above, one must bear in mind that due to the inability to separate bulk and grain boundary paths in the EIS Nyquist plots (Fig. 6.12), and therefore the total conductivity measured consists of both components. From the TEM analysis in Fig. 6.8, it may be clearly seen that the size of the grains is not uniform with thickness. It would be non-trivial to obtain an accurate distribution of the grain sizes with thickness, but as an approximation the grains were taken to be 30-70 nm for the region greater than ∼70 nm from the interface, and 5-30 nm for the region in closer proximity to the substrate. As discussed in Section 2.3.1, the specific conductivity of the grain boundary, σ_{gp}^{sp}, in YSZ is typically found to be at least two orders of magnitude lower than that of bulk, σ_{bulk}^{sp}. Therefore, due to the high density of grain boundaries, the total resistance of the films will be heavily dependent on the grain boundary resistance, $R_{tot} \propto R_{gb}$. It follows that the conductivity measured for the films will be dependent upon

$$\sigma_{tot} \propto \frac{Ld}{D}\sigma_{gb}^{sp}\frac{d_g}{\delta_{gb}} \tag{6.11}$$

where L is the length of the electrodes and D the distance between them, d_g the grain width, and δ_{gb} the grain boundary width. It can been seen that the total conductivity measured in the films σ_{tot} should be proportional to the grain size, d_g. Therefore a decrease in the average grain size from 30-70 nm to 5-30 nm would account account for the drop in the transport properties at reduced layer thicknesses. The effect would be more pronounced for the

transport measured by tracer diffusion, as the diffusivity measured is due to the fastest transport path in the material. Hence for the thick films (>180nm), the diffusivity measured is only due to the region of the films with large grain size and there would be no contribution from the interfacial region as with EIS. This model agrees well with results shown in Fig. 6.19, and therefore we may assume that the density of grain boundaries in the films plays a significant role in the transport properties.

To investigate the effect of lattice strain caused by substrate mismatch and layer thickness on the transport properties in the films, the conductivity measured by EIS and IETD is plotted for the films grown by PLD as a function of lattice parameter in Fig. 6.20a. The error bars for the data obtained by EIS were calculated as described in Appendix A.4. The uncertainty in the σ values obtained by IETD should be dominated by changes in the edge of the Au blocking layer between the areas used to map the ^{18}O distribution before and after the diffusion step. This could not be analytically determined and hence an upper limit of 10% error is assumed. The highest conductivity was found by IETD in the 183 nm thick films grown on LAO and NGO substrates. Comparing films with similar thickness the transport was always found to be higher in the films grown on LAO and NGO compared to MgO and Al_2O_3, however no immediate trend with lattice parameter is obeyed for all films.

Comparison between the films in Fig. 6.20a is challenging. The differing orientations of the films on each substrate implies grain boundaries with varying symmetry, which have previously been shown to have varying specific conductivities [53]. Also from Fig. 6.19, it has been shown that the transport is depressed as the thickness is reduced for each substrate, which is most likely caused by a decrease in the grain size at the interface. Furthermore, measurements by EIS and IETD are not directly comparable for different film thicknesses, also due to the anisotropy of the grain size distribution.

Therefore to isolate the effect of the lattice spacing on the oxygen transport, films of similar thickness were annealed to relax the lattice parameter for comparison with films grown on the same substrate. From the TEM images in Fig. 6.8, it may be seen that no significant coarsening of the

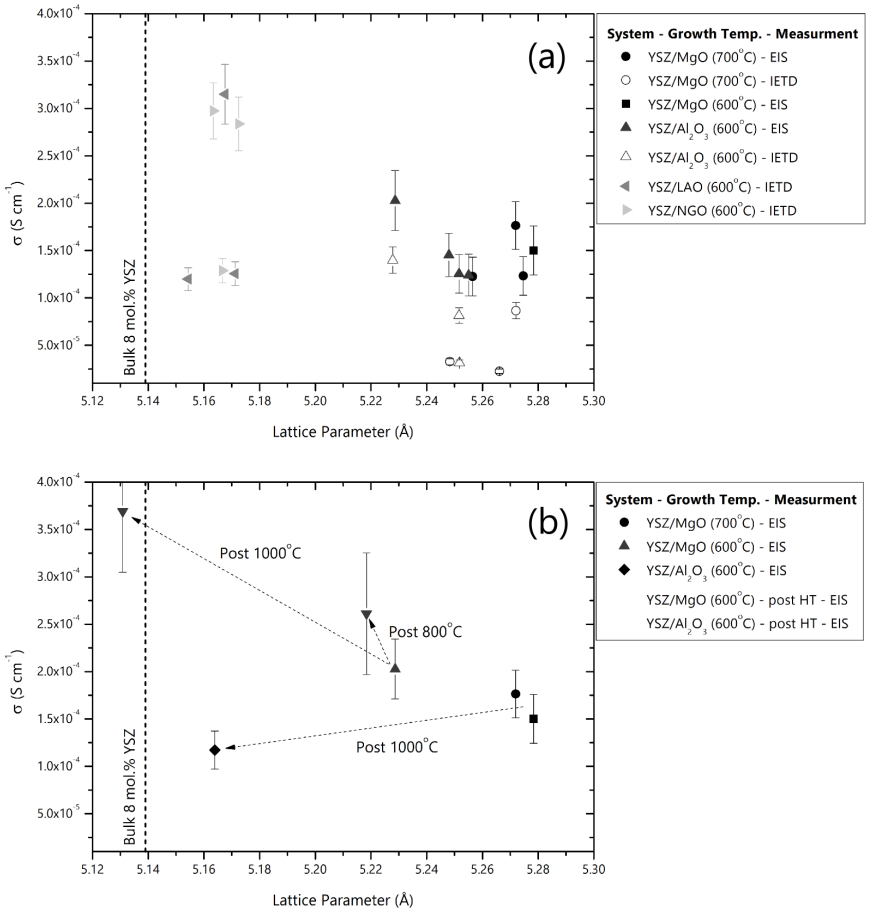


Figure 6.20: Conductivity measured by EIS and IETD for the films as a function of lattice parameter. All the measurements were carried out at approximately 500°C as detailed in Table 6.1. (a) shows the as-grown films with no heat treatment other than the diffusion conductions or the electrode sintering. (b) shows the comparison between the as-grown films and the films after a high temperature (≥800°C) anneal.

grains is observed, even after a heat treatment of 1000°C for 6 hours. For the layers grown on Al_2O_3, the conductivity increased by a factor of 1.8 as the lattice spacing relaxed back to close to the bulk parameter. This would suggest a significant decrease in the conductivity has been achieved due to the strain induced in the films grown on Al_2O_3. However the same trend was not observed for films grown on MgO, where only slight decrease in the conductivity is observed despite a dramatic reduction in the lattice parameter. The source of the different response of these two systems to a change in lattice parameter is not clear at present. A better understanding of the change in the lattice volume, rather than simply the out-of-plane lattice parameter may help to elucidate the causes of these findings.

Dislocations

Dislocations form due to stress fields in ceramics, thereby limiting the strain present at interfaces. However as discussed in Section 2.3.2, dislocations represent a highly localised strain field and may present a path for enhanced oxygen ion diffusivity. In a number of studies on the transport of heterogeneous interfaces, the presence of dislocations are used to explain dramatic increases in the conductivity, as reviewed in Chapter 3.

At the interface between the YSZ films and the Al_2O_3 substrates, a high density of dislocations were observed such that the missing plane occurred in the YSZ film. This would result in an expansive strain field in the YSZ and compressive strain field in the substrate. The effect is the opposite at the YSZ/LAO and YSZ/NGO interfaces, where a compressive strain field is observed in the YSZ and expansive in the substrates. At the YSZ/MgO interface a high density of dislocations, with the tensile field in the YSZ is expected, however this could not be confirmed.

Across the range of thin films grown, a high density of both types of dislocation are observed at the interface, yet none display a dramatic enhancement in the conductivity such as that observed by Kosacki *et. al.* [106, 107], Karthikeyan *et. al* [114] and Sillassen *et. al.* [115]. As discussed above, there is evidence to suggest that the distribution of grain boundaries, the texture, and the lattice strain each play a role in dictating the transport properties

in the films, and therefore isolating the contribution of the dislocations is not possible.

Recalling that the diffusivity measured by IETD will be representative of the fastest transport path in the material, one would expect to see an increase in the diffusivity over that expected for single crystals if dislocations did facilitate enhanced ionic transport. However, the diffusivity was found to be lower than that of single crystal for all films, and hence a significant improvement in the ionic transport seems unlikely.

YSZ/Al_2O_3 Films Fabricated by RF Sputtering

From the EIS measurement reported in Ref. [119], an approximately nine fold increase in the conductivity is expected for YSZ films grown on Al_2O_3 by RF sputtering, however from the IETD measurements in this work a seven fold *decrease* was observed. This contradiction is apparent in the Haven ratios calculated using the EIS data from Ref. [119]. For the 100 nm thick film, a Haven ratio of 0.2 is calculated, which is in reasonable agreement, and similar to the ratios calculated for some of the PLD films and from other studies [37, 118]. However, for the 6 nm thick film the Haven ratio is 0.0041 and therefore a 50 times increase in the diffusivity would be required to achieve a ratio of 0.2 with the EIS data.

Comparing the films grown by PLD and RF sputtering, both sets have the same orientation relationship as characterised by XRD, and comparable lattice strain as determined from the out-of-plane lattice parameter. In addition, from the TEM data published in Ref. [119] and that performed on the PLD grown films in this work, one may see that the microstructures are similar with columnar grains 10-20 nm in width and dislocations observed for each set. Therefore, if the results reported employing EIS did represent oxygen transport in the films, the absence of any enhancement in the conductivity seen for the PLD grown films in this study, does not support the attribution of either dislocations or lattice strain as the cause of the observed improvement in the conductivity as discussed in Ref. [119].

6.5 Conclusion

YSZ thin films have been fabricated by PLD onto MgO, Al_2O_3, LAO, and NGO substrates, representing a range of compressive and expansive lattice mismatches. The films were found to be highly textured, each displaying preferential orientation both out-of-plane and in-plane. All films were found to be strained to varying extents, however the expanded out-of-plane lattice parameter could not be accounted for by purely considering the lattice mismatch originating from the substrates, and the exact cause remains elusive. From TEM analysis, all films were found to display a columnar structure, with grains separated by low-angle grain boundaries. The substrate-film interfaces were all found to be sharp and a high density of dislocations was found for films grown on Al_2O_3, LAO, and NGO substrates.

The oxygen ion conductivity of the films was assessed by EIS and IETD, with both results in good agreement. Despite considerable lattice strain and a large number of dislocations, none of the films displayed an enhancement in the transport properties above that of single crystal YSZ, when measured by either EIS or IETD. As the thickness of the films was decreased the conductivity and diffusivity were found to decease for all films, regardless of the mismatch or lattice strain. This was attributed to anisotropic distribution of grain boundaries, whereby the grain size decreased in close proximity to the interface. After annealing at high temperature, the lattice parameter of the films was found to relax toward the bulk lattice spacing. This was accompanied by a 1.8 fold increase in the conductivity for films grown on Al_2O_3, although no substantial change was observed for films grown on MgO.

In addition, YSZ films grown on Al_2O_3 by RF sputtering, fabricated by Dr. Jun Jiang and Prof. Josh Hertz at the University of Delaware (Newark, USA), in an identical fashion to those reported upon in Ref. [119], were also analysed by IETD in an attempt to confirm the enhancement in the conductivity observed by EIS. However, no increase in the diffusivity was found, and a dramatic decrease was observed for the thinnest film. The findings here cast considerable doubt of the validity of the previously reported results.

Chapter 7

Surface Segregation in Strained CGO Films

As discussed in Chapter 3, the effects of interfacial lattice strain on the transport properties of ionic conductors have been widely studied, albeit with inconsistent findings. Segregation to dopants to surfaces in such films is rarely considered, however as the thickness of films are reduced the volume fraction of the surface and subsurface region increases and will potentially have a much greater effect on the total properties of the system. In this chapter, the segregation of Gd to the surface of CGO films is investigated, exploring the effects of thermal treatment at times and temperatures similar to those typically used for the sintering of electrodes or transport measurements.

To date, most work on dopant segregation in the fluorite oxides has been focused on bulk materials after exposure to sintering temperatures. However, thin films devices, such as μSOFCs, which operate at temperatures similar to the fabrication temperature of the system, have gained increased interest. An understanding of the segregation effects in these systems is vital for commercialisation.

In addition, the interplay between the degradation effects and induced strain has been entirely overlooked. In this chapter, the effects of surface orientation and lattice strain on the Gd segregation will also be discussed.

7.1 Sample Production

The films discussed in this chapter were fabricated using PLD by the author, as described in Section 4.1, from a 10 mol.% CGO target prepared according to the description given in Section 4.1.2. The substrates used were (100) oriented LAO, (100) oriented STO (Pi-Kem ltd., UK), and (0001) oriented Al_2O_3 (MaTeck Material Technologie & Kristalle GmbH, Germany). The nominal substrate temperature during fabrication was 700°C for films grown on STO and LAO, and 600°C for films grown on Al_2O_3. The thickness of the films was varied by changing the number of pulses used during deposition. The layer thicknesses quoted hereafter are estimates taken from TEM imaging done on a film fabricated under identical conditions.

The heat treatments of the as-grown films were performed using a tubular furnace, in a clean alumina tube under static laboratory air. A heat rate of 10°/min was used, followed by a dwell at the desired temperature for two hours, after which the samples were quickly removed and quenched back to room temperature, in order to freeze in the surface segregation.

After the heat treatment, the samples were cleaned for 5 minutes in an ultrasonic bath in acetone followed by ethanol and then ultra-pure Milli-Q water. They were then quickly dried using ash-free paper and loaded directly into the LEIS. Once under high vacuum, samples were cleaned using atomic oxygen to remove hydrocarbon contamination from the laboratory air while periodically analysing the surface using ^{4}He primary ions to monitor the surface species. Once the LEIS spectra showed minimal change upon further oxygen cleaning, the primary ion was switched to ^{20}Ne to resolve the Ce and Gd masses, and a Ar ion sputter gun used to obtain information as a function of depth.

7.2 Structural Characterisation

7.2.1 Orientation and Texture

XRD $\theta/2\theta$ scans were obtained for the films to assess the out-of-plane orientation. Fig. 7.1 shows typical scans taken from CGO films grown on Al_2O_3,

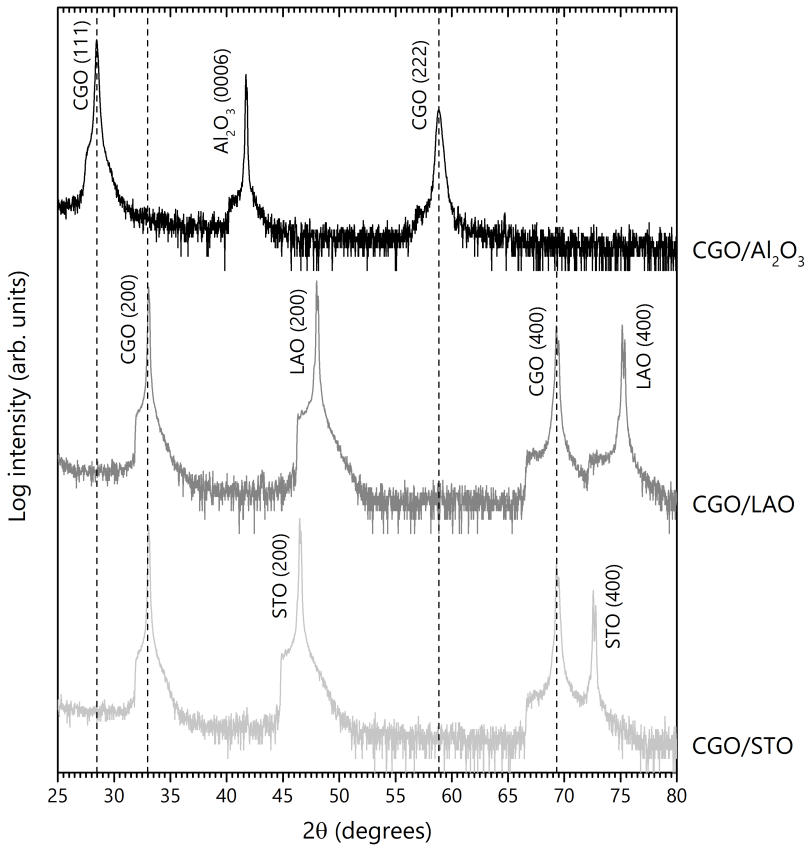


Figure 7.1: XRD $\theta/2\theta$ spectra for 330 nm thick CGO films deposited on Al_2O_3, LAO and STO substrates.

LAO and STO substrates. Well defined peaks are observed for each, implying highly crystalline layers. For all films discussed in this chapter, a single orientation was observed in the XRD $\theta/2\theta$ scans. For CGO layers grown on Al_2O_3, only peaks relating to the (111) orientation are observed, whereas for LAO and STO only peaks from the (100) orientation are visible in the patterns.

To assess the in-plane orientation of the films, pole figures were taken for a film grown on each substrate and are displayed in Fig. 7.2. Scans around the (111) Bragg reflections are displayed for each CGO layer as well as a reflection from the substrate. The film and substrate scans were obtained

without removing the samples from the diffractometer, and hence the signal in the ϕ-axis may be compared to obtain the orientation relationships.

Figs. 7.2a and 7.2b, show the CGO (111) and Al_2O_3 (104)[1] reflections for an 83 nm thick CGO film. In Fig. 7.2a, one maxima is seen at $\phi = 0°$, and three maxima are observed at $\psi = 70.5°$, which correspond to an out-of-plane orientation of (111), as found from the $\theta/2\theta$ scans. The peaks at $\psi = 70.5°$ are equally spaced, implying a single in-plane orientation of the CGO films. Furthermore it may be seen that the maxima are found at the same ϕ position as the (104) peaks from the Al_2O_3 substrate. The following orientation relationship is inferred between the film and substrate:

$$\text{CGO } (111)||\text{Al}_2\text{O}_3 \text{ } (0001)$$

$$\text{CGO } [01\bar{1}]||\text{Al}_2\text{O}_3 \text{ } [11\bar{2}0]$$
$$\text{CGO } [2\bar{1}\bar{1}]||\text{Al}_2\text{O}_3 \text{ } [1\bar{1}00]$$

For easy visualisation the orientation between the CGO film and Al_2O_3 substrate is shown schematically in Fig. 7.3a. In the (112) direction, the spacing of the Ce cations is equal to 3/2 of the lattice spacing, $d_{CGO(112)}$, of the CGO planes, and in the (011) direction, the Ce cations are separated by 1/2 the lattice spacing, $d_{CGO(110)}$. For Al_2O_3, the close packed spacing of the O anions is equal to the lattice spacing, $d_{Al_2O_3(11\bar{2}0)}$, in the $(11\bar{2}0)$ direction and equal to 1/3 the lattice spacing, $d_{Al_2O_3(1\bar{1}00)}$, in the $(1\bar{1}00)$ direction. Therefore the theoretical lattice mismatches in each direction may be calculated according to:

$$f_{Al_2O_3(11\bar{2}0),CGO(01\bar{1})} = \frac{d_{Al_2O_3(11\bar{2}0)} - \frac{1}{2}d_{CGO(011)}}{\frac{1}{2}d_{CGO(011)}} = 24.09\%. \qquad (7.1)$$

$$f_{Al_2O_3(1\bar{1}00),CGO(2\bar{1}\bar{1})} = \frac{\frac{1}{3}d_{Al_2O_3(1\bar{1}00)} - \frac{3}{2}d_{CGO(211)}}{\frac{3}{2}d_{CGO(211)}} = -58.64\%. \qquad (7.2)$$

Both calculated values are much higher than would be expected to yield a

[1] $(10\bar{1}4)$ in 4-axis Miller-Bravais notation.

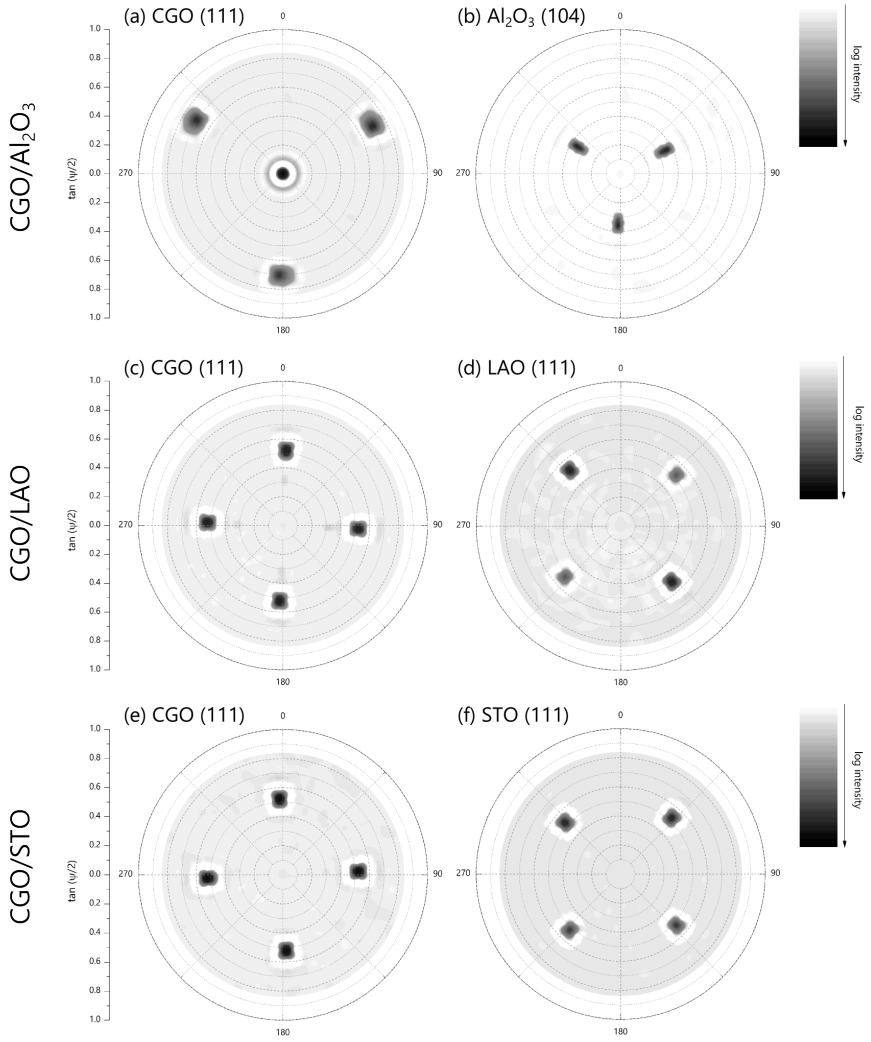


Figure 7.2: (a, c, e) are XRD pole figures about the (111) CGO peak for films deposited on Al_2O_3, LAO and STO substrates respectively. Also shown are the pole figures from the (b) Al_2O_3 (104), (d) LAO (111), and (f) STO (111) reflections.

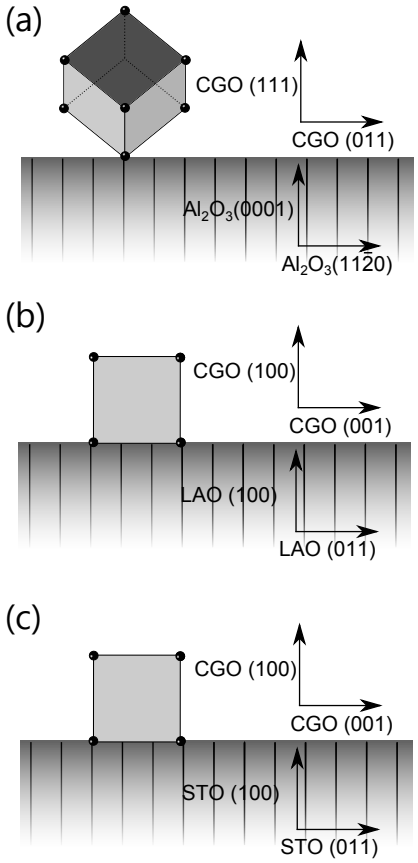


Figure 7.3: Schematic showing the orientations of the CGO films grown on (a) Al_2O_3, (b) LAO, and (c) STO.

coherent interface. Therefore a high density of misfit dislocations is expected in both directions to relieve the interfacial strain.

The pole figures taken from a layer grown on an LAO substrate are shown in Figs. 7.2c and 7.2d. In the pole figure corresponding to the CGO (111) reflection (Fig. 7.2c), four equally spaced maxima are observed at $\psi = 45°$. This implies a single in-plane orientation of the CGO layer, with a (100) out-of-plane orientation, as shown by the $\theta/2\theta$ scans. The pole figure taken from the (111) reflections of the LAO substrate in Fig. 7.2d is very similar, with again four peaks at $\psi = 45°$, but rotated in the ϕ-axis by 45°. Therefore

the orientation relationship between the CGO layer and LAO substrate is:

$$\begin{aligned} &\text{CGO (100)}||\text{LAO (100)} \\ &\text{CGO [001]}||\text{LAO [011]} \end{aligned}$$

This represents a cube-on-cube epitaxial relationship, with a 45° rotation of the CGO unit cell in the azimuth. This is shown schematically in Fig. 7.3b. Here, the LAO is assumed to have a cubic perovskite structure. The spacing of the close packed Ce cations in the (100) direction are equal to the lattice spacing, $d_{CGO(100)}$. As in Chapter 6, an AO termination is assumed for the LAO surface, and hence in the (110) direction, the spacing between the O anions is twice the lattice spacing, $d_{LAO(110)}$. Therefore the theoretical lattice mismatch is given by:

$$f_{LAO(011),CGO(001)} = \frac{2\,d_{LAO(011)} - d_{CGO(001)}}{d_{CGO(001)}} = -1.05\%. \qquad (7.3)$$

The pole figures taken from a CGO film grown on STO are shown in Figs. 7.2e and 7.2f. They can be seen to yield maxima in the same positions as those from the layer grown on the LAO substrate, and hence the orientation relationship is equivalent and is given by:

$$\begin{aligned} &\text{CGO (100)}||\text{STO (100)} \\ &\text{CGO [001]}||\text{STO [011]} \end{aligned}$$

This also represents cube-on-cube growth with a 45° rotation of the CGO unit cell, as shown in Fig. 7.3c. As STO has the same cubic perovskite structure assumed for LAO, the interfacial mismatch may be calculated according to:

$$f_{STO(011),CGO(001)} = \frac{2\,d_{STO(011)} - d_{CGO(001)}}{d_{CGO(001)}} = 1.66\%. \qquad (7.4)$$

7.2.2 Lattice Strain

Fig. 7.4 shows the (111) or (200) peak positions of the CGO films in the $\theta/2\theta$ scans, for a range of thicknesses grown on each substrate. The peaks

are fitted with either pseudo-Voigt function, or a Cu K_α doublet peak. It may be seen that for films grown on Al_2O_3 and LAO, as the thickness of the layer decreases, the peak position shifts to a lower 2θ angle. The case is the opposite for the films grown on STO, where a shift in the peak position toward a higher 2θ angle is observed.

From the fitted peak positions the out-of-plane lattice parameters may be calculated according to Eq. 4.2. In Fig. 7.5 the lattice spacings calculated for films are shown as a function of layer thickness. The lattice parameter obtained by refining the CGO target using the Le Bail method (see Appendix A.1) is also displayed for comparison. As in Chapters 5 and 6, the error bars displayed were calculated assuming an uncertainty in the peak position of twice the distance between the measurement points.

For the thickest films grown on LAO and STO, the lattice parameters agree very well with those calculated from the bulk material. Films of a similar thickness grown on Al_2O_3, display a slightly expanded parameter, corresponding to a strain of approximately 0.2%. For films grown on LAO and Al_2O_3, as the thickness of the layers are decreased the out-of-plane lattice parameter increases. For the CGO/LAO system this is explained by the theoretical interfacial lattice mismatch (Eq. 7.3) and a Poisson relaxation (approximately 0.3 for 10 mol.% CGO [239]), but assuming a coherent interface. For the CGO/Al_2O_3 system, a coherent interface is implausible, however from the increase in out-of-plane lattice spacing with decreasing thickness, a certain degree of compressive bi-axial strain at the interface seems the likely cause. For the CGO films grown on STO, the effect is the opposite, with a decrease in the lattice parameter with decreasing film thickness. As with the CGO/LAO system, this would be expected from the tensile bi-axial strain due to the calculated interfacial lattice mismatch (Eq. 7.4) and a Poisson relaxation.

To observe the effect of heat treatment on the lattice parameter, films grown on STO and LAO were measured by XRD $\theta/2\theta$ scans directly after growth and after a 800°C anneal for 2 hours. The (200) peaks are shown in Fig. 7.6. From the peak positions, it may be seen that both films remain strained after the high temperature anneal. Hence, it will be assumed from hereon that the films retain the original strain state after thermal anneals

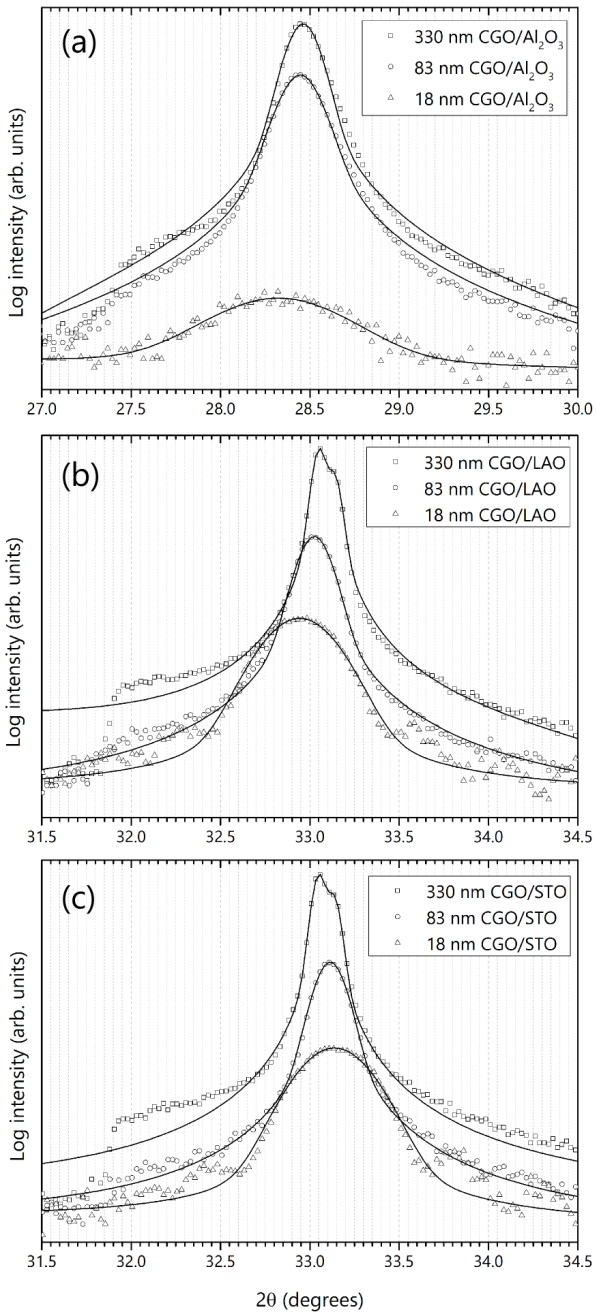


Figure 7.4: (a) (111) and (b, c) (200) CGO peaks in the XRD $\theta/2\theta$ spectra for a range of film thicknesses grown on (a) Al_2O_3, (b) LAO and (c) STO substrates.

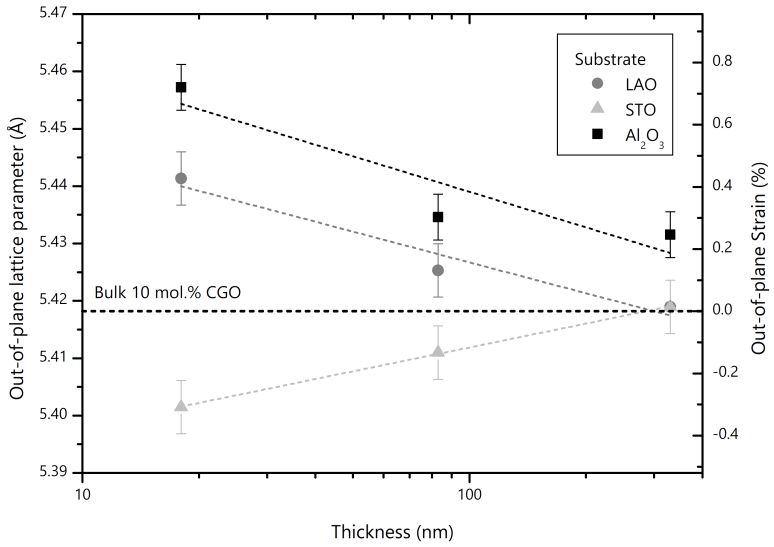


Figure 7.5: Out-of-plane lattice parameters as a function of thickness calculated from the peak position in the XRD $\theta/2\theta$ scans. The lines act only as a guide to the eye.

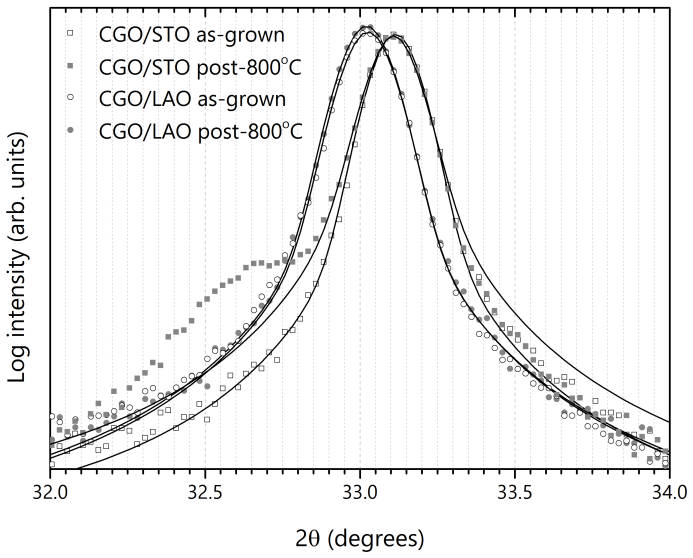


Figure 7.6: (200) CGO peaks in the XRD $\theta/2\theta$ spectra for films fabricated on LAO and STO substrates directly as-grown and after annealing at 800°C.

of up to at least 800°C.

7.3 Surface Segregation

Typical ^{4}He LEIS spectra of CGO film surfaces are shown in Fig. 7.7, after atomic oxygen cleaning. The spectrum in Fig. 7.7a is taken from a film without the solvent cleaning procedure described in Section 7.1, and the spectrum in Fig. 7.7b from a film after the solvent cleaning. In both spectra clear peaks corresponding to O, Ce, and Gd are observed, however the Ce and Gd peaks could not be separated due to the proximity of their masses and the poor mass resolution of the ^{4}He ion for target species with such a high mass.

For the sample which had not undergone solvent cleaning, strong peaks assigned to F, Na and Ca were observed. However for the film cleaned using the solvent procedure only very weak peaks are observed for F and Ca, and the Na peak is no longer present. This is combined with much stronger O

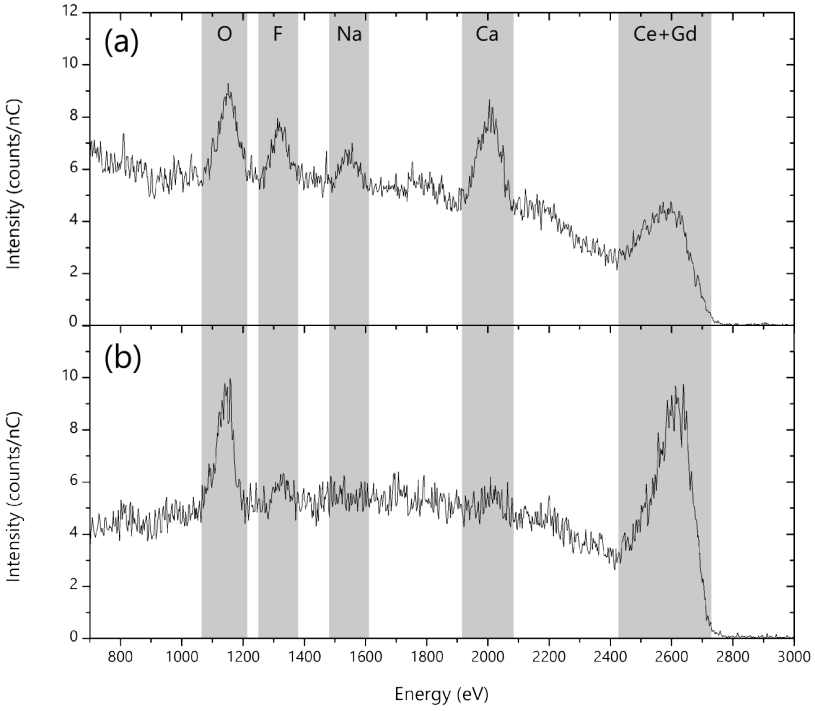


Figure 7.7: Surface 3 keV ^{4}He LEIS spectra for CGO films after heat treatment (a) without any solvent cleaning and (b) after solvent cleaning.

and Ce+Gd peaks, due to the increased surface coverage of these species. Due to the much higher signal-to-noise ratio achieved for the Ce+Gd peak, all samples discussed from here on have undergone solvent cleaning.

Fig. 7.8a shows a typical ^{20}Ne surface spectra, with the Ce and Gd peaks clearly resolved. These are fitted using Gaussian functions in the SurfaceLab software [196]. The flat plateau on the left of the Ce peak is due to the signal from Ce and Gd cations below the outer atomic layer, which have undergone reionisation whist scattering out of the surface. This feature of the spectra was fitted using a Gauss error function. The centre of the error function was confined to 15-25 eV less than the centre of the Ce peak position, as the charge changing cycle of the projectile from positive to neutral to positive cost ∼20 eV [209]. The peak at an energy of ∼3250 eV, is most likely caused by a double collision with the Gd cations or is part of

the secondary ion background due to sputtered material from the analysis beam, and was not included in the fitting.

Analyses were taken as a function of depth using the Ar sputter gun to remove material between each analysis. The dose per cycle was kept to 1.1×10^{13} ions/cm^2 for the ^{20}Ne analysis gun, and to 4.7×10^{14} ions/cm^2 for the Ar sputter gun. This was to ensure that a much higher proportion of the sputtering is carried out by the low energy sputter gun to allow for a reasonable depth calibration and to minimise intermixing from the higher energy ^{20}Ne projectiles. Fig. 7.8b shows a subsurface spectrum, acquired after a single sputter cycle, and a spectrum obtained after 30 sputter cycles is shown in Fig. 7.8c. The height of the Ce and Gd peaks increase significantly from the surface spectra after sputtering has taken place. This is attributed to surface contamination from residual hydrocarbons remaining despite the oxygen cleaning, and small amounts of surface F and Ca (as observed in Fig. 7.7b), which are preferentially sputtered by the Ar beam with respect to the Ce and Gd cations. A dramatic change in the relative height of the Gd peak with respect to the Ce peak is observed as the dose density is increased.

In Fig. 7.9, the peak areas, S_i', are plotted as a function of sputter dose. Here the depth has been estimated from the sputter rate calculated from the SRIM software [240]. Excluding the first data point, it can be seen that the Gd signal decreased away from the surface and the Ce signal increases. This implies a segregation of the Gd cations to the surface and subsurface region of the CGO films. While the Gd signal reaches a stable value with increased sputtering, the Ce signal continues to decrease. The decreasing Ce signal was observed for all obtained depth profiles, the longest of which extended to a dose of 34×10^{15} ions/cm^2, corresponding to an estimated depth of 25 nm. Preferential sputtering between Ce and Gd seems unlikely due to their proximity in mass, also as there is no obvious increase in the Gd signal. A misalignment of the analysis and sputter areas has also been ruled out by reconstructing the depth profile using a smaller region-of-interest. It is possible that reduced ceria (Ce_2O_3) exists at the surface of the films, despite the high pO_2 during the thermal treatment. This phase would have a higher density of Ce compared to O at the surface and would hence yield a higher Ce signal. However, the exact cause of this artefact remains unclear.

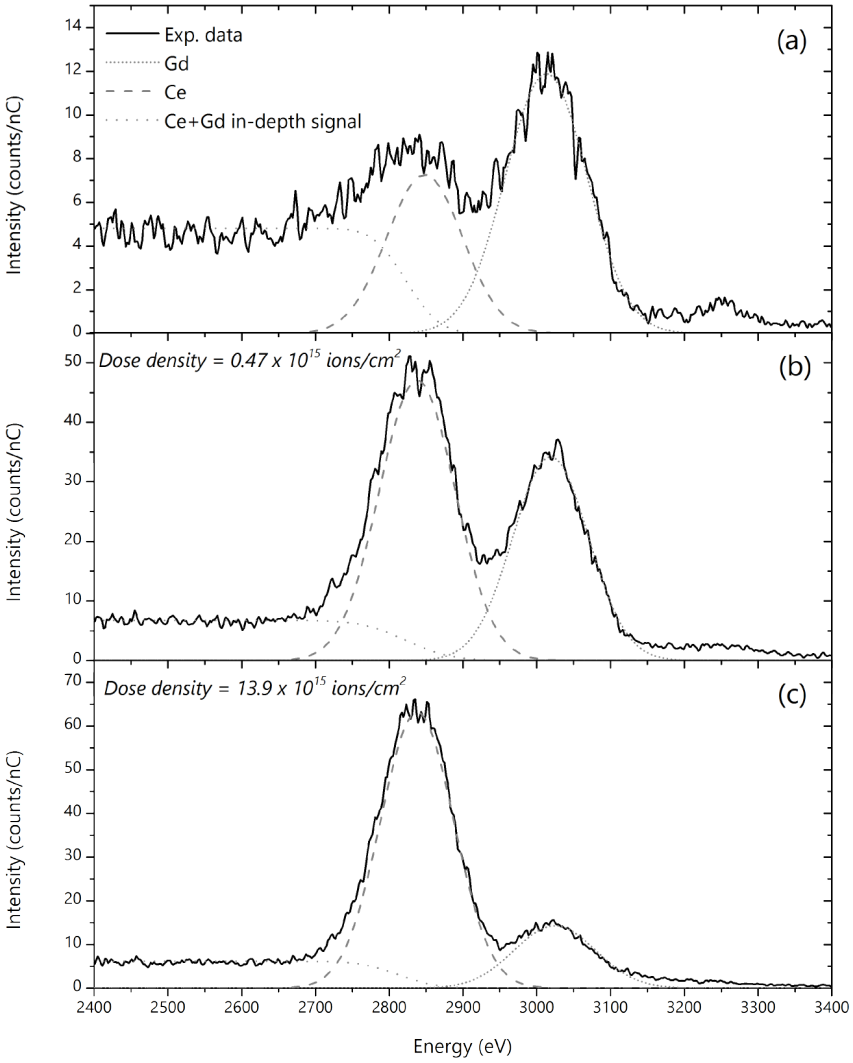


Figure 7.8: Typical 5 keV ^{20}Ne LEIS spectra for a CGO films (a) of the outermost surface, and after a sputter dose of (b) 0.47×10^{15} ions/cm^2, and (c) 13.9×10^{15} ions/cm^2.

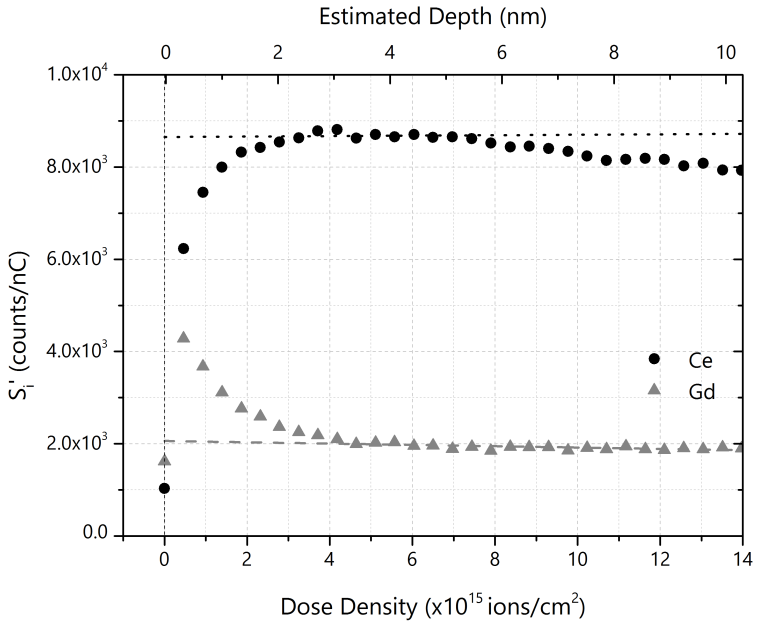


Figure 7.9: Typical area of the Ce and Gd peaks as a function of sputter dose. The estimated depth was calibrated using a calculation in the SRIM software. The horizontal dashed lines are the peak areas taken as the bulk reference signal, $S'_{i,bulk}$.

As discussed in Section 4.6, the surface coverage of a given species, N_i, may be calculated from the yield normalised to the analysis beam dose, S'_i, according to

$$S'_i = \alpha \eta_i N_i, \tag{7.5}$$

where α takes into account an instrumental factor, the surface roughness and screening from neighbouring atoms as given in Eq. 4.28[2] and should remain constant during each depth profile measurement. The primary ion current was measured before and after each depth profile in order to reduce the effect of any changes on the normalised signal, S'_i. η_i is the sensitivity factor, which will depend on the scattering cross section and neutralisation probability for the scattered ion, i. As η_i is unknown for Ce and Gd, the surface coverage may be calculated using a bulk reference signal $S'_{i,bulk}$ taken from a region of the depth profile where the bulk stoichiometry, $N_{i,bulk}$, is assumed, such that

$$N_i = S'_i \frac{N_{i,bulk}}{S'_{i,bulk}}. \tag{7.6}$$

However, from the ^{20}Ne spectra, only the surface coverage of the Ce and Gd species are measured and therefore the signals are subject to change due to the varying presence of oxygen and contaminating species which may be preferentially sputtered during the depth profiles. Therefore the signal from the cations, Ce and Gd, have been normalised to the total cation signal to obtain a relative surface coverage.

$$N'_i = \frac{N_i}{\sum_i N_i} \tag{7.7}$$

In Fig. 7.10, the normalised surface coverage for the Ce and Gd cations are plotted as a function of depth, as calculated from the signal yield displayed in Fig. 7.9. A Gd enriched region is clearly visible at the surface extending up to a depth of approximately 3 nm. No sign of a subsurface region depleted in the Gd dopant is observed.

[2]Here the signal, S'_i, has been normalised to the analysis beam dose such that $S'_i = S_i/(I_p\, t)$, where I_p is the primary ion beam current and t is the acquisition time.

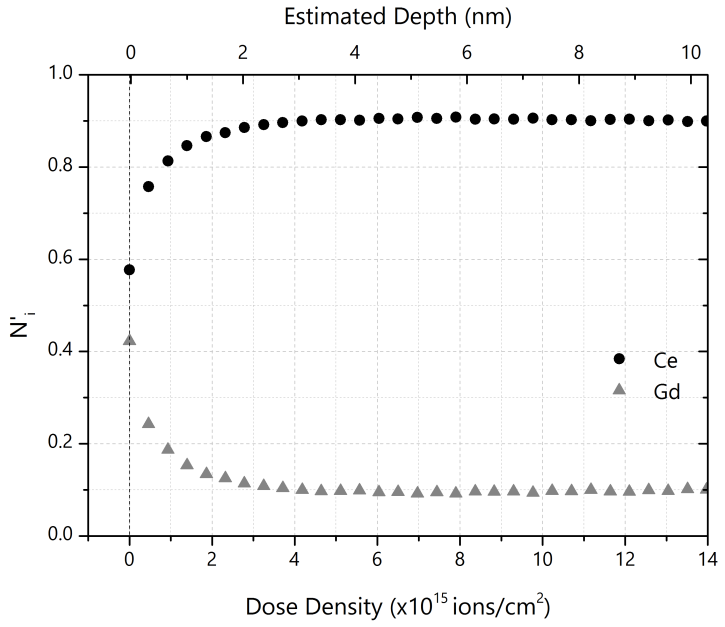


Figure 7.10: Normalised cation coverage of Ce and Gd as a function of sputter dose.

7.3.1 Temperature Dependence

To study the effects of post-growth thermal treatment on the surface segregation, 83 nm CGO films deposited on STO substrates were analysed as-grown and after a subsequent heat treatment of 600°C, 800°C, or 1000°C for 2 hours. The normalised Gd signal for each is plotted as a function of sputter dose in Fig. 7.11. Unfortunately for these analysis, a much lower sputter dose was used in relation to the analysis dose, and therefore the depth could not be estimated using a SRIM calculation. However for all the depth profiles in Fig. 7.11, the relative ratio between the sputter and analysis dose remained constant and therefore the relative length of the profiles may be compared.

Dopant segregation is observed to occur in the PLD grown films, without any additional thermal treatment. A surface cation fraction of 0.17 is observed in the as-grown film, representing a 70% increase from the bulk concentration. After annealing at 600°C for 2 hours, the cation fraction at the surface increased to 0.21, but with no noticeable increase in the width of

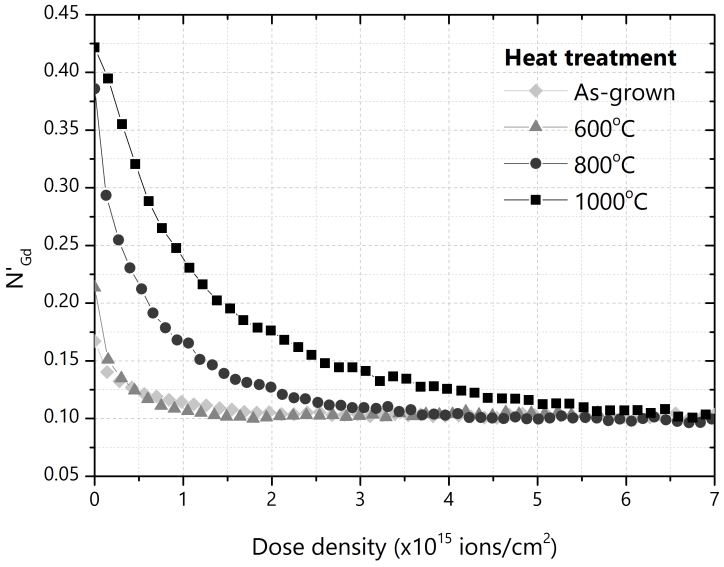


Figure 7.11: Normalised Gd ratio as a function of sputter dose for CGO films grown on STO after a heat treatment at a range of temperatures.

the enriched region. A heat treatment at 800°C for 2 hours yielded a significant increase in the surface cation fraction to 0.39, and a substantially wider subsurface region with a higher concentration of Gd dopant. The highest surface cation fraction of 0.42 was observed for the film annealed at 1000°C, which was coupled by a further increase in the width of the Gd enriched zone. This represents an increase in the surface concentration by a factor of 42. The fractional concentration of the Gd segregated to the surface and subsurface region, $X_{Gd}^{int}/X_{Ce}^{int}$, was calculated from Fig. 7.11 and Ce is plotted as a function of temperature in the form of an Arrhenius diagram in Fig. 7.12. From Eq. 2.54, the activation energy should be equal to the enthalpy of segregation, provided the segregation has reached the equilibrium value. In Fig. 7.12 a value of 11.6 kJ/mol is calculated from the fitted slope.

7.3.2 Lattice Strain and Orientation Dependence

To assess the effect of the CGO orientation and lattice parameter on the Gd segregation, films grown on Al_2O_3, LAO and STO at a range of thicknesses

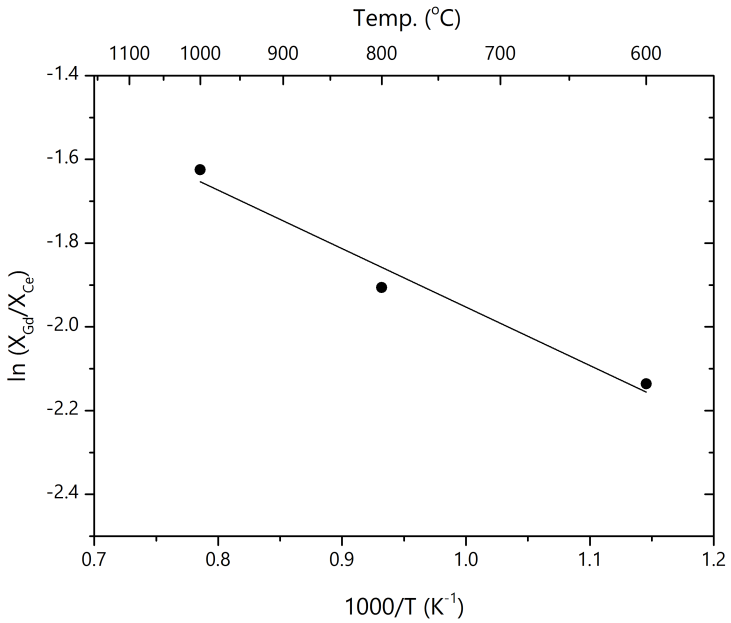


Figure 7.12: Arrhenius plot for the surface ratio of cation fractions of CGO films as a function of post growth heat treatment. The activation energy calculated from the fitted slope is 11.6 kJ/mol.

were heat treated at 800°C for 2 hours and measured by LEIS. The depth profiles for each sample discussed is displayed in Appendix A.5. There is no obvious difference in the width of the Gd enriched region in any of the samples. The surface cation fraction was calculated for each using the same values for $S'_{Gd,bulk}$ and $S'_{Ce,bulk}$. This was to avoid introducing further error into the calculated N', due to multiple calculations of the bulk Ce and Gd signals.

Fig. 7.13a shows the normalised Gd ratio, calculated for the surface spectra as a function of the out-of-plane lattice parameter. All samples displayed significant dopant enrichment from 0.1 in the bulk to between 0.28 and 0.45 at the surface. In the thickest (100) oriented films on STO and LAO substrates, which displayed the bulk lattice parameter, the same Gd fraction of 0.42 is observed. The Gd fraction increases for the STO films with the smallest out of plane lattice parameter to 0.45, and decreases for the LAO film with the largest out-of-plane lattice parameter to 0.37. However the trend is not clear for all the films analysed, with the film displaying intermediate strain both showing a decrease in the extent of segregation compared to the unstrained films. The (111) oriented films on Al_2O_3 consistently displayed a reduced Gd fraction than the films grown on STO and LAO. A slight decrease is seem as the film thickness is reduced and the strain increases, but the trend is not abundantly clear.

Due to the low signal-to-noise ratio of the surface spectrum (as shown in Fig. 7.8a), the Gd fraction taken from the second acquired spectra after a single sputter cycle is displayed as a function of lattice parameter in Fig. 7.13b. Caution must be taken here, as the Gd fraction quickly reduces as a function of sputter dose, and therefore a slight change in the dose density per sputter cycle could introduce significant errors. Here the sputter dose per cycle was kept between 0.44-0.47$\times10^{15}$ ions/cm^2 for the films grown on STO and LAO, and between 0.40-0.47$\times10^{15}$ ions/cm^2 for the films grown on Al_2O_3. The effect of the lattice parameter on the extent of segregation for the films grown on each substrate is clearer. However and offset between the films grown on LAO and STO has been introduced, with the unstrained films no longer displaying the same Gd fraction at the surface.

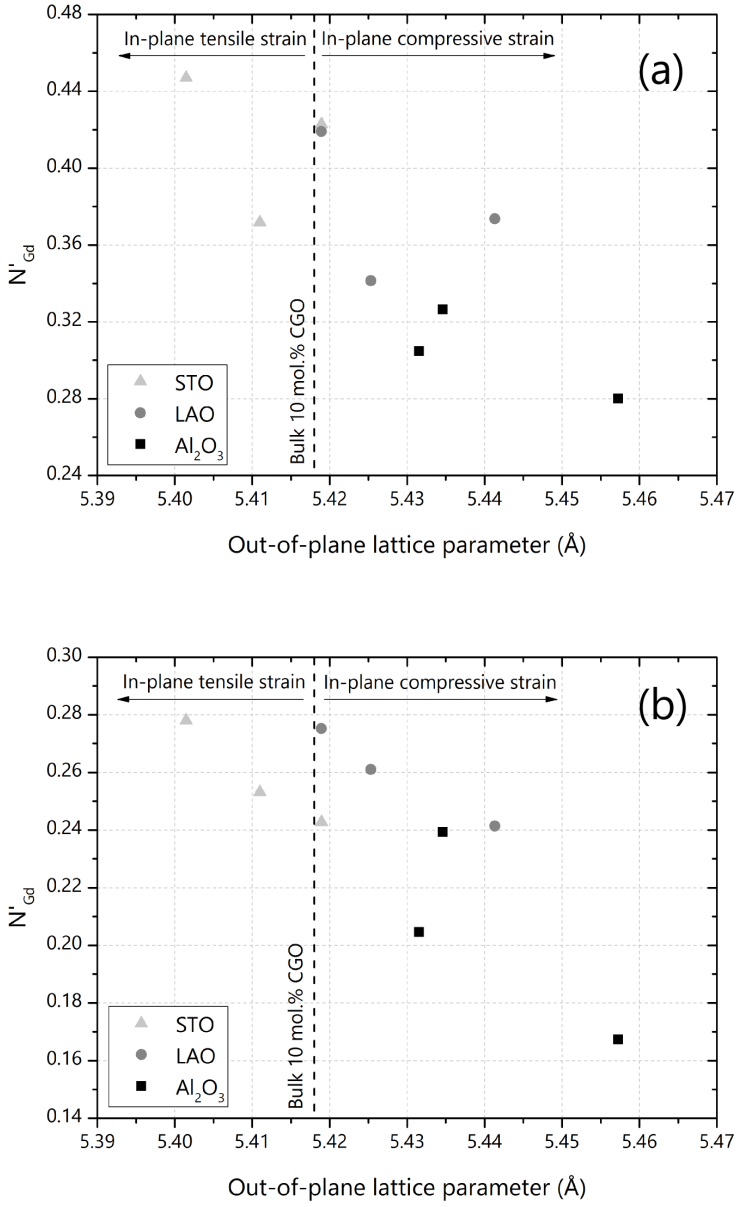


Figure 7.13: Normalised Gd ratios as function of out-of-plane lattice parameter for films of various thickness grown on Al_2O_3, LAO and STO substrates. The N'_{Gd} values are taken from (a) the surface spectra and (b) the sub-surface spectra after a sputter dose of 0.4-0.47$\times 10^{15}$ ions/cm^2.

7.4 Discussion

F, Na and Ca impurities were observed at the surface of the CGO films after heat treatment, as shown in Fig. 7.7. Na and Ca are common impurities in the doped-fluorites and have previously been reported to segregate to the surface of YSZ pellets [109, 179] and single crystals [207] after high temperature annealing. In addition Ca has also been previously reported to segregate to the surface of CGO pellets [180]. The most likely origin of the impurities is from the target material, which was transferred during the PLD process and then segregated to the surface after heat treatment. Great care was taken to avoid surface contamination of the films while transferring the samples to the LEIS chamber, however contamination at this point cannot be excluded. Surprisingly the impurities were found to be substantially reduced by an ultrasonic solvent clean in acetone, ethanol and ultra-pure Milli-Q water. It has been assumed that the solvent cleaning procedure does not affect the relative ratio of the Ce and Gd cations at the surface, however this was not confirmed.

Segregation of the Gd dopant was present in all samples, even the as-grown films fabricated at 700°C. In Chapter 2 two models of the surface structure of YSZ were introduced, as shown in Fig. 3.21. De Ridder *et al.* [177] suggested an impurity overlayer, followed by an enriched region and then a depleted region before reaching bulk stoichiometry. Alternatively, Hughes [176] proposed an impurity layer followed by a single enriched region before bulk stoichiometry was attained. In this work the segregation region was found to extend up to 3 nm into the CGO, but with no obvious depletion region (Fig. 7.10), supporting the model postulated by Hughes.

The extent of the Gd segregation to the surface was observed to increase as the temperature of the heat treatment was increased as seen in Fig. 7.11. The Gd fraction was found to rise from 0.1 in the bulk to 0.42 at the surface after annealing at 1000°C. This is very similar to the value of 0.5 reported by Scanlon *et al.* [180] for CGO polycrystalline pellets annealed at 1300°C to 1600°C as measured by LEIS. The solubility limit of Gd in CeO_2, is approximately 0.5 [241], and although the maximum surface segregation reported in this work is below that value, the formation of a new Gd phase

without the fluorite structure at the surface remains plausible.

Fig. 7.12 shows the Gd surface ratio as a function of temperature on an Arrhenius diagram. If one were to assume the system to be in equilibrium, the slope would yield the enthalpy of segregation, ΔH_S, according to Eq. 2.54. From Fig. 7.12 a value of ΔH_S =11.6 kJ/mol is calculated, implying a positive free energy of segregation. For YSZ pellets, ΔH_S has been calculated to be -12.3 kJ/mol [176] and measured to be -21±3 kJ/mol [109, 179]. Although a positive free energy of segregation has been also been observed previously for YSZ [176], a more likely explanation would be that the system has not reached equilibrium due to the relatively short annealing times and slow cation diffusivity. If this is the case, then for the temperature and time of the annealing in this work, the Gd fraction measured will be due to *non-equilibrium* segregation and an additional factor given by Eq. 2.60 must be taken into account. Therefore the surface segregation observed will be a function of both the free energy of segregation and the diffusivity of the Gd cations, as shown in Fig. 2.18.

The CGO films grown by PLD have been shown to have a single orientation both out-of-plane and in-plane by XRD analysis. Due to the lattice mismatch with the substrates, the films grown on LAO and Al_2O_3 displayed an increase in the out-of-plane lattice parameter as the layer thickness was reduced, while the lattice parameters of the films grown on STO were seen to decrease. This was attributed to compressive and tensile biaxial strain at the film/substrate interface respectively. Note that this represents a decrease in unit cell volume for the thin CGO films grown on LAO and Al_2O_3, and an increase for the films grown on STO.

Cation diffusion is known to be substantially higher in grain boundaries compared to the bulk in doped fluorites [171]. Although no information on the microstructure is available here, from the high degree of texture displayed in the XRD analysis, an abundance of highly misoriented grain boundaries can be excluded.

As described in Section 2.4.1, the free energy for segregation is a sum of the interfacial energy contribution, ΔH_{int}, the binary interaction contribution, ΔH_{bin}, the solute strain energy contribution, ΔH_ϵ, and an electrostatic contribution ΔH_{SC} as well as entropic effects. As the lattice volume of the

CGO varies, one would expect that the change in the free energy of segregation would predominantly originate from the solute strain energy term. The ionic radii of the Gd cation ($1.06\mathring{A}$) is ∼8.5% larger than that of the Ce in the host lattice ($0.97\mathring{A}$). Therefore an expansion of the CGO unit cell would be expected to decrease the driving force for segregation due to a reduction in the solute strain energy. From the surface Gd fraction as a function of out-of-plane lattice parameter as shown in Figs. 7.13a and 7.13b, one may see a tentative trend such that as the lattice volume increases the surface Gd concentration increases and as the lattice volume is compressed the Gd concentration decreases. This implies the opposite to what is expected from considerations of the driving force for segregation. However, it must be noted that Eq. 2.54 only applies to systems in thermodynamic equilibrium.

As discussed above, the most likely explanation of the positive gradient in Fig. 7.12 is that the system has not reached equilibrium for the times and temperatures used in the heat treatments in this study. Therefore the surface concentration of Gd will also be a function of the diffusivity as given in Eq. 2.60. Thus the effect of compressive and expansive strain in the films on the diffusivity of the cations must also be considered. Cation diffusion is expected to occur though a vacancy hopping mechanism in the doped fluorites [165], and hence the considerations on the pressure dependence of the O diffusivity in Section 2.3.2 are also valid for Gd cation migration. A decrease in the cation diffusivity would be expected due to compressive strain and an increase would be expected due to tensile strain. This is in agreement with the results shown in Fig. 7.13 if the segregation is diffusion limited.

The (100) surface of the fluorite structure is a polar Type 3 Tasker surface, whereas the (111) surface is a neutral Type 1 Tasker surface [66]. It follows that a reduction in the electrostatic driving force for segregation, ΔH_{SC}, would be expected for a (111) oriented surface compared to a (100) oriented one. Comparing the Gd fraction of the surface in Fig. 7.13, the (111) oriented films grown on Al_2O_3 substrates consistently display a reduced segregation compared to the (100) oriented films on STO and LAO. However, the films grown on Al_2O_3 also displayed the largest change in the out-of-plane lattice parameter, and therefore isolating the difference in seg-

regation due to a change in the electrostatic driving force and change in the cation diffusivity as a result of the compressive strain is not possible.

Unfortunately, there is significant scatter in the data in Fig. 7.13 making it difficult to identify trends in the Gd surface fraction with lattice parameter and film orientation. There are a number of factors which could account for the scatter in the data. Changes in the density of grain boundaries, might be expected to have a significant effect on the cation diffusivity in the films. In Chapter 6, it was shown that in YSZ films grown by PLD the grains size was smaller in closer proximity to the interface. Grain boundary effects cannot be excluded, however both an increase and decrease in the extent of the segregation was seen as the films thickness was reduced for the films grown on the STO substrates and those grown on the LAO or Al_2O_3 substrates respectively. Also, it has been assumed that the surface concentration of Gd cations was the same in all the films due to the fabrication process prior to heat treatment. However, the thickest films were grown over a period of 20 minutes, whereas the thinnest films were grown in 65 seconds. The thermal annealing of the films was carried out at a temperature at least 100°C higher than the growth temperature and for substantially longer (2 hours) in an attempt to mitigate this source of error. Furthermore, if the segregation after the heat treatment was heavily affected by the surface concentration of the as-grown films, this would not explain the increase in the surface Gd fraction for thinner CGO films grown on STO.

An additional source of error originates from the low signal-to-noise ratio for the spectra from the outermost surface (Fig. 7.8a). A much higher signal-to-noise ratio was obtained by using the subsurface spectra after a single sputter cycle (Fig. 7.8b), however this introduces a further error due to variations in the sputter beam current. Finally, despite great care to ensure a consistent method of thermal treatment, slight changes in the temperature during the sample annealing are possible over the time period this study took place over.

7.5 Conclusion

CGO films have been fabricated by PLD onto Al_2O_3, LAO and STO substrates. All films were found to be highly textured, with a single orientation both out-of-plane and in-plane. The films grown on Al_2O_3 displayed a (111) orientation out-of-plane, while the layers deposited on LAO and STO were (100) oriented. From measurements of the out-of-plane lattice parameter and considerations from the orientation relationships, it was found that the films grown on LAO and Al_2O_3 were under compressive biaxial strain and the films deposited on STO were under tensile biaxial strain originating from the films-substrate interface. The strain was found to increase as the thickness of the CGO layers were reduced.

Segregation of the Gd dopant occurred in all films, even those analysed directly after deposition, with no thermal treatment. For heat treatments 2 hours in duration, an increase in the segregation was observed for higher temperatures, implying the segregation had not yet reached equilibrium and was limited due to the diffusivity of the cations. After annealing at 800°C for 2 hours, the Gd enriched region was found to extend approximately 3 nm into the film.

An increase in the surface Gd fraction was observed for tensile strained films, and a decrease for compressively strained films. This was found to be the opposite of that expected from considerations of the driving force for segregation. Hence, a decrease in the diffusivity of the Gd cations is thought to occur due to compressive tensile strain and an increase due to tensile lattice strain. A further decrease in the Gd segregation was observed for the (111) oriented films compared to the (100) oriented ones. This was expected due to a decrease in the electrostatic driving force for segregation, however the effect could not be separated from the lattice strain.

Chapter 8

Conclusions and Outlook

Over the last decade there has been substantial interest in the modification of the ionic transport properties of oxide electrolyte materials, such as doped ZrO_2 and CeO_2, for applications including SOFCs. As discussed in Chapter 3, huge enhancements in the ionic conductivity have been reported, but the literature is plagued with inconsistencies leading to doubt over the potential of this approach. From analysis of the previously reported findings, common themes were identified for investigation in this work, to assess their effect on ionic transport.

The primary purpose of this study was to explore the influence of a variation in the lattice parameter on the conductivity of YSZ thin films. Both a change in the average lattice parameter and a highly localised strain field surrounding dislocations were considered.

Segregation to the surface of thin films and the effects of strain on the high temperature degradation properties has been entirely overlooked in the literature. As an extension of the work on transport properties, segregation to the surface of CGO films as function of thermal history, orientation and lattice strain was investigated.

8.1 Conclusions

The orientation relationship between a film and the substrate will play a crucial role in the interfacial lattice mismatch and hence the lattice strain

and density of dislocations. Therefore, understanding the growth factors influencing these properties is vital for fabricating thin film systems for systematic study.

The effect of substrate pre-treatment and growth temperature on the orientation and lattice parameter of YSZ films was investigated, as detailed in Chapter 5. It was shown that the orientation of YSZ films fabricated on MgO substrates by PLD, would change from a (111) out-of-plane orientation for polished substrates to a (100) orientation for unpolished substrates. The cause of this is thought to be due to an increase in the density of nucleation sites which, facilitate the preferential nucleation of the (100) oriented YSZ phase.

The (100) oriented YSZ was found to display cube-on-cube epitaxial growth with the unpolished MgO substrate, and a regular dislocation network was also observed along the interface. This implied the same orientation relationship as reported by Kosacki *et al.* [106, 107] and Sillassen *et. al.* [115] in YSZ films grown on MgO that displayed an enhancement in the conductivity of 2 and 3.5 orders of magnitude respectively. Both of which have been attributed to a dislocation network at the film/substrate interface [110].

Reliable transport measurements were not possible due to the extreme roughness of the unpolished substrates and therefore the ability to reproduce crystallographically identical structures on microscopically flat substrates would be highly beneficial to confirm the previous results and investigate the underlying phonomena. However, despite substantial investigations, structurally similar films could not be consistently reproduced using homoepitaxial buffer layers, substrate heat treatment, or by varying the substrate miscut, or growth temperature.

An expanded out-of-plane lattice parameter was found for all YSZ films deposited by PLD. Further analysis of the studies in the literature showed this finding to be consistent with YSZ grown for a range of substrates and PVD techniques. The out-of-plane lattice parameter was found to increase as the substrate temperature was decreased from 800°C to 600°C during deposition. A 1000°C post-growth heat treatment caused the lattice to relax to almost the expected bulk lattice parameter. In addition, the orientation

of the films and choice of substrate also was found to affect the observed expansion. A range of possible causes to explain the observed behaviour were discussed, including interfacial lattice mismatch, thermal expansion coefficient, non-stoichiometry, and changes in the defect structure, however none provided a satisfactory explanation.

To isolate the effects of lattice strain and dislocations on the ionic transport of YSZ, thin films were grown on MgO, Al_2O_3, LAO, and NGO substrates, representing a range of interfacial lattice mismatches, as described in Chapter 6. Films were fabricated for a variety of thicknesses, in order to probe the interfacial contribution for each system.

All films were found to be highly textured, each displaying an expansion of the out-of-plane lattice parameter, which varied for each substrate. Dislocation networks were observed at the film/substrate interfaces, with a density which was dependent on the interfacial mismatch. For dislocations occurring at the film/substrate interface for YSZ grown on Al_2O_3, the tensile strain field was found in the YSZ and the compressive strain field in the Al_2O_3. The opposite was for case for the films grown on LAO and NGO, with the compressive strain field in the YSZ and the tensile strain field in the substrate.

The ionic transport properties of the films was measured by EIS and IETD, with techniques in good agreement when performed on equivalent samples. None of the films displayed an increase in the transport properties over that expected for single crystal YSZ. Hence, the findings in this work suggest that dislocations do not provide routes for fast oxygen diffusivity, which may enhance the conductivity of a film by the orders of magnitude reported in previous studies.

All the films fabricated displayed a decrease in the ionic transport as the thickness of the films was reduced, despite tensile interfacial strain expected from the lattice mismatch for layers grown on LAO and NGO. The reduction in the diffusivity was attributed to an anisotropic distribution of grain sizes whereby a higher density of low angle grain boundaries was observed in closer proximity to the film/substrate interface. This highlights the importance for microstructural control when studying the transport properties of materials in confined systems such as thin films.

By annealing the films at 1000°C, the lattice parameter was found to relax back to close to the bulk value, with minimal effect on the grain size. For films grown on Al_2O_3, this was accompanied by an increase in the conductivity of almost a factor of two, suggestive of a reduction in the oxygen transport of the as-grown films due to compressive lattice strain. However, no substantial change in the activation was seen, nor was any improvement for films fabricated on MgO after an identical heat treatment.

In an attempt to confirm the previously reported enhancement in the conductivity observed in YSZ films grown by RF sputtering onto Al_2O_3 substrates [119], equivalent films fabricated by Dr Jun Jiang and Prof. Josh Hertz at the University of Delaware were analysed by IETD to provide a direct measurement of the oxygen diffusivity. Rather than a nine-fold enhancement in the transport properties for decreasing layer thickness as previously reported, a seven-fold reduction in the diffusivity was found. The lack of any increase in the diffusion as measured by IETD suggest that the EIS measurement performed by Jiang *et al.* were not representative of oxygen transport in the films and therefore brings into question the validity of the published results. Furthermore, in the previous work the enhanced conductivity was attributed to the change in out-of-plane lattice parameter and presence of dislocations, however films grown in this work by PLD displayed similar orientation, lattice strain, and dislocations yet no enhancement was found. Hence, if the improvement reported in Ref. [119] is genuine, these properties of the films are not likely to be the cause.

The study of Gd segregation to the surface and subsurface of CGO films using LEIS is reported in Chapter 7. Gd segregation was found to occur for all films, even those which were analysed as-grown, without any heat treatment. After annealing for two hours, an increase in the surface Gd fraction and the width of segregated region was observed as the temperature was raised from 600°C to 1000°C. For a heat treatment at 800°C the enriched region was found to extend several nanometres into the film.

These findings have significant implications for studies of thin film electrolytes such as doped ZrO_2 and CeO_2. Typical electrode sintering conditions and transport measurements are performed in the time and temperature range investigated here. As the thickness of a film is reduced to

<10nm, it approaches the width of the segregation region, which could have significant consequences on the transport properties. Here, even as-grown CGO films have been shown to be enriched in Gd at the surface. A similar behaviour might be expected for YSZ films. YSZ also has the fluorite crystal structure and the dopant cations have a large ionic radii than the host cations, as with CGO. However, Y segregation in YSZ could not be investigated using LEIS due to the proximity in mass of Zr and Y and limited mass resolution of the technique. These results also have implications for the integration of thin films into μSOFCs and memristors where degradation plays a significant role in the device performance.

Single orientation CGO films were fabricated for a range of thicknesses on Al_2O_3, LAO and STO substrates. The films were found to be oriented in the (111) direction out-of-plane when grown on Al_2O_3, and in the (100) direction when grown on LAO and STO. The films were shown to be under tensile strain when fabricated on STO and compressed for LAO and Al_2O_3, with the level of strain increasing at the thickness was reduced.

The Gd concentration was found to increase with tensile strain in the films and decrease due to compressive strain. This is opposite to what was expected from considerations of the elastic driving force, due to the large ionic radii of the Gd cation compared to Ce in the host lattice. However, the increase in the Gd concentration with increasing temperature implied that for the heat treatments used, the segregation in the films had not reached equilibrium, and hence the observed segregation was both a function of the driving force and diffusivity of the dopant cations.

It follows the most likely cause for the observed relationship between the Gd segregation and the lattice parameters of the films is an increase in the Gd diffusivity with tensile strain and a decrease due to compressive strain. A further reduction in the Gd surface fraction was found for the (111) oriented films on Al_2O_3 compared to films on either LAO or STO. A decrease in the electrostatic driving force for segregation is possible due to the non-polar natural of the (111) surface compared to the (100) surface. However this effect could not be separated from the compressive lattice strain in the films.

To date, studies into the effect of lattice strain on oxide electrolytes have been primarily focused upon the transport properties. The work presented

here hints at the possibility of using lattice strain for controlling the degradation properties of functional oxides, which remains the one of the largest barriers for SOFC commercialisation.

8.2 Outlook

Based on the findings of this work, there are several open questions remaining which would benefit from further study.

Despite significant effort, cube-on-cube epitaxial growth could not be consistently achieved for YSZ films deposited on microscopically flat MgO substrates. It has been shown that thermal treatment of the substrate prior to growth facilitates a partial change in the orientation, however the exact conditions for full oriented cube-on-cube films remains unknown. Interfaces with this orientation remain a topic of interest due to previously reported enhancements of the ionic conductivity in this system facilitated by interfacial dislocations. If such films could be reliably produced, then the validity of the prior results could be assessed by a more direct means such as IETD.

The origin of the expanded out-of-plane lattice parameter in the YSZ films remains elusive. Measurements of the in-plane lattice parameter would be highly beneficial for further investigation into the cause. As of writing, attempts are being made to obtain this information for the films using XRD reciprocal space maps. This will also allow for the calculation of a lattice volume for the films, which is a more physically meaningful figure of merit for comparison against the transport properties.

The importance of the effect of grain boundaries on the ionic transport in thin films has been demonstrated. Using the electrode geometry employed in this work, separation of the grain and grain boundary responses in the impedance spectra is not possible. However using fine, closely spaced interdigitated electrodes the two responses may be isolated [117]. This would allow the variation in the lattice parameter of films to be investigated without interference from changes in the grain boundary density, and the effect of strain on the grains of YSZ to be probed.

Further investigation is still required to understand the interplay of lattice strain and surface segregation. Care must be taken to clearly separate

the effects due to changes in the cation diffusivity and the driving force for segregation. Thin films are an ideal model systems for study, where the surface orientation, grain boundary density, and lattice parameter can be modified in a systematic fashion. In addition, a greater understanding of degradation in thin film electrolyte materials is vital for applications in thin film electrochemical devices such as μSOFCs and memristors.

Appendix A

Appendices

A.1 XRD $\theta/2\theta$ Patterns from the PLD Targets

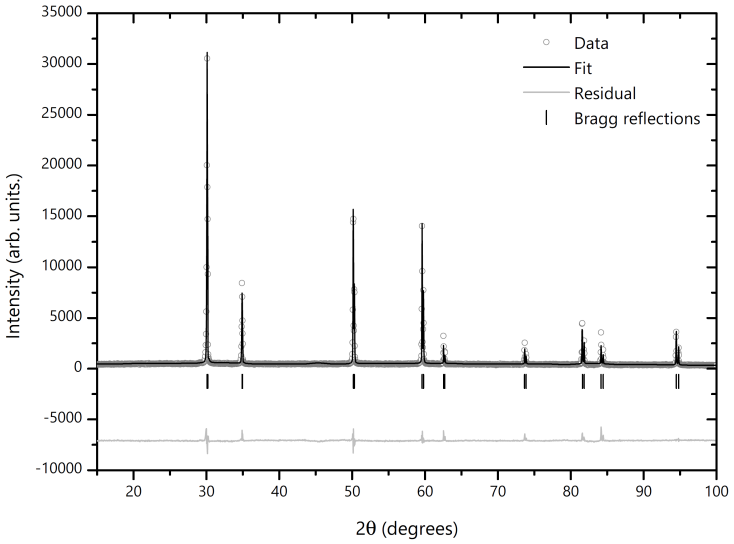


Figure A.1: XRD $\theta/2\theta$ pattern from the sintered YSZ PLD target prior to deposition. The pattern has been refined using the Le Bail method for a cubic fluorite structure yield a lattice parameter of $a_{YSZ} = 0.5139$ nm.

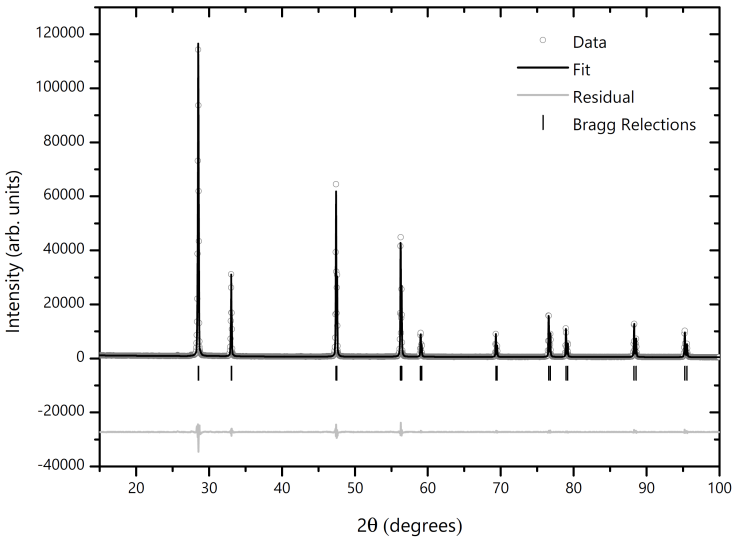


Figure A.2: XRD $\theta/2\theta$ pattern from the sintered CGO PLD target prior to deposition. The pattern has been refined using the Le Bail method for a cubic fluorite structure yield a lattice parameter of $a_{CGO} = 0.5418$ nm.

A.2 XRD $\theta/2\theta$ Patterns from YSZ Films in Chapter 6

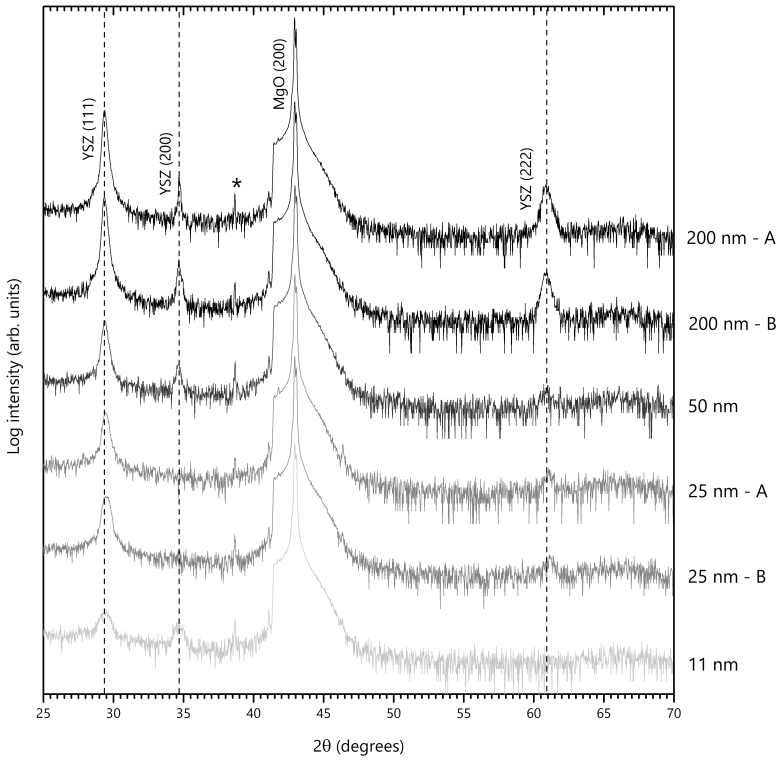


Figure A.3: XRD $\theta/2\theta$ patterns from the YSZ films grown on MgO substrates with a nominal substrate temperature of 700°C during deposition. The peak marked with a $*$ are due to the substrate peaks. The samples labels correspond to those in Table 6.1.

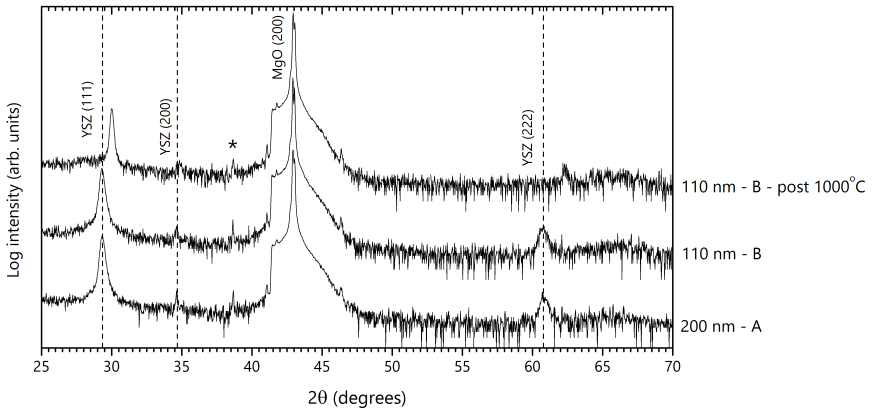


Figure A.4: XRD $\theta/2\theta$ patterns from the YSZ films grown on MgO substrates with a nominal substrate temperature of 600°C during deposition. The peak marked with a $*$ are due to the substrate peaks. The samples labels correspond to those in Table 6.1.

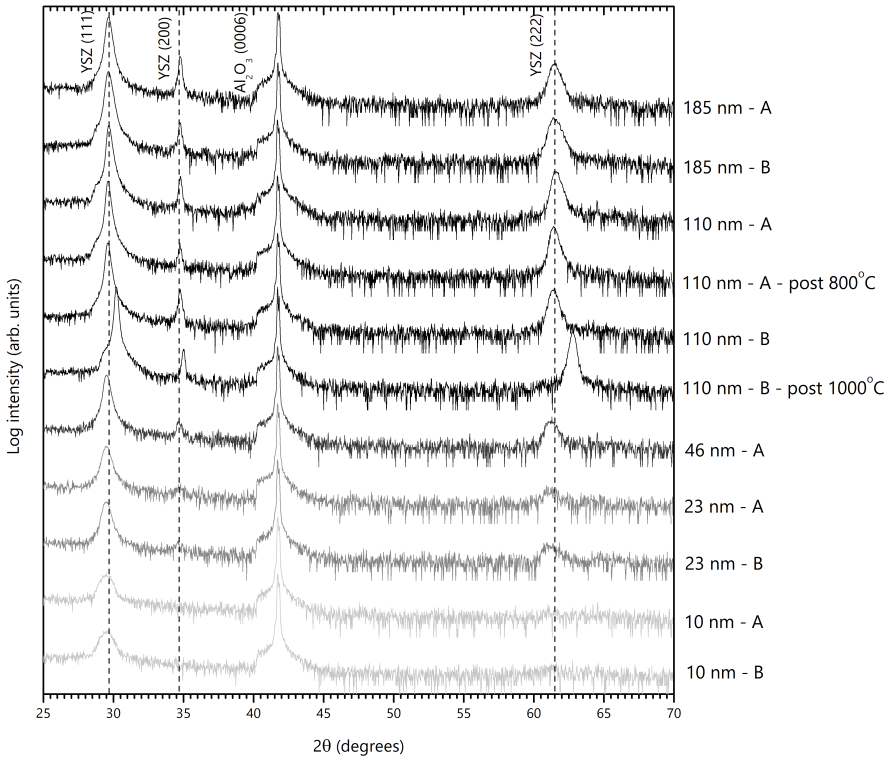


Figure A.5: XRD $\theta/2\theta$ patterns from the YSZ films grown on Al_2O_3 substrates with a nominal substrate temperature of 600°C during deposition. The peak marked with a $*$ are due to the substrate peaks. The samples labels correspond to those in Table 6.1.

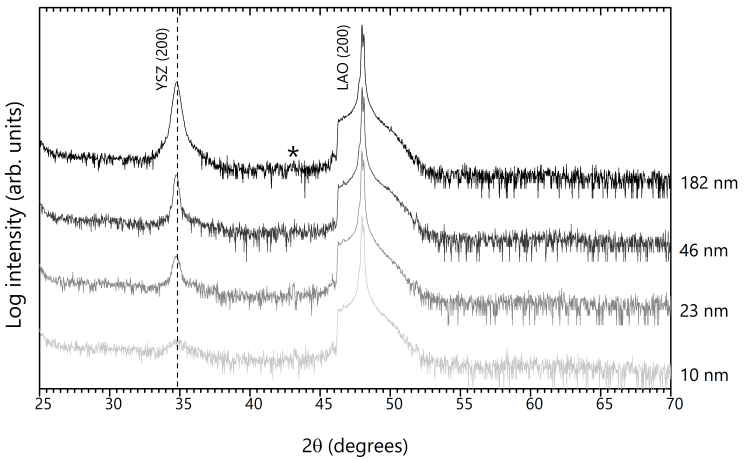


Figure A.6: XRD $\theta/2\theta$ patterns from the YSZ films grown on LAO substrates with a nominal substrate temperature of 600°C during deposition. The peak marked with a $*$ are due to the substrate peaks.

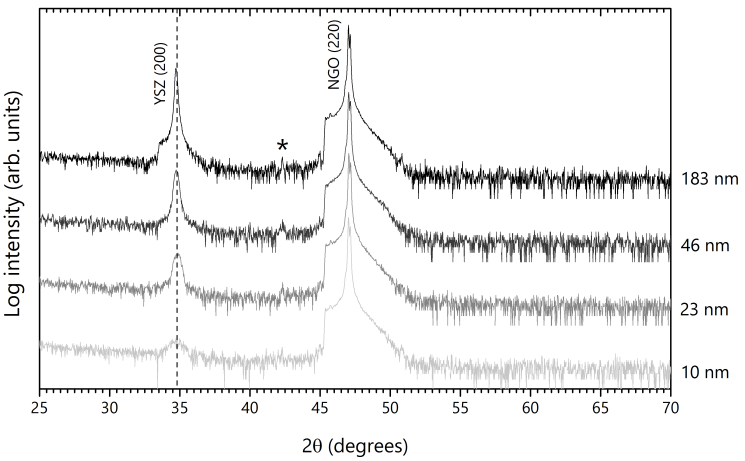


Figure A.7: XRD $\theta/2\theta$ patterns from the YSZ films grown on NGO substrates with a nominal substrate temperature of 600°C during deposition. The peak marked with a $*$ are due to the substrate peaks.

A.3 ^{18}O Lateral Diffusion Profiles for the YSZ Films in Chapter 6

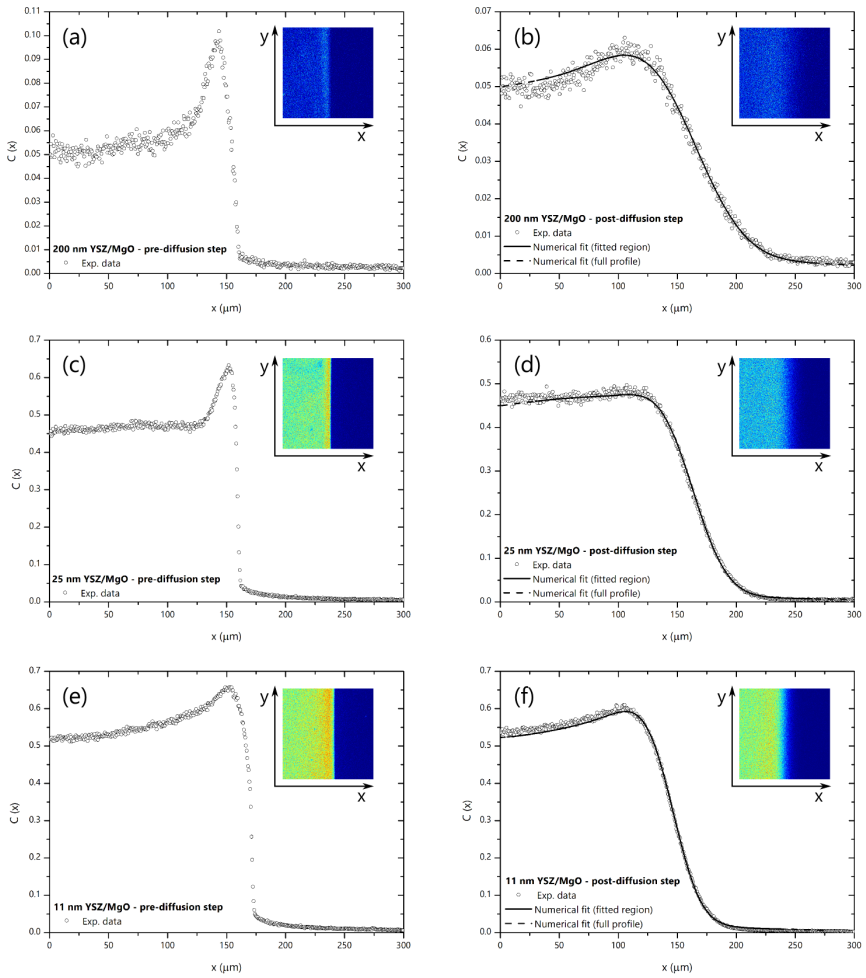


Figure A.8: Lateral profiles of the ^{18}O isotope fraction for YSZ films grown on MgO. The insets show the ^{18}O isotope fraction integrated in the z-axis direction. In (a, c, and e) the ^{18}O distribution across the Au covered and uncovered region is shown after the incorporation step of 30 minutes at 300°C in ^{18}O enriched gas. In (b, d, and f) the subsequent ^{18}O distribution after annealing for 14 hours at 500°C is shown. The profiles in (b, d, and f) are fitted using the numerical method in Section 4.5.5.

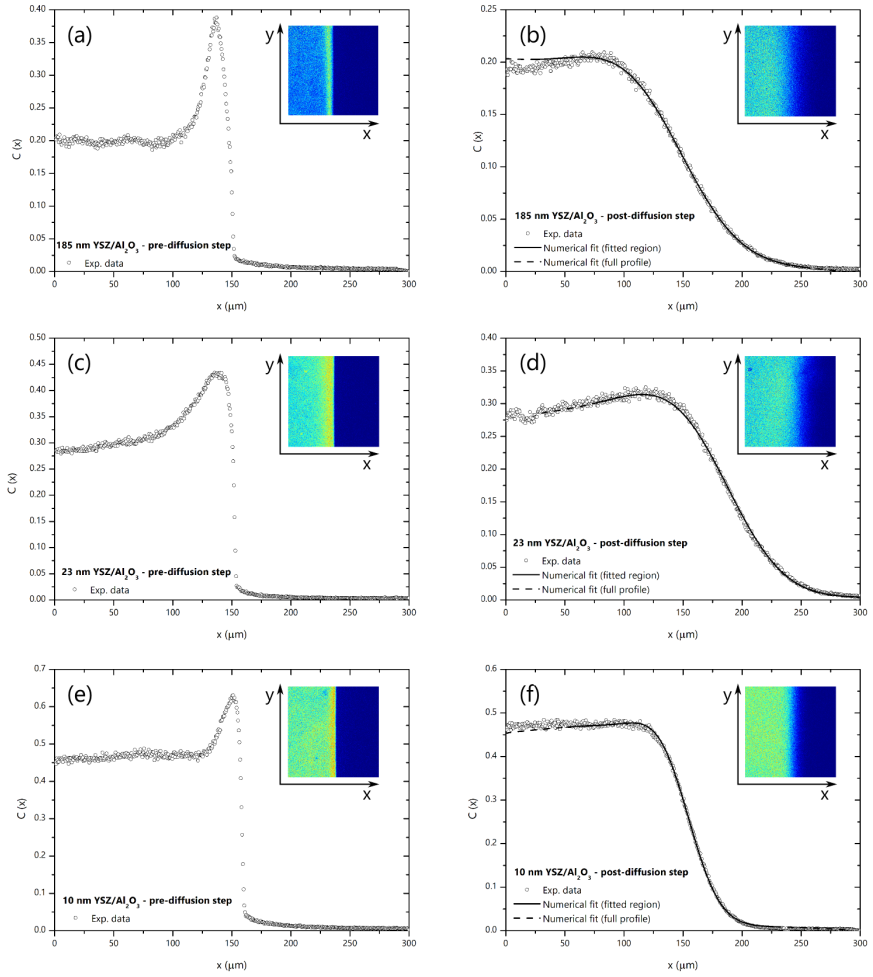


Figure A.9: Lateral profiles of the ^{18}O isotope fraction for YSZ films grown on Al_2O_3. The insets show the ^{18}O isotope fraction integrated in the z-axis direction. In (a, c, and e) the ^{18}O distribution across the Au covered and uncovered region is shown after the incorporation step of 30 minutes at 300°C in ^{18}O enriched gas. In (b, d, and f) the subsequent ^{18}O distribution after annealing for 14 hours at 500°C is shown. The profiles in (b, d, and f) are fitted using the numerical method in Section 4.5.5.

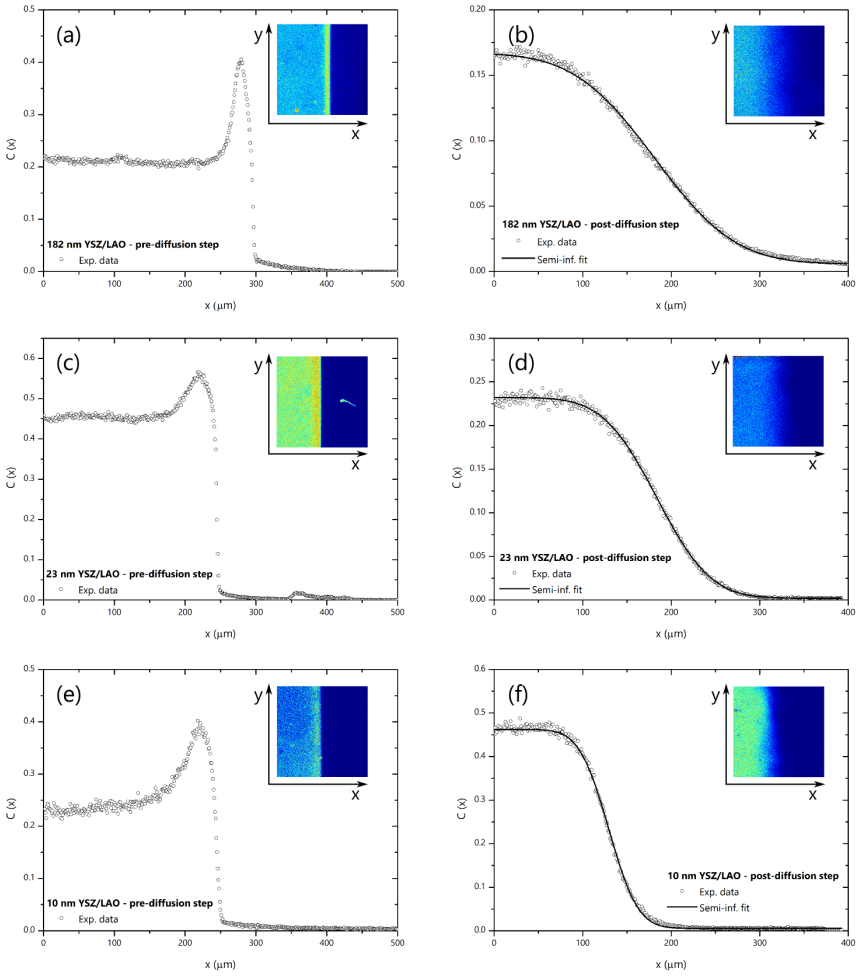


Figure A.10: Lateral profiles of the ^{18}O isotope fraction for YSZ films grown on LAO. The insets show the ^{18}O isotope fraction integrated in the z-axis direction. In (a, c, and e) the ^{18}O distribution across the Au covered and uncovered region is shown after the incorporation step of 30 minutes at 300°C in ^{18}O enriched gas. In (b, d, and f) the subsequent ^{18}O distribution after annealing for 14 hours at 500°C is shown. The profiles in (b, d, and f) are fitted according to Eq. 4.21.

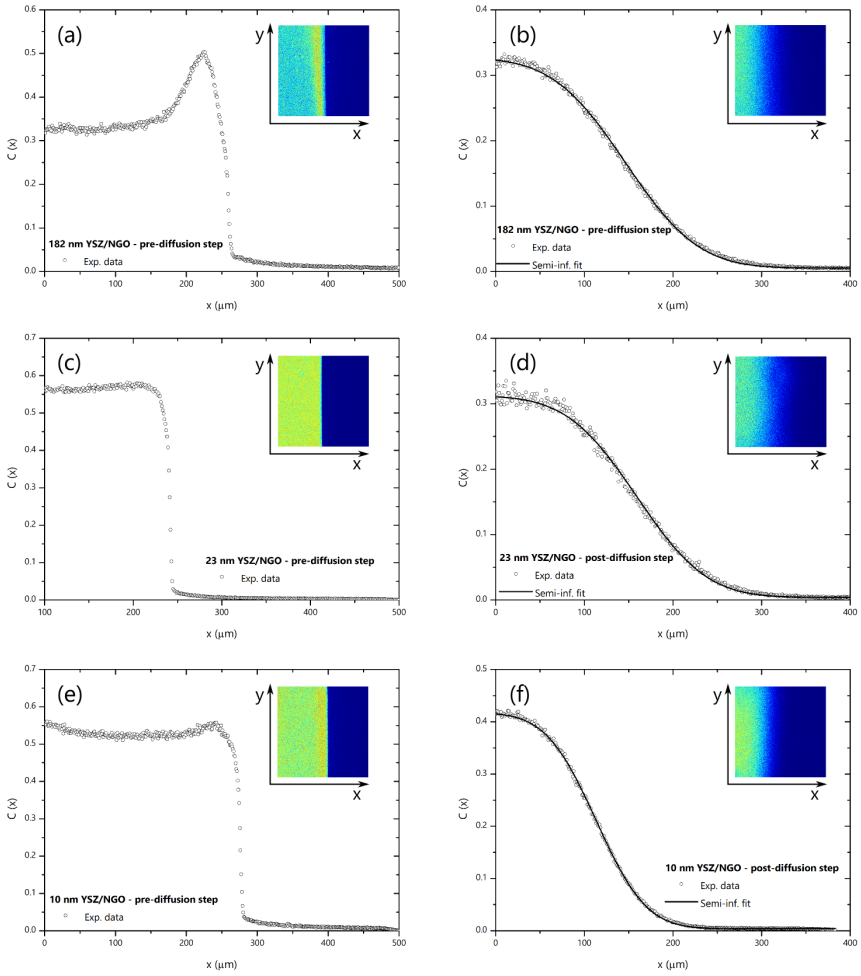


Figure A.11: Lateral profiles of the ^{18}O isotope fraction for YSZ films grown on NGO. The insets show the ^{18}O isotope fraction integrated in the z-axis direction. In (a, c, and e) the ^{18}O distribution across the Au covered and uncovered region is shown after the incorporation step of 30 minutes at 300°C in ^{18}O enriched gas. In (b, d, and f) the subsequent ^{18}O distribution after annealing for 14 hours at 500°C is shown. The profiles in (b, d, and f) are fitted according to Eq. 4.21.

A.4 Consideration of Errors from EIS Measurements in Chapter 6

The typical accuracy of the Solartron Analytical 1260 FRA and 1296 dielectric interface used in this work is provided from the manufacturer and reproduced in Fig. A.12. Despite measuring the impedance down to a frequency of 1 Hz, the impedance spectra in this work were fitted typically up to a frequency of 100 Hz to avoid any electrode contributions to the resistance. The total resistance, R, of the films at 500°C, (corresponding to Fig. 6.20), were in the range of 10^7-10^{10} Ω, yielding an error, ΔR, of between 0.2-5% depending on the sample.

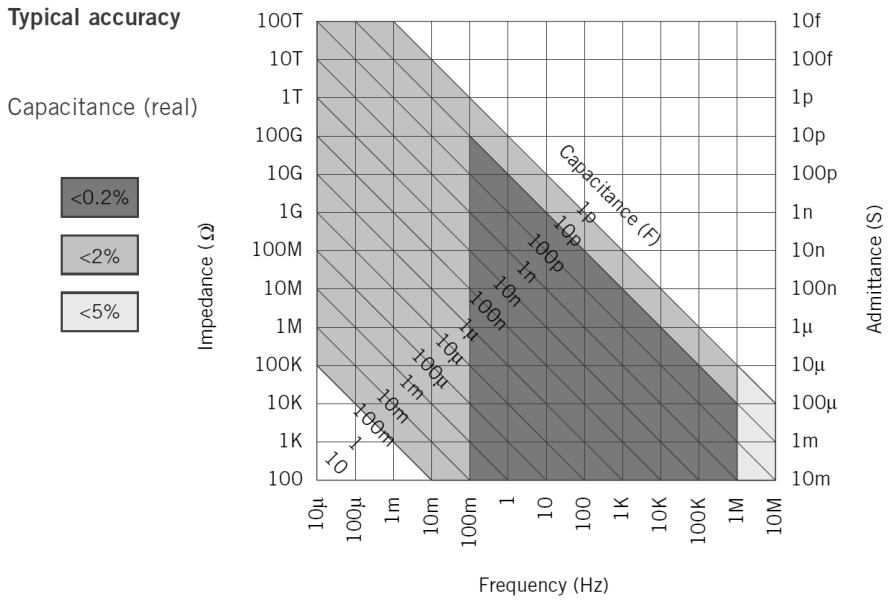


Figure A.12: Typical accuracy using a Solartron Analytical 1260 FRA and 1296 dielectric interface [242].

Additional error originates from the uncertainty in the sample dimensions. An accuracy in the thickness of the films, Δd, of 10% is assumes due to slight changes in the plume size and position with respect to the substrate. These would most likely originate from variations in the laser alignment, laser energy and pO_2 during deposition. An optical image of a

typical set of electrodes deposited onto a YSZ film is shown in Fig. A.13. An uncertainty in the electrode spacing, ΔD, and the length, ΔL, was taken to be 100 μm and 400 μm respectively. The total error on the conductivity, $\Delta\sigma$, was calculated according to:

$$\frac{\Delta\sigma}{\sigma} = \sqrt{\frac{\Delta R^2}{R} + \frac{\Delta d^2}{d} + \frac{\Delta D^2}{D} + \frac{\Delta L^2}{L}} \tag{A.1}$$

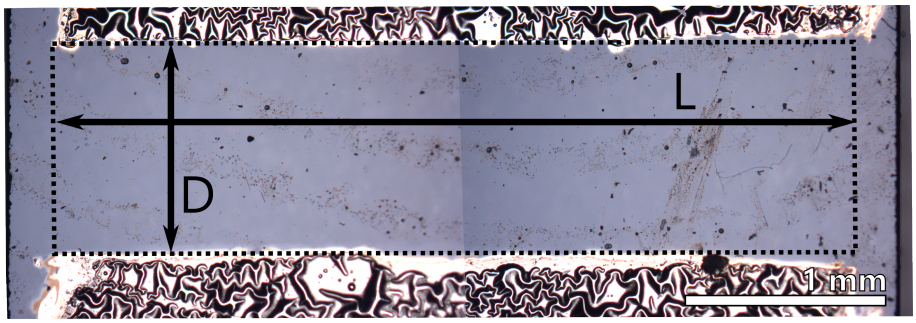


Figure A.13: Optical image of a typical set of Pt sputtered electrodes after electrical measurements.

A.5 LEIS Depth Profiles of CGO Films in Chapter 7

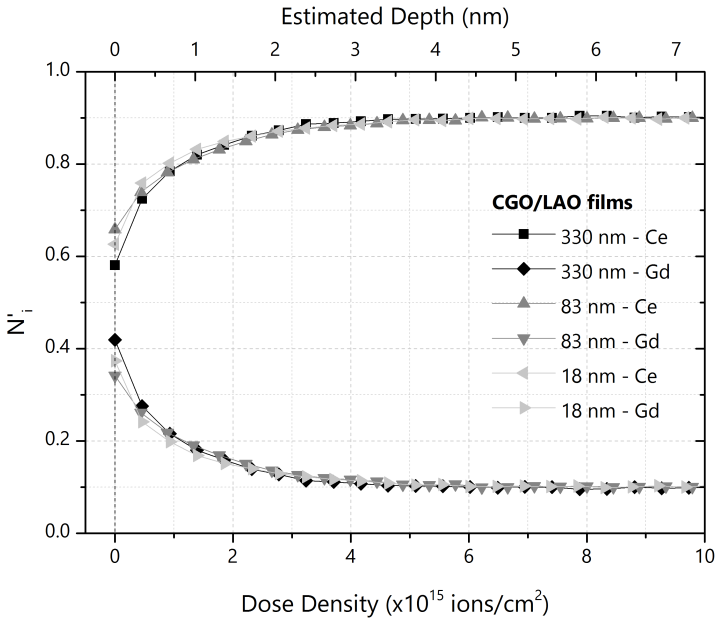


Figure A.14: Normalised cation coverage of Ce and Gd as a function of sputter dose for CGO films grown on LAO for a range of thicknesses.

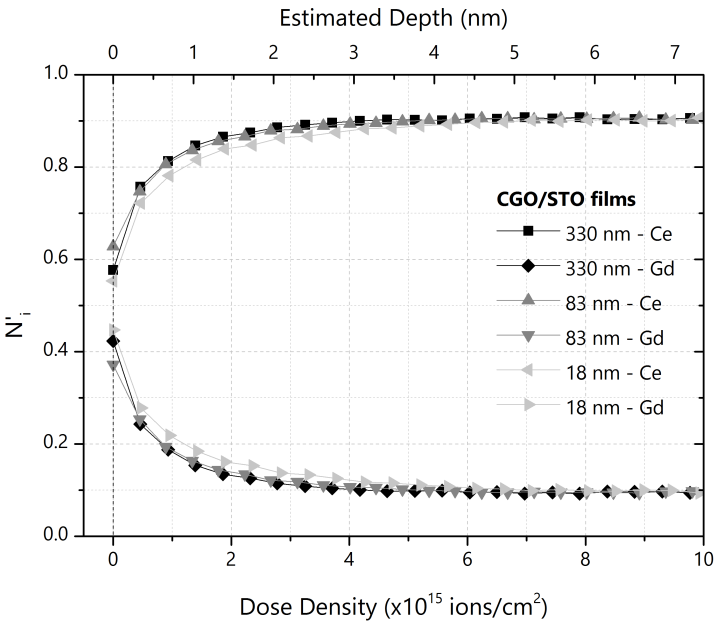


Figure A.15: Normalised cation coverage of Ce and Gd as a function of sputter dose for CGO films grown on STO for a range of thicknesses.

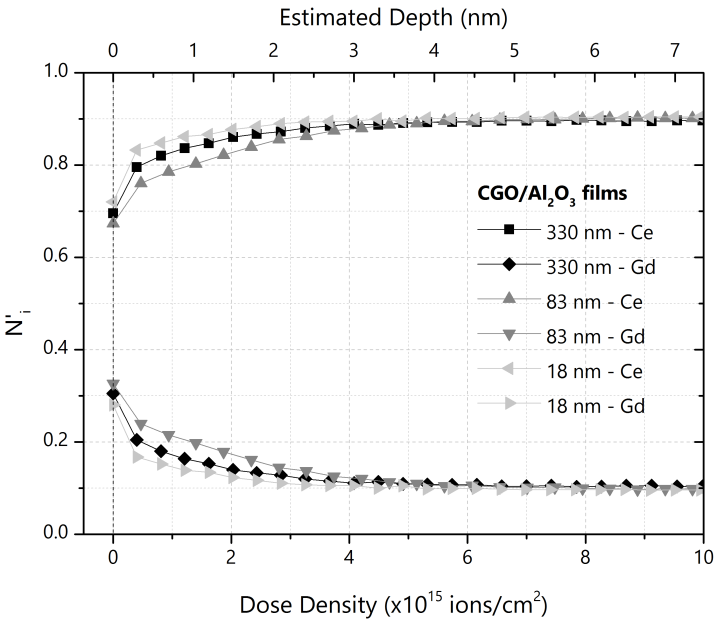


Figure A.16: Normalised cation coverage of Ce and Gd as a function of sputter dose for CGO films grown on Al_2O_3 for a range of thicknesses.

Bibliography

[1] BP. Energy Outlook 2035. *http://www.bp.com/content/dam/bp/pdf/Energy-economics/Energy-Outlook/Energy_Outlook_2035_booklet.pdf*, 2014.

[2] International Energy Agency. *Key World Energy Statistics. http://www.iea.org/*, 2014.

[3] Intergovermental Panel on Climate Change. *Fifth Assesment Report (AR5). http://www.ipcc.ch/*, 2014.

[4] P. Ekins and J. Watson. UK Energy in a Global Context - Synthesis Report. *http://www.ukerc.ac.uk/*, 2014.

[5] E. Ivers-Tiffée, K. H. Härdtl, W. Menesklou, and J. Riegel. Principles of solid state oxygen sensors for lean combustion gas control. *Electrochimica Acta*, 47(5):807–814, 2001.

[6] P. Seeharaj, A. Berenov, E. Raj, R. Rudkin, and A. Atkinson. Mixed-conducting LSC/CGO composites for passive oxygen separation membranes. *Solid State Ionics*, 192(1):638–641, 2011.

[7] F. A. Kröger and H. J. Vink. *Relations between the Concentrations of Imperfections in Crystalline Solids*, volume 3, pages 307–435. Academic Press, 1956.

[8] EG&G Technical Services, US Department of Energy, Office of Fossil Energy. *Fuel Cell Handbook*. Morgantown, WV, 2004.

[9] National Renewable Energy Laboratory, US Department of Energy. *110 kW Stationary Combined Heat and Power Systems and Technical Potential*. 2010.

[10] S. A. Sherif, D. Yogi-Goswami, E. K. Stefanakos, and A. Steinfeld. *Handbook of Hydrogen Energy*. 2014.

[11] S. C. Singhal and K. Kendall. *High temperature solid oxide fuel cells: fundamentals, design, and applications*. Elsevier Science, 2003.

[12] B. C. H. Steele and A. Heinzel. Materials for fuel-cell technologies. *Nature*, 414(6861):345–352, 2001.

[13] E. Wachsman, T. Ishihara, and J. Kilner. Low-temperature solid-oxide fuel cells. *MRS Bulletin*, 39(09):773–779, 2014.

[14] A. Evans, A. Bieberle-Hütter, J. L. M. Rupp, and L. J. Gauckler. Review on microfabricated micro-solid oxide fuel cell membranes. *Journal of Power Sources*, 194(1):119–129, 2009.

[15] A. Bieberle-Hütter, D. Beckel, A. Infortuna, U. P. Muecke, J. L. M. Rupp, L. J. Gauckler, S. Rey-Mermet, P. Muralt, N. R. Bieri, N. Hotz, M. J. Stutz, D. Poulikakos, P. Heeb, P. Müller, A. Bernard, R. Gmür, and T. Hocker. A micro-solid oxide fuel cell system as battery replacement. *Journal of Power Sources*, 177(1):123–130, 2008.

[16] R. Waser and M. Aono. Nanoionics-based resistive switching memories. *Nat Mater*, 6(11):833–840, 2007.

[17] J. J. Yang, D. B. Strukov, and D. R. Stewart. Memristive devices for computing. *Nat Nano*, 8(1):13–24, 2013.

[18] X. Guo. Can we achieve significantly higher ionic conductivity in nanostructured zirconia? *Scripta Materialia*, 65(2):96–101, 2011.

[19] V. V. Kharton, F. M. B. Marques, and A. Atkinson. Transport properties of solid oxide electrolyte ceramics: a brief review. *Solid State Ionics*, 174(14):135–149, 2004.

[20] L. Malavasi, C. A. J. Fisher, and M. S. Islam. Oxide-ion and proton conducting electrolyte materials for clean energy applications: structural and mechanistic features. *Chemical Society Reviews*, 39(11):4370–4387, 2010.

[21] H. G. Scott. Phase relationships in the zirconia-yttria system. *Journal of Materials Science*, 10(9):1527–1535, 1975.

[22] Y. M. Chiang, D. P. Birnie, and W. D. Kingery. *Physical Ceramics: Principles for Ceramic Science and Engineering*. Wiley, 1996.

[23] A. M. Diness and R. Roy. Experimental confirmation of major change of defect type with temperature and composition in ionic solids. *Solid State Communications*, 3(6):123–125, 1965.

[24] S. J. Hong and A. V. Virkar. Lattice Parameters and Densities of Rare-Earth Oxide Doped Ceria Electrolytes. *Journal of the American Ceramic Society*, 78(2):433–439, 1995.

[25] D. Marrocchelli, S. R. Bishop, H. L. Tuller, and B. Yildiz. Understanding Chemical Expansion in Non-Stoichiometric Oxides: Ceria and Zirconia Case Studies. *Advanced Functional Materials*, 22(9):1958–1965, 2012.

[26] D. Marrocchelli, S. R. Bishop, and J. Kilner. Chemical expansion and its dependence on the host cation radius. *Journal of Materials Chemistry A*, 1(26):7673–7680, 2013.

[27] H. L. Tuller. *6 - Mixed Conduction in Nonstoichiometric Oxides*, pages 271–335. Academic Press, 1981.

[28] H. L. Tuller. Mixed ionic-electronic conduction in a number of fluorite and pyrochlore compounds. *Solid State Ionics*, 52(13):135–146, 1992.

[29] H. L. Tuller, J. Schoonman, and I. Riess. Oxygen Ion and Mixed Conductors and their Technological Applications. In Harry L. Tuller, Johannes Schoonman, and Ian Riess, editors, *NATO Advanced Study Institute*.

[30] H. L. Tuller and A. S. Nowick. Doped Ceria as a Solid Oxide Electrolyte. *Journal of the Electrochemical Society*, 122(2):255–259, 1975.

[31] H. L. Tuller and A. S. Nowick. Defect Structure and Electrical Properties of Nonstoichiometric CeO_2 Single Crystals. *Journal of the Electrochemical Society*, 126(2):209–217, 1979.

[32] A. R. West. *Solid State Chemistry and its Applications*. John Wiley and Sons Ltd., 1987.

[33] J. A. Kilner and B. C. H. Steele. *5 - Mass Transport in Anion-Deficient Fluorite Oxides*, pages 233–269. Academic Press, 1981.

[34] D. Y. Wang, D. S. Park, J. Griffith, and A. S. Nowick. Oxygen-ion conductivity and defect interactions in yttria-doped ceria. *Solid State Ionics*, 2(2):95–105, 1981.

[35] T. H. Etsell and S. N. Flengas. Electrical properties of solid oxide electrolytes. *Chemical Reviews*, 70(3):339–376, 1970.

[36] A. S. Nowick. The Golden Age of Crystal Defects. *Annual Review of Materials Science*, 26(1):1–19, 1996.

[37] P. S. Manning, J. D. Sirman, R. A. De Souza, and J. A. Kilner. The kinetics of oxygen transport in 9.5 mol % single crystal yttria stabilised zirconia. *Solid State Ionics*, 100(12):1–10, 1997.

[38] J. E. Bauerle and J. Hrizo. Interpretation of the resistivity temperature dependence of high purity $(ZrO_2)_{0.90}(Y_2O_3)0.10$. *Journal of Physics and Chemistry of Solids*, 30(3):565–570, 1969.

[39] J. Faber, C. Geoffroy, A. Roux, A. Sylvestre, and P. Alélard. A Systematic investigation of the dc electrical conductivity of rare-earth doped ceria. *Applied Physics A*, 49(3):225–232, 1989.

[40] J. A. Kilner and R. J. Brook. A study of oxygen ion conductivity in doped non-stoichiometric oxides. *Solid State Ionics*, 6(3):237–252, 1982.

[41] J. A. Kilner. Fast anion transport in solids. *Solid State Ionics*, 8(3):201–207, 1983.

[42] J. A. Kilner. Fast oxygen transport in acceptor doped oxides. *Solid State Ionics*, 129(14):13–23, 2000.

[43] J. A. Kilner. Defects and Conductivity in Ceria-based Oxides. *Chemistry Letters*, 37(10):1012–1015, 2008.

[44] L. Minervini, M. O. Zacate, and R. W. Grimes. Defect cluster formation in M_2O_3-doped CeO_2. *Solid State Ionics*, 116(34):339–349, 1999.

[45] M. O. Zacate, L. Minervini, D. J. Bradfield, R. W. Grimes, and K. E. Sickafus. Defect cluster formation in M_2O_3-doped cubic ZrO_2. *Solid State Ionics*, 128(14):243–254, 2000.

[46] J. E. Bauerle. Study of solid electrolyte polarization by a complex admittance method. *Journal of Physics and Chemistry of Solids*, 30(12):2657–2670, 1969.

[47] X. Guo and R. Waser. Electrical properties of the grain boundaries of oxygen ion conductors: Acceptor-doped zirconia and ceria. *Progress in Materials Science*, 51(2):151–210, 2006.

[48] J. Maier. Thermodynamic aspects and morphology of nano-structured ion conductors: Aspects of nano-ionics Part I. *Solid State Ionics*, 154-155:291–301, 2002.

[49] J. Maier. Defect chemistry and ion transport in nanostructured materials: Part II. Aspects of nanoionics. *Solid State Ionics*, 157(14):327–334, 2003.

[50] J. Maier. Nano-sized mixed conductors (Aspects of nano-ionics. Part III). *Solid State Ionics*, 148(34):367–374, 2002.

[51] J. Maier. Ionic transport in nano-sized systems. *Solid State Ionics*, 175(14):7–12, 2004.

[52] K. L. Merkle, G. R. Bai, Z. Li, C. Y. Song, and L. J. Thompson. High-Resolution Studies of Grain Boundary Structure in Yttria-Stabilized Cubic Zirconia Thin Films Grown by MOCVD. *physica status solidi (a)*, 166(1):73–89, 1998.

[53] C. A. J. Fisher and H. Matsubara. The influence of grain boundary misorientation on ionic conductivity in YSZ. *Journal of the European Ceramic Society*, 19(67):703–707, 1999.

[54] Y. Lei, Y. Ito, N. D. Browning, and T. J. Mazanec. Segregation Effects at Grain Boundaries in Fluorite-Structured Ceramics. *Journal of the American Ceramic Society*, 85(9):2359–2363, 2002.

[55] M. J. Verkerk, B. J. Middelhuis, and A. J. Burggraaf. Effect of grain boundaries on the conductivity of high-purity ZrO_2-Y_2O_3 ceramics. *Solid State Ionics*, 6(2):159–170, 1982.

[56] J. Maier. Nano-Ionics: More Than Just a Fashionable Slogan. *Journal of Electroceramics*, 13(1):593–598, 2004.

[57] S. J. Litzelman, J. L. Hertz, W. Jung, and H. L. Tuller. Opportunities and Challenges in Materials Development for Thin Film Solid Oxide Fuel Cells. *Fuel Cells*, 8(5):294–302, 2008.

[58] C. Korte, A. Peters, J. Janek, D. Hesse, and N. Zakharov. Ionic conductivity and activation energy for oxygen ion transport in superlattices-the semicoherent multilayer system YSZ (ZrO_2 + 9.5 mol% Y_2O_3)/Y_2O_3. *Physical Chemistry Chemical Physics*, 10(31), 2008.

[59] J. Hinterberg, T. Zacherle, and R. A. De Souza. Activation Volume Tensor for Oxygen-Vacancy Migration in Strained CeO_2 Electrolytes. *Physical Review Letters*, 110(20):205901, 2013.

[60] M. J. Aziz. Thermodynamics of diffusion under pressure and stress: Relation to point defect mechanisms. *Applied Physics Letters*, 70(21):2810–2812, 1997.

[61] C. Korte, N. Schichtel, D. Hesse, and J. Janek. Influence of interface structure on mass transport in phase boundaries between different ionic materials. *Monatshefte für Chemie / Chemical Monthly*, 140(9):1069–1080, 2009.

[62] M. Greenberg, E. Wachtel, I. Lubomirsky, J. Fleig, and J. Maier. Elasticity of Solids with a Large Concentration of Point Defects. *Advanced Functional Materials*, 16(1):48–52, 2006.

[63] C. Korte, J. Keppner, A. Peters, N. Schichtel, H. Aydin, and J. Janek. Coherency strain and its effect on ionic conductivity and diffusion in solid electrolytes - an improved model for nanocrystalline thin films and a review of experimental data. *Physical Chemistry Chemical Physics*, 16(44):24575–24591, 2014.

[64] E. T. Park and J. H. Park. *Proceedings of the 3rd International Meeting of Pacific Rim Ceramic Societies*, 1998.

[65] D. Hull and D. J. Bacon. *Chapter 4 - Elastic Properties of Dislocations*, pages 63–83. Butterworth-Heinemann, Oxford, 2011.

[66] P. W. Tasker. The stability of ionic crystal surfaces. *Journal of Physics C: Solid State Physics*, 12(22):4977, 1979.

[67] D. McLean. *Grain boundaries in metals*. Clarendon Press, 1957.

[68] P. Wynblatt and R. C. Ku. Surface energy and solute strain energy effects in surface segregation. *Surface Science*, 65(2):511–531, 1977.

[69] R. C. McCune and P. Wynblatt. Calcium Segregation to a Magnesium Oxide (100) Surface. *Journal of the American Ceramic Society*, 66(2):111–117, 1983.

[70] J. Friedel. Electronic structure of primary solid solutions in metals. *Advances in Physics*, 3(12):446–507, 1954.

[71] C. Lea and M. P. Seah. Kinetics of surface segregation. *Philosophical Magazine*, 35(1):213–228, 1977.

[72] X. Guo and Z. Zhang. Grain size dependent grain boundary defect structure: case of doped zirconia. *Acta Materialia*, 51(9):2539–2547, 2003.

[73] P. Mondal, A. Klein, W. Jaegermann, and H. Hahn. Enhanced specific grain boundary conductivity in nanocrystalline Y_2O_3-stabilized zirconia. *Solid State Ionics*, 118(34):331–339, 1999.

[74] M. Aoki, Y.-M. Chiang, I. Kosacki, L. J.-R. Lee, H. Tuller, and Y. Liu. Solute Segregation and Grain-Boundary Impedance in High-Purity Stabilized Zirconia. *Journal of the American Ceramic Society*, 79(5):1169–1180, 1996.

[75] O. J. Durá, M. A. López de la Torre, L. Vázquez, J. Chaboy, R. Boada, A. Rivera-Calzada, J. Santamaria, and C. Leon. Ionic conductivity of nanocrystalline yttria-stabilized zirconia: Grain boundary and size effects. *Physical Review B*, 81(18):184301, 2010. PRB.

[76] H. J. Park and Y. H. Choa. The Grain Boundary Conduction Property of Highly Dense and Nanostructured Yttrium-Doped Zirconia. *Electrochemical and Solid-State Letters*, 13(5):K49–K52, 2010.

[77] N. Perry, S. Kim, and T. Mason. Local electrical and dielectric properties of nanocrystalline yttria-stabilized zirconia. *Journal of Materials Science*, 43(14):4684–4692, 2008.

[78] N. H. Perry and T. O. Mason. Grain core and grain boundary electrical/dielectric properties of yttria-doped tetragonal zirconia polycrystal (TZP) nanoceramics. *Solid State Ionics*, 181(57):276–284, 2010.

[79] G. Knöner, K. Reimann, R. Röwer, U. Södervall, and H.-E. Schaefer. Enhanced oxygen diffusivity in interfaces of nanocrystalline ZrO_2-Y_2O_3. *Proceedings of the National Academy of Sciences*, 100(7):3870–3873, 2003.

[80] R. A. De Souza, M. J. Pietrowski, U. Anselmi-Tamburini, S. Kim, Z. A. Munir, and M. Martin. Oxygen diffusion in nanocrystalline

yttria-stabilized zirconia: the effect of grain boundaries. *Physical Chemistry Chemical Physics*, 10(15):2067–2072, 2008.

[81] I. Kosacki, T. Suzuki, V. Petrovsky, and H. U. Anderson. Electrical conductivity of nanocrystalline ceria and zirconia thin films. *Solid State Ionics*, 136-137(0):1225–1233, 2000.

[82] C. Peters, A. Weber, B. Butz, D. Gerthsen, and E. Ivers-Tiffee. Grain-Size Effects in YSZ Thin-Film Electrolytes. *Journal of the American Ceramic Society*, 92(9):2017–2024, 2009.

[83] J. H. Joo and G. M. Choi. Electrical conductivity of YSZ film grown by pulsed laser deposition. *Solid State Ionics*, 177(11-12):1053–1057, 2006.

[84] M. V. F. Schlupp, B. Scherrer, H. Ma, J. G. Grolig, J. Martynczuk, M. Prestat, and L. J. Gauckler. Influence of microstructure on the cross-plane oxygen ion conductivity of yttria stabilized zirconia thin films. *physica status solidi (a)*, 209(8):1414–1422, 2012.

[85] S.-Y. Chun and N. Mizutani. The transport mechanism of YSZ thin films prepared by MOCVD. *Applied Surface Science*, 171(12):82–88, 2001.

[86] S. Heiroth, T. Lippert, A. Wokaun, and M. Döbeli. Microstructure and electrical conductivity of YSZ thin films prepared by pulsed laser deposition. *Applied Physics A: Materials Science & Processing*, 93(3):639–643, 2008.

[87] W. Jung, J. L. Hertz, and H. L. Tuller. Enhanced ionic conductivity and phase meta-stability of nano-sized thin film yttria-doped zirconia (YDZ). *Acta Materialia*, 57(5):1399–1404, 2009.

[88] S. Sanna, V. Esposito, D. Pergolesi, A. Orsini, A. Tebano, S. Licoccia, G. Balestrino, and E. Traversa. Fabrication and Electrochemical Properties of Epitaxial Samarium-Doped Ceria Films on $SrTiO_3$-Buffered MgO Substrates. *Advanced Functional Materials*, 19(11):1713–1719, 2009.

[89] J. H. Joo and G. M. Choi. Electrical conductivity of thin film ceria grown by pulsed laser deposition. *Journal of the European Ceramic Society*, 27(1315):4273–4277, 2007.

[90] L. Chen, C. L. Chen, X. Chen, W. Donner, S. W. Liu, Y. Lin, D. X. Huang, and A. J. Jacobson. Electrical properties of a highly oriented, textured thin film of the ionic conductor Gd:$CeO_{2-\delta}$ on (001) MgO. *Applied Physics Letters*, 83(23):4737–4739, 2003.

[91] J. L. M. Rupp, A. Infortuna, and L. J. Gauckler. Thermodynamic Stability of Gadolinia-Doped Ceria Thin Film Electrolytes for Micro-Solid Oxide Fuel Cells. *Journal of the American Ceramic Society*, 90(6):1792–1797, 2007.

[92] G. Chiodelli, L. Malavasi, V. Massarotti, P. Mustarelli, and E. Quartarone. Synthesis and characterization of $Ce_{0.8}Gd_{0.2}O_{2-y}$ polycrystalline and thin film materials. *Solid State Ionics*, 176(1718):1505–1512, 2005.

[93] R. Frison, S. Heiroth, J. L. M. Rupp, K. Conder, E. J. Barthazy, E. Müller, M. Horisberger, M. Döbeli, and L. J. Gauckler. Crystallization of 8 mol.% yttria-stabilized zirconia thin-films deposited by RF-sputtering. *Solid State Ionics*, 232(0):29–36, 2013.

[94] T. Suzuki, I. Kosacki, and H. U. Anderson. Microstructure-electrical conductivity relationships in nanocrystalline ceria thin films. *Solid State Ionics*, 151(14):111–121, 2002.

[95] N. I. Karageorgakis, A. Heel, J. L. M. Rupp, M. H. Aguirre, T. Graule, and L. J. Gauckler. Properties of Flame Sprayed $Ce_{0.8}Gd_{0.2}O_{1.9-\delta}$ Electrolyte Thin Films. *Advanced Functional Materials*, 21(3):532–539, 2011.

[96] J. L. M. Rupp. Ionic diffusion as a matter of lattice-strain for electroceramic thin films. *Solid State Ionics*, 207:1–13, 2012.

[97] J. L. M. Rupp, E. Fabbri, D. Marrocchelli, J.-W. Han, D. Chen, E. Traversa, H. L. Tuller, and B. Yildiz. Scalable Oxygen-Ion Trans-

port Kinetics in Metal-Oxide Films: Impact of Thermally Induced Lattice Compaction in Acceptor Doped Ceria Films. *Advanced Functional Materials*, 24(11):1562–1574, 2014.

[98] A. Cavallaro, G. F. Harrington, S. J. Skinner, and J. A. Kilner. Controlling the surface termination of $NdGaO_3$ (110): the role of the gas atmosphere. *Nanoscale*, 6(13):7263–7273, 2014.

[99] A. Cavallaro, B. Ballesteros, R. Bachelet, and J. Santiso. Heteroepitaxial orientation control of YSZ thin films by selective growth on SrO-, TiO_2-terminated $SrTiO_3$ crystal surfaces. *CrystEngComm*, 13(5):1625–1631, 2011.

[100] A. Ohtomo and H. Y. Hwang. A high-mobility electron gas at the $LaAlO_3/SrTiO_3$ heterointerface. *Nature*, 427(6973):423–426, 2004.

[101] M. L. Reinle-Schmitt, C. Cancellieri, A. Cavallaro, G. F. Harrington, S. J. Leake, E. Pomjakushina, J. A. Kilner, and P. R. Willmott. Chemistry and structure of homoepitaxial $SrTiO_3$ films and their influence on oxide-heterostructure interfaces. *Nanoscale*, 6(5):2598–2602, 2014.

[102] A. Cavallaro, M. Burriel, J. Roqueta, A. Apostolidis, A. Bernardi, A. Tarancón, R. Srinivasan, S. N. Cook, H. L. Fraser, J. A. Kilner, D. W. McComb, and J. Santiso. Electronic nature of the enhanced conductivity in YSZ-STO multilayers deposited by PLD. *Solid State Ionics*, 181(13-14):592–601, 2010.

[103] S. Kim, P. Jain, H. J. Avila-Paredes, A. Thron, K. van Benthem, and S. Sen. Strong immobilization of charge carriers near the surface of a solid oxide electrolyte. *Journal of Materials Chemistry*, 20(19):3855–3858, 2010.

[104] H.-R. Kim, J.-C. Kim, K.-R. Lee, H.-I. Ji, H.-W. Lee, J.-H. Lee, and J.-W. Son. 'Illusional' nano-size effect due to artifacts of in-plane conductivity measurements of ultra-thin films. *Physical Chemistry Chemical Physics*, 13(13):6133–6137, 2011.

[105] M. C. Gobel, G. Gregori, X. Guo, and J. Maier. Boundary effects on the electrical conductivity of pure and doped cerium oxide thin films. *Physical Chemistry Chemical Physics*, 12(42):14351–14361, 2010.

[106] I. Kosacki, C. M. Rouleau, P. F. Becher, J. Bentley, and D. H. Lowndes. Surface/Interface-Related Conductivity in Nanometer Thick YSZ Films. *Electrochemical and Solid-State Letters*, 7(12):A459–A461, 2004.

[107] I. Kosacki, C. M. Rouleau, P. F. Becher, J. Bentley, and D. H. Lowndes. Nanoscale effects on the ionic conductivity in highly textured YSZ thin films. *Solid State Ionics*, 176(13-14):1319–1326, 2005.

[108] N. J. Simrick, J. A. Kilner, and A. Atkinson. Thermal stability of silver thin films on zirconia substrates. *Thin Solid Films*, 520(7):2855–2867, 2012.

[109] M. de Ridder, R. G. van Welzenis, A. W. D. van der Gon, H. H. Brongersma, S. Wulff, W. F. Chu, and W. Weppner. Subsurface segregation of yttria in yttria stabilized zirconia. *Journal of Applied Physics*, 92(6):3056–3064, 2002.

[110] C. Korte. *Zur Wechselwirkung von Ionentransport und Mikrostruktur in inneren Grenzflaechen.* Habilitation Thesis, Justus-Liebig-Universität Giessen, 2008.

[111] N. Schichtel, C. Korte, D. Hesse, and J. Janek. Elastic strain at interfaces and its influence on ionic conductivity in nanoscaled solid electrolyte thin films-theoretical considerations and experimental studies. *Physical Chemistry Chemical Physics*, 11(17):3043–3048, 2009.

[112] B. Yildiz. Stretching the energy landscape of oxides-Effects on electrocatalysis and diffusion. *MRS Bulletin*, 39(02):147–156, 2014.

[113] X. Guo, E. Vasco, S. Mi, K. Szot, E. Wachsman, and R. Waser. Ionic conduction in zirconia films of nanometer thickness. *Acta Materialia*, 53(19):5161–5166, 2005.

[114] A. Karthikeyan, C.-L. Chang, and S. Ramanathan. High temperature conductivity studies on nanoscale yttria-doped zirconia thin films and size effects. *Applied Physics Letters*, 89(18):183116–3, 2006.

[115] M. Sillassen, P. Eklund, N. Pryds, E. Johnson, U. Helmersson, and J. Bttiger. Low-Temperature Superionic Conductivity in Strained Yttria-Stabilized Zirconia. *Advanced Functional Materials*, 20(13):2071–2076, 2010.

[116] M. Gerstl, T. Frömling, A. Schintlmeister, H. Hutter, and J. Fleig. Measurement of ^{18}O tracer diffusion coefficients in thin yttria stabilized zirconia films. *Solid State Ionics*, 184(1):23–26, 2011.

[117] M. Gerstl, G. Friedbacher, F. Kubel, H. Hutter, and J. Fleig. The relevance of interfaces for oxide ion transport in yttria stabilized zirconia (YSZ) thin films. *Physical Chemistry Chemical Physics*, 15:1097 – 1107, 2013.

[118] M. Gerstl, E. Navickas, G. Friedbacher, F. Kubel, M. Ahrens, and J. Fleig. The separation of grain and grain boundary impedance in thin yttria stabilized zirconia (YSZ) layers. *Solid State Ionics*, 185(1):32–41, 2011.

[119] J. Jiang, X. Hu, W. Shen, C. Ni, and J. L. Hertz. Improved ionic conductivity in strained yttria-stabilized zirconia thin films. *Applied Physics Letters*, 102(14):143901, 2013.

[120] E. Navickas, M. Gerstl, G. Friedbacher, F. Kubel, and J. Fleig. Measurement of the across-plane conductivity of YSZ thin films on silicon. *Solid State Ionics*, 211(0):58–64, 2012.

[121] E. Navickas, M. Gerstl, F. Kubel, and J. Fleig. Simultaneous Measurement of the In- and Across-Plane Ionic Conductivity of YSZ Thin Films. *Journal of the Electrochemical Society*, 159(4):B411–B416, 2012.

[122] L. Chen, C. L. Chen, D. X. Huang, Y. Lin, X. Chen, and A. J. Jacobson. High temperature electrical conductivity of epitaxial Gd-doped CeO_2 thin films. *Solid State Ionics*, 175(14):103–106, 2004.

[123] D. X. Huang, C. L. Chen, and A. J. Jacobson. Interface structures and periodic film distortions induced by substrate-surface steps in Gd-doped ceria thin-film growth. *Journal of Applied Physics*, 97(4):043506–5, 2005.

[124] D. Pergolesi, V. Roddatis, E. Fabbri, W. Schneider, C., T. Lippert, E. Traversa, and A. Kilner, J. Probing the bulk ionic conductivity by thin film hetero-epitaxial engineering. *Science and Technology of Advanced Materials*, 16(1):015001, 2015.

[125] K. M. Kant, V. Esposito, and N. Pryds. Strain induced ionic conductivity enhancement in epitaxial $Ce_{0.9}Gd_{0.1}O_{2-\delta}$ thin films. *Applied Physics Letters*, 100(3):033105–3, 2012.

[126] J. Jiang, W. Shen, and J. L. Hertz. Structure and ionic conductivity of nanoscale gadolinia-doped ceria thin films. *Solid State Ionics*, 249250(0):139–143, 2013.

[127] A. Peters, C. Korte, D. Hesse, N. Zakharov, and J. Janek. Ionic conductivity and activation energy for oxygen ion transport in superlattices The multilayer system CSZ (ZrO_2 + CaO)/Al_2O_3. *Solid State Ionics*, 178(12):67–76, 2007.

[128] N. Schichtel, C. Korte, D. Hesse, N. Zakharov, B. Butz, D. Gerthsen, and J. Janek. On the influence of strain on ion transport: microstructure and ionic conductivity of nanoscale YSZ-Sc_2O_3 multilayers. *Physical Chemistry Chemical Physics*, 12(43):14596–14608, 2010.

[129] H. Aydin, C. Korte, M. Rohnke, and J. Janek. Oxygen tracer diffusion along interfaces of strained Y_2O_3/YSZ multilayers. *Physical Chemistry Chemical Physics*, 2013.

[130] H. Aydin, C. Korte, and J. Janek. ^{18}O-tracer diffusion along nanoscaled Sc_2O_3/yttria stabilized zirconia (YSZ) multilayers: on the

influence of strain. *Science and Technology of Advanced Materials*, 14(3):035007, 2013.

[131] M. Kubicek, G. Holzlechner, A. K. Opitz, S. Larisegger, H. Hutter, and J. Fleig. A novel ToF-SIMS operation mode for sub 100 nm lateral resolution: Application and performance. *Applied Surface Science*, 289(0):407–416, 2014.

[132] A. Karthikeyan and S. Ramanathan. Temperature-dependent interfacial carrier transport in low-dimensional oxides using ionic conductor-insulator (YDZ-SiO_2) superlattices. *Journal of Applied Physics*, 104(12):124314, 2008.

[133] J. Garcia-Barriocanal, A. Rivera-Calzada, M. Varela, Z. Sefrioui, E. Iborra, C. Leon, S. J. Pennycook, and J. Santamaria. Colossal Ionic Conductivity at Interfaces of Epitaxial ZrO2:Y_2O_3/$SrTiO_3$ Heterostructures. *Science*, 321(5889):676–680, 2008.

[134] J. A. Kilner. Ionic conductors: Feel the strain. *Nat Mater*, 7(11):838–839, 2008.

[135] X. Guo. Comment on "Colossal Ionic Conductivity at Interfaces of Epitaxial ZrO2:Y_2O_3/$SrTiO_3$ Heterostructures". *Science*, 324(5926):465, 2009.

[136] J. Garcia-Barriocanal, A. Rivera-Calzada, M. Varela, Z. Sefrioui, E. Iborra, C. Leon, S. J. Pennycook, and J. Santamara. Response to Comment on "Colossal Ionic Conductivity at Interfaces of Epitaxial ZrO2:Y_2O_3/$SrTiO_3$ Heterostructures". *Science*, 324(5926):465, 2009.

[137] T. J. Pennycook, M. J. Beck, K. Varga, M. Varela, S. J. Pennycook, and S. T. Pantelides. Origin of Colossal Ionic Conductivity in Oxide Multilayers: Interface Induced Sublattice Disorder. *Physical Review Letters*, 104(11):115901, 2010.

[138] A. Rivera-Calzada, M. R. Diaz-Guillen, O. J. Dura, G. Sanchez-Santolino, T. J. Pennycook, R. Schmidt, F. Y. Bruno, J. Garcia-Barriocanal, Z. Sefrioui, N. M. Nemes, M. Garcia-Hernandez,

M. Varela, C. Leon, S. T. Pantelides, S. J. Pennycook, and J. Santamaria. Tailoring Interface Structure in Highly Strained YSZ/STO Heterostructures. *Advanced Materials*, 23(44):5268–5274, 2011.

[139] T. J. Pennycook, M. P. Oxley, J. Garcia-Barriocanal, F. Y. Bruno, C. Leon, J. Santamaria, S. T. Pantelides, M. Varela, and S. J. Pennycook. Seeing oxygen disorder in YSZ/$SrTiO_3$ colossal ionic conductor heterostructures using EELS. *The European Physical Journal - Applied Physics*, 54(03), 2011.

[140] W. Cheah and M. W. Finnis. Structure of multilayer ZrO2/$SrTiO_3$. *Journal of Materials Science*, 47(4):1631–1640, 2012.

[141] R. A. De Souza and A. H. H. Ramadan. Ionic conduction in the $SrTiO_3$-YSZ-$SrTiO_3$ heterostructure. *Physical Chemistry Chemical Physics*, 15(13):4505–4509, 2013.

[142] D. Pergolesi, E. Fabbri, S. N. Cook, V. Roddatis, E. Traversa, and J. A. Kilner. Tensile Lattice Distortion Does Not Affect Oxygen Transport in Yttria-Stabilized Zirconia-CeO_2 Heterointerfaces. *ACS Nano*, 6(12):10524–10534, 2012.

[143] B. Li, J. Zhang, T. Kaspar, V. Shutthanandan, R. C. Ewing, and J. Lian. Multilayered YSZ/GZO films with greatly enhanced ionic conduction for low temperature solid oxide fuel cells. *Physical Chemistry Chemical Physics*, 15(4):1296–1301, 2013.

[144] S. Azad, O. A. Marina, C. M. Wang, L. Saraf, V. Shutthanandan, D. E. McCready, A. El-Azab, J. E. Jaffe, M. H. Engelhard, C. H. F. Peden, and S. Thevuthasan. Nanoscale effects on ion conductance of layer-by-layer structures of gadolinia-doped ceria and zirconia. *Applied Physics Letters*, 86(13):131906, 2005.

[145] C. M. Wang, S. Azad, V. Shutthanandan, D. E. McCready, C. H. F. Peden, L. Saraf, and S. Thevuthasan. Microstructure of ZrO_2-CeO_2 hetero-multi-layer films grown on YSZ substrate. *Acta Materialia*, 53(7):1921–1929, 2005.

[146] C. M. Wang, M. H. Engelhard, S. Azad, L. V. Saraf, D. E. McCready, V. Shutthanandan, Z. Q. Yu, S. Thevuthasan, M. Watanabe, and D. B. Williams. Distribution of oxygen vacancies and gadolinium dopants in ZrO_2-CeO_2 multi-layer films grown on α-Al_2O_3. *Solid State Ionics*, 177(15-16):1299–1306, 2006.

[147] Y. Wang, L. An, L. Saraf, C. Wang, V. Shutthanandan, D. McCready, and S. Thevuthasan. Microstructure and ionic conductivity of alternating-multilayer structured Gd-doped ceria and zirconia thin films. *Journal of Materials Science*, 44(8):2021–2026, 2009.

[148] L. Yao, W. Liu, G. Ou, H. Nishijima, and W. Pan. Enhanced ionic conductivity in magnetron-sputtered $Ce_{0.8}Sm_{0.2}O_{2-\delta}/Al_2O_3$ multilayers. *Electrochimica Acta*, 158(0):196–201, 2015.

[149] S. Sanna, V. Esposito, A. Tebano, S. Licoccia, E. Traversa, and G. Balestrino. Enhancement of Ionic Conductivity in Sm-Doped Ceria/Yttria-Stabilized Zirconia Heteroepitaxial Structures. *Small*, 6(17):1863–1867, 2010.

[150] W. Shen, J. Jiang, and J. L. Hertz. Reduced ionic conductivity in biaxially compressed ceria. *RSC Advances*, 4(41):21625–21630, 2014.

[151] S. Schweiger, M. Kubicek, F. Messerschmitt, C. Murer, and J. L. M. Rupp. A Microdot Multilayer Oxide Device: Let Us Tune the Strain-Ionic Transport Interaction. *ACS Nano*, 8(5):5032–5048, 2014.

[152] J. M. Perkins, S. Fearn, S. N. Cook, R. Srinivasan, C. M. Rouleau, H. M. Christen, G. D. West, R. J. H. Morris, H. L. Fraser, S. J. Skinner, J. A. Kilner, and D. W. McComb. Anomalous Oxidation States in Multilayers for Fuel Cell Applications. *Advanced Functional Materials*, 20(16):2664–2674, 2010.

[153] W. Araki, Y. Imai, and T. Adachi. Mechanical stress effect on oxygen ion mobility in 8 mol.% yttria-stabilized zirconia electrolyte. *Journal of the European Ceramic Society*, 29(11):2275–2279, 2009.

[154] K. Otsuka, A. Kuwabara, A. Nakamura, T. Yamamoto, K. Matsunaga, and Y. Ikuhara. Dislocation-enhanced ionic conductivity of yttria-stabilized zirconia. *Applied Physics Letters*, 82(6):877–879, 2003.

[155] W. Araki and Y. Arai. Oxygen diffusion in yttria-stabilized zirconia subjected to uniaxial stress. *Solid State Ionics*, 181(810):441–446, 2010.

[156] A. Kushima and B. Yildiz. Oxygen ion diffusivity in strained yttria stabilized zirconia: where is the fastest strain? *Journal of Materials Chemistry*, 20(23), 2010.

[157] A. Tarancón and A. Morata. New insights into the origin of the oxide ionic diffusion change in strained lattices of yttria stabilized zirconia. *Computational Materials Science*, 2015.

[158] J. A. Hirschfeld and H. Lustfeld. First-principles study and modeling of strain-dependent ionic migration in ZrO_2. *Physical Review B*, 84(22):224308, 2011.

[159] R. A. De Souza, A. Ramadan, and S. Horner. Modifying the barriers for oxygen-vacancy migration in fluorite-structured CeO_2 electrolytes through strain: a computer simulation study. *Energy & Environmental Science*, 5(1):5445–5453, 2012.

[160] M. Burbano, D. Marrocchelli, and G. Watson. Strain effects on the ionic conductivity of Y-doped ceria: A simulation study. *Journal of Electroceramics*, 32(1):28–36, 2014.

[161] M. J. D. Rushton and A. Chroneos. Impact of uniaxial strain and doping on oxygen diffusion in CeO_2. *Sci. Rep.*, 4, 2014.

[162] T. X. T. Sayle, S. C. Parker, and D. C. Sayle. Ionic conductivity in nano-scale CeO_2/YSZ heterolayers. *Journal of Materials Chemistry*, 16(11):1067–1081, 2006.

[163] S. K. Sankaranarayanan and S. Ramanathan. Interface proximity effects on ionic conductivity in nanoscale oxide-ion conducting yttria

stabilized zirconia: an atomistic simulation study. *The Journal of chemical physics*, 134(6):064703, 2011.

[164] A. Infortuna, A. S. Harvey, and L. J. Gauckler. Microstructures of CGO and YSZ Thin Films by Pulsed Laser Deposition. *Advanced Functional Materials*, 18(1):127–135, 2008.

[165] M. Kilo, M. A. Taylor, C. Argirusis, G. Borchardt, B. Lesage, S. Weber, S. Scherrer, H. Scherrer, M. Schroeder, and M. Martin. Cation self-diffusion of ^{44}Ca, ^{88}Y, and ^{96}Zr in single-crystalline calcia- and yttria-doped zirconia. *Journal of Applied Physics*, 94(12):7547–7552, 2003.

[166] M. A. Taylor, C. Argirusis, M. Kilo, G. Borchardt, K. D. Luther, and W. Assmus. Correlation between ionic radius and cation diffusion in stabilised zirconia. *Solid State Ionics*, 173(14):51–56, 2004.

[167] M. Kilo, M. A. Taylor, C. Argirusis, G. Borchardt, S. Weber, H. Scherrer, and R. A. Jackson. Lanthanide transport in stabilized zirconias: Interrelation between ionic radius and diffusion coefficient. *The Journal of chemical physics*, 121(11):5482–5487, 2004.

[168] K. Kowalski, A. Bernasik, and A. Sadowski. Bulk and grain boundary diffusion of titanium in yttria-stabilized zirconia. *Journal of the European Ceramic Society*, 20(7):951–958, 2000.

[169] K. Kowalski, A. Bernasik, and A. Sadowski. Diffusion of calcium in yttria stabilized zirconia ceramics. *Journal of the European Ceramic Society*, 20(12):2095–2100, 2000.

[170] T. Bak, J. Nowotny, K. Prince, M. Rekas, and C. C. Sorrell. Grain Boundary Diffusion of Magnesium in Zirconia. *Journal of the American Ceramic Society*, 85(9):2244–2250, 2002.

[171] H. Drings, U. Brossmann, H.-D. Carstanjen, A. g. Szökefalvi-Nagy, C. Noll, and H.-E. Schaefer. Enhanced ^{95}Zr diffusion in grain boundaries of nano-crystalline ZrO_2-9.5 mol% Y_2O_3. *physica status solidi (a)*, 206(1):54–58, 2009.

[172] C. Rockenhäuser, B. Butz, N. Schichtel, J. Janek, R. Oberacker, M. J. Hoffmann, and D. Gerthsen. Microstructure evolution and cation interdiffusion in thin Gd_2O_3 films on CeO_2 substrates. *Journal of the European Ceramic Society*, 34(5):1235–1242, 2014.

[173] A. E. Hughes and S. P. S. Badwal. Impurity segregation study at the surface of yttria-zirconia electrolytes by XPS. *Solid State Ionics*, 40-41, Part 1(0):312–315, 1990.

[174] A. E. Hughes and S. P. S. Badwal. Impurity and yttrium segregation in yttria-tetragonal zirconia. *Solid State Ionics*, 46(34):265–274, 1991.

[175] G. S. A. M. Theunissen, A. J. A. Winnubst, and A. J. Burggraaf. Segregation aspects in the ZrO_2-Y_2O_3 ceramic system. *Journal of Materials Science Letters*, 8(1):55–57, 1989.

[176] A. E. Hughes. Segregation in Single-Crystal Fully Stabilized Yttria-Zirconia. *Journal of the American Ceramic Society*, 78(2):369–378, 1995.

[177] M. de Ridder, R. G. van Welzenis, H. H. Brongersma, and U. Kreissig. Oxygen exchange and diffusion in the near surface of pure and modified yttria-stabilised zirconia. *Solid State Ionics*, 158(12):67–77, 2003.

[178] J. Nowotny, C. C. Sorrell, and T. Bak. Segregation in zirconia: equilibrium versus non-equilibrium segregation. *Surface and Interface Analysis*, 37(3):316–324, 2005.

[179] M. de Ridder, R. G. van Welzenis, H. H. Brongersma, S. Wulff, W. F. Chu, and W. Weppner. Discovery of the rate limiting step in solid oxide fuel cells by LEIS. *Nuclear Instruments and Methods in Physics Research Section B: Beam Interactions with Materials and Atoms*, 190(14):732–735, 2002.

[180] P. J. Scanlon, R. A. M. Bink, F. P. F. van Berkel, G. M. Christie, L. J. van Ijzendoorn, H. H. Brongersma, and R. G. van Welzenis. Surface composition of ceramic CeGd-oxide. *Solid State Ionics*, 112(12):123–130, 1998.

[181] H. B. Lee, F. B. Prinz, and W. Cai. Atomistic simulations of surface segregation of defects in solid oxide electrolytes. *Acta Materialia*, 58(6):2197–2206, 2010.

[182] A. Ismail, J. B. Giorgi, and T. K. Woo. On the Atomistic Interactions That Direct Ion Conductivity and Defect Segregation in the Bulk and Surface of Samarium-Doped Ceria: A Genetic Algorithm Study. *The Journal of Physical Chemistry C*, 116(1):704–713, 2011.

[183] C. R. Stanek, R. W. Grimes, M. J. D. Rushton, K. J. McClellan, and R. D. Rawlings. Surface dependent segregation of Y_2O_3 in t-ZrO_2. *Philosophical Magazine Letters*, 85(9):445–453, 2005.

[184] R. Eason. *Pulsed Laser Deposition of Thin Films: Applications-Led Growth of Functional Materials*. John Wiley & Sons, 2007.

[185] M. N. R. Ashfold, F. Claeyssens, G. M. Fuge, and S. J. Henley. Pulsed laser ablation and deposition of thin films. *Chemical Society Reviews*, 33(1):23–31, 2004.

[186] FullProf Suite. *Version 5.60 - Jan2015-ILL JRC*. 2015.

[187] M. Birkholz. *Thin Film Analysis by X-Ray Scattering*. Wiley-VCH Verlag GmbH & Co. KGaA, 2006.

[188] L. D. Doucette, M. P. da Cunha, and R. J. Lad. Precise orientation of single crystals by a simple x-ray diffraction rocking curve method. *Review of Scientific Instruments*, 76(3):036106, 2005.

[189] D. B. Williams and C. B. Carter. *Transmission Electron Microscopy: A Textbook for Materials Science*. Plenum Press, New York, EE. UU,, 2009.

[190] R. M. Langford and A. K. Petford-Long. Preparation of transmission electron microscopy cross-section specimens using focused ion beam milling. *Journal of Vacuum Science & Technology A*, 19(5):2186–2193, 2001.

[191] J. T. S. Irvine, D. C. Sinclair, and A. R. West. Electroceramics: Characterization by Impedance Spectroscopy. *Advanced Materials*, 2(3):132–138, 1990.

[192] B. E. McNealy and J. L. Hertz. On the use of the constant phase element to understand variation in grain boundary properties. *Solid State Ionics*, 256(0):52–60, 2014.

[193] ZView. *Version 3.3a.* Scribner Associates, Inc., Southern Pines, North Carolina, USA, 2014.

[194] J. C. Vickerman and I. S. Gilmore. *Surface Analysis - The Principal Techniques.* John Wiley & Sons, Ltd, 2009.

[195] R. A. De Souza, J. Zehnpfenning, M. Martin, and J. Maier. Determining oxygen isotope profiles in oxides with Time-of-Flight SIMS. *Solid State Ionics*, 176(1516):1465–1471, 2005.

[196] Surface Lab. *version 6.2.* ION-TOF, Münster, Germany, 2012.

[197] MATLAB. *version 7.14.0 (R2012a).* The MathWorks Inc., Natick, Massachusetts, USA, 2012.

[198] A. Fick. On liquid diffusion. *The London, Edinburgh, and Dublin Philosophical Magazine and Journal of Science*, 10(63):30–39, 1855.

[199] J. A. Kilner, B. C. H. Steele, and L. Ilkov. Oxygen self-diffusion studies using negative-ion secondary ion mass spectrometry (SIMS). *Solid State Ionics*, 12(0):89–97, 1984.

[200] R. J. Chater, S. Carter, J. A. Kilner, and B. C. H. Steele. Development of a novel SIMS technique for oxygen self-diffusion and surface exchange coefficient measurements in oxides of high diffusivity. *Solid State Ionics*, 5356, Part 2(0):859–867, 1992.

[201] J. Crank. *The Mathematics of Diffusion.* Clarendon Press, 1979.

[202] M. Burriel, G. Garcia, J. Santiso, J. A. Kilner, R. J. Chater, and S. J. Skinner. Anisotropic oxygen diffusion properties in epitaxial thin films of $La_2NiO_{4+\delta}$. *Journal of Materials Chemistry*, 18(4):416–422, 2008.

[203] L. Wang, R. Merkle, J. Maier, T. Acartrk, and U. Starke. Oxygen tracer diffusion in dense $Ba_{0.5}Sr_{0.5}Co_{0.8}Fe_{0.2}O_{3\delta}$ films. *Applied Physics Letters*, 94(7):071908, 2009.

[204] M. Berglund and M. E. Wieser. Isotopic compositions of the elements 2009 (IUPAC Technical Report). *Pure Appl. Chem.*, 83(2), 2011.

[205] D. R. Killoran. The Effective Duration of a Linear Slow-Cool. *Journal of the Electrochemical Society*, 109:107–171, 1963.

[206] R. A. De Souza, J. A. Kilner, and J. F. Walker. A SIMS study of oxygen tracer diffusion and surface exchange in $La_{0.8}Sr_{0.2}MnO_{3+\delta}$. *Materials Letters*, 43(12):43–52, 2000.

[207] M. J. Pietrowski, R. A. De Souza, M. Fartmann, R. ter Veen, and M. Martin. Oxygen Isotope Transport Properties of Yttria-Stabilized Zirconia (YSZ) in O_2- and H_2O-Containing Atmospheres. *Fuel Cells*, 13(5):673–681, 2013.

[208] M. Daniel and D. Astruc. Gold nanoparticles: assembly, supramolecular chemistry, quantum-size-related properties, and applications toward biology, catalysis, and nanotechnology. *Chemical reviews*, 104(1):293–346, 2004.

[209] H. H. Brongersma, M. Draxler, M. de Ridder, and P. Bauer. Surface composition analysis by low-energy ion scattering. *Surface Science Reports*, 62(3):63–109, 2007.

[210] E. Taglauer. Surface cleaning using sputtering. *Applied Physics A*, 51(3):238–251, 1990.

[211] S. Kim and S. Baik. Effects of surface structures of MgO(100) single crystal substrates on ferroelectric $PbTiO_3$ thin films grown by radio frequency sputtering. *Journal of Vacuum Science & Technology A*, 13(1):95–100, 1995.

[212] S. Kim and S. Baik. Rutherford Backscattering and Channeling Studies of Cleaved, Polished, and Annealed MgO (100) Single Crystals. *Journal of the American Ceramic Society*, 77(1):230–234, 1994.

[213] D. K. Aswal, K. P. Muthe, S. Tawde, S. Chodhury, N. Bagkar, A. Singh, S. K. Gupta, and J. V. Yakhmi. XPS and AFM investigations of annealing induced surface modifications of MgO single crystals. *Journal of Crystal Growth*, 236(4):661–666, 2002.

[214] G. Ballabio, M. Bernasconi, F. Pietrucci, and S. Serra. *Ab initio* study of yttria-stabilized cubic zirconia surfaces. *Physical Review B*, 70(7):075417, 2004.

[215] V. G. Tsirelson, A. S. Avilov, Y. A. Abramov, E. L. Belokoneva, R. Kitaneh, and D. Feil. X-ray and Electron Diffraction Study of MgO. *Acta Crystallographica Section B*, 54(1):8–17, 1998.

[216] K. Sangwal, F. Sanz, J. Servat, and P. Gorostiza. Nature of multilayer steps on the 100 cleavage planes of MgO single crystals. *Surface Science*, 383(1):78–87, 1997.

[217] K. Sangwal, F. Sanz, and P. Gorostiza. Study of the surface morphology of the (100) cleavage planes of MgO single crystals by atomic force microscopy. *Surface Science*, 424(1):139–144, 1999.

[218] J. B. Nelson and D. P. Riley. An experimental investigation of extrapolation methods in the derivation of accurate unit-cell dimensions of crystals. *Proceedings of the Physical Society*, 57(3):160, 1945.

[219] J. Jiang, X. Hu, N. Ye, and J. L. Hertz. Microstructure and Ionic Conductivity of Yttria-Stabilized Zirconia Thin Films Deposited on MgO. *Journal of the American Ceramic Society*, 97(4):1131–1136, 2014.

[220] E. Fabbri, D. Pergolesi, and E. Traversa. Ionic conductivity in oxide heterostructures: the role of interfaces. *Science and Technology of Advanced Materials*, 11(5):054503, 2010.

[221] T. Kushi, K. Sato, A. Unemoto, K. Amezawa, and T. Kawada. Investigation of High Temperature Elastic Modulus and Internal Friction of SOFC Electrolytes Using Resonance Method. *ECS Transactions*, 25(2):1673–1677, 2009.

[222] J. A. Krogstad, Y. Gao, J. Bai, J. Wang, D. M. Lipkin, and C. G. Levi. In Situ Diffraction Study of the High-Temperature Decomposition of t-Zirconia. *Journal of the American Ceramic Society*, 98(1):247–254, 2015.

[223] H. Hayashi, T. Saitou, N. Maruyama, H. Inaba, K. Kawamura, and M. Mori. Thermal expansion coefficient of yttria stabilized zirconia for various yttria contents. *Solid State Ionics*, 176(56):613–619, 2005.

[224] I. Yasuda and M. Hishinuma. Lattice expansion of acceptor-doped lanthanum chromites under high-temperature reducing atmospheres. *Electrochemistry*, 68(6):526–530, 2000.

[225] G. K. White and O. L. Anderson. Grüneisen Parameter of Magnesium Oxide. *Journal of Applied Physics*, 37(1):430–432, 1966.

[226] W. M. Yim and R. J. Paff. Thermal expansion of AlN, sapphire, and silicon. *Journal of Applied Physics*, 45(3):1456–1457, 1974.

[227] S. R. Bishop. Chemical expansion of solid oxide fuel cell materials: A brief overview. *Acta Mechanica Sinica*, 29(3):312–317, 2013.

[228] V. M. Orera, R. I. Merino, Y. Chen, R. Cases, and P. J. Alonso. Intrinsic electron and hole defects in stabilized zirconia single crystals. *Physical Review B*, 42(16):9782–9789, 1990.

[229] M. B. Pomfret, C. Stoltz, B. Varughese, and R. A. Walker. Structural and Compositional Characterization of Yttria-Stabilized Zirconia: Evidence of Surface-Stabilized, Low-Valence Metal Species. *Analytical Chemistry*, 77(6):1791–1795, 2005.

[230] R. Eason. *Pulsed Laser Deposition of Thin Films: Applications-Led Growth of Functional Materials*. Wiley, 2007.

[231] D. G. Lamas and N. E. Walsöe De Reca. X-ray diffraction study of compositionally homogeneous, nanocrystalline yttria-doped zirconia powders. *Journal of Materials Science*, 35(22):5563–5567, 2000.

[232] J. Jiang and J. Hertz. On the variability of reported ionic conductivity in nanoscale YSZ thin films. *Journal of Electroceramics*, 32(1):37–46, 2014.

[233] J. Jiang, W. Shen, and J. L. Hertz. Fabrication of epitaxial zirconia and ceria thin films with arbitrary dopant and host atom composition. *Thin Solid Films*, 522(0):66–70, 2012.

[234] J. Krupka, R. G. Geyer, M. Kuhn, and J. H. Hinken. Dielectric properties of single crystals of Al_2O_3, $LaAlO_3$, $NdGaO_3$, $SrTiO_3$, and MgO at cryogenic temperatures. *IEEE Transactions on Microwave Theory and Techniques*, 42(10):1886–1890, 1994.

[235] A. Nakatsuka, O. Ohtaka, H. Arima, N. Nakayama, and T. Mizota. Cubic phase of single-crystal $LaAlO_3$ perovskite synthesized at 4.5 GPa and 1273 K. *Acta Crystallographica Section E*, 61(8):i148–i150, 2005.

[236] R. J. Angel, J. Zhao, N. L. Ross, C. V. Jakeways, S. A. T. Redfern, and M. Berkowski. High-pressure structural evolution of a perovskite solid solution $(La_{1-x},Nd_x)GaO_3$. *Journal of Solid State Chemistry*, 180(12):3408–3424, 2007.

[237] J. Druce, H. Tellez, M. Burriel, M. D. Sharp, L. J. Fawcett, S. N. Cook, D. S. McPhail, T. Ishihara, H. H. Brongersma, and J. A. Kilner. Surface termination and subsurface restructuring of perovskite-based solid oxide electrode materials. *Energy & Environmental Science*, 7(11):3593–3599, 2014.

[238] X. Guo and J. Maier. Grain boundary blocking effect in zirconia: A Schottky barrier analysis. *Journal of the Electrochemical Society*, 148(3):E121–E126, 2001.

[239] A. Atkinson and A. Selcuk. Mechanical behaviour of ceramic oxygen ion-conducting membranes. *Solid State Ionics*, 134(12):59–66, 2000.

[240] SRIM - The Stopping and Range of Ions in Solids. *SRIM-2013*. J. F. Ziegler, 2013.

[241] T. Kudo and H. Obayashi. Oxygen Ion Conduction of the Fluorite-Type Ce_{1-x} Ln_x $O_{2-x/2}$(Ln=Lanthanoid Element). *Journal of The Electrochemical Society*, 122(1):142–147, 1975.

[242] R. Burdett. 1296 Dielectric Interface - Datasheet. *Solartron Analytical, Tech. Rep.*, 2008.

List of Publications

Journal Publications from this Thesis

[1] G. F. Harrington, A. Cavallaro, D. McComb, S. J. Skinner, and J. A. Kilner, "The effect of substrate roughness on the orientation of YSZ films grown by PLD," *in preparation*.

[2] G. F. Harrington, A. Cavallaro, D. McComb, S. J. Skinner, and J. A. Kilner, "Isolating the origins of modified oxygen transport in YSZ thin films," *in preparation*.

[3] G. F. Harrington, D. McComb, S. J. Skinner, and J. A. Kilner, "Gd segregation in CGO thin films: effects of thermal history and lattice strain," *in preparation*.

Conference Contributions from this Thesis

[1] G. F. Harrington, A. Cavallaro, D. McComb, S. J. Skinner, and J. A. Kilner, "Mechano-chemical engineering: Can strained oxide ion conductors provide a route to next-generation energy and information storage devices?", *Energy Materials Symposium*, Bath, UK, 2014 (oral presentation)

[2] G. F. Harrington, A. Cavallaro, D. McComb, S. J. Skinner, and J. A. Kilner, "Isolating the influence of microstructural and strain properties on the oxygen ion transport in YSZ thin films", *European Fuel Cell Forum*, Lucerne, Switzerland, 2014 (oral presentation)

[3] G. F. Harrington, A. Cavallaro, D. McComb, S. J. Skinner, and J. A. Kilner, "Isolating the influence of microstructural and strain properties on the oxygen ion transport in YSZ thin films", *European-Materials Research Society Spring Meeting*, Lille, France, 2014 (oral presentation)

[4] G. F. Harrington, D. McComb, S. J. Skinner, and J. A. Kilner, "The effect of orientation, thickness and lattice strain of the surface segregation in CGO thin films", *European Fuel Cell Forum*, Lucerne, Switzerland, 2014 (oral presentation)

[5] G. F. Harrington, A. Cavallaro, D. McComb, S. J. Skinner, and J. A. Kilner, "Isolating microstructural and strain effects on the transport properties in YSZ thin

films", *Materials Research Society Spring Meeting*, San Francisco, USA, 2014 (oral presentation)

[6] G. F. Harrington, D. McComb, S. J. Skinner, and J. A. Kilner, "Surface segregation in CGO films as a function of orientation, thickness and lattice strain", *Materials Research Society Spring Meeting*, San Francisco, USA, 2014 (poster presentation)

[7] G. F. Harrington, A. Cavallaro, D. McComb, S. J. Skinner, and J. A. Kilner, "Mechano-chemical engineering: Can strained oxide ion conductors provide a route to next-generation energy and information storage devices?", *RSC Solid State Group Christmas Meeting*, Bath, UK, 2013 (poster presentation)

[8] G. F. Harrington, A. Cavallaro, D. McComb, S. J. Skinner, and J. A. Kilner, "Can strained oxide ion conductors provide a route to low-temperature SOFCs?", *H2FC Supergen Researchers Meeting*, Birmingham, UK, 2013 (oral presentation)

[9] G. F. Harrington, A. Cavallaro, D. McComb, S. J. Skinner, and J. A. Kilner, "Strained YSZ interfaces: A pathway to super ionic conductivity?", *Early Career Energy Sector Chemists Symposium*, London, UK, 2013 (poster presentation)

[10] G. F. Harrington, A. Cavallaro, D. McComb, S. J. Skinner, and J. A. Kilner, "Strained YSZ interfaces: A pathway to super ionic conductivity?", *Functional Inorganic Materials*, Liverpool, UK, 2013 (poster presentation)

[11] G. F. Harrington, A. Cavallaro, D. McComb, S. J. Skinner, and J. A. Kilner, "Interfacial properties of YSZ films on MgO", *SIMS & Scattering Workshop*, Surrey, UK, 2013 (poster presentation)

[12] G. F. Harrington, A. Cavallaro, D. McComb, S. J. Skinner, and J. A. Kilner, "Interfacial properties of YSZ films on MgO", *19th Solid State Ionics conference*, Kyoto, Japan, 2013 (poster presentation)

[13] G. F. Harrington, A. Cavallaro, D. McComb, S. J. Skinner, and J. A. Kilner, "The Effect of Interface Quality on the Conductivity of YSZ Thin Films Grown on MgO by PLD", *Materials Research Society Fall Meeting*, Boston, USA, 2012 (oral presentation)